

# Characterisation of Fibre Metal Laminates under Thermo-mechanical Loadings



# Characterisation of Fibre Metal Laminates under Thermo-mechanical Loadings

## **PROEFSCHRIFT**

ter verkrijging van de graad van doctor  
aan de Technische Universiteit Delft,  
op gezag van de Rector Magnificus prof. dr. ir. J.T. Fokkema,  
in het openbaar te verdedigen ten overstaan van een commissie,  
door het College voor Promoties aangewezen,  
op dinsdag 15 november 2005 te 13:00 uur

door

**Michiel HAGENBEEK**

ingenieur luchtvaart en ruimtevaart  
geboren te Nunspeet

Dit proefschrift is goedgekeurd door de promotor:

Prof. dr. ir. R. de Borst

Samenstelling promotiecommissie:

Rector Magnificus,	Voorzitter
Prof. dr. ir. R. de Borst,	Technische Universiteit Delft, promotor
Prof. dr. ir. R. Benedictus,	Technische Universiteit Delft
Prof. Dr.-Ing. R. Rolfes,	Technische Universität Hannover, Duitsland
Dr. S.R. Turteltaub,	Technische Universiteit Delft
Prof. dr. ir. S. van der Zwaag,	Technische Universiteit Delft
Prof. dr. Z. Gürdal,	Technische Universiteit Delft
Dr. ir. G.H.J.J. Roebroeks,	GTM Consulting (oud- technology manager bij Fibre Metal Laminates centre of Competence)

Copyright © 2005 by M. Hagenbeek

Cover design by M. Hagenbeek - Painting by artist Willemien van Ineveld -  
*In remembrance of Ad Vlot*

ISBN-10 90-9020093-2

ISBN-13 978-90-90200-93-4

Keywords: fibre metal laminates, thermo-mechanical, numerical modelling,  
experiments, glass-fibre epoxy, damage, plasticity, temperature, off-axis effects

All rights reserved. No part of the material protected by this copyright notice  
may be reproduced or utilised in any form or by any means, electronic or  
mechanical, including photocopying, recording or by any other information  
storage and retrieval system, without written permission from the author.

Printed in The Netherlands by PrintPartners Ipskamp, Enschede

# Acknowledgements

The research presented in this thesis has been carried out as a joint research project of the Engineering Mechanics and the Aircraft Materials chair, which both are part of the faculty of Aerospace Engineering at Delft University of Technology.

I would like to gratefully acknowledge my promoter René de Borst for his encouragement and support right from the start and during the project. The name of Ad Vlot must be mentioned as well, since without his enthusiastic and warm-hearted management of the Glare Research Group the idea to start a more in-depth research on the Glare behaviour would not have been born. The admirable testimony of his faith in the living God during his illness, expressed in his last writings and the impressive funeral, are dear memories.

Moreover, I am grateful to all my dear colleagues in the Engineering Mechanics group, in the Aircraft Materials laboratory, and at the Fibre Metal Laminates centre of Competence. It has always been a great privilege to work in such a dynamic and stimulating environment together with social and enthusiastic people. It is impossible to mention them all, but some need to be mentioned in particular. I am much indebted to Jos Sinke, Joris Remmers, Sergio Turteltaub and Cees van Hengel for all their time in advising, discussing, and improving my research. Finally, the good conversations over a cup of coffee with Christian Michler, Doo Bo Chung, André Vaders, and Bart Koene amongst others should be mentioned here, I appreciated it!

*Michiel Hagenbeek  
Delft, July 2005*



# Summary

Fibre metal laminates, such as Arall or Glare, can offer improved properties compared to monolithic materials. Glare for example shows improved fatigue, residual strength, burn-through, impact and corrosion properties with respect to aluminium 2024, together with a considerable weight reduction and competitive costs. A large research program has proven the technological readiness of Glare and the fibre metal laminate has seen its application today in the primary structure of the Airbus A380 super jumbo.

However, the effect of temperature on the performance of the fibre metal laminates has not been fully characterised. Differences in thermal expansion coefficients cause residual stresses after curing of the laminate. In service the temperature of the aircraft skin can vary between -55 up to 70 °C due to solar radiation and convection, which will affect the thermal and mechanical properties of Glare. A detailed understanding of the behaviour of these laminates is necessary for further improvement of their performance and durability. With the increase in complexity of structures and material systems, the need for powerful design tools becomes evident.

In this thesis, the thermo-mechanical behaviour of fibre metal laminates has been characterised via experimental testing and numerical modelling. Experimental tests have been performed to determine the temperature-dependent thermal and mechanical behaviour of unidirectional (UD) glass-fibre epoxy. Calculations based on these test results at room temperature and 80 °C for the tension and shear stiffness of three different composite laminate lay-ups showed a good agreement with experimental test results. The UD glass-fibre epoxy data is used as input for the finite element model, together with aluminium 2024-T3 data from the literature.

Glare laminates with a special lay-up have been experimentally tested to determine the effect of temperature and mechanical loadings on the laminate characteristics. The test results show that the off-axis and temperature effect can give a reduction of 24% in ultimate strength at room temperature due to off-axis loading and a further reduction of 17% at

80 °C temperature. For standard Glare from the literature, where tests at elevated temperature have only been performed in fibre direction, the strength and stiffness reductions are at most 12% compared to room temperature.

Numerical simulation is a very powerful tool to investigate the behaviour of materials and structures. Therefore, a thermo-mechanical finite element model, based on a solid-like shell element and including thermal expansion and heat transfer, has been developed to capture the behaviour of Glare in a fully three-dimensional state. The through-the-thickness temperature and stress distributions can thereby be determined, which allows for a straight-forward implementation of damage and plasticity models. Moreover, the solid-like shell element is ideal for thin-walled (aerospace) structures since it can have high aspect ratios without showing Poisson-thickness locking, which occurs in standard continuum elements, and can have multiple layers in one element.

To account for physical nonlinearities, a strain hardening model for the aluminium 2024-T3 and an orthotropic damage model for the UD glass-fibre epoxy layers in Glare are used. The strain hardening behaviour of aluminium has been modelled with a yield function based on an isotropic Von Mises plasticity formulation. An exponentially saturating hardening law has been assumed, which gives a good agreement with the experimental aluminium 2024-T3 stress-strain curve. A return-mapping algorithm is used to project the stress back onto the yield surface when the stress state violates the loading condition.

The concept of continuum damage mechanics is used, with a separate damage parameter for fibre and matrix, to describe the appearance of microcracks that lead to ultimate failure. The equivalent strain measure is obtained by rewriting the yield function of the orthotropic Hoffman plasticity model into a strain-based format. The damage parameters are directly implemented into the stiffness matrix to avoid undesirable coupling terms in the damage matrix. The simulations of the shear and tensile test in transverse direction show a good fit with the experimental curves for the UD glass-fibre epoxy.

The transient behaviour is captured by taking the heat capacity, inertia forces and damping into account. Park's method is used to solve the dynamic system of equations. The good performance of the thermo-mechanical solid-like shell element and the transient solver have been demonstrated for a single element under thermo-mechanical loadings and the snap-through of a cylindrical panel subjected to a concentrated load.

Via a number of benchmark tests for practical applications the obtained numerical model is compared with the experimental test results. Blunt



notch test simulations have been performed on Glare3-3/2-0.4 and on a special Glare laminate (tested at 0, 45, 67.5, and 90° off-axis angle), which show a good agreement with experimental results. Simulations of off-axis tensile tests on a 0/90 composite, tensile tests on standard Glare laminates, and off-axis tensile tests on special Glare laminates with additional fibre layers in -45 and 45° direction, also showed a good agreement with experimental results.

The thermo-mechanical solid-like shell element and the experimentally obtained material data, presented in this thesis, together create a powerful simulation tool for the effective and accurate characterisation of fibre metal laminates under thermo-mechanical loadings.



# Notation

## Latin symbols

$A$	Area	$\text{mm}^2$
$\mathbf{B}$	Transformation matrix (strain-displacement/temperature)	$\text{m}^{-1}$
$c_p$	Specific heat coefficient	$\text{J/g-K}$
$\mathbf{C}$	Damping matrix	$\text{Ns/m}$
$d$	Notch diameter	$\text{mm}$
$\mathbf{d}$	Damping operator	$\text{kg m/s}$
$\mathbf{D}$	Shell thickness director	-
$\mathbf{D}^{GL}$	Tangential stiffness matrix for Green-Lagrange strains	$\text{GPa}$
$\mathbf{D}^\alpha$	Thermal expansion matrix	$\text{Pa/K}$
$E$	Young's modulus	$\text{GPa}$
$E_1$	Young's modulus in fibre direction	$\text{GPa}$
$E_2$	Young's modulus in transverse direction	$\text{GPa}$
$\mathbf{E}_k$	Covariant surface vector	-
$\mathbf{F}$	Deformation gradient tensor	-
$f$	Yield or damage loading function	-
$\mathbf{f}$	Force vector	$\text{N}$
$g$	Plastic potential	-
$\mathbf{g}$	Gravitation vector	$\text{m}^4/\text{s}^2$
$\mathbf{g}_k$	Base vectors in the deformed configuration	-
$G_{ij}$	Shear modulus	$\text{GPa}$
$\mathbf{G}_k$	Base vectors in the undeformed configuration	-
$h$	Thickness	$\text{mm}$
$h_c$	Convective heat transfer coefficient	$\text{W/m}^2\text{-K}$
$h_r$	Radiative heat transfer coefficient	$\text{W/m}^2\text{-K}$
$\mathbf{h}$	History vector of the generalised momentum	$\text{kg m/s}$
$\mathbf{H}$	Interpolation matrix	-
$\mathbf{I}$	Identity matrix	-

<b>J</b>	Jacobian	-
<b>k</b>	Material conductivity matrix	W/m-K
$k_1$	In-plane heat conduction coefficient in fibre direction	W/m-K
$k_2$	In-plane heat conduction coefficient in transverse direction	W/m-K
$k_3$	Out-of-plane heat conduction coefficient	W/m-K
<b>K</b>	Global stiffness matrix	GPa
<b>K<sup>c</sup></b>	Convection matrix	W/m-K
<b>K<sup>e</sup></b>	Element stiffness matrix	GPa
<b>K<sup>k</sup></b>	Conductivity matrix	W/m-K
<b>K<sup>r</sup></b>	Radiation matrix	W/m-K
$l$	Length	mm
<b>m</b>	Direction of the plastic flow	-
<b>n</b>	Outward normal to surface	-
$S$	Surface	m <sup>2</sup>
$t$	Time	s
$t_\beta$	Modified time-step	s
<b>t</b>	Boundary traction	MPa
<b>u</b>	Displacement vector	m
<b><math>\dot{\mathbf{u}}</math></b>	Velocity vector	m/s
<b><math>\ddot{\mathbf{u}}</math></b>	Acceleration vector	m/s <sup>2</sup>
$v$	Deflection	mm
<b>v</b>	Generalised momentum auxiliary vector	kg m/s
$V$	Volume	m <sup>3</sup>
$w_i$	Integration weights	-
$W$	Width	mm
$W_{\text{int}}$	Internal work	J
$W_{\text{ext}}$	External work	J
$q_c$	Convection heat flux	W/m <sup>2</sup>
$q_r$	Radiation heat flux	W/m <sup>2</sup>
$Q$	Heat flow input	W
<b>x</b>	Position of a material point in the deformed state	-
<b>X</b>	Position of a material point in the undeformed state	-
<b>Z<sub>e</sub></b>	Transformation matrix for global to element coordinate system	-
<b>Greek symbols</b>		
$\alpha$	Rayleigh damping factor	$\mu\text{m}/\text{m-K}$
$\alpha_1$	Thermal expansion coefficient in fibre direction	$\mu\text{m}/\text{m-K}$
$\alpha_2$	Thermal expansion coefficient in transverse direction	$\mu\text{m}/\text{m-K}$
$\beta$	Rayleigh damping factor	-

$\gamma$	Shear strain or Rayleigh damping factor	-
$\gamma$	Green-Lagrange strain tensor	-
$\delta(\ )$	Virtual variation of a quantity	-
$\delta_{ij}$	Kronecker delta	-
$\Delta(\ )$	Increment of given quantity	-
$\epsilon$	Strain	-
$\tilde{\epsilon}$	Equivalent strain	-
$\epsilon$	Eulerian strain tensor	-
$\zeta$	Curvilinear coordinate	-
$\eta$	Curvilinear coordinate	-
$\theta$	Temperature (see the additional notes)	K or °C
$\Theta$	Isoparametric coordinates vector	-
$\kappa$	Hardening parameter, or damage history parameter	-
$\kappa$	Curvature	$m^{-1}$
$\dot{\lambda}$	Plastic flow (plastic multiplier)	-
$\Lambda$	Matrix consisting of (derivatives of) shape function vectors	-
$\mu$	Shell tensor	-
$\nu_{ij}$	Poisson's ratio	-
$\xi$	Curvilinear coordinate	-
$\Pi$	Vector of isoparametric shape functions	-
$\rho$	Density	$g/cm^3$
$\sigma$	Stress	MPa
$\sigma_B$	Stefan-Boltzmann constant	$W/m^2-K^4$
$\sigma$	Piola-Kirchhoff stress tensor	MPa
$\tau$	Shear stress	MPa
$\tau$	Cauchy stress tensor	MPa
$\phi$	Fibre orientation angle	degree
$\phi$	Displacement field vector	m
$\psi$	Factor including emissivity and geometric view factors	$K^3$
$\Psi$	Residual function	-
$\omega$	Internal stretch parameter, or damage parameter	-
$\omega_f$	Fibre damage parameter	-
$\omega_i$	Matrix damage parameters	-
$\Omega$	Damage matrix	-

### Mathematical operators

$\dot{(\ )}$	Material time derivative (undeformed or Lagrangian configuration)
$(\ )'$	Spatial time derivative (deformed or Eulerian configuration)
$\hat{(\ )}$	Nodal representation of a given quantity

---

$( )^T$	Transpose of a given matrix
$( )^{-1}$	Inverse of a given matrix
$\det( )$	Determinant of given matrix
$\text{div}$	$\equiv \text{tr}\left(\frac{\partial( )}{\partial \mathbf{x}}\right)$ Divergence in the deformed configuration
$\text{Div}$	$\equiv \text{tr}\left(\frac{\partial( )}{\partial \mathbf{X}}\right)$ Divergence in the undeformed configuration
$\text{grad}$	$\equiv \frac{\partial( )}{\partial \mathbf{x}}$ Gradient in the deformed configuration
$\nabla$	$\equiv \frac{\partial( )}{\partial \mathbf{X}}$ Gradient in the undeformed configuration
$\text{tr}(\mathbf{A})$	$\equiv \sum_{i=1}^n a_{ii}$ The trace of a given matrix $\mathbf{A}$ with order $n$
$\sum( )$	Summation of given quantity

### Indices

b	Bottom
c	Compression, or convection
e	Specific element
env	Environment
ext	External
el	Elastic
gross	Gross value, i.e. considering the total width
GL	Green-Lagrange
int	Internal
k	Conductivity
max	Maximum
n	Normal to the surface
nel	Number of elements
net	Net value, i.e. considering the effective width
nint	Number of integration points
pl	Plastic
r	Radial, or radiation
RT	Room temperature
t	Top, or tangent
trial	Trial, i.e. estimation
u	Ultimate
y	Yield
0	Undeformed state
1	Fibre direction
2	Transverse direction, perpendicular to the fibre direction
3	Out-of-plane direction
$\alpha$	Thermal quantity
$\phi$	Circumferential

**Abbreviations**

Arall	Aramid reinforced aluminium laminate
BWP	Batch Witness Panel
CLT	Classical Laminate Theory
FML	Fibre Metal Laminate
FVF	Fibre volume fraction
Glare	Glass reinforced aluminium
ID	Identification number
L	Longitudinal direction (aluminium rolling and 0° fibre layer direction)
LT	Longitudinal transverse direction (in-plane)
MVF	Metal Volume Fraction
RT	Room temperature
SEM	Scanning Electron Microscope
ST	Sideways transverse direction (out-of-plane)
UD	Unidirectional

**Additional notes**

In addition to the list of used symbols, indices, and abbreviations some other conventions have to be mentioned. In the chapters about the numerical modelling a vector-matrix notation is applied in this thesis. However, in the description of the thermo-mechanical solid-like shell element tensor notation is used. This tensor notation is transformed into the vector-matrix notation when the element stiffness matrix and the internal force vector are set up. Here, the engineering strains  $\gamma = (\epsilon_{11}, \epsilon_{22}, \epsilon_{33}, 2\epsilon_{12}, 2\epsilon_{23}, 2\epsilon_{31})$  are applied. The stresses are collected in the vector  $\sigma$  with:  $\sigma = (\sigma_{11}, \sigma_{22}, \sigma_{33}, \sigma_{12}, \sigma_{23}, \sigma_{31})$ .

In principle, bold letters represent a vector or a matrix. The corresponding components are denoted by a subscript and sometimes by a superscript. The superscript refers to the contra-variant basis which is applied to describe the solid-like shell element. A subscript preceded by a comma, e.g.  $(\cdot)_{,\lambda}$  denotes the partial derivative with respect to  $\lambda$ . The range of indices belonging to the vector-matrix or tensor notation is introduced when they are applied first.

The temperature can be expressed in degrees Celsius unless radiation is involved, in that case the temperature unit is given in degrees Kelvin ( $K = ^\circ C + 273.15$ ).





# Contents

<b>Acknowledgements</b>	<b>i</b>
<b>Summary</b>	<b>iii</b>
<b>Notation</b>	<b>vii</b>
<b>1 Introduction</b>	<b>1</b>
1.1 Background . . . . .	2
1.2 Objectives . . . . .	4
1.3 Outline . . . . .	4
<b>2 Fibre Metal Laminates</b>	<b>7</b>
2.1 The development of Arall and Glare . . . . .	7
2.2 The constituents and build-up . . . . .	12
2.3 Characteristics of Glare . . . . .	15
2.4 The effect of temperature . . . . .	20
2.5 Summary . . . . .	22
<b>3 The Glare constituents' data</b>	<b>23</b>
3.1 Introduction . . . . .	23
3.2 The S <sub>2</sub> glass-fibre and FM94 epoxy . . . . .	26
3.3 The UD glass-fibre epoxy lamina . . . . .	28
3.3.1 Experimental test set-up . . . . .	28
3.3.2 Mechanical properties of UD glass-fibre epoxy. . . . .	30
3.3.3 Thermal properties of UD glass-fibre epoxy . . . . .	35
3.4 Composite lay-up properties . . . . .	38
3.5 The aluminium 2024-T3 sheet material . . . . .	42
3.5.1 Mechanical properties of aluminium 2024-T3 . . . . .	42
3.5.2 Thermal properties of aluminium 2024-T3 . . . . .	45
3.6 Summary . . . . .	47

<b>4</b>	<b>Experimental tests on Glare</b>	<b>49</b>
4.1	Introduction . . . . .	49
4.2	Test results including temperature and off-axis effect . . . . .	51
4.2.1	Tension tests on special and standard Glare . . . . .	51
4.2.2	Compression tests on special and standard Glare . . . . .	55
4.2.3	Blunt notch tests on special and standard Glare . . . . .	58
4.2.4	Shear tests on special Glare . . . . .	61
4.3	Summary . . . . .	63
<b>5</b>	<b>General numerical framework</b>	<b>65</b>
5.1	Introduction . . . . .	65
5.2	The Finite Element Method . . . . .	66
5.3	Governing equations and discretisation . . . . .	67
5.3.1	The mechanical system of equations . . . . .	67
5.3.2	The weak formulation of the mechanical system . . . . .	68
5.3.3	Discretisation of the mechanical system . . . . .	70
5.3.4	The thermal system of equations . . . . .	71
5.3.5	The weak formulation of the thermal system . . . . .	74
5.3.6	Discretisation of the thermal system . . . . .	76
5.4	Analysis and solution procedure . . . . .	78
5.4.1	Transient analysis . . . . .	78
5.4.2	Nonlinear static analysis . . . . .	81
5.4.3	The incremental-iterative solution procedure . . . . .	82
5.5	Physical nonlinearities . . . . .	85
5.5.1	Strain hardening . . . . .	85
5.5.2	The return-mapping algorithm . . . . .	87
5.5.3	The consistent tangent stiffness matrix . . . . .	89
5.5.4	Damage growth . . . . .	90
5.6	The Jem/Jive numerical software . . . . .	95
5.7	Summary . . . . .	96
<b>6</b>	<b>The thermo-mechanical solid-like shell element</b>	<b>97</b>
6.1	Introduction . . . . .	97
6.2	Element definitions . . . . .	98
6.2.1	Geometry and kinematical description . . . . .	99
6.2.2	The base vectors and the metric matrices . . . . .	101
6.2.3	Green-Lagrange and thermal strain field . . . . .	102
6.2.4	Constitutive relations . . . . .	107
6.2.5	The temperature field . . . . .	108
6.3	Finite element implementation . . . . .	110
6.3.1	The shape functions . . . . .	110

---

6.3.2	Stress independent part of the stiffness matrix . . . . .	112
6.3.3	Stress dependent part of the stiffness matrix . . . . .	113
6.3.4	The strain increment and internal force vector . . . . .	115
6.3.5	Modifications of the stiffness matrix . . . . .	116
6.4	Benchmark tests . . . . .	119
6.4.1	Strip subjected to a heat source . . . . .	119
6.4.2	Bi-material strip subjected to a heat source . . . . .	120
6.4.3	Thick-walled cylinder subjected to temperature . . . . .	122
6.5	Summary . . . . .	129
<b>7</b>	<b>The isotropic hardening model</b>	<b>131</b>
7.1	Introduction . . . . .	131
7.2	The aluminium hardening behaviour . . . . .	132
7.2.1	The Von Mises yield criterion . . . . .	132
7.2.2	The hardening law . . . . .	133
7.2.3	The uniaxial stress-strain curve . . . . .	134
7.3	Benchmark tests . . . . .	135
7.3.1	Blunt notch test on a standard Glare laminate . . . . .	136
7.3.2	Blunt notch tests on special Glare laminates . . . . .	139
7.4	Summary . . . . .	142
<b>8</b>	<b>The orthotropic damage model</b>	<b>143</b>
8.1	Introduction . . . . .	143
8.2	The glass-fibre epoxy damage behaviour . . . . .	144
8.2.1	The equivalent strain . . . . .	144
8.2.2	The effect of damage on the stiffness matrix . . . . .	147
8.2.3	The damage growth laws . . . . .	147
8.3	The tangent stiffness matrix with damage . . . . .	148
8.4	Simulated and experimental stress-strain curves . . . . .	150
8.5	Benchmark tests . . . . .	153
8.5.1	Off-axis tests on 0/90 cross-ply glass-fibre epoxy . . . . .	153
8.5.2	Tensile tests on standard Glare laminates . . . . .	155
8.5.3	Tensile tests on special Glare laminates . . . . .	159
8.6	Summary . . . . .	162
<b>9</b>	<b>The transient model</b>	<b>163</b>
9.1	Introduction . . . . .	163
9.2	Dynamic system response . . . . .	164
9.3	Benchmark tests . . . . .	165
9.3.1	Dynamic response to thermo-mechanical loadings . . . . .	165
9.3.2	Cylindrical panel subjected to a concentrated load . . . . .	168

---

9.4 Summary . . . . .	174
<b>10 Conclusions</b>	<b>175</b>
<b>A Analytical solution for the thick-walled cylinder</b>	<b>177</b>
<b>References</b>	<b>191</b>
<b>Index</b>	<b>193</b>
<b>Samenvatting</b>	<b>195</b>
<b>Publications</b>	<b>202</b>
<b>Curriculum Vitae</b>	<b>203</b>

# Chapter 1

## Introduction

Aviation has taken a giant leap since the first powered flight in aviation history made by the Wright brothers in 1903. Today, the new Airbus A380 super jumbo speaks to the imagination with its sheer size. This aircraft could not have been realised without the invention of new technologies. Besides performance and costs, durability is a major issue in aircraft design and the search for care-free or even self-healing materials and structures continues.

With the increase in complexity of structures and material systems the need for powerful design tools becomes evident. The finite element method

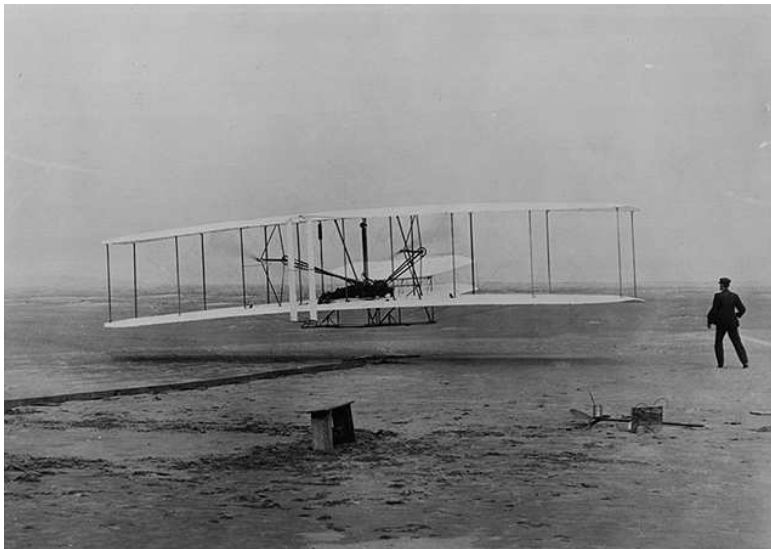


Figure 1.1: The first powered flight in aviation history made by Orville Wright in 1903 at Kitty Hawk, North Carolina.

has become very popular and will also be used in this thesis to characterise the thermo-mechanical behaviour of fibre metal laminates. Though an extensive experimental test program has been carried out on Glare, still a more fundamental knowledge of the material behaviour, especially regarding the effect of temperature, is required. After the description of the background and objectives of this research the chapter is finished with an outline of the thesis.

## 1.1 Background

Since the Second World war, metals—especially aluminium, steel and titanium—are predominantly used in the primary aircraft structure. Fatigue related problems arose amongst others after the pressurisation of the fuselage and the reduction of the skin thickness to increase the aircraft economy. These problems, such as crack growth and multiple-site damage, have been effectively dealt with.

Though accidents still happen, the year 2004 was the safest in commercial aviation since the end of the Second World War according to the International Air Transport Association (IATA 2005). In accidents 428 people died, approximately as much as in 1945, but in 1945 less than 9 million flew while last year about 1.8 billion people travelled by air. For comparison: only in the Netherlands, with 16 million inhabitants, the number of people killed in traffic accidents was about 881 in 2004 (which is the lowest number since the Second World War), as stated by the Centraal Bureau voor de Statistiek (CBS 2005). The aim of the IATA is to reduce the number of fatalities even further with one hundred people before 2007.

These figures show that air travel has reached an eminent safety level, but there are still many opportunities for further improvement left. For the aircraft industry there are three major technology drivers: performance, costs and durability (of which safety aspects are part) with costs being by far the most important one. Besides the improvements in metals through new alloys and manufacturing processes, the use of composites has increased. An extensive use of composites is however mostly limited to commuters and military aircraft. In these areas the form-flexibility and high stiffness properties are highly valued, whereas costs are less important (due to the high demands or the already labour-intensive process).

A real break-through in the application of composites has not yet been seen, though the recently launched Boeing B787 Dreamliner is designed to be a 50%-composite aircraft (Boeing 2005), due to several reasons. An important issue is the damage tolerance of composites. This has led to the

definition of barely visible damage, which despite the difficult detection can already mean a large reduction in strength and stiffness of the structure. Though, in the search for a care-free structure, fatigue-insensitive materials such as composites are likely to play an important role.

In light of the previous considerations, the development of fibre metal laminates is a logic one, in which the best of both worlds are combined. The fatigue performance of Arall and Glare is for example much improved compared to conventional aluminium alloys and the residual strength is higher. However, the use of different constituents also raises new questions especially regarding the thermo-mechanical properties. Differences in thermal expansion coefficients cause residual stresses after curing of the laminate. In service, when the temperature can vary between -55 up to 70 °C due to solar radiation and convection, internal stresses can be expected as well. For asymmetric lay-ups this will lead to secondary bending.

On the other hand, the combination of constituents appears to possess unexpectedly good thermal insulation as observed by (Roebroeks 1997). This property leads to a relative low temperature on the inside of Glare panels in burn-through tests. Moreover, the final burn-through time increases significantly, as shown by (Hooijmeijer and Kuijpers 1999). For civil passenger aircraft, a considerable number of fatalities, in otherwise survivable accidents, are associated with the effects of fire. (van der Kevie 1997) mentions a number of about 19 fatalities per accident involving fire, which has a frequency of occurrence of about 1.5% per ten million flight hours. The application of Glare in the fuselage skin could therefore mean a major improvement in aircraft safety.

Between July 1997 and January 2003 the Glare Research Program was carried out, which was initiated by Structural Laminates Industries and later guided by the Fibre Metal Laminates centre of Competence. In this extensive program the faculty of Aerospace Engineering, the Dutch Aerospace Laboratory and Stork-Fokker participated to achieve readiness for the application of Glare technology in the Airbus A380, see (Vlot 2001a). Besides experimental testing, analytical and numerical methods were established to reduce time-consuming and expensive testing. However, the further development of fibre-metal laminates is important in order to keep a competitive edge with respect to other materials, such as aluminium-lithium, or carbon reinforced polymer. The aircraft design tends to shift more and more towards analytical and numerical methods as the structure and material systems become increasingly complex and the requirements more difficult to achieve. A commonly used numerical method to analyse the structure and to include the specific material behaviour is the finite element method.

## 1.2 Objectives

The aim of the current research is to characterise the thermo-mechanical behaviour of fibre-metal laminates. A profound understanding of the behaviour of these laminates is necessary for further improvement of the performance and durability.

In line with the previously mentioned trend in aircraft design from experiments towards numerical methods, a thermo-mechanical finite element model will be developed. This model, based on a displacement-based (mechanical) solid-like shell element, will be able to capture the thermal and mechanical behaviour in a fully three-dimensional state. To account for physical nonlinearities the following numerical models will be derived:

- A strain hardening model which accounts for the isotropic material behaviour of the metal part in fibre metal laminates, and in specific the aluminium 2024-T3 in Glare.
- An orthotropic damage model which accounts for the fibre and matrix damage in the fibre layers, i.e. the unidirectional glass-fibre epoxy layers in Glare.

The transient behaviour is captured by taking the heat capacity, inertia forces and damping into account. Especially the rate of heat transfer is here of interest. For experimental characterisation, derivation of model input data, and model verification the following program is pursued:

- Experimental tests are performed on glass-fibre epoxy to determine the thermal and mechanical material characteristics. The data is used as input in the finite element model together with experimental data for the aluminium.
- Experimental tests are performed on Glare laminates to determine the effect of temperature and mechanical loadings on the laminate characteristics. An overview of the available data from the literature will be given as well.

Via a number of benchmark tests for practical applications, the obtained numerical model is compared with the experimental test results.

## 1.3 Outline

The research presented in the current thesis consists of both experimental and numerical work performed in two different departments at the faculty



of Aerospace Engineering. The experimental program has been carried out at the Structures and Materials Laboratory, which is amongst others used by the Aerospace Materials department. The numerical tools have been developed in the Engineering Mechanics department. The multidisciplinary contents of the thesis implies that readers with different professional backgrounds may utilise the results. Therefore, in Chapter 2, fibre metal laminates are described in detail. Beside the development of fibre metal laminates (in particular Arall and Glare), the constituents and variants, and the main characteristics are given. Also the concerns regarding the thermo-mechanical behaviour are discussed, which will be the main focus of the present thesis.

In Chapters 3 and 4 the experimental results on, respectively, the Glare constituent properties and Glare laminates are discussed. The aim of Chapter 3 is to determine the temperature-dependent thermal and mechanical properties of glass-fibre epoxy and aluminium in the common service temperature range of a conventional airliner. The data will be used as input in the numerical thermo-mechanical model. In Chapter 4 the effect of temperature on the Glare laminates is shown, which will be used for verification of the model as well.

Chapter 5 describes the general numerical framework, which is used to set up the numerical model and to perform the simulations. In the geometrically and physically nonlinear finite element model the thermo-mechanical behaviour is taken into account. In Chapter 6 the element description is specified. A solid-like shell element is used to cover the behaviour of fibre-metal laminates. The element can have a very high aspect ratio, consist of more layers, and gives a 3D stress-state description. Thus, it allows for the modelling of delamination through the use of interface elements and for easy implementation of physical nonlinearities, such as strain hardening and damage growth.

The topic of strain hardening is dealt with in Chapter 7, in which a Von Mises model is used. Simulations of blunt notch tests are performed and compared with experimental test results. In Chapter 8 the effect of fibre and matrix damage of the glass-fibre epoxy is included in the numerical model. An orthotropic damage model is described, which is derived from a strain-based Hoffman model. The calibration of the model is done with the experimental test results on glass-fibre epoxy described in Chapter 3.

In Chapter 9 the transient analysis is further detailed. Especially the rate of heat transfer is discussed, while the dynamic mechanical response is only briefly mentioned. Finally, in Chapter 10 conclusions are drawn on the performed research and results.



# Chapter 2

## Fibre Metal Laminates

The concept of combining metal and fibre layers into a so-called fibre metal laminate is discussed in this chapter. A brief historical background is given of the development of two specific laminates, Arall and Glare, at the Delft University of Technology. The constituents and build-up of Glare are described in Section 2.2 and the main characteristics in Section 2.3. The characteristics include the high fatigue resistance and residual strength of the material, which were the original objectives in the Glare development.

The different thermal and mechanical behaviour of the constituents also raises new questions, especially in relation with temperature. The difference in thermal expansion of aluminium and glass-fibre epoxy for example leads to internal residual stresses after curing. What will as a consequence of the internal stresses happen in a notched area in the structure when it is subjected to mechanical or thermal loadings?

By means of numerical simulations or experiments the behaviour of the notched laminate can be investigated, see for example the experimental blunt notch test set-up depicted in Figure 2.1. The effect of temperature on the thermo-mechanical laminate properties will be discussed more elaborately in Section 2.4. Experimental results describing the effect of temperature on the constituents and on Glare laminates will be given in Chapters 3 and 4 respectively.

### 2.1 The development of Arall and Glare

The history of the development of fibre metal laminates, in particular Arall and Glare, has been well documented by (Vlot 2001a). A short overview can also be found in (Vlot 2001b). The aircraft manufacturer De Havilland, famous from the wooden fighter-bomber aircraft 'Mosquito', was the first

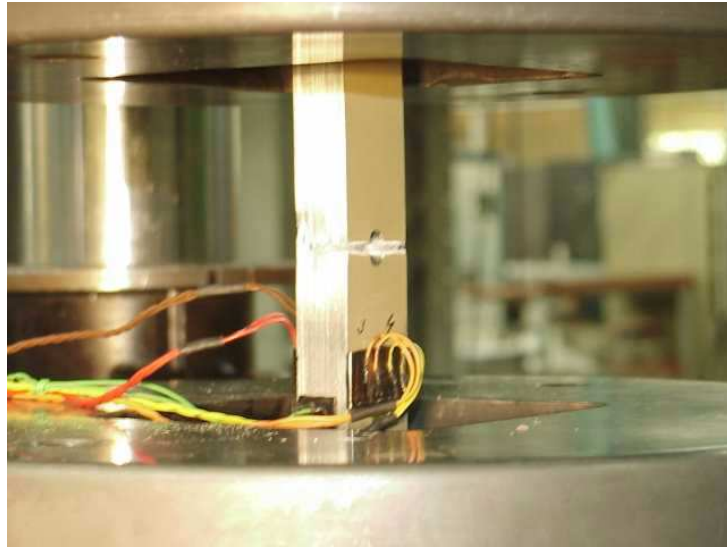


Figure 2.1: Experimental blunt notch test set-up. The specimen can be subjected to a high temperature by means of a temperature chamber (not depicted).

to use metal bonding. A suitable adhesive for metal bonding was discovered in the early 1940's by a British researcher named De Bruijne from Cambridge University. At the same time glass fibres became available on a large scale together with polyester resins that could be cured without high pressure, see (van Tooren 1998). With the introduction of metal bonding and the use of composites by Schliekelmann, who had worked as a trainee at De Havilland in 1946, two major technologies incorporated in Glare became in use at the Fokker company in the 1950's.

Though metal bonding was introduced as an alternative for machining with less investment costs and as an improvement of the compression properties, the laminated structure also appeared to have good fatigue properties due to the crack bridging effect: The inner layers of a laminated material were bridging the fatigue crack in the outer layer. This was an important finding since by then fatigue had become a major issue in aviation due to the Comet accidents, that took place only two years after the introduction of the aircraft in 1952 (Figure 2.2). The cyclic loading of the pressurised cabin caused fatigue crack initiation around rivet holes near the windows and escape/equipment hatches, which led to rupture and explosive decompression of the fuselage.

The damage tolerance of the laminates was even further improved by



Figure 2.2: On 2 May 1952, the world's first commercial jet airline service commenced with the departure from London's Heathrow Airport by De Havilland Comet G-ALYP.

adding fibres to the adhesive, which started in the late 1970's. Moreover, by using unidirectional fibres, the loads in the cracked metal layers were transmitted to the fibres via the adhesive, thus unloading the metal layers and slowing down the crack growth in these layers. This effect is called 'fibre bridging'. Fatigue tests on Arall performed by (Marissen 1988) showed the potential of fibre metal laminates as the crack growth rate could be reduced by a factor 10 to 100. Since the late 1970s aircraft were designed to be damage tolerant and unstable crack growth, found in the two Comets, was prevented by means of crack stoppers and fail-safe structures with multiple load paths, frequent inspection and repair.

Due to the ageing of the aircraft fleet new fatigue problems arose however, which became apparent in an accident with a Boeing 737 of Aloha Airlines in 1988. The presence of accumulated fatigue cracks at many rivets, called multiple site damage, caused one-third of the upper fuselage to be teared open, as shown in Figure 2.3. Fatigue again became an important issue that stimulated the further development of Arall.

However, a disadvantage of the Arall material was the residual tensile stress in the metal layers after curing due to the different coefficients of thermal expansion. Moreover, the aramid fibre yielded a too low residual strength for a cross-ply laminate, absorbed moisture and was sensitive to environmental degradation. The aramid fibres also behaved weakly un-



Figure 2.3: Accident with a Boeing 737 of Aloha Airlines in 1988 due to multiple site damage showing the importance of fatigue for ageing aircraft and of proper inspection and maintenance.

der compression and would be damaged and break after closure of a crack under loading conditions similar to that of a fuselage, which was discovered by (Homan 1984). By post-stretching, the internal stress distribution could be reversed to create compression in the aluminium and tension in the fibres. The fibre breakage phenomenon was also not shown anymore for the stretched Arall laminates. However, this meant extra costs in the manufacturing process and it left part of the laminate as waste, since the edges of the laminate needed to be clamped.

With the commercial introduction of Arall products, a new version of the fibre metal laminate with glass fibres instead of aramid fibres was being developed in the late 1980s and early 1990s. The material became known as Glare, the acronym for Glass reinforced aluminium. Carbon fibres, which have an even higher stiffness to weight ratio than aramid or glass fibres, were not considered due to their electrical conductivity that could give rise to significant corrosion problems. Instead, (Vermeeren 1988) came up with a carbon-titanium laminate for high temperature application in space structures. The pioneer in the Glare development was (Roebroeks 1991), who changed his Ph.D. research from Arall to Glare. The road towards the application of Glare in a primary aircraft structure still had several years to go, since material and operational cost reduction due to weight savings only was not enough. New production techniques, such as the splicing concept meant a major breakthrough for Glare. It allowed for larger panels, reduced the number of parts and thus reduced the

manufacturing costs. In a paper by (Vogelesang, Schijve, and Fredell 1995) newly discovered beneficial Glare features and properties, amongst which the splicing concept and the impact and fire resistance, were published.

Characteristics	Units	Airbus A380	Boeing 747
Length	[m]	73.0	70.7
Wingspan	[m]	79.8	64.4
Height	[m]	24.1	19.4
Cabinewidth	[m]	6.6	6.1
Max. take-off weight	[tons]	560	397
Max. fuel capacity	[tons]	250	175
Max. engine thrust	[kN]	311	282
No. of passengers		555	416
Maximum range	[km]	15000	13450
Price	[million \$]	218	198

Table 2.1: Comparison between the characteristics of the Airbus A380 and the Boeing 747.

In July 1997 a large project was started for basic Glare technology development, subsidised with 34 million euros by the Dutch Ministry of Economic Affairs. The project was initiated by Structural Laminates Industries (which later merged in the Fibre Metal Laminates centre of Competence) and had the faculty of Aerospace Engineering, the Dutch Aerospace Laboratory (NLR) and Stork-Fokker as participants. The project, which was first known as GTO (Glare Technologie Ontwikkeling) and later as GRP (Glare Research Program) has run until January 2003 and during this period the technology readiness of Glare was proven and accepted for final application in the new Airbus A380 super jumbo, depicted in Figure 2.4. This aircraft fills the gap for the large-aircraft segment in the Airbus family and will give strong competition to the Boeing 747. Table 2.1 shows the characteristics of both aircraft. The leap forward of the Airbus A380 in aircraft size and economics could only be made possible with the introduction of new technologies such as Glare. A brief overview of important developments and test results for Glare from 1997 through 2000 was presented by (Gunnink, Vlot, de Vries, and van der Hoeven 2002). In April 2001 the Fibre Metal Centre of Competence was founded to support customers worldwide in the development, design and production of fibre metal laminate applications.

Though the important issues regarding the behaviour and application of Glare have been solved thanks to the extensive test programs, certainly not all questions have been addressed. Especially in the field of the temperature effect on the material properties a more thorough understanding



Figure 2.4: The new Airbus A380 super jumbo, in which Glare will be applied on a large scale, before take-off from Le Bourget at the Paris Airshow. Photograph by Hans Weerheim.

was still lacking. This will be further discussed in Section 2.4. First the Glare constituents and build-up of the standard configurations and the main characteristics of Glare will be discussed.

## 2.2 The constituents and build-up

Five different standard Glare configurations have been designed until now with either aluminium 7475-T761 and FM906 epoxy, which are the newest laminates designated as High Strength Glare, or aluminium 2024-T3 in combination with FM94 epoxy. The specific fibre lay-up and each their own beneficial characteristics, as shown in Table 2.2 given by (Roebroeks 2001). In between two aluminium alloy sheets two, three or four unidirectional glass-fibre epoxy layers are laid-up in specified orientations.

A schematic picture of the laminate build-up and stacking sequence is given in Figure 2.5. The unidirectional glass-fibre epoxy layer on their turn consists of  $S_2$ -glass-fibres, approximately  $10 \mu\text{m}$  thick, embedded in FM94 epoxy adhesive resulting in a nominally  $0.127 \text{ mm}$  thick prepreg with a fibre volume fraction of 59%. Although the epoxy adhesive is very weak compared to the fibres it provides a very high bond-strength between fibre and metal layers and between the individual fibres. These bond lines often remain intact until cohesive adhesive failure occurs, (Roebroeks 2001).



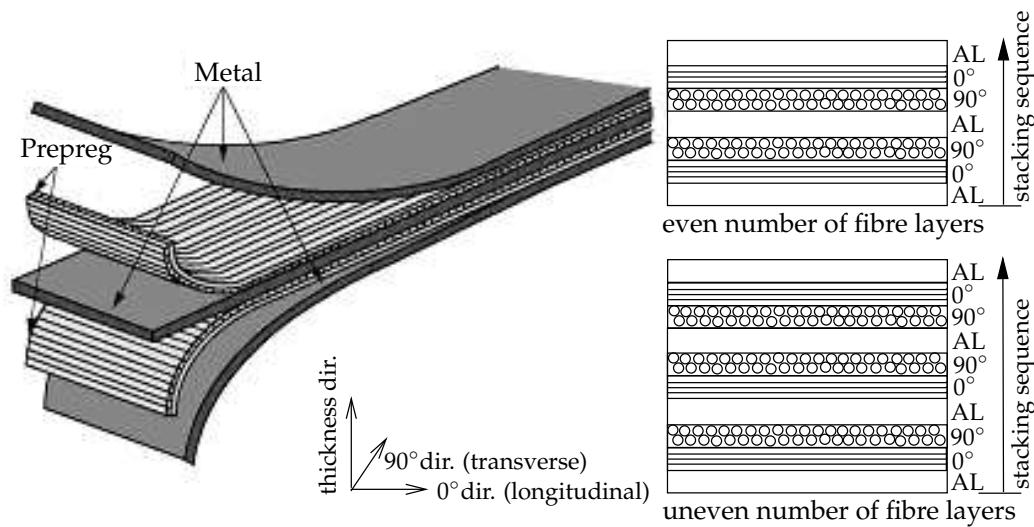


Figure 2.5: Typical laminate lay-up for Glare and stacking sequence in case of an even and uneven number of fibre layers (with  $0^\circ$ ,  $\pm 45^\circ$  or  $90^\circ$  unidirectional glass-fibre epoxy).

The initially developed configurations, Glare 1 and Glare 2, only have fibres in one direction together with respectively aluminium 7075-T6, later replaced by 7475-T761, and aluminium 2024-T3. Both configurations have excellent fatigue properties and extremely high strength. This makes them ideally suited for application in structural parts with mainly one load direction, such as stringers and crack stoppers. The aluminium 7475-T761 in Glare 1 improves the yield stress of the laminate. Nowadays, the Glare 1 laminate has been replaced by a whole new family of laminates with aluminium 7475-T761 in combination with FM906 epoxy (in stead of FM94 epoxy) and similar lay-ups as the original Glare 2 to 6. The  $180^\circ\text{C}$  curing system of FM906 has an improved behaviour at elevated temperature compared to the conventional  $120^\circ\text{C}$  curing system of FM94 epoxy.

For fuselage applications in 1990 'cross-plyed' variants were defined: Glare 3 with 50% of the fibres in one direction and 50% in the transverse direction and Glare 4 with twice as many fibre layers in one direction as in the other direction. Glare 4 is especially suited for locations in the fuselage where the load in the one direction is twice as high as in the other direction. Glare 3 on the other hand is designed for the crown panels of the fuselage where this ratio is one-to-one, due to the combination of pressure loads and the bending of the fuselage under its own weight. Two more

material grades have been developed; Glare 5, which shows in particular good, impact behaviour and has been applied in cargo floors. Glare 6 has improved off-axis and shear properties and was designed for structural parts with high shear loading.

Material grade	Sub	Metal layers		Fibre layers <sup>a</sup>		Main beneficial characteristics
		Alloy type	Thickness [mm]	Orientation <sup>b</sup> [°]	Thickness [mm]	
Glare 2	A	2024-T3	0.2-0.5	0/0	0.254	fatigue, strength
	B	2024-T3	0.2-0.5	90/90	0.254	fatigue, strength
Glare 3	-	2024-T3	0.2-0.5	0/90	0.254	fatigue, impact
Glare 4	A	2024-T3	0.2-0.5	0/90/0	0.381	fatigue, strength in 0° direction
	B	2024-T3	0.2-0.5	90/0/90	0.381	fatigue, strength in 0° direction
Glare 5	-	2024-T3	0.2-0.5	0/90/90/0	0.508	impact
Glare 6	A	2024-T3	0.2-0.5	+45/-45	0.508	shear, off-axis properties
	B	2024-T3	0.2-0.5	-45/+45	0.508	shear, off-axis properties
Glare HS <sup>c</sup> (with FM906)	-	7475-T761	0.3-0.4	see 2-5	see 2-5	fatigue, strength, yield stress

<sup>a</sup> The number of orientations and the thickness listed in this column are equal to the number of UD glass-fibre epoxy prepregs (each nominally 0.127 mm thick) and the total lay-up thickness in between two aluminium layers respectively.

<sup>b</sup> All aluminium rolling directions in standard laminates are in the same orientation; the rolling direction is defined as 0°, the transverse rolling direction is defined as 90°.

<sup>c</sup> High Strength (HS) Glare has similar standard fibre lay-ups for Glare 2 to 5, though with aluminium 7475-T761 and FM906 epoxy instead of aluminium 2024-T3 and FM94 epoxy.

Table 2.2: Material composition and main beneficial characteristics of Glare laminates. Source: (Roebroeks 2001).

For Glare 2, Glare 4, and Glare 6 two sub variants exists named A and B, where the whole fibre lay-up has obtained a 90° rotation. All standard laminates are laid-up symmetrically and start with the orientation indicated in Table 2.2 (and in the centre layer as well in case of uneven number of fibre lay-up stacks). The designation of a specific Glare lay-up, for example Glare 4B-4/3-0.4 consists of the grade (4), the sub variant (B), the number of aluminium sheets (4) and fibre lay-up stacks (3), and the aluminium sheet thickness (0.4) respectively.

The UD glass-fibre epoxy layers between two aluminium layers are stacked symmetrically for Glare 2, Glare 4 and Glare 5. This is not the case for Glare 3 and Glare 6 lay-up which therefore needs further definition.

For Glare 3 the first UD glass-fibre epoxy layer, which is laid on the outer aluminium layer, is placed in the aluminium rolling direction ( $0^\circ$ ). In case of a Glare 3 with an uneven amount of fibre layers, the first UD glass-fibre epoxy layer laid-up in the centre section during production is in the aluminium rolling direction ( $0^\circ$ ). For Glare 6 the situation is comparable, where in case of Glare 6A the  $0^\circ$  direction in the definition of Glare 3 is replaced by  $+45^\circ$  and for Glare 6B the  $0^\circ$  direction is replaced by  $-45^\circ$ .

The thickness sheet metal in the Glare laminates can vary between 0.2 and 0.5 mm for aluminium 2024-T3, and between 0.3 and 0.4 for the aluminium 7475-T761. Different aluminium layer thicknesses can in practice be combined in one laminate in order to change the metal volume fraction and thereby adapting the properties.

Usually a skin panel is a unique product that consists of the baseline skin and a number of doublers, wherein the orientation of the fibre layers, the thicknesses, etcetera can be varied. Thus, special lay-ups can be build for critical parts in the aircraft structure, that are highly and multi-axially loaded, for example around cutouts. Static test performed at room and elevated temperature on thick special-lay-up Glare are described in Chapter 3. In the next section the advantages of Glare will be further discussed.

## 2.3 Characteristics of Glare

The development of Glare was initiated by the fact that the fatigue resistance of bonded metal sheets could even be further improved by adding unidirectional fibres as we saw in Section 2.1. Since glass-fibres are known to be fatigue insensitive it could be asked why the aluminium is still needed. There are several reasons. An important reason is that the aluminium increases the (impact) damage tolerance, which has been an issue for composites since the large-scale introduction in the 1970s. Further on the aluminium allows for easy material handling and construction. Glare material can be milled, drilled, riveted, etcetera in a similar way as monolithic aluminium. The glass fibre epoxy layers on their turn also increase the residual strength of the laminate.

However, there are more advantages of Glare showing that the material combines the 'best of both worlds'. The glass-fibre epoxy layer prevent the occurrence of through-the-thickness corrosion, as shown in Figure 2.6. Moreover, it was found that the thin aluminium 2024-T3 alloy sheet used in Glare is significantly more corrosion-resistant compared to thicker sheet often used in aircraft. The much faster quench of the thin sheet after rolling results in less alloy elements at the crystal boundaries of the material, re-

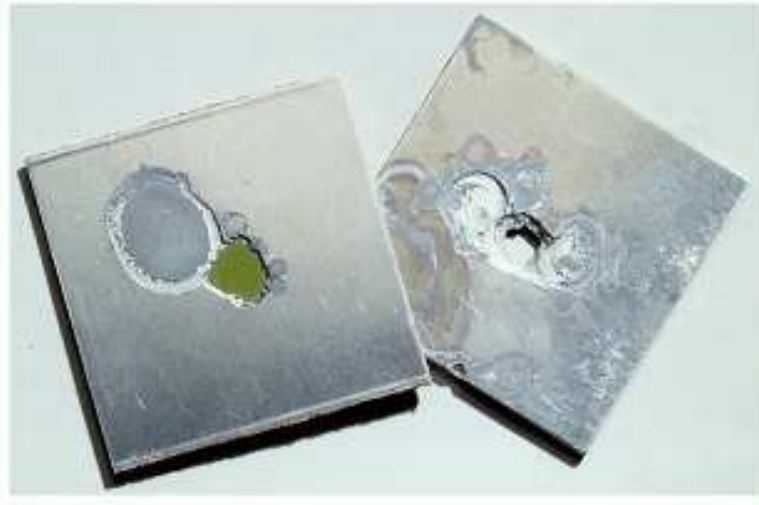


Figure 2.6: Corrosion in Glare is limited to the outer aluminium layer, whereas in monolithic aluminium through-the-thickness corrosion is reached eventually.

sulting in an improved corrosion behaviour, see (Roebroeks 2001).

Complementary to the corrosion protection of the glass-fibre epoxy, the aluminium sheet offers protection of the glass-fibre epoxy layers for degradation due to moisture and ultraviolet-radiation, which both can be a serious threat to the laminate strength and stiffness. The sealant used to prevent moisture penetration at rivet or bolt holes in a conventional aluminium structure at the same time inhibits the moisture absorption in Glare laminates.

Further on, the glass-fibre epoxy layers have a considerably lower weight than monolithic aluminium, 1.96 versus 2.77 g/cm<sup>3</sup>, and can offer approximately 10% material and 20-30% structural weight reduction even for 'cross-plyed' laminates. Since in aircraft design the selection of a material is always a trade-off between many technical, financial and environmental issues, weight is not the only factor, though it is an important one. A weight reduction of one kilogram in the structure means that less lift has to be generated, which reduces the drag and fuel consumption, thus reducing the weight further, etc. This so-called 'snowball effect' therefore has a large impact on the aircraft efficiency and operating costs.

The glass fibres show a favourable strain rate effect; when the strain in the fibres is applied faster the strength and stiffness of the fibres increase. This leads to a better impact resistance for Glare than monolithic alu-



Figure 2.7: Glare leading edges as used in the Airbus A380 horizontal and vertical tail plane. Courtesy Fibre Metal Laminates centre of Competence.

minium. For aramid fibres the strain rate effect is much less pronounced and therefore the impact properties of Arall are less than for Glare. (Vlot 1991) showed that at low velocities Glare is as good as monolithic aluminium and superior to carbon fibre composites, while at higher speeds Glare outperforms aluminium thanks to the strain rate effect and the increased strain hardening caused by the fibres. For this reason, Glare is applied in the horizontal and vertical tail plane leading edges of the Airbus A380, which besides the aerodynamic function must be able to withstand bird impact (Figure 2.7). The numerical modelling and simulations of the bird impact on the leading edge has been presented in a two-part paper; (McCarthy, Xiao, Petrinic, Kamoulakos, and Melito 2004) and (McCarthy, Xiao, McCarthy, Kamoulakos, Ramos, Gallard, and Melito 2004).

An important feature shown after impact is that the damage in Glare, permanent deformation and denting of the aluminium layers, can be easily found by visual inspection. Delamination, matrix cracking or fibre breakage was also found to be limited to the dented area, see impact overview given by (Hagenbeek 2001). In impact tests with ice-balls to simulate hailstorm encounters during approach, see Figure 2.8, damage or delamination was not even found at all (Hagenbeek 1999).

Composites on the other hand do not deform plastically and with barely visible damage on the outside, the laminate can show large delaminations and fibre/matrix damage at the inside. The Glare 5 variant has extra fibre layers to optimise the impact properties and in 1990 this variant was

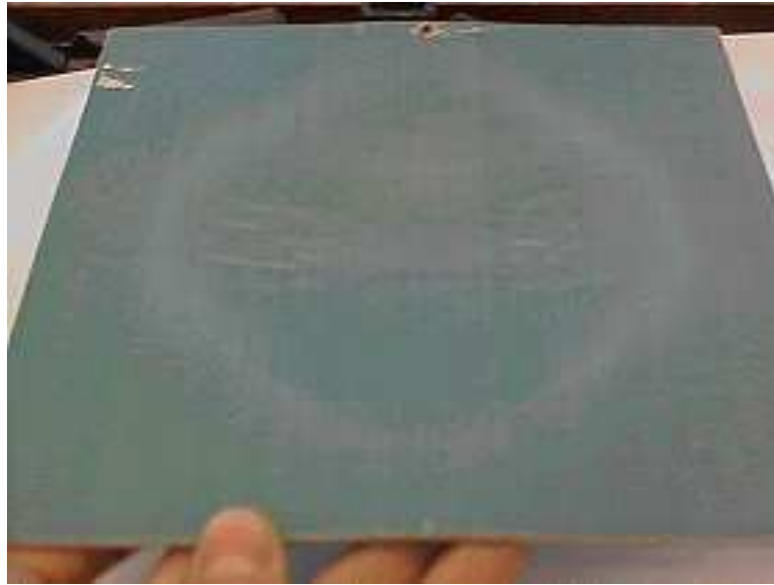


Figure 2.8: No damage or delamination shows after etching away the outer aluminium layer of a Glare 4B-4/3-0.5 specimen, impacted with a 5.7 cm ice ball at a speed of 140m/s.

implemented in the Boeing 777 cargo floor.

In addition to the excellent impact properties it was also found that Glare had good burn-through resistance. Boeing performed fire resistance tests up to 1200 degrees Celsius, which showed that Glare prevented fire from penetrating for more than fifteen minutes. In Figure 2.9 a picture of the burn-through test set-up is shown. The outer aluminium layer quickly melted, but the next layers were able to withstand the flame temperature. While the adhesive carbonised and separated the layers, the insulation was improved and the inside air temperature remained in the order of only one hundred degrees Celsius, (Roebroeks 1997) and (Vlot 2001b). The high value of the heat conduction coefficient for aluminium in this case is favourable for the heat transfer to the surrounding structure. Both damage and fire resistance were demonstrated in a blast-resistant cargo container, shown in Figure 2.10, which was developed by Galaxy Aviation Security and tested by the FAA in 1995. The container is able to withstand the harmful effects of a blast and any flame resulting from the blast is fully contained, (Evancho 2001).

In the early stage of the development Glare was perceived as a material, which had to be transformed to the right shape by the same standard

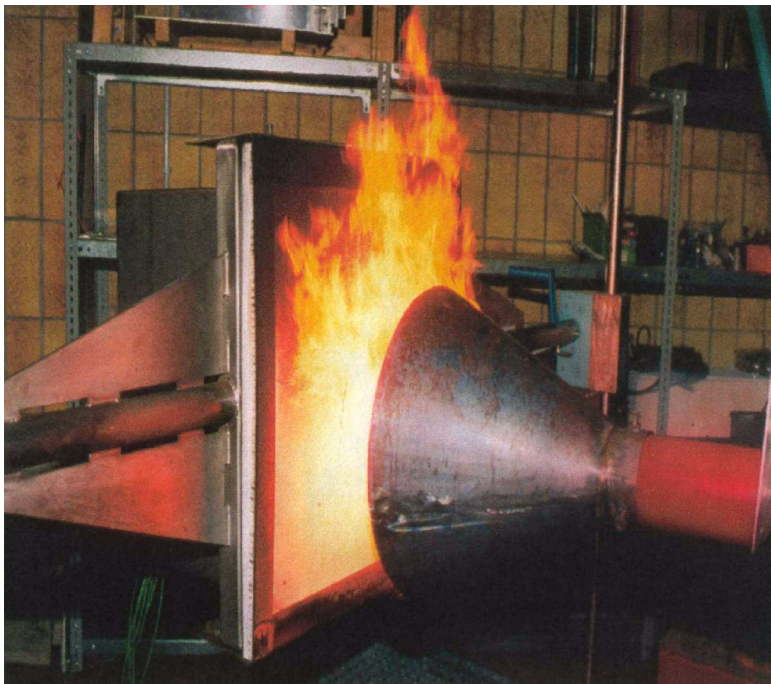


Figure 2.9: Burn-through test set-up to simulate an aircraft post-crash fire condition.

manufacturing tools, such as rubber or stretch forming, as for monolithic aluminium. However, this approach would not lead to success due to the high material costs for Glare and formability limits of the material. The splicing concept and self-forming technique were invented, which allow for relatively easy manufacturing of large structural components. In a splice two adjacent aluminium sheets are connected through uninterrupted fibre layers and optional internal or external doublers. Self-forming means the use of open moulds to produce complete panels, i.e. the skin with stringers and additional doublers, generally in two curing cycles. Both concepts meant a competitive pricing for Glare, since panel prices become comparable, and a break-through in the application of Glare.

This new manufacturing technique for Glare also opened up the way to explore the tailoring of the structure even further. Extra doublers can be added, for example at cutouts, to locally strengthen the structure in the desired direction. Thus by changing the total lay-up, the laminate can be tailored to obtain optimal advantage of the diverse properties. A thick special-lay-up obtained with this approach is tested at room and elevated temperature in Chapter 4. Methods to calculate the total stress-strain be-



Figure 2.10: Glare blast-resistant cargo container. Courtesy Galaxy Aviation Security.

haviour of the laminate must account for the anisotropy of the glass-fibre epoxy layers and the aluminium plasticity, see also (Hagenbeek, van Hengel, Bosker, and Vermeeren 2003).

The high material costs and the lower stiffness compared to aluminium are drawbacks of Glare, which indicates that the material should be applied in fatigue sensitive tension loaded areas, for example in fuselage structures, and manufactured in large-scale (semi-final) products as discussed previously. The possibility of laminate tailoring allows to improve for example the shear properties at desired locations, however the analysis tools also need to be more advanced. The use of different ingredients into one laminate also raises new issues compared to monolithic aluminium, such as the effect of moisture, local defects, or residual stresses after curing due to differences in the thermal expansion coefficients. The temperature related issues will be discussed in the next section.

## 2.4 The effect of temperature

In the search for optimal performance, aluminium and fibre-reinforced epoxy are combined in Glare to obtain 'the best of both worlds'. However,



both materials react very differently to temperature thus raising new questions that need to be addressed. The properties of the Glare constituents can be found in Chapter 3, which presents aluminium 2024-T3 data and the results of a thermal and mechanical test program on glass-fibre epoxy.

The difference in thermal expansion coefficients for aluminium and glass-fibre epoxy causes residual stresses in the laminate after curing. At 120°C the epoxy adhesive starts to solidify by building cross-links in the material. When cooling down from the initial (assumed) stress-free temperature at 120°C, the aluminium sheets shrink more than the glass-fibres. The contraction is prevented and leads to tension in the aluminium and compression in the fibres. Calculations based on Classical Laminate Theory by (Hagenbeek, van Hengel, Bosker, and Vermeeren 2003) show that for Glare 3-3/2-0.3 at room temperature the residual stresses in the aluminium are approximately 20 MPa in tension and 78 MPa in compression for the 0° glass-fibre layer, when loaded in the 0° direction. In the 90° glass-fibre layer the residual stress is much smaller, around 5 MPa in tension. It should be noticed also that the coefficients of thermal expansion are dependent on the temperature as well, see Sections 3.2 and 3.4.

The glass-fibre epoxy has a much smaller thermal conductivity coefficient than aluminium and therefore acts as an isolator. The thermal conductivity of Glare is dominated by the behaviour of the glass-fibre epoxy and is very low as well. Temperature has a large influence on the thermal conductivity of glass-fibre epoxy, though the conductivity remains only a fraction of that of aluminium. The difference in specific heat for aluminium 2024-T3 and glass-fibre epoxy is not that large, 0.89 versus 0.91 J/g-°C respectively at room temperature (see Sections 3.2 and 3.4). Both materials show a clearly temperature-dependent behaviour of the specific heat, which is described in more detail in Chapter 3. Besides the thermal conductivity, the heat capacity is an important property for example if we want to determine how quickly the aircraft skin heats up due to solar radiation.

Thus far, the effect of temperature on the thermal properties and the internal stress distribution has been indicated. The temperature also influences the rate of moisture ingress (Borgonje and van der Hoeven 2001) and the fatigue properties (Alderliesten 2001). From a structural point of view the effect of temperature on the mechanical properties is very important. Due to the plasticising of the epoxy at elevated temperatures the strength and stiffness can be largely reduced. In Chapters 3 and 4 test results including the temperature effect will be discussed for the Glare constituents and standard and special Glare laminates.

## 2.5 Summary

The development of fibre metal laminates started with the idea to improve the fatigue performance of bonded monolithic aluminium sheets by adding fibres to the adhesive. With the replacement of the aramid fibres with glass fibres the best of both the composite and metal world was further explored and Glare laminates were born. Besides fatigue resistance, the material offers higher residual strength, weight reduction, improved impact and corrosion properties, and better fire resistance than monolithic aluminium. With the splicing concept large structural panels can be made at a cost-effective price. The lower yield stress and shear properties can be improved by aluminium 7475-T761 and extra fibre layers under 45°.

Though the important issues regarding the behaviour and application of Glare have been solved thanks to an extensive test program, certainly not all questions have been addressed. Due to the difference in thermal expansion coefficient for aluminium and glass-fibre epoxy it is clear that after curing residual stresses will be present in the laminate. However, the thermal properties, such as the thermal expansion coefficient, thermal conductivity and the heat capacity, are also dependent on the temperature. The temperature affects the mechanical properties of Glare as well, due to the plasticising of the epoxy at elevated temperatures. In Chapters 3 and 4 the effect of temperature on the Glare constituents, and standard and special Glare laminates is determined and described in detail.

# Chapter 3

## The Glare constituents' data

In the previous chapter the lay-up configuration and constituents of Glare were already mentioned together with the main advantages of both the aluminium and the glass-fibre epoxy as present in Glare. In this chapter the thermal and mechanical behaviour of the Glare constituents will be described in detail.

In the introduction the importance and background of a separate investigation on the constituents will be discussed in conjunction with the physical phenomena we want to capture and the corresponding scale of modelling. In the consecutive sections thermal and mechanical properties of the separate glass-fibre and epoxy matrix, the unidirectional (UD) glass-fibre epoxy, the composite lay-up from UD glass-fibre epoxy, and the aluminium 2024-T3 are given as obtained by testing or literature in case of aluminium.

A bottom-up approach is followed, starting from the ingredients towards the complete laminate, to gain insight in the accuracy of the material data. The data will be used in the numerical thermo-mechanical model described in this thesis. For verification of the model an overview of test results on Glare laminates, including the effect of temperature, is given in the next chapter.

### 3.1 Introduction

Glare consists of alternating layers of UD glass-fibre epoxy and thin aluminium sheets, as described in the previous chapter. The behaviour of these two constituents is different, both mechanical and thermal. The UD glass-fibre epoxy for example is a strongly orthotropic material with complex damage mechanisms for the fibre and matrix, whereas aluminium is

an isotropic material that shows plasticity. Though it should be mentioned that due to the rolling process thin aluminium sheets obtain a different behaviour in longitudinal (rolling) direction and transverse direction. Expansion, conduction, and heat capacity also show this orthotropy for the UD glass-fibre epoxy and isotropy for aluminium. The different behaviour of the Glare constituents requires a specific material model for UD glass-fibre epoxy and for aluminium to capture the total laminate behaviour.

One could also follow an engineering approach and determine the behaviour of the whole Glare laminate for each property and configuration. From this data the correlation between the property values of each configuration can then be established. An example of this approach is the Metal Volume Fraction (MVF) method described by (Roebroeks 2000). Though this method reduces the elaborate testing of laminate lay-ups, still many tests on possible laminate lay-ups with inherently complex failure modes (which are determined by both aluminium and the glass-fibre epoxy layers in several orientations) remain necessary. Not yet to speak of the influence temperature can have in all this. Thus, for studying the total laminate behaviour too many variables exist, which makes an accurate investigation of the influence of one of the variables on the behaviour difficult.

For a numerical model to describe the behaviour of fibre metal laminates, and more specifically Glare, accurate material property data is necessary. As discussed above deriving the input data for the laminate as a whole is not a good option. Since the constituents show a different thermal and mechanical behaviour they each require their specific material model and there are too many variables that influence the Glare laminate behaviour. However, the scale of modelling, which depends on the phenomena we want to capture, still needs to be determined. Important physical phenomena that influence the strength and stiffness of a Glare laminate are the effect of plasticity in the aluminium, fibre and matrix damage, delamination, and the effect of temperature on the material properties.

Creep could also play a role, though is expected to be limited. The FM94 glass-fibre epoxy used in Glare was amongst others selected due to the absence of creep effects in fibre direction in the temperature range from  $-55\text{ }^{\circ}\text{C}$  to  $80\text{ }^{\circ}\text{C}$ , as stated by the manufacturer in (Cytac Engineered Materials 2000). The mentioned temperature range is the common service temperature range of the conventional airliner and therefore also considered in the material description of this thesis.

The physical phenomena mentioned above all play an important role on a length scale of 0.1 mm to 1.0 m, the mesoscopic scale, which is the intermediate level between the macroscopic (larger than 1.0 m) and the microscopic scale (less than 0.1 mm). At the macroscopic scale whole struc-

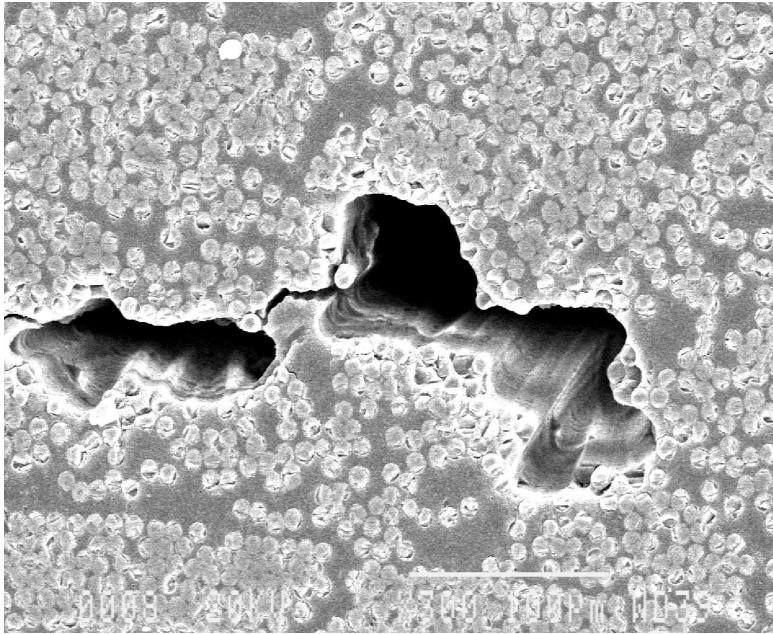


Figure 3.1: The microscopic scale: a SEM picture of a UD glass-fibre epoxy cross-section with voids. Magnification: 300x.

tures, such as for example aircraft fuselages are considered. Whereas at the micro scale small (hair) cracks and fibres become visible such that for example fibre volume fraction or void content can be determined, see Figure 3.1. The mesoscopic scale is the meeting ground of failure mechanisms and structural effects and therefore is of special interest.

The fibre layers as present in Glare can be homogenised to form an orthotropic or quasi-isotropic composite layer. However, it is more advantageous to consider the elementary unidirectional ply. The properties of all possible lay-ups can directly be determined from the elementary ply properties, assuming the different plies interact but do not change each other's properties and all mechanisms are captured with this approach.

Tests on cross-ply lay-ups have been performed to check the prediction methods for the lay-up, based on the elementary ply. The elementary ply properties itself can be compared with property estimates from the fibre and matrix separately. Thus a bottom-up approach is followed which supplies the links between the different levels of homogenisation and clarifies if the total laminate behaviour is the combination of all individual plies (tested in isolation).

### 3.2 The S<sub>2</sub> glass-fibre and FM94 epoxy

In this section the properties of the separate S<sub>2</sub> glass-fibre and the epoxy are discussed and the UD glass-fibre epoxy ply properties at room temperature are calculated. Despite the fact that both the S<sub>2</sub> glass-fibre and the FM94 epoxy are commonly used materials, it is hard to find accurate and complete data. Specific FM94 epoxy data for the thermal and mechanical properties has not been found. The internal data information sheet of (Structural Laminates Industries 1993b) mentions S<sub>2</sub> glass-fibre and AF163-2 epoxy. Most data comes from (Matweb 2004), which besides S<sub>2</sub> glass-fibre data gives general epoxy properties. In Table 3.1 below the S<sub>2</sub> glass-fibre and epoxy properties at room temperature are listed. The effect of temperature on the properties has not been found in the literature.

Property	Unit	S <sub>2</sub> glass-fibre	Epoxy	UD laminate
E <sub>1</sub>	[GPa]	86.9 (88.0 <sup>f</sup> )	3.9 <sup>a</sup> (1.85 <sup>f</sup> )	53.7 (54.0 <sup>f</sup> )
E <sub>2</sub>	[GPa]	86.9 (88.0 <sup>f</sup> )	3.9 <sup>a</sup> (1.85 <sup>f</sup> )	9.1 (9.4 <sup>f</sup> )
$\nu_{12}$	[-]	0.23 (0.33 <sup>f</sup> )	0.37 <sup>b</sup> (0.33 <sup>f</sup> )	0.29 (0.33 <sup>f</sup> )
G <sub>12</sub>	[GPa]	35.3 <sup>c</sup> (33.1 <sup>f</sup> )	1.4 <sup>c</sup> (0.695 <sup>f</sup> )	3.4 (5.5 <sup>f</sup> )
$\alpha_1$	[ $\mu\text{m}/\text{m}\cdot^\circ\text{C}$ ]	1.6 (5.2 <sup>f</sup> )	100.0 (75.0 <sup>f</sup> )	4.5 (6.1 <sup>f</sup> )
$\alpha_2, \alpha_3$	[ $\mu\text{m}/\text{m}\cdot^\circ\text{C}$ ]	1.6 (5.2 <sup>f</sup> )	100.0 (75.0 <sup>f</sup> )	41.0 - 55.2 <sup>d</sup> (26.2 <sup>f</sup> )
$c_p$	[J/g $\cdot^\circ\text{C}$ ]	0.737	1.0	0.84
k <sub>1</sub>	[W/m $\cdot^\circ\text{C}$ ]	1.121 <sup>e</sup> 1.45	0.166 <sup>e</sup> 0.2	0.74 <sup>e</sup> 0.95
k <sub>2, k<sub>3</sub></sub>	[W/m $\cdot^\circ\text{C}$ ]	1.121 <sup>e</sup> 1.45	0.166 <sup>e</sup> 0.2	0.43 <sup>e</sup> 0.53
$\rho$	[g/cm <sup>3</sup> ]	2.46	1.2	1.96 (2.0 <sup>f</sup> )

<sup>a</sup> Estimated stiffness value based on (Spies 1978) and (Shenoi and Wellicome 1993).

<sup>b</sup> Poisson's ratio is taken from (Shenoi and Wellicome 1993).

<sup>c</sup> Calculated value with  $G_{12} = E/2(1 + \nu_{12})$ .

<sup>d</sup> Calculation is based on the alternative rule of mixtures given by (Hyer 1998).

<sup>e</sup> Constituents' data is taken from (Graafmans 1995). The calculation for the UD laminate is based on this data and a rule of mixtures given by (Behrens 1968).

<sup>f</sup> (Structural Laminates Industries 1993b) data and calculation (1993a), based on Classical Laminate Theory found for example in (Spies 1978), (Gürdal, Haftka, and Hajela 1998), (Jones 1999) and (Hyer 1998) amongst others.

Table 3.1: Calculation of the glass-fibre epoxy properties from S<sub>2</sub> glass-fibre and epoxy data from literature and a fibre volume fraction of 60%. If not stated otherwise the constituents' data is taken from (Matweb 2004).

From the separate fibre and matrix properties the UD glass-fibre epoxy

ply properties can be calculated assuming a fibre volume fraction of 60%. This is a general value for prepregs and confirmed by (Hagenbeek 2004b) in which SEM pictures, as shown in Figure 3.2, have been used for the FVF determination. Different calculation methods, from a simple or alternative rule-of-mixtures to a (Voigt 1889) or (Reuss 1929) bound derivation, have been used to come up with realistic calculations. The details can be found in (Hagenbeek 2004b), here we will only mention the results, which will be compared with tested UD glass-fibre epoxy material in the next section.

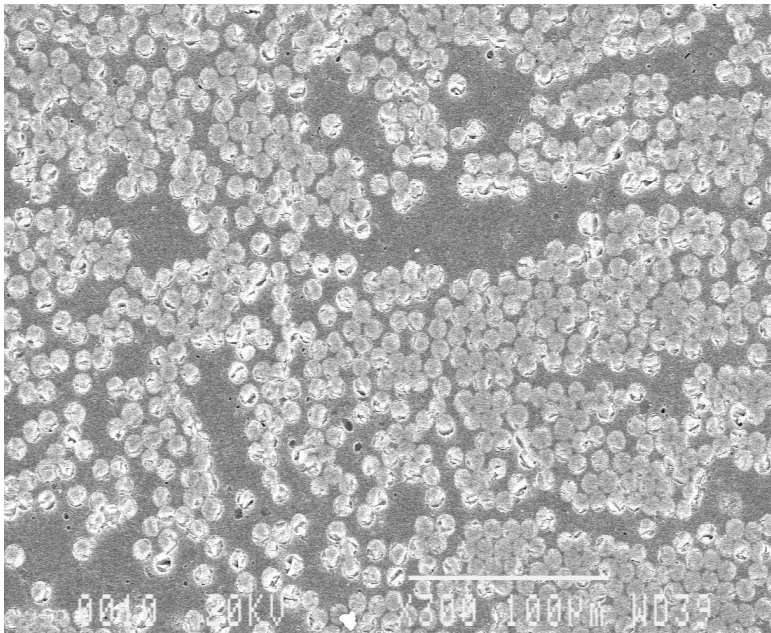


Figure 3.2: SEM picture of a UD glass-fibre epoxy cross-section used for the determination of the fibre volume fraction. Magnification: 300x.

From Table 3.1 it is clear that a concise calculation of the UD glass-fibre epoxy material properties is difficult for several reasons. There is a large variety in property data of the ingredients and specific data for FM94 does not exist. Further on, different calculation methods can be used, which is also a cause of variation in the outcome. The difference in the calculation by (Structural Laminates Industries 1993a) and (Hagenbeek 2004b) is for example 62% for the shear modulus  $G_{12}$  and 53% for the thermal expansion coefficient in transverse direction (either  $\alpha_2$  or  $\alpha_3$ ), therefore the calculated values do not provide a sound basis as input data for numerical models. Moreover, the test values are only given at room temperature, and most properties are expected to be temperature dependent.

### 3.3 The UD glass-fibre epoxy lamina

In the previous section the calculation of the UD glass-fibre epoxy properties showed that they do not provide a sound basis as input data for (numerical) models and can only serve as an estimate. Moreover, the temperature dependency of the properties cannot be derived, since the values are only given at room temperature. Therefore it is necessary to perform both thermal and mechanical tests on the UD glass-fibre epoxy lamina in the temperature range from  $-55\text{ }^{\circ}\text{C}$  to  $80\text{ }^{\circ}\text{C}$ , which is the common service temperature range of the conventional airliner.

In the next section the experimental test set-up will be briefly discussed. Details can be found in the test report written by (Hagenbeek 2004b). An overview of the thermal and mechanical results will be given in Sections 3.3.2 and 3.3.3 respectively, together with a comparison with the calculated properties from Chapter 2 and mechanical tests performed on cross-ply laminates by (Out and Hagenbeek 2002), and (Hagenbeek 2004a). In the mentioned references the shear modulus of the UD glass-fibre epoxy lamina is determined from a tensile test with fibres under  $\pm 45^{\circ}$ .

#### 3.3.1 Experimental test set-up

In the test report by (Hagenbeek 2004b) thermal and mechanical tests performed on the elementary unidirectional FM94 glass-fibre epoxy ply are described. Tensile, compression and shear tests have been performed in fivefold at  $-55\text{ }^{\circ}\text{C}$ , room temperature, and  $80\text{ }^{\circ}\text{C}$ . These temperatures all fall in the temperature range from  $-55\text{ }^{\circ}\text{C}$  to  $80\text{ }^{\circ}\text{C}$ , which is the common service temperature range of the conventional airliner. Though, it should be mentioned that higher temperatures of the aircraft skin have been found on the ground and (Tessmer, Waitz, Rolfes, Ackva, and de Vries 2003) included convection at takeoff to reduce the determined material temperature.

In this temperature range the epoxy manufacturer (Cytac Engineered Materials 2000), states that no creep effects are present in the FM94 glass-fibre epoxy in fibre direction (similar to the aluminium). Though creep might be present perpendicular to the fibre direction in the glass-fibre epoxy, the effect is expected to be small in a Glare laminate and therefore no creep tests have been performed. Additional tests have been performed in transverse direction (LT) to determine the stiffness at intermediate temperatures. In tension the additional tests are performed at 40, 50, 60, 65, 70, 75 and  $80\text{ }^{\circ}\text{C}$ , in compression at 60, 70 and  $75\text{ }^{\circ}\text{C}$ , and in shear at  $-55$ ,  $-20$ ,  $0$ ,  $20$ ,  $40$ ,  $60$ ,  $65$ ,  $70$ ,  $75$ ,  $80\text{ }^{\circ}\text{C}$ . In these cases only one specimen, instead of the standard 3 to 5 specimens, for each type of test is used. This specimen



is loaded repeatedly to a low stress level to avoid that matrix damage will influence the next test, at the above-mentioned temperatures.

The thermal tests include the determination of coefficients of thermal expansion in both 0 (L) and 90 degrees direction (LT) and heat capacity of the glass-fibre epoxy. The coefficients of thermal expansion are determined in the temperature range from -70 to 100 °C. The out-of-plane (ST) thermal expansion coefficient  $\alpha_3$  is equal to the in-plane transverse (LT) coefficient  $\alpha_2$  due to the transverse isotropy of the glass-fibre epoxy. The temperature range for the determination of the heat capacity is from -55 to 180 °C. The heat conduction listed in this report is derived with equations and data from literature and has not been tested. Qualitative analysis, i.e. (micro) voids content and fibre volume fraction (FVF), on the material is done by means of ultrasonic C-scan and Scanning Electron Microscope imaging.

In Table 3.2 below the test matrix is given, which lists all performed thermal and mechanical tests, corresponding test standards, and the number of specimen used for the specific tests. The panel consists of a unidirectional (UD) FM94 glass-fibre epoxy lay-up with 16 layers,  $[0]_{16}$ , and a total nominal thickness of 2.0 mm (16 x 0.127 mm).

Test	Test norm	Number of specimens					
		0° direction (L)			90° direction (LT)		
		-55 °C	RT	80 °C	-55 °C	RT	80 °C
Tension <sup>a</sup>	(ISO-527-5 1997) / (ASTM-D3039 2000)	5	5	5	5	5	5
Compression <sup>b</sup>	(ISO-14126 1999)	5	5	5	5	5	5
Shear <sup>c</sup>	(ASTM-D-5379 1999)	5	5	5	5	5	5
Expansion	(ISO-11359-2 1999)	1			1		
Heat capacity	(ASTM-1269E 2001)	1					
SEM		8					

<sup>a</sup> Additional tests to determine the tension stiffness in transverse direction (LT) have been performed at intermediate temperatures, viz.: 40, 50, 60, 65, 70, 75 and 80 °C.

<sup>b</sup> Additional tests to determine the compression stiffness in transverse direction (LT) have been performed at intermediate temperatures, viz.: 60, 70 and 75 °C.

<sup>c</sup> Additional tests to determine the shear stiffness in transverse direction (LT) have been performed at intermediate temperatures, viz.: -55, -20, 0, 20, 40, 60, 65, 70, 75, 80 °C.

Table 3.2: Test matrix for thermal and mechanical tests on UD glass-fibre epoxy.

### 3.3.2 Mechanical properties of UD glass-fibre epoxy.

The mechanical test results for UD glass-fibre epoxy are listed in this section. From the measured stress-strain curves in tension, compression, and shear, several material properties can be derived: the Young's or shear modulus and the Poisson's ratios in fibre and (longitudinal) transverse direction, the ultimate strength and strain (in case of a correct failure mechanism in the test). An overview of the results is given here, details can be found in the test report, see (Hagenbeek 2004b). In Table 3.3 the mechanical glass-fibre epoxy properties at room temperature are shown and compared with the calculated values based on the constituents' data and a fibre volume fraction of 60%, see Section 3.2. The value for the shear modulus of 3.7 GPa is equal to the mean test value found by (Out and Hagenbeek 2002). The correspondence with the mean value of 3.6 GPa for the UD glass-fibre epoxy lamina determined in the report on the composite lay-up properties, see (Hagenbeek 2004a), is also very good.

Property	Unit	Test	Calculation	Difference [%]
$E_1$ ( $E_{c1}$ )	[GPa]	50.6 (49.9)	53.7	5.8
$E_2$ ( $E_{c2}$ )	[GPa]	9.9 (10.8)	9.1	-8.8
$\nu_{12}$ ( $\nu_{c12}$ )	[-]	0.32 (0.30)	0.29	-10.3
$\nu_{21}$ ( $\nu_{c21}$ )	[-]	0.063 (0.067)	0.05	-28.2
$G_{12}$ ( $G_{c12}$ )	[GPa]	3.7	3.4	-8.8
$\epsilon_{u1}$	[%]	2.5 (4.5) <sup>a</sup>		
$\epsilon_{u2}$	[%]	0.5		

<sup>a</sup> The experimental value is extrapolated to 4.5% strain for use in the numerical model.

Table 3.3: Tested and calculated (see Section 3.2) mechanical UD glass-fibre epoxy properties at room temperature.

In Figure 3.3 the extrapolated uniaxial tension/compression stress-strain curves for UD glass-fibre epoxy in fibre direction are given at the three test temperatures: -55, 22 (room temperature), and 80 °C. The extrapolation is performed since the tests do not give an ultimate strain value in this direction. It is assumed that the ultimate tensile strain is 4.5%, which is a general value from Glare tension test results with correct failure mode. In the tests the ultimate strain is not reached and the specimens fail at the clamping, which is an undesired failure mode. The use of tabs might improve the failure strain, however a correct failure mode is often hard to obtain in composite testing. In compression the same ultimate strain of 4.5% as in tension is assumed, though this value is rather arbitrary since in both the current testing and in Glare testing an undesired (though ex-

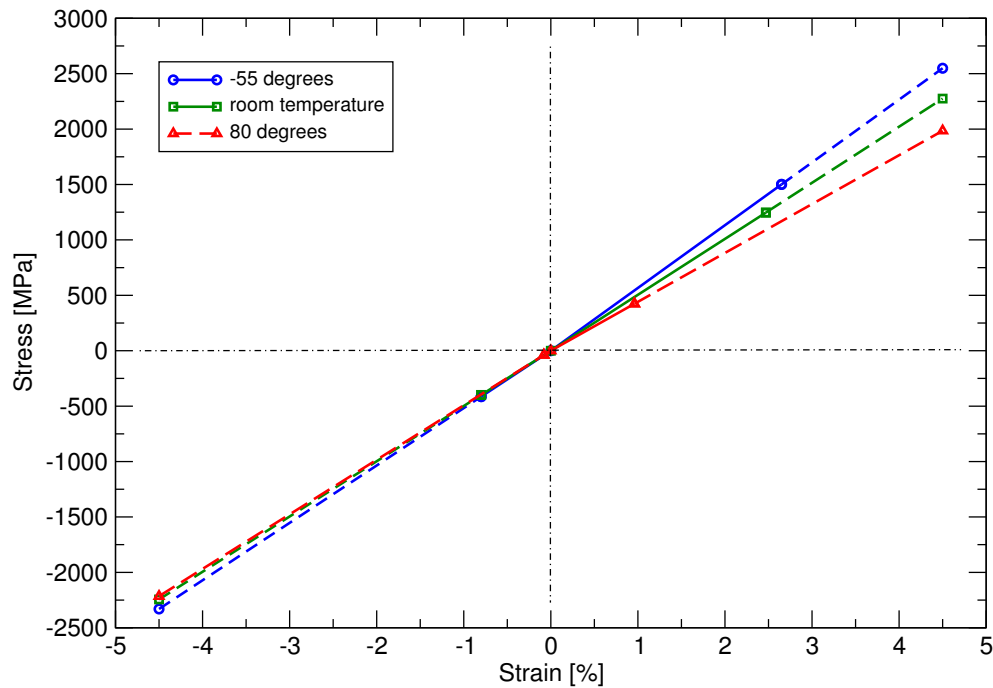


Figure 3.3: Extrapolated uniaxial stress-strain curves for UD glass-fibre epoxy in fibre direction (L) at -55, 22 (room temperature), and 80 °C.

pected) failure mode is found, that is buckling or failure at the edge of the open section in the test fixture.

In Figure 3.4 the experimental uniaxial tension/compression stress-strain curves for UD glass-fibre epoxy in transverse direction (LT) are given at the three test temperatures: -55, 22 (room temperature), and 80 °C. In this case the given failure strains are indeed ultimate strains, since a correct failure mode was found in the tests. From this figure it is clear that there is a significant drop in tension stiffness at 80 °C. The epoxy matrix is very sensitive for high temperature.

The experimental in-plane shear stress-strain curves for UD glass-fibre epoxy at -55, 22 (room temperature), and 80 °C are found in Figure 3.5. The curves are derived from the (Iosipescu) test specimens with the applied loading in fibre direction (L), which show an earlier failure than the specimens loaded transverse to the fibre direction (LT), namely; 4.3% versus a (by the test norm limited) value of 5.0% at room temperature respectively, see (Hagenbeek 2004b). The difference in failure strain can be explained by the axial loading of the fibres in this direction after undesirable bending in the test fixture. Like the tension stiffness, the shear stiffness has a

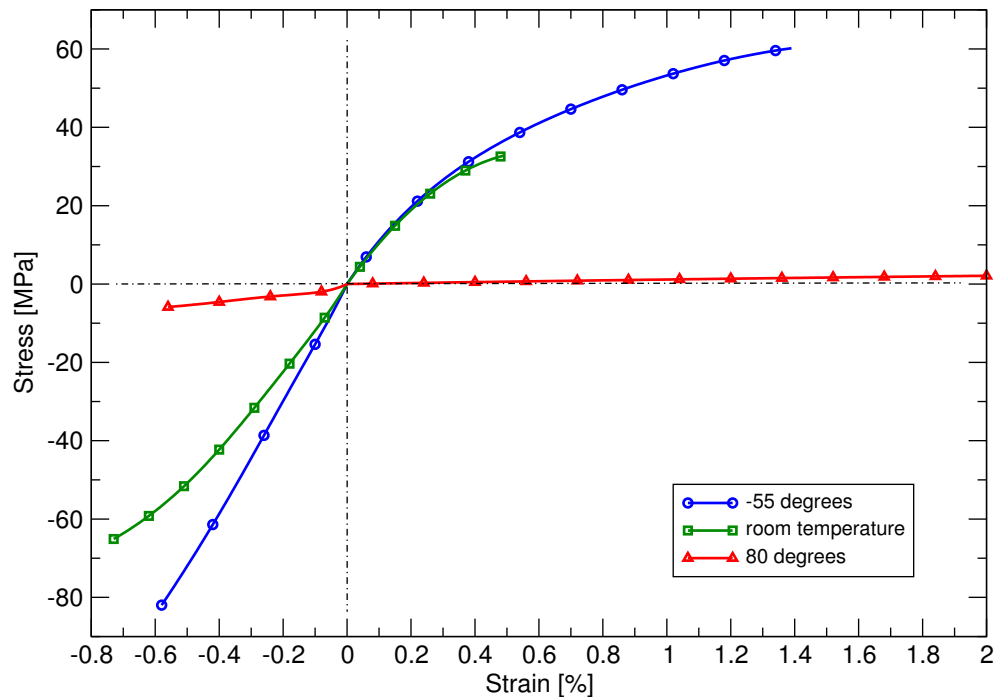


Figure 3.4: Uniaxial stress-strain curves for UD glass-fibre epoxy in transverse direction (LT) at -55, 22 (room temperature), and 80 °C.

significant drop at 80 °C, which is predominately due to the sensitivity of the epoxy matrix for high temperature.

The effect of temperature on the tangent tension, compression and shear stiffness of the UD glass-fibre epoxy is summarised in Figure 3.6 for the fibre direction (L) and Figure 3.7 for the transverse direction (LT). The additional tests for the stiffness determination at intermediate temperatures have been used to obtain the behaviour in the whole temperature range of -55 to 80 °C. The shear stiffness in both figures is determined from the tests with the applied loading in fibre direction.

The (Military Handbook 2002) states that composite laminates should not be used in a temperature range, where the properties do not increase or decrease rapidly and where the glass-transition point is above the maximum operating temperature. Both conditions are not met for the FM94 epoxy as can be seen in Figures 3.7 and 3.9. Though, the overall effect on a Glare laminate is small (see Chapter 4), the use of an epoxy with higher glass-transition point, such as FM906, is sensible.

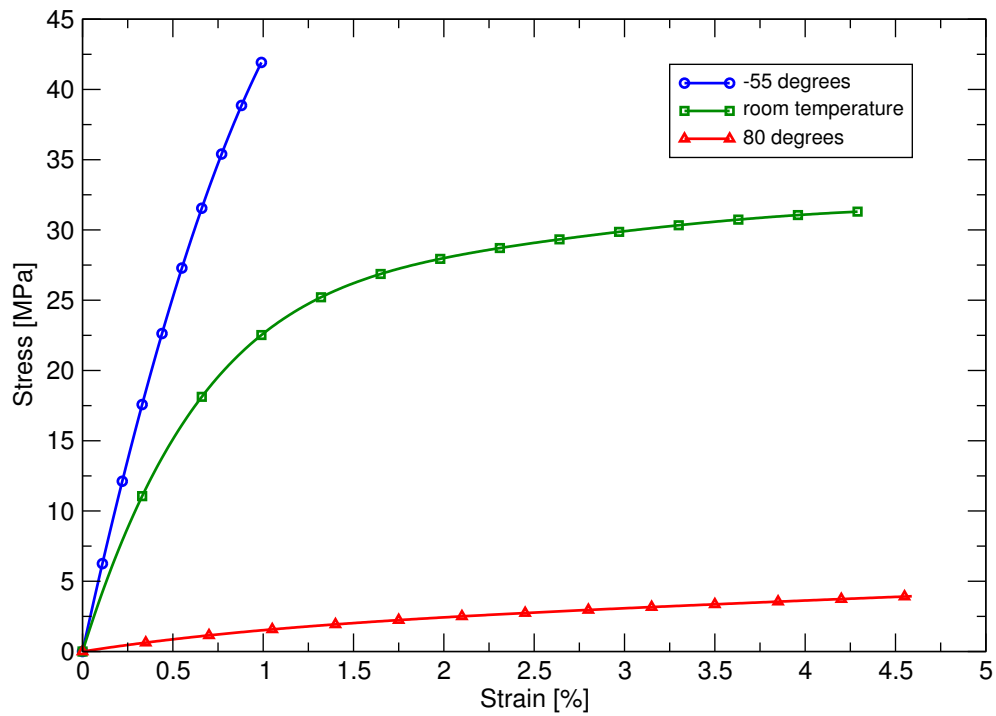


Figure 3.5: Shear stress-strain curves for UD glass-fibre epoxy with applied loading in fibre direction (L) at -55, 22 (RT), and 80 °C.

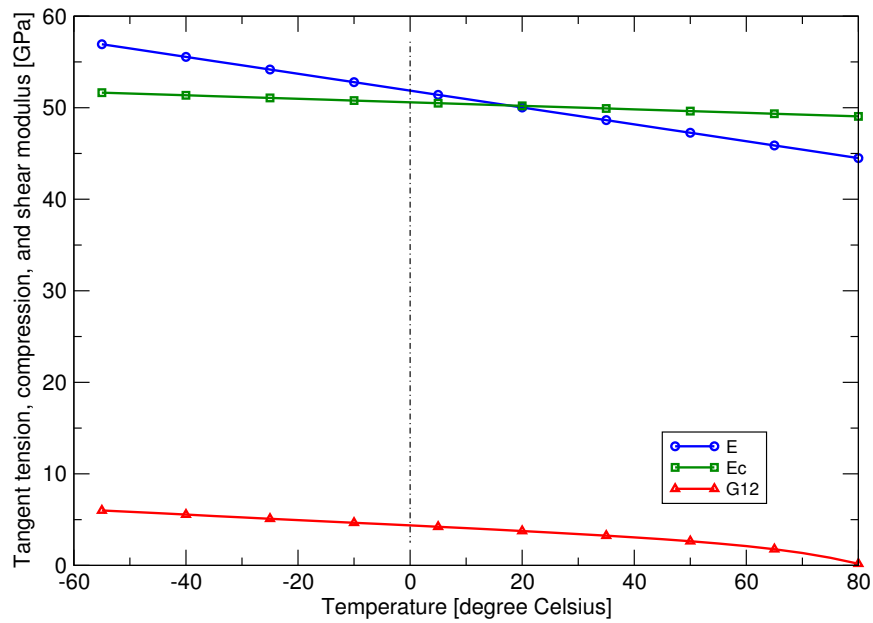


Figure 3.6: Effect of temperature on the tangent tension, compression and shear stiffness in fibre direction (L) of the UD glass-fibre epoxy.

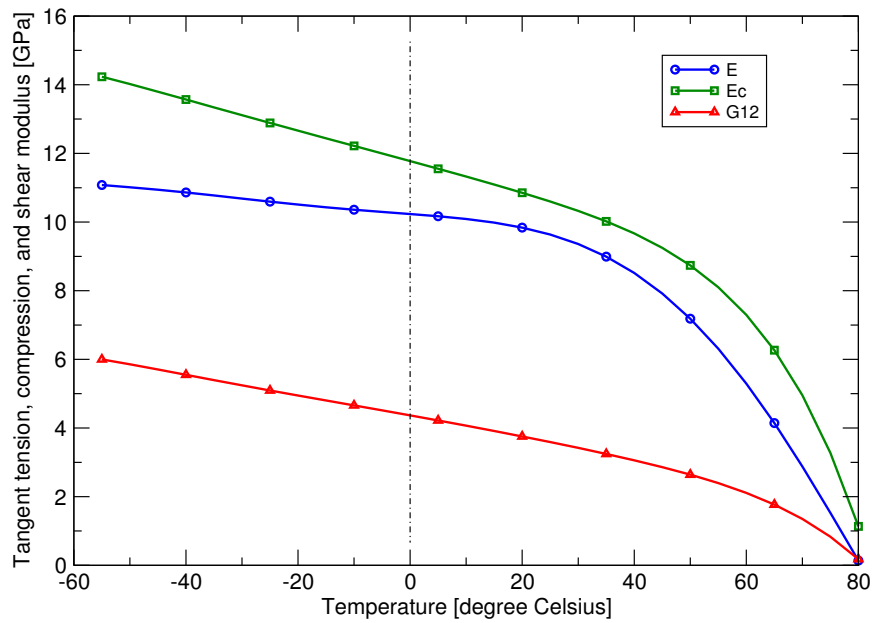


Figure 3.7: Effect of temperature on the tangent tension, compression and shear stiffness in transverse direction (LT) of the UD glass-fibre epoxy.

### 3.3.3 Thermal properties of UD glass-fibre epoxy

The results of the thermal expansion coefficients and the heat capacity tests for UD glass-fibre epoxy at room temperature are given in Table 3.4. The conductivity coefficients for UD glass-fibre epoxy, derived from literature test result for Glare and aluminium, see (Hagenbeek 2004b), are listed in this table as well. The test results are compared with the calculation of the glass-fibre epoxy properties from  $S_2$  glass-fibre and epoxy data from literature and a fibre volume fraction of 60%, as described in Section 3.2.

Property	Unit	Test	Calculation	Difference [%]
$\alpha_1$	$[\mu\text{m}/\text{m}\cdot^\circ\text{C}]$	3.9	4.5	15.4
$\alpha_2$	$[\mu\text{m}/\text{m}\cdot^\circ\text{C}]$	49.7	41.0 - 55.2	-17.5 / 11.1
$c_p$	$[\text{J}/\text{g}\cdot^\circ\text{C}]$	0.91	0.84	-7.7
$k_1$	$[\text{W}/\text{m}\cdot^\circ\text{C}]$	0.929 <sup>a</sup>	0.74 - 0.95	-20.3 / 2.3
$k_2, k_3$	$[\text{W}/\text{m}\cdot^\circ\text{C}]$	0.544 <sup>a</sup>	0.43 - 0.53	-21.0 / -2.6

<sup>a</sup> The data is derived from test data for Glare and aluminium.

Table 3.4: Tested and calculated (see Section 3.2) thermal UD glass-fibre epoxy properties at room temperature. If not stated otherwise the constituents' data is taken from (Matweb 2004).

In Figure 3.8 the thermal expansion coefficients are given in the temperature range from -75 to 105 °C. From the figure it is clear that the coefficient in fibre direction (L) decreases above room temperature. At 105 °C the value is only 3.9 % of the value at 22 °C, whereas the coefficient in transverse direction (LT) shows a significant increase of more than twice the value at room temperature (219 % increase).

The specific heat also shows a clear temperature dependency, as shown in Figure 3.9. Apart from the steady increase with temperature, around 67 °C a peak is found. The region around this peak, from 45 to 80 °C indicates the glass-rubber transition region of the epoxy matrix. In this region also a significant change in expansion coefficient is found as described above and shown in Figure 3.8.

The out-of-plane (ST) thermal conductivity has been derived from Glare 3-3/2-0.2 and aluminium 2024-T3 literature test data. Based on this data a linear out-of-plane (ST) thermal conductivity behaviour is assumed in the temperature range of -100 to 100 °C for both the Glare and the aluminium, see (Hagenbeek 2004b). This yields a linear behaviour for the UD glass-fibre epoxy, shown in Figure 3.10. The in-plane transverse (LT) thermal conductivity for UD glass-fibre epoxy is taken the same as the out-of-plane

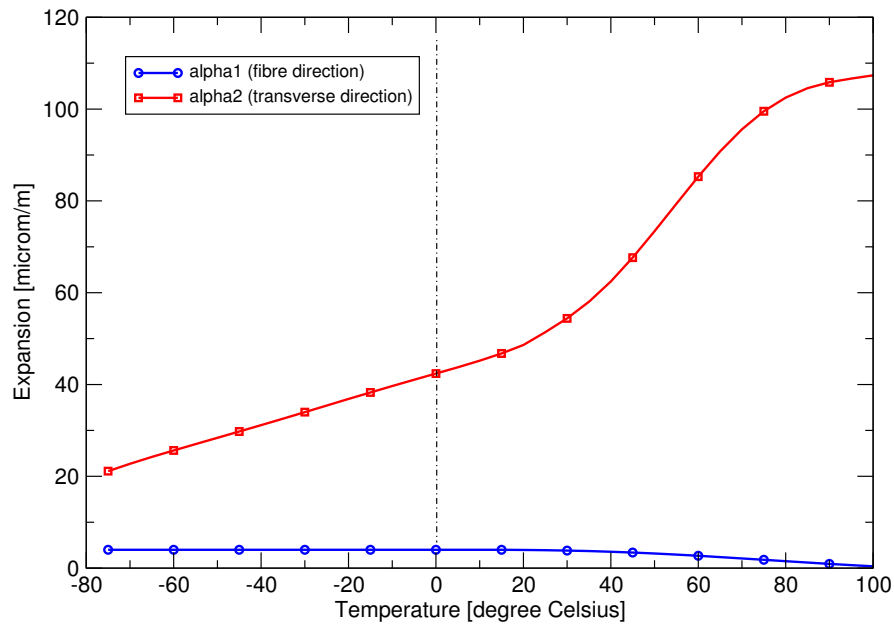


Figure 3.8: The thermal expansion coefficients of UD glass-fibre epoxy in fibre (L) and transverse direction (LT) as a function of temperature.

(ST) thermal conductivity, since the material is transversely isotropic. In fibre direction (L) a similar linear relationship between the temperature and the thermal conductivity is assumed and adapted to a calculated value at room temperature, since test data in this direction is not available for UD glass-fibre epoxy. Other approaches and formulae for the calculation of the transverse conductivity are possible and discussed and validated by (Rolfes and Hammerschmidt 1995).

The thermal conductivity in fibre direction is 71% larger than in transverse direction, though still just 0.7% of the aluminium 2024-T3 value in the temperature range of -100 to 100 °C. The UD glass-fibre epoxy behaves as an isolator in comparison with the aluminium and will dominate the behaviour of Glare, see test report by (Hagenbeek 2004b).



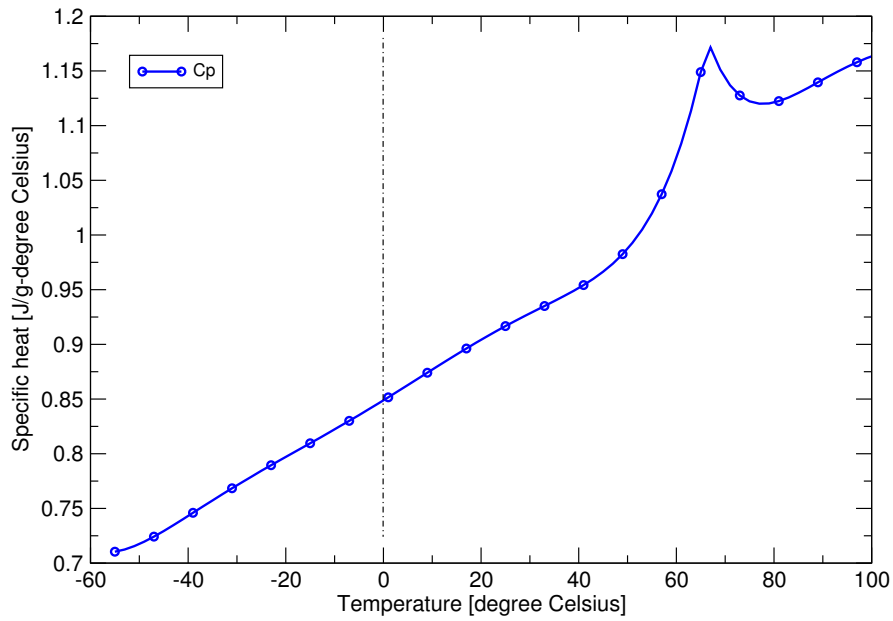


Figure 3.9: The specific heat of UD glass-fibre epoxy as a function of temperature.

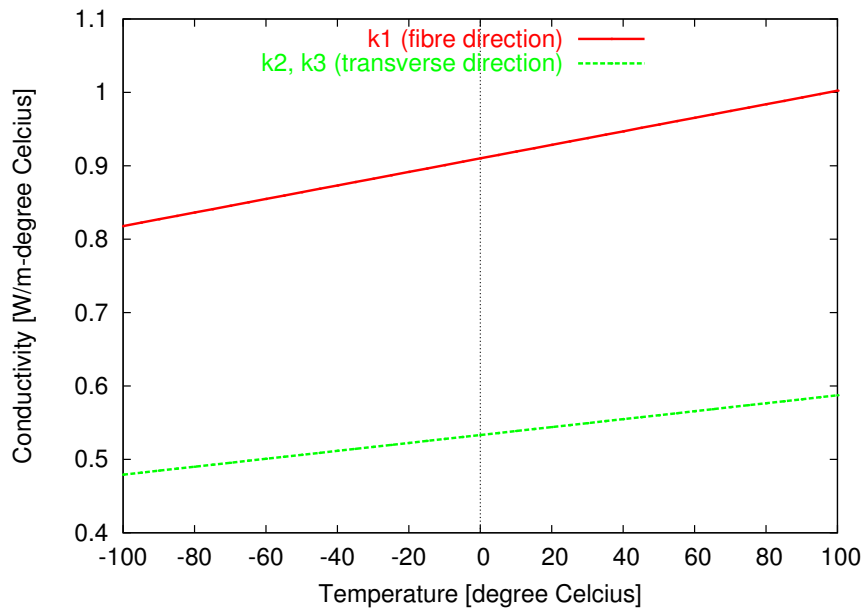


Figure 3.10: The thermal conductivity coefficients in fibre (L) and transverse dir. (LT, ST) of UD glass-fibre epoxy as a function of temperature.

### 3.4 Composite lay-up properties

From the properties for the UD glass-fibre epoxy the properties of a specific composite laminate lay-up can be calculated by summing up over the thickness. This approach is followed in the Classical Laminate Theory and in this section it will be shown that this indeed gives a good agreement with test results for  $[0/90]_{4s}$ ,  $[0/90/0]_{3s}$ , and  $[0/90/\pm 45]_{2s}$  composite laminate lay-up configurations. The tests have been performed for tension and shear at both room temperature and 80 °C. The results can be found in detail in the test report on the composite lay-up properties, see (Hagenbeek 2004a). Here we will give an overview of the most important results. In Figures 3.11 through 3.13, and 3.14 through 3.16 a comparison between the tested and calculated tension and shear stiffness respectively is depicted for the  $[0/90]_{4s}$ ,  $[0/90/0]_{3s}$ , and  $[0/90/\pm 45]_{2s}$  composite laminate lay-ups.

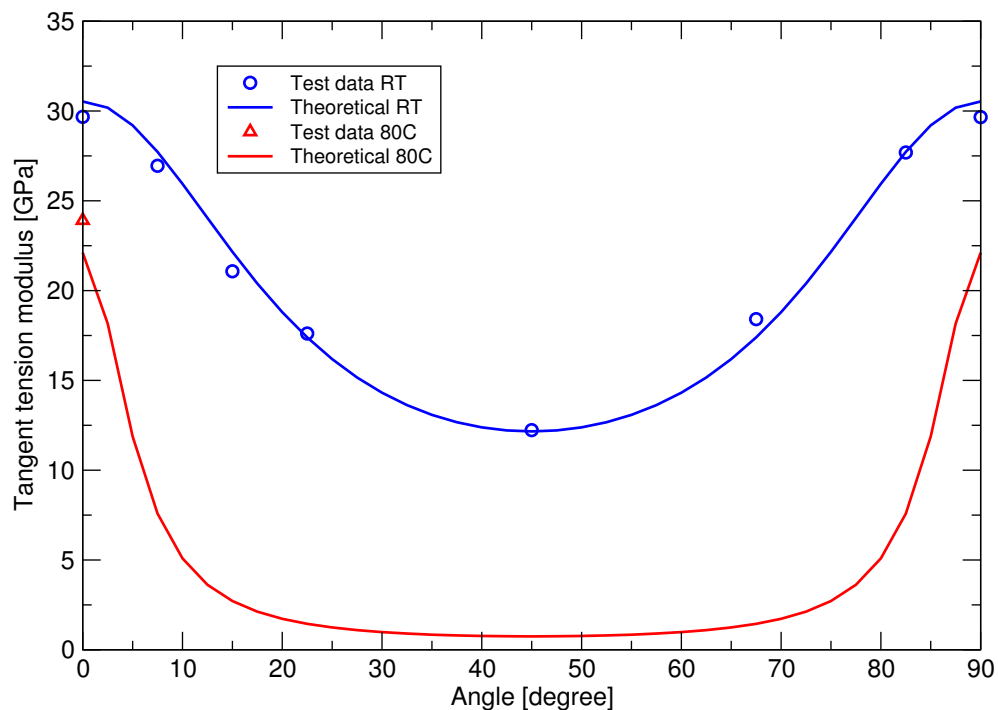


Figure 3.11: Comparison of tested and calculated tangent tension stiffness for the  $[0/90]_{4s}$  composite laminate lay-up.

The maximum difference between theory and test for the tensile tests is 9.1%, in general the difference is however much smaller, see (Hagen-

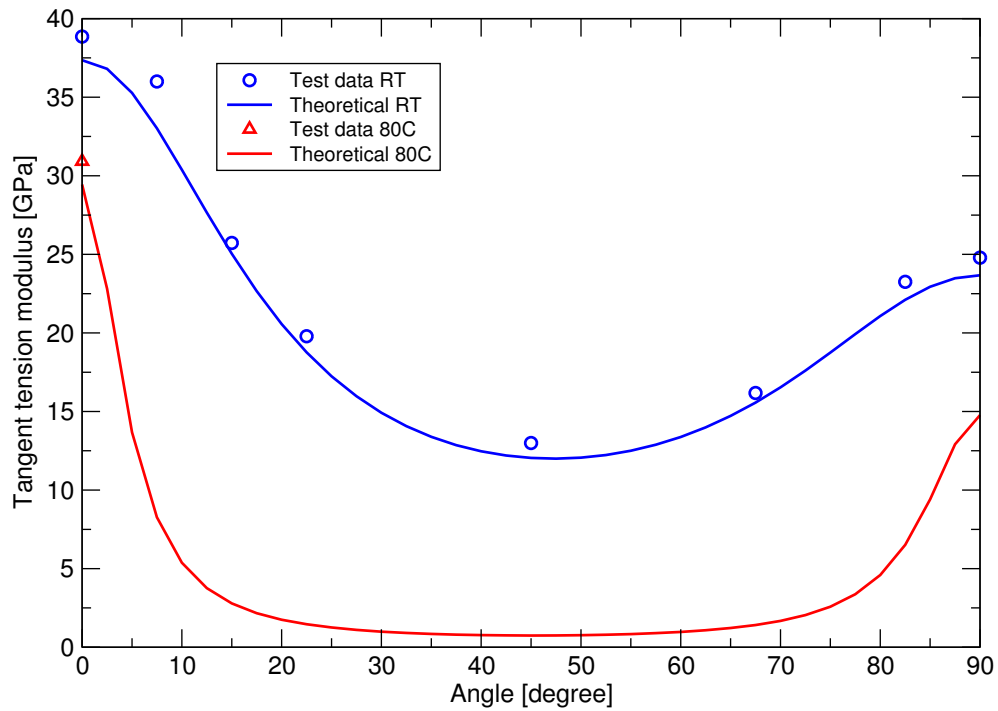


Figure 3.12: Comparison of tested and calculated tangent tension stiffness for the  $[0/90/0]_{3s}$  composite laminate lay-up.

beek 2004a) for the exact numbers. The difference can be largely influenced by the scatter in the results, which reaches up to  $\pm 7\%$  from the mean value. For the shear tests maximum difference is larger than for the tension tests and reaches up to 19.7%, in general the difference is however much smaller, see (Hagenbeek 2004a) for the exact numbers. Also in this case the difference can be largely influenced by the scatter in the results, which reaches up to  $\pm 13.8\%$  from the mean value.

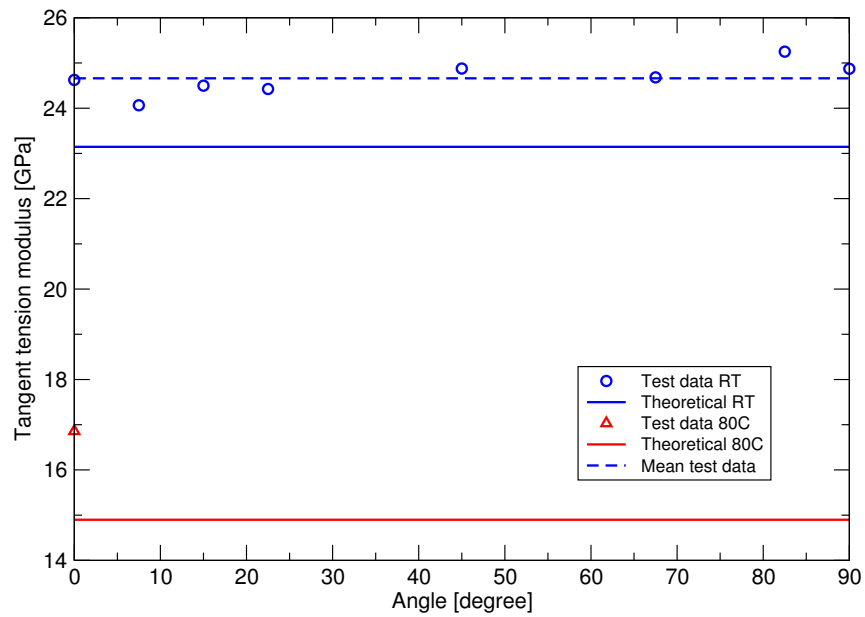


Figure 3.13: Comparison of tested and calculated tangent tension stiffness for the  $[0/90/\pm 45]_{2s}$  composite laminate lay-up.

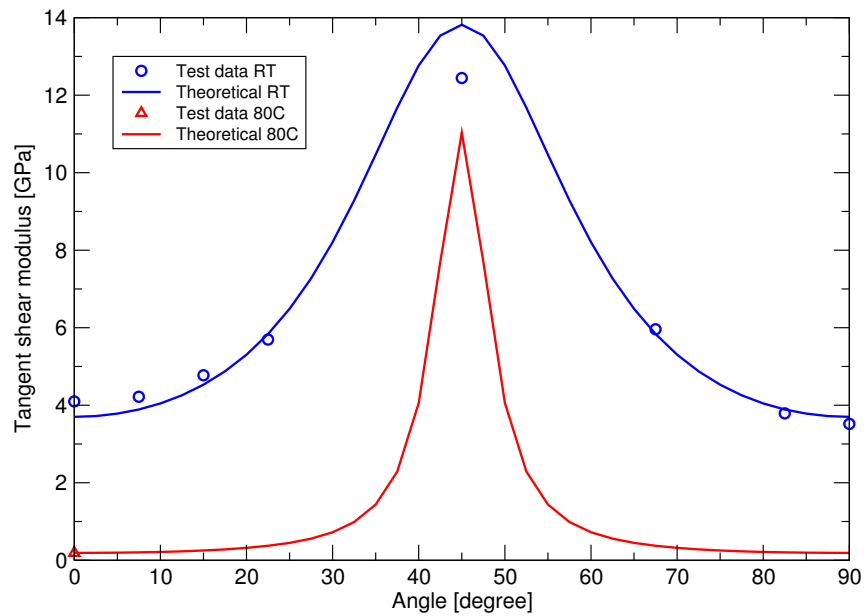


Figure 3.14: Comparison of tested and calculated tangent shear stiffness for the  $[0/90]_{4s}$  composite laminate lay-up.

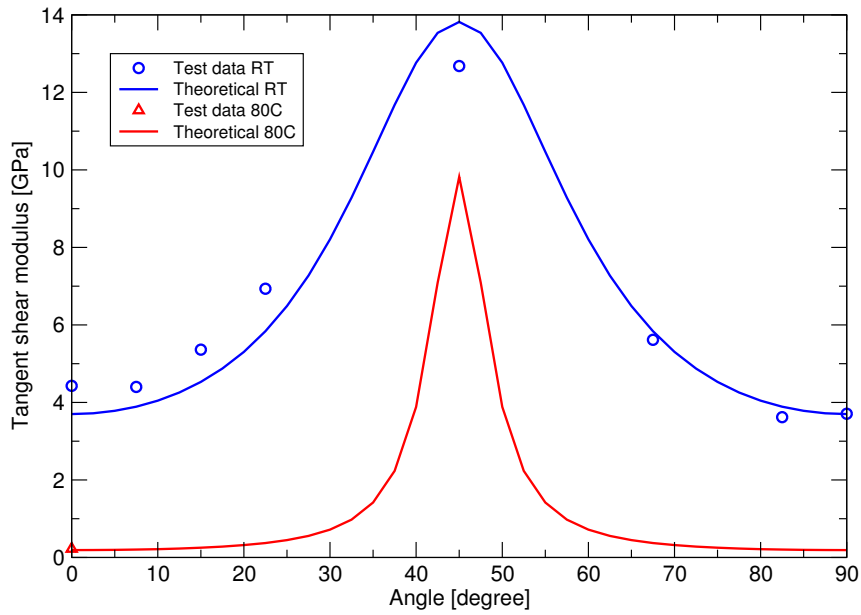


Figure 3.15: Comparison of tested and calculated tangent shear stiffness for the  $[0/90/0]_{3s}$  composite laminate lay-up.

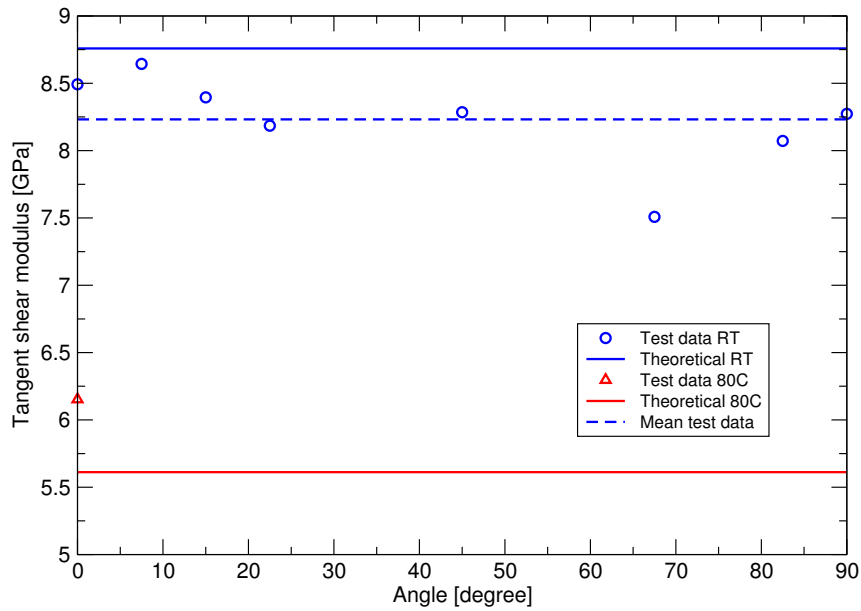


Figure 3.16: Comparison of tested and calculated tangent shear stiffness for the  $[0/90/\pm 45]_{2s}$  composite laminate lay-up.

### 3.5 The aluminium 2024-T3 sheet material

Thermal and mechanical temperature properties of aluminium 2024-T3 sheet material are available to a large extent at room temperature in the literature, see for example (Aluminum Association 1982) and (Hatch 1983). The effect of temperature on the properties is much more limited, but the (Military Handbook 1998) presents a very extensive research.

#### 3.5.1 Mechanical properties of aluminium 2024-T3

An overview of the mechanical properties of aluminium 2024-T3 sheet material, with thickness between 0.254 and 0.508 mm, at room temperature is given below in Table 3.5.

Property	Unit	Value
E	[GPa]	72.4
$E_c$	[GPa]	73.8
$\nu_{12}$	[-]	0.33
$G_{12}$	[GPa]	27.2

Table 3.5: Mechanical properties of aluminium 2024-T3 sheet material at room temperature (Military Handbook 1998).

The aluminium stress-strain curve in longitudinal or aluminium rolling direction is different from the (longitudinal) transverse direction, as shown in Figure 3.17. Up to 1% strain this curve is obtained directly from the (Military Handbook 1998), beyond 1% the curve is obtained by shifting the curve for clad aluminium upward. The clad layer gives the sheet a better corrosion protection and in combination with an anodising process a suitable surface for a paint or adhesive. This cladding is not expected to change the overall stress-strain curve, though the strength of the sheet slightly decreases.

The difference in longitudinal (rolling) direction and the (longitudinal) transverse direction is due to the rolling process of the aluminium sheet and gives a distinct difference in the yield value in the two directions. This effect is however not taken into account in the model, which is shown in Figure 3.17 as well. The model is based on the average of the two directions and can be described by an exponential power law. In compression the same strain hardening behaviour is assumed.

The directionality of the aluminium is less significant when compared with the enormous scatter in stress-strain curves of different sources. This is evident from Figure 3.18 where a variety of stress-strain curves from

other sources are given; (Military Handbook 1998), (van der Hoeven and Nijhuis 2004), and (Schipperen 2001a). The major sources of this scatter in the test results is expected to be caused by differences in material specification and in the manufacturing process between companies, this is indicated by the test curves of (Schipperen 2001a) for both Hoogovens and Alcoa aluminium.

In Figure 3.19 the effect of the temperature on the tangent stiffness in tension, compression, and shear is given for aluminium 2024-T3. In this figure a gradual decrease in stiffness with temperature can be found for the given loadings.

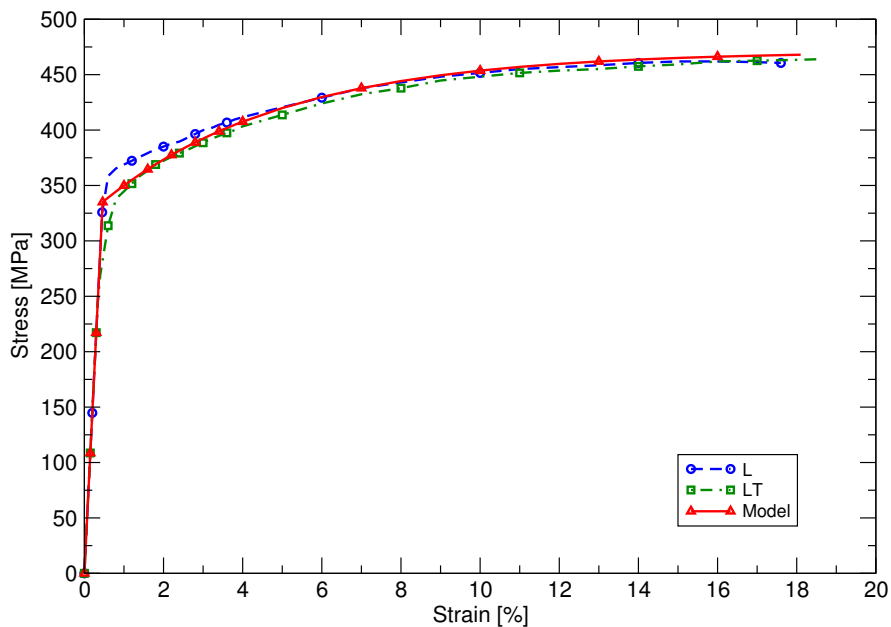


Figure 3.17: The aluminium 2024-T3 stress-strain curve based on (Military Handbook 1998) in longitudinal (L) and transverse direction (LT).

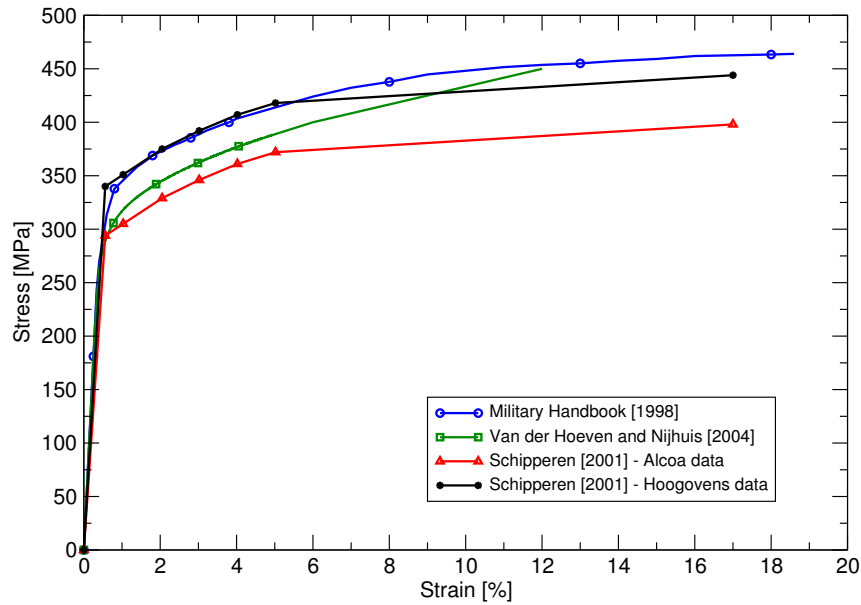


Figure 3.18: Stress-strain curves for aluminium 2024-T3 in transverse direction (LT) from several sources, viz.; (Military Handbook 1998), (van der Hoeven and Nijhuis 2004), and (Schipperen 2001a).

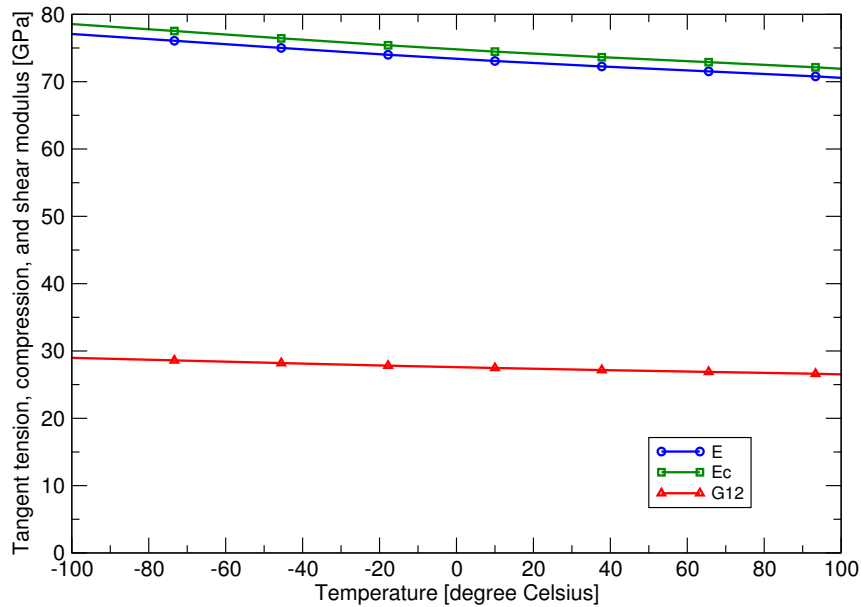


Figure 3.19: Effect of temperature on the aluminium 2024-T3 tangent tension, compression, and shear stiffness.



### 3.5.2 Thermal properties of aluminium 2024-T3

In Table 3.6 the thermal properties for aluminium 2024-T3 at room temperature are listed. The values are taken from the (Military Handbook 1998).

Property	Unit	Value
$\alpha$	$[\mu\text{m}/\text{m}\cdot^{\circ}\text{C}]$	22.4
$c_p$	$[\text{J}/\text{g}\cdot^{\circ}\text{C}]$	0.89
$k$	$[\text{W}/\text{m}\cdot^{\circ}\text{C}]$	122.2
$\rho$	$[\text{g}/\text{cm}^3]$	2.77

Table 3.6: Thermal properties and density of aluminium 2024-T3 at room temperature.

In Figures 3.20, 3.21, and 3.22 the thermal expansion coefficient, the specific heat, and thermal conductivity as a function of temperature are given. The curves are based on the data from the (Military Handbook 1998).

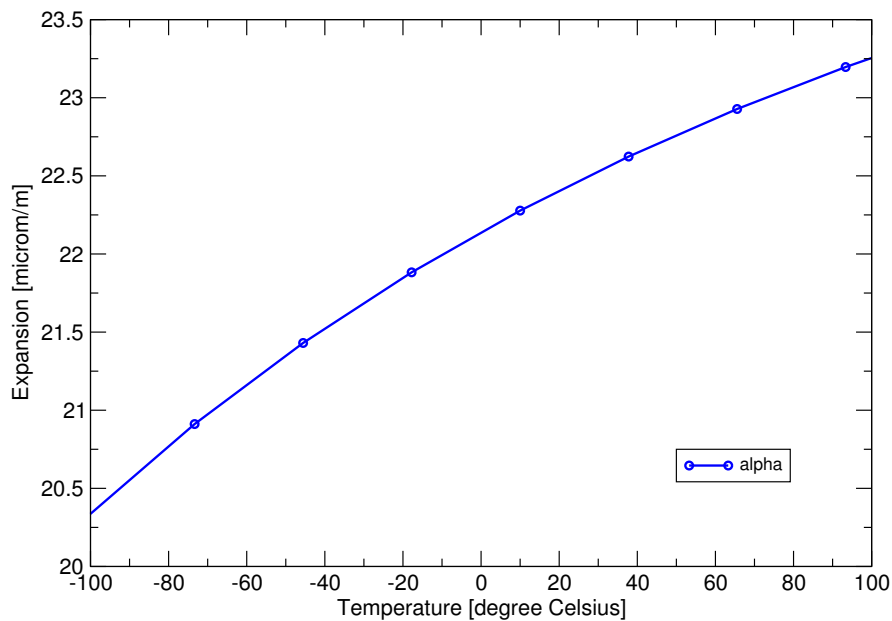


Figure 3.20: The thermal expansion coefficient of aluminium 2024-T3 as a function of temperature.

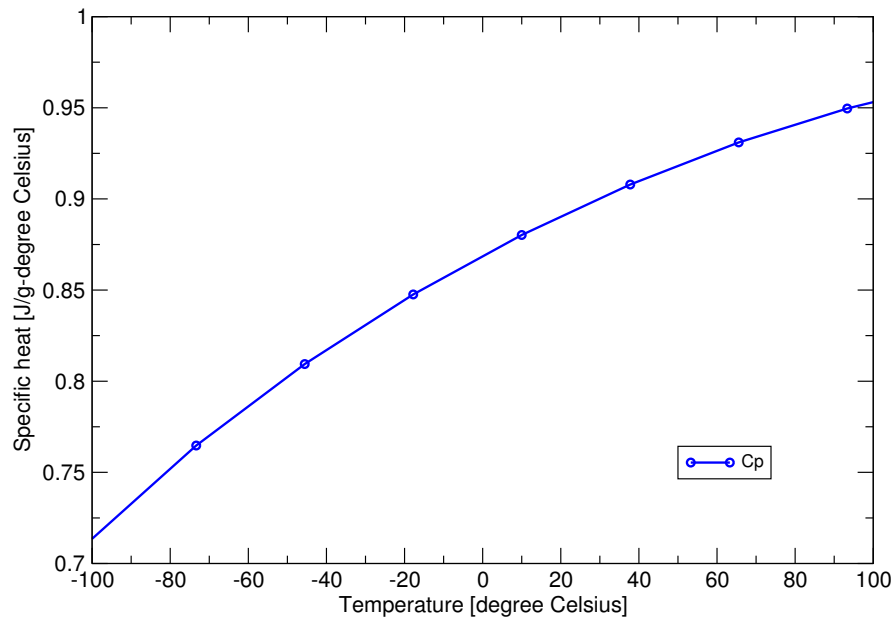


Figure 3.21: The specific heat of aluminium 2024-T3 as a function of temperature.

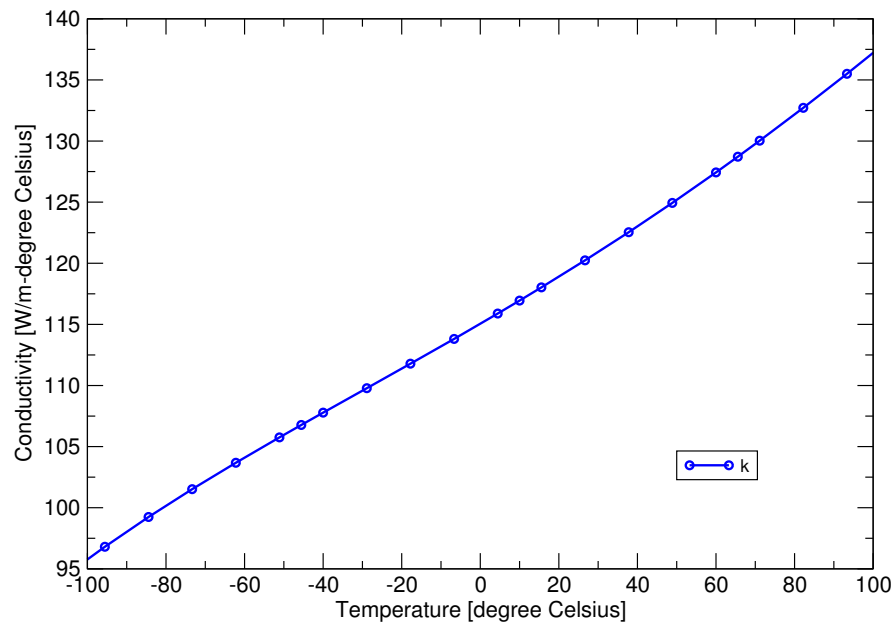


Figure 3.22: The thermal conductivity of aluminium 2024-T3 as a function of temperature.

## 3.6 Summary

Starting from the  $S_2$ -glass-fibre and the epoxy data available in the literature the thermal and mechanical properties of UD glass-fibre epoxy at room temperature can be calculated. Test results for the UD glass-fibre epoxy showed that these calculations give a rough estimate, since the available ingredient data for literature is not always consistent, but also different calculation methods can be used. The temperature-dependent thermal and mechanical behaviour of UD glass-fibre epoxy has been derived from tests. With the test results at room temperature and 80 °C, calculations have been performed with the Classical Laminate Theory on the tension and shear stiffness of three different composite laminate lay-ups:  $[0/90]_{4s}$ ,  $[0/90/0]_{3s}$ , and  $[0/90/\pm 45]_{2s}$ . These calculations on their turn showed a good agreement with tension and shear tests on the previously mentioned composite laminate lay-ups. Finally, an overview was given of the thermal and mechanical properties of aluminium 2024-T3 as obtained from literature.



# Chapter 4

## Experimental tests on Glare

In Chapter 3 an overview of the constituents' data of Glare has been given. This data serves as input for the numerical model described in the chapters hereafter. The sensitivity of the epoxy to high temperatures, the strong directionality of the fibre (and to a minor extent the aluminium) layers, and the (in general multi-axial) loading condition all play a role in the behaviour of the laminate. The given test results on standard Glare laminates from the literature only show the effect of temperature in fibre direction and give only limited insight in the laminate behaviour.

Therefore, the results of a large experimental test program on the static strength of thick special-lay-up Glare laminates are described as well. In these tests both the effect of the off-axis angle and the temperature is investigated. The test results give insight in the behaviour of the special-lay-up Glare laminates and will be used for verification of the numerical model.

### 4.1 Introduction

Tests have been performed for  $0^\circ$  on-axis, and  $45^\circ$ ,  $67.5^\circ$ , and  $90^\circ$  off-axis angles at room temperature and  $80^\circ\text{C}$ . From the total test program on 16.6 mm and 9.1 mm thick special-lay-up Glare laminates, given in (Hagenbeek 2002a) and (Hagenbeek 2002b) respectively, only the results of the latter are given here.

Both laminate lay-ups are asymmetrically built up from a Glare 3 baseline, with Glare 6 and Glare 2 (under  $45^\circ$  off-axis angle) lay-up configurations as doublers at one side (see Chapter 2). The configurations are used around door and window cut-outs in order to improve the strength and stiffness locally. In total seven glass-fibre epoxy layers in  $0^\circ$  and  $90^\circ$  direction, eight in  $45^\circ$  and two in  $-45^\circ$  direction are present in the 9.1 mm thick lami-

nate, together with fifteen aluminium layers of 0.4 mm or 0.3 mm thickness (in case of two layers).

Off-axis testing on several alternative, i.e. quasi-isotropic and fanned, laminates for Glare3 were performed by (Dop 2002). With calculations he showed that the maximum difference between the real and apparent stiffness was less than 0.5%, due to the fact that the two main direction had a stiffness with the same order of magnitude. Further more, no serious edge delaminations were found after testing, which indicated that the standard narrow dog bone configuration of the tensile test specimen could be used. Therefore, the standard tensile test specimen configuration has been used as well in the off-axis tensile tests presented in this thesis.

Further details on the exact lay-up and the test set-up can be found in the test report by (Hagenbeek 2002b). Only the tension, compression, blunt notch, and shear test results are listed here, and not the compression filled hole and bearing test results. In Figure 4.1 some of the compression test results are shown as an example.

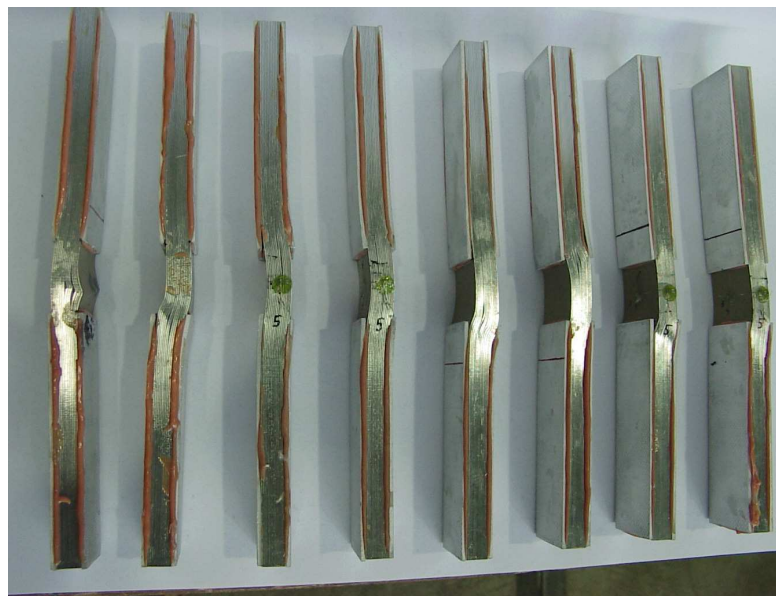


Figure 4.1: Side view of compression test specimens for the 9.1 mm thick special-lay-up Glare tested at  $67.5^\circ$  off-axis angle (left four) and  $0^\circ$  on-axis angle (right four) at room temperature.

The slight curvature due to the asymmetric lay-up of the specimens after curing causes secondary bending. The difference in measured strain at the front and back of the specimen is however small (in the order of 0.2%

strain for compression, and less for tension and blunt notch) and an average value has been determined. The scatter in the results is very limited, the standard deviation is in most cases less than 2% of the mean value. For the exact values the reader is referred to the test report, see (Hagenbeek 2002b).

Besides the testing on thick special-lay-up Glare laminates, a large number of tests on Glare laminates have been performed in the literature. An overview of all the test performed on Glare before June 2000 is given by (Ypma 2000). For the tension, compression, blunt notch and shear test results the overview of the temperature effect for these laminates is given here.

## 4.2 Test results including temperature and off-axis effect

### 4.2.1 Tension tests on special and standard Glare

In table 4.1 the tension properties of the 9.1 mm thick special-lay-up Glare are given. From the results in this table it can be seen that the 45° off-axis direction is the strongest test direction and the 67.5° off-axis direction is the least strong (and stiff) direction, as expected. However, at 80 °C the difference in strength between the 45° off-axis direction and the 0° on-axis and 90° off-axis direction becomes less pronounced, and the stiffness in the latter directions is even better.

$\phi$ [°]	$\theta$ [°C]	E [GPa]	$\sigma_y$ [MPa]	$\sigma_u$ [MPa]	E/E <sub>RT</sub> [%]	$\sigma_y/\sigma_{y RT}$ [%]	$\sigma_u/\sigma_{u RT}$ [%]	$\nu_{12}$ [-]	$\nu_{21}$ [-]	$\nu_{13}$ [-]
0	RT	55.3	277.2	525.0	100.0	100.0	100.0	0.27	0.37	0.33
0	80	52.6	265.9	468.4	95.1	95.9	89.2	-	-	-
45	RT	55.2	251.4	547.4	100.0	100.0	100.0	0.39	0.34	0.32
45	80	50.8	245.4	470.9	92.0	97.6	86.0	-	-	-
67.5	RT	53.9	238.8	416.4	100.0	100.0	100.0	0.33	0.30	0.37
67.5	80	48.9	225.0	345.8	90.7	94.2	83.0	-	-	-
90	RT	55.5	252.5	515.0	100.0	100.0	100.0	0.27	0.36	0.32
90	80	52.9	241.4	446.2	95.2	95.6	86.7	-	-	-

Table 4.1: The effect of temperature and off-axis angle on the tension properties of 9.1 mm thick special-lay-up Glare, as given by (Hagenbeek 2002b).

The yield and ultimate strength are minimal in 67.5° off-axis direction, 239 MPa and 416 MPa respectively, which is due to the absence of fibres

in loading direction and a lower aluminium yield value in this direction. For aluminium 2024-T3 the yield value in rolling direction ( $0^\circ$  direction) is largest and in transverse direction ( $90^\circ$  direction) smallest. An ultimate strength reduction of 24% is found in the (least stiff)  $67.5^\circ$  off-axis direction with respect to the (stiffest)  $45^\circ$  off-axis direction at room temperature.

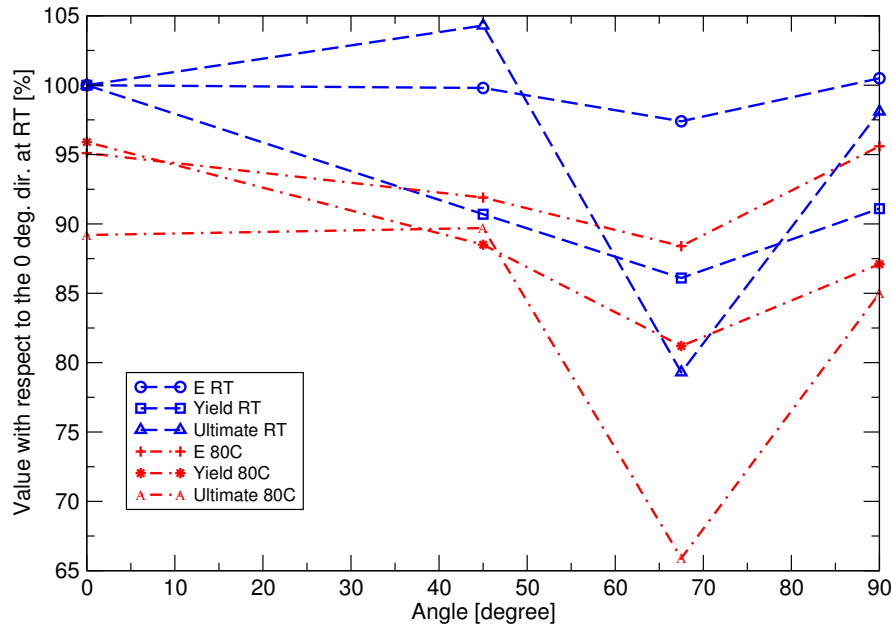


Figure 4.2: The effect of temperature and off-axis angle on the tensile stiffness, yield and ultimate strength of 9.1 mm thick special-lay-up Glare with respect to the  $0^\circ$  direction at room temperature, see (Hagenbeek 2002b).

The Young's modulus and tangent modulus (in the plastic region) decrease at elevated temperature, and the yield and ultimate strength decreases likewise. In  $67.5^\circ$  off-axis direction the decrease in yield and ultimate strength due to temperature is largest, 6 and 17%, and the values at elevated temperature are 225 MPa and 346 MPa respectively. Thus on top of the above mentioned ultimate strength reduction of 24% due to off-axis loading (with respect to the  $45^\circ$  off-axis direction), a reduction of 17% due to the  $80^\circ\text{C}$  temperature is found in  $67.5^\circ$  off-axis direction. In Figure 4.2 the effect of the temperature and the off-axis angle on the tensile stiffness, yield and ultimate strength is shown. The values of these quantities are given as a percentage of the values in  $0^\circ$  direction at room temperature.

In Table 4.2 the test data from (Ypma 2000) for three different Glare 3 lay-up configurations is given. The tensile stiffness shows an increase



of at most 3% at -55 °C, and a decrease of 4% at 70/80 °C with respect to the room temperature values. The tensile yield and ultimate strength respectively increase with at most 4 and 11% at -55 °C, and decrease with at most 5 and 12% at 70/80 °C. In Figure 4.3 the effect of temperature on the tensile stiffness of the standard Glare laminates is shown. The values are given with respect to the value at room temperature.

From the tension test results on the special-lay-up and standard Glare it can be seen that the strength and stiffness reduction due to temperature and/or off-axis angle can be significant. The design of the lay-up configuration for the structure should therefore adequately match the expected loading conditions, since the strength and stiffness reduction is much less pronounced when loaded in fibre direction.

$\phi$ [°]	$\theta$ [°C]	E [GPa]	$\sigma_y$ [MPa]	$\sigma_u$ [MPa]	E/E <sub>RT</sub> [%]	$\sigma_y/\sigma_{y RT}$ [%]	$\sigma_u/\sigma_{u RT}$ [%]	Note
Glare 3 3/2 0.3								
L	RT	-	-	689.0	-	-	-	a,b
LT	RT	-	-	673.0	-	-	-	a,b
L	-55	55.5	275.0	-	104.7	103.8	-	c
L	RT	53.0	265.0	-	100.0	100.0	-	c
L	70	47.0	252.0	-	88.7	95.1	-	c
Glare 3 3/2 0.4								
L	RT	58.7	305.9	647.3	-	-	-	d
LT	RT	58.8	280.2	640.1	100.0	100.0	100.0	d
LT	80	56.1	278.5	581.2	95.4	99.4	90.8	d
Glare 3 5/4 0.4								
L	-55	58.9	311.5	751.6	102.7	100.7	110.6	e
L	RT	57.3	309.3	679.8	100.0	100.0	100.0	e
L	70	55.5	305.0	609.8	96.7	98.6	89.7	e
LT	-55	58.4	267.9	729.0	100.6	101.8	110.5	e
LT	RT	58.0	263.1	659.6	100.0	100.0	100.0	e
LT	70	56.0	260.8	583.0	96.5	99.1	88.4	e

<sup>a</sup> (Roebroeks 1996).

<sup>b</sup> (Boertien 1996).

<sup>c</sup> (Horst 1995).

<sup>d</sup> (van der Hoeven and Schra 1999).

<sup>e</sup> (van der Hoeven and Schra 2000).

Table 4.2: The effect of temperature on the tension properties of standard Glare laminates, see (Ypma 2000).

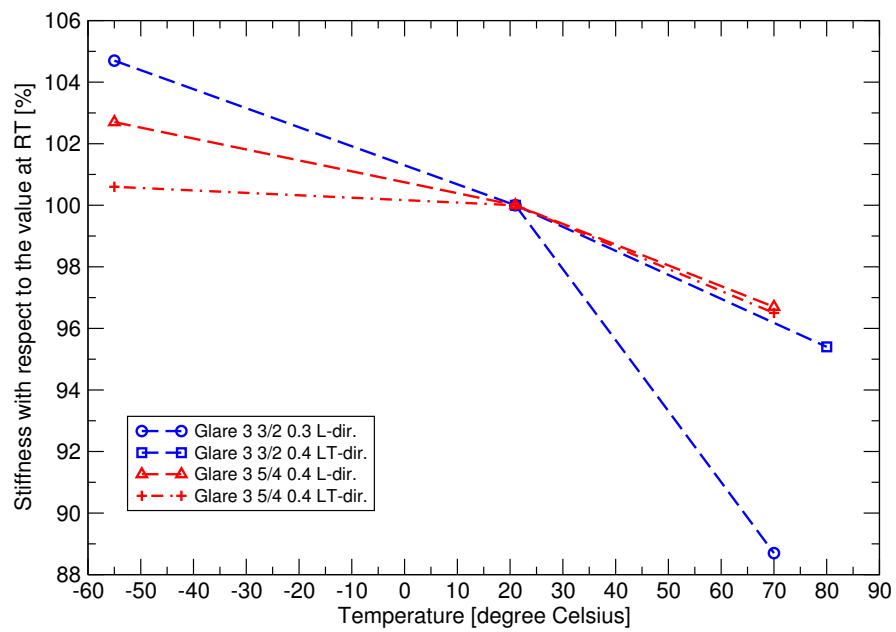


Figure 4.3: The effect of temperature on the tensile stiffness of standard Glare laminates with respect to the value at room temperature.

### 4.2.2 Compression tests on special and standard Glare

In Table 4.3 the compression properties of the 9.1 mm thick special-lay-up Glare are given. From the results in this table it can be seen that the 90° off-axis direction is the stiffest and the 67.5° off-axis direction is the less stiff test direction. The stiffness in 45° off-axis direction is lower than expected (it should still be the stiffest direction), though the yield and failure strength still have the largest values in this direction, 282 MPa and 375 MPa respectively.

The yield and failure strength are minimal in 67.5° off-axis direction, 264 MPa and 338 MPa respectively, which is due to the absence of fibres and the lower aluminium yield value in this direction. The yield value in rolling direction (0° direction) is larger than in transverse direction (90° off-axis direction). The yield and failure strength reduction (in the (least strong) 67.5° off-axis direction) is respectively 6% and 10% of the (strongest) 45° off-axis direction at room temperature. In Figure 4.4 the

$\phi$ [°]	$\theta$ [°C]	E [GPa]	$\sigma_y$ [MPa]	$\sigma_f$ [MPa]	$\nu_{12}$ [-]	$\nu_{21}$ [-]	$\nu_{13}$ [-]
0	RT	53.6	274.6	367.9	0.28	0.37	0.31
45	RT	54.2	281.5	374.7	0.32	0.37	0.26
67.5	RT	52.1	264.2	337.5	0.32	0.31	0.30
90	RT	54.6	281.5	362.6	0.28	0.37	0.28

Table 4.3: The effect of the off-axis angle on the compression properties of 9.1 mm thick special-lay-up Glare as given by (Hagenbeek 2002b).

effect of the off-axis angle on the compression stiffness, yield and failure strength is shown for the 9.1 mm thick laminate with respect to the 0° direction. The effect of temperature has not been tested.

In Table 4.4 the overview is shown of compression tests for standard Glare laminates at elevated temperature, as given by (Ypma 2000). The compression stiffness and yield strength respectively increase with at most 4 and 9% at -55 °C, and decrease with at most 4 and 5% at 70/80 °C with respect to the room temperature values. In Figure 4.5 the effect of temperature on the compression stiffness of the standard Glare laminates is shown. The values are given with respect to the value at room temperature.

The compression test results on the special-lay-up and standard Glare show similar trends for the strength and stiffness reduction due to off-axis angle and also temperature, for standard Glare, as the tensile tests in Section 4.2.1. Thus also in compression the design of the lay-up configuration for the structure is important to avoid strength and stiffness reductions.

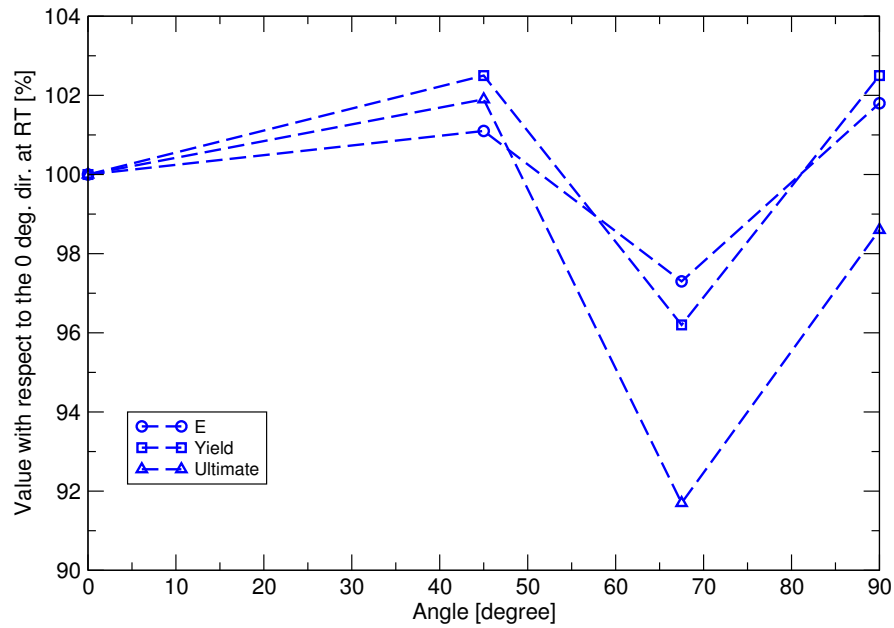


Figure 4.4: The effect of off-axis angle on the compression stiffness, yield and failure strength of 9.1 mm thick special-lay-up Glare with respect to the 0° direction, as given by (Hagenbeek 2002b).

$\phi$ [°]	$\theta$ [°C]	E [GPa]	$\sigma_y$ [MPa]	E/E <sub>RT</sub> [%]	$\sigma_y/\sigma_{y RT}$ [%]	Note
Glare 3 3/2 0.4						
L	RT	60.7	308.3	-	-	a
LT	RT	60.8	319.9	100.0	100.0	a
LT	80	58.3	303.2	95.9	94.8	a
Glare 3 5/4 0.4						
L	-55	61.5	318.6	103.7	108.7	b
L	RT	59.3	293.1	100.0	100.0	b
L	70	58.9	285.6	99.2	97.4	b
LT	-55	60.6	319.7	103.0	104.7	b
LT	RT	58.9	305.4	100.0	100.0	b
LT	70	57.4	289.2	97.5	94.7	b

<sup>a</sup> (van der Hoeven and Schra 1999).

<sup>b</sup> (van der Hoeven and Schra 2000).

Table 4.4: The effect of temperature on the compression properties of standard Glare laminates, see (Ypma 2000).

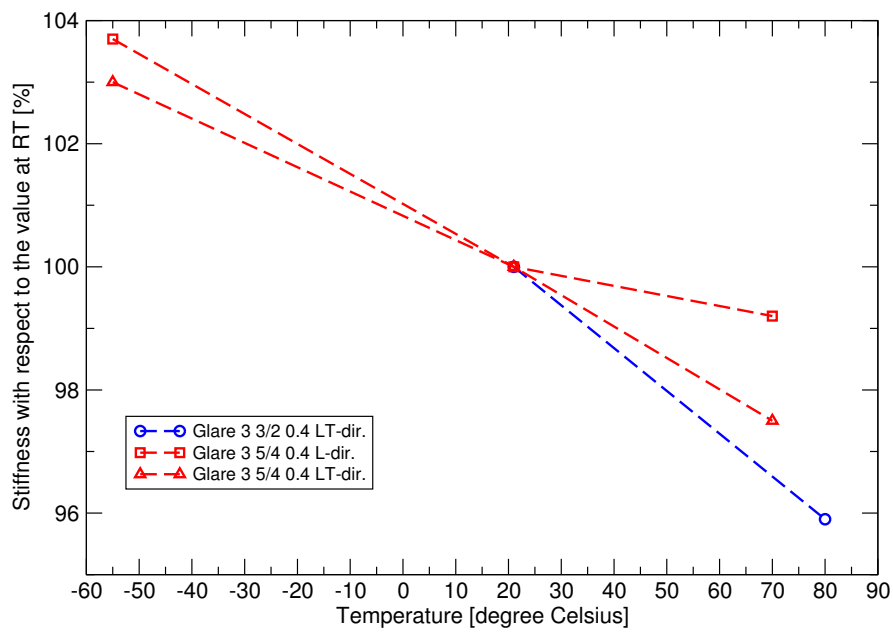


Figure 4.5: The effect of temperature on the compression stiffness of standard Glare laminates with respect to the value at room temperature.

### 4.2.3 Blunt notch tests on special and standard Glare

The blunt notch properties of the 9.1 mm thick special-lay-up Glare are given in Table 4.5 . The test results in this table show that the 45° off-axis direction is the stiffest and strongest and the 67.5° off-axis direction is the least stiff and strong test direction, as expected. The yield and blunt notch strength are minimal in 67.5° off-axis direction, 234 MPa and 361 MPa (net, 285 MPa gross) respectively, which is due to the absence of fibres and the lower aluminium yield value in this direction as explained previously for tension and compression. The yield and blunt notch strength reduction in the (least strong) 67.5° off-axis direction is respectively 5% and 17% of the (strongest) 45° off-axis direction at room temperature.

$\phi$ [°]	$\theta$ [°C]	E [GPa]	$\sigma_y$ [MPa]	$\sigma_{gross}$ [MPa]	$\sigma_{net}$ [MPa]	E/E <sub>RT</sub> [%]	$\sigma_y/\sigma_{y RT}$ [%]	$\sigma_{gross}/\sigma_{gross RT}$ [%]	$\nu_{12}$ [-]	$\nu_{21}$ [-]	$\nu_{13}$ [-]
0	RT	55.0	275.5	323.2	410.0	100.0	100.0	100.0	0.25	0.36	0.32
0	80	49.2	252.0	308.1	390.8	89.5	91.5	95.3	-	-	-
45	RT	55.8	247.3	342.4	434.3	100.0	100.0	100.0	0.39	0.29	0.25
45	80	49.3	233.4	324.5	411.7	88.4	94.4	94.8	-	-	-
67.5	RT	53.0	234.0	284.5	360.9	100.0	100.0	100.0	0.33	0.30	0.32
67.5	80	49.1	215.5	266.3	337.7	92.6	92.1	93.6	-	-	-
90	RT	55.7	250.8	313.3	397.4	100.0	100.0	100.0	0.26	0.38	0.35
90	80	50.1	232.0	297.8	377.8	90.0	92.5	95.0	-	-	-

Table 4.5: The effect of temperature and off-axis angle on the blunt notch properties of 9.1 mm thick special-lay-up Glare, see (Hagenbeek 2002b).

The Young's modulus and tangent modulus (in the plastic region) decrease at elevated temperature, and the yield and ultimate strength decreases likewise. In 67.5° off-axis direction the decrease in ultimate strength due to temperature is largest, 6%, and the value at elevated temperature is 338 MPa.

The maximum decrease in yield strength value of 9% is found in the 0° on-axis direction, though the 67.5° off-axis direction was expected to give the maximum decrease. The decrease in 0° direction seems too large in comparison with the 90° off-axis or 45° off-axis direction and the observations in the tensile tests. The minimum yield strength value at elevated temperature is 216 MPa for the 67.5° off-axis direction.

The effect of temperature on the blunt notch ultimate strength is smaller than for the tensile ultimate strength, 6 versus 17% decrease respectively. In Figure 4.6 the effect of the temperature and the off-axis angle on the blunt notch yield and ultimate strength is shown. The values of these quantities are given as a percentage of the values in 0° direction at room

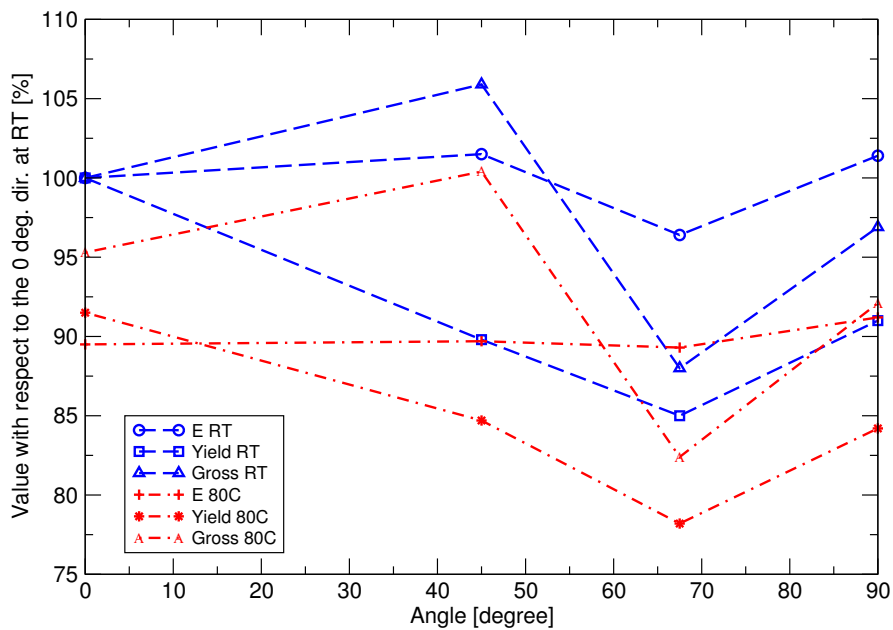


Figure 4.6: The effect of temperature and off-axis angle on the blunt notch stiffness, yield and ultimate strength of 9.1 mm thick special-lay-up Glare with respect to the 0° direction, as given by (Hagenbeek 2002b).

temperature.

In Table 4.6 the blunt notch test data from (Ypma 2000) for Glare 3-3/2-0.3 is given. The ultimate (gross and net) strength shows a large increase of 13% at -55 °C. At elevated temperature, the strength initially decreases to 3% at 60 °C, but then increases again even to 2% at 80 °C. Scatter in the results might well cause this since the deviation of the ultimate strength values at elevated temperature is small with respect to the room temperature value. In Figure 4.7 the effect of temperature on the blunt notch stiffness of the standard Glare laminates is shown. The values are given with respect to the value at room temperature.

Thus, the blunt notch test results on the special-lay-up and standard Glare show a similar off-axis behaviour as the tension and compression test. The strength and stiffness reduction due to elevated temperature however is very limited for the special-lay-up Glare. For the standard Glare laminate the reduction due to elevated temperature is even smaller and can be neglected.

$\phi$ [°]	$\theta$ [°C]	d [mm]	W [mm]	$\sigma_{gross}$ [MPa]	$\sigma_{net}$ [MPa]	$\sigma_{gross}/\sigma_{gross RT}$ [%]	Note
Glare 3 3/2 0.3							
L	RT	3.3	25.0	432.0	497.7	-	a
L	RT	4.8	25.0	392.0	485.1	-	a
L	RT	4.8	50.0	427.0	472.0	100.0	b
L	55	4.8	50.0	418.0	462.0	97.9	b
L	60	4.8	50.0	416.0	460.0	97.4	b
L	65	4.8	50.0	424.0	469.0	99.3	b
L	70	4.8	50.0	422.0	467.0	98.8	b
L	75	4.8	50.0	423.0	468.0	99.1	b
L	80	4.8	50.0	437.0	484.0	102.3	b
LT	-55	25.0	100.0	475.0	633.3	113.1	c
LT	RT	25.0	100.0	420.0	560.0	100.0	c
LT	80	25.0	100.0	435.0	580.0	103.6	c

<sup>a</sup> (Boertien 1996).

<sup>b</sup> (Borgonje 2000).

<sup>c</sup> (Bär 1992)

Table 4.6: The effect of temperature on the blunt notch properties of standard Glare laminates, see (Ypma 2000).

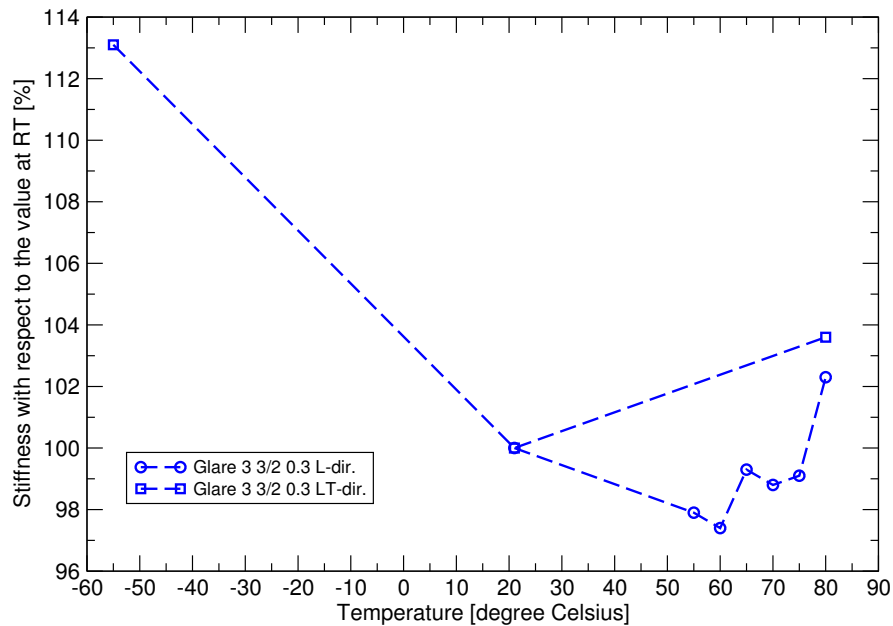


Figure 4.7: The effect of temperature on the blunt notch stiffness of standard Glare laminates with respect to the value at room temperature.



#### 4.2.4 Shear tests on special Glare

The shear properties of the 9.1 mm thick special-lay-up Glare are given in Table 4.7. The table shows that the shear yield value is largest in 45° off-axis direction, 140 MPa. Most of the fibres run parallel to the shear load direction in this case, which increases the strength. The 90° off-axis direction is with the same reasoning the weakest direction.

$\phi$ [°]	$\theta$ [°C]	$G$ [GPa]	$\sigma_y$ [MPa]	$G/G_{RT}$ [%]	$\sigma_y/\sigma_{y RT}$ [%]
0	RT	23.4	135.0	100.0	100.0
0	80	18.1	116.0	77.4	85.9
45	RT	27.7	139.5	100.0	100.0
45	80	22.9	120.0	82.7	86.0
67.5	RT	21.6	134.0	100.0	100.0
67.5	80	19.6	129.0	90.8	96.3
90	RT	20.3	115.0	100.0	100.0
90	80	19.6	106.0	96.3	92.2

Table 4.7: The effect of temperature and off-axis angle on the shear properties of 9.1 mm thick special-lay-up Glare as given by (Hagenbeek 2002b).

At elevated temperature the 0° on-axis direction shows the largest decrease in shear modulus (22.6%) and the largest decrease in yield (14.1%). The large decrease in shear modulus in 45° off-axis direction is presumably caused by fibre reorientation (shearing) to which the laminate is most prone in this test direction. The largest value for the shear yield is therefore found in 67.5° off-axis direction, 129 MPa. Only in this test direction all fibres are able to carry (some of) the shear load, despite the non-optimal orientation in general. The reduction of the yield due to the temperature is the least in this direction. The largest shear modulus at elevated temperature is still found in 45° off-axis direction, 23 GPa. In Figure 4.8 the effect of the temperature and the off-axis angle on the shear yield strength is shown. The values of these quantities are given as a percentage of the values in 0° direction at room temperature.

Shear test results on the off-axis or temperature effect for standard Glare configurations are not given in the overview of (Ypma 2000).

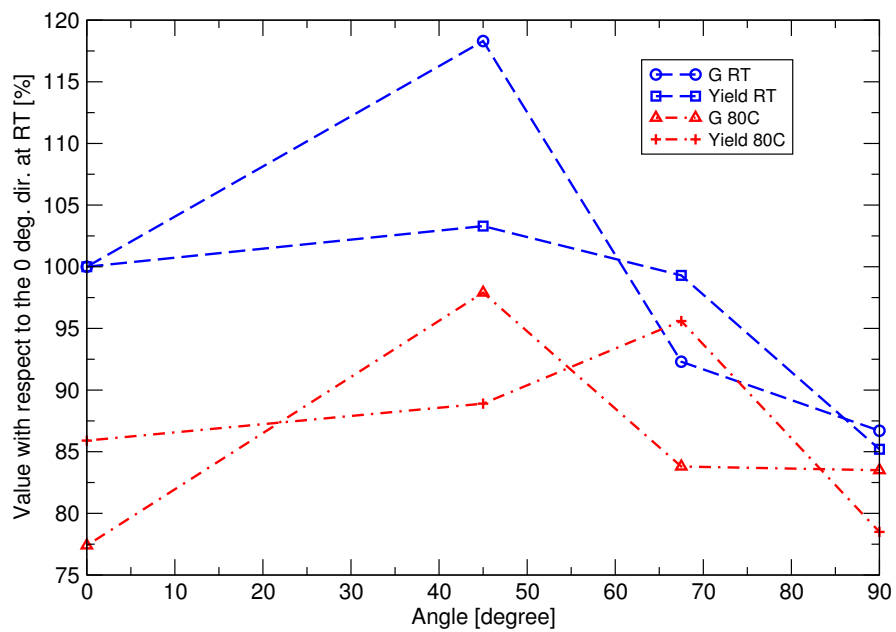


Figure 4.8: The effect of temperature and off-axis angle on the shear yield strength of 9.1 mm thick special-lay-up Glare, see (Hagenbeek 2002b).

### 4.3 Summary

The off-axis and temperature effect can be large. For the 9.1 mm special lay-up Glare a reduction of 24% in ultimate strength is found at room temperature in the least stiff 67.5° off-axis direction with respect to the stiffest 45° off-axis direction. The 80 °C temperature gives a further maximum found reduction of 17% of the ultimate strength value in 67.5° off-axis direction. The maximum shear stiffness reduction is 22.6%, which is found in the 0° direction. The effect of temperature in compression cannot be mentioned, since no tests at elevated temperature have been performed.

At other angles the effect of temperature is less, but still more than 13%. The off-axis and temperature effect on the stiffness and the yield strength is clearly less. In shear the 45° off-axis direction has the largest stiffness and yield strength, and the 90° direction is in this case the weakest direction. The largest stiffness and yield strength reduction is however found in the 0° direction. For standard Glare, where tests at elevated temperature have only been performed in fibre direction, the strength and stiffness reductions are at most 12%.

The test results for the special lay-up Glare indicate that a strong account must be given to the possible strength and stiffness reductions due to off-axis loading and/or temperature. The test results on standard Glare only show the effect of temperature in fibre direction. The sensitivity of the epoxy to high temperatures, the strong directionality of the fibre (and to a minor extent the aluminium) layers, and the (in general multi-axial) loading condition all play a role in the behaviour of the laminate. The test results give only limited insight and show that the laminate behaviour can best be considered in a model that take all factors separately into account.



# Chapter 5

## General numerical framework

### 5.1 Introduction

The test results discussed in the previous chapter only describe the laminate behaviour for specific loading and environmental conditions. In general the most critical test cases are selected, since it is impossible to account for all possible variations in the laminate lay-up and test conditions. To gain more insight in the laminate behaviour and avoid the time-consuming and costly testing a model is needed that takes all factors separately into account. By considering the constituents the effect of each layer on the total laminate properties can be determined.

In the derivation of the model it is important to consider the possible interaction effects between the material properties, the mechanical field (i.e. the displacements or stresses) and the thermal field (i.e. the temperature distribution). The thermal and mechanical properties of a material are influenced by the temperature of the material. The specific heat, thermal conduction and density of materials depend on the temperature, see Figure 5.1 (1). To be able to include this the temperature-dependency of the Glare constituents have been determined in Chapter 3. On the other hand, the temperature distribution within the material is determined by the thermal properties of the material (2). The stress state or mechanical field, due to internal or external forces, are determined by the mechanical properties of the material (3). The mechanical field also influences the mechanical properties of the material. Materials can have a hardening behaviour and the transformation kinetics (microstructure and mechanical properties) depend in this case on the stresses (4). Heat generated by plastic deformations warms the material up, thereby changing the temperature field in the material. Deformations of the material may thus change

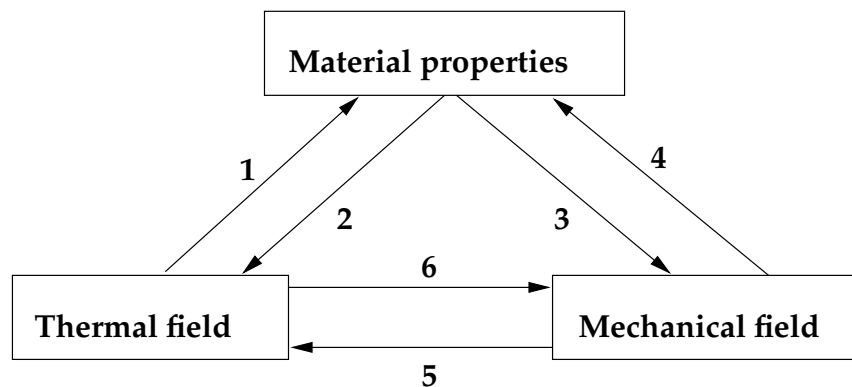


Figure 5.1: Coupling between thermal field, mechanical field and material properties

the temperature distribution in the material (5). In the present thesis this effect will not be taken into account. Heating and cooling of a material causes thermal expansion and shrinkage, and may generate stresses in the material (6).

The governing equations and solution techniques for the displacement based finite element model are presented in this chapter. The equations form the general framework for the numerical element described in the chapters hereafter. The finite element method is used to obtain the system of thermo-mechanical equations and solve them in a numerically efficient way. The framework for the implementation of physical nonlinearities, such as plasticity and damage, into the model is given as well.

## 5.2 The Finite Element Method

To obtain a realistic thermo-mechanical model, including geometrical and physical nonlinearities such as plasticity and damage, the finite element method is very well suited. Starting from the fundamental laws of mechanics and thermodynamics a thermo-mechanical system of equations is derived to describe the behaviour of the considered body or structure. In the finite element method the structure is subdivided into a number of finite elements and the weak formulation of the governing thermo-mechanical equations is discretised. That is, the thermo-mechanical behaviour of these elements is described as a function of the displacements and temperatures of some characteristic points, the nodes, of the element. Neighbouring elements are connected in a physically consistent manner

at the boundaries by applying boundary conditions for the displacements.

Depending on the type of analysis we want to perform, that is static or dynamic, the final system of equations and solution procedure is obtained. The nodal displacements of each element are obtained when the total system of equations is solved. Since the thermo-mechanical equations are in general nonlinear an incremental iterative solution procedure, the Newton-Raphson method, is required. The efficient numerical way to solve the system of equations is one of the main advantages of the finite element method. From the nodal displacements the strains and stresses can be calculated in any point in the element and structure.

## 5.3 Governing equations and discretisation

### 5.3.1 The mechanical system of equations

The general three-dimensional equations of motion of an elementary volume  $V$  in a continuum can be written in matrix-vector notation as follows

$$\operatorname{div}\boldsymbol{\tau} + \rho\mathbf{g} = \rho\ddot{\mathbf{u}}, \quad (5.1)$$

where the vector  $\boldsymbol{\tau}$  contains the six independent components of the stress tensor, referred to as Cauchy stresses. The scalar quantity  $\rho$  is the mass density and the vector  $\mathbf{u}$  is the displacement vector. A superimposed dot denotes differentiation with respect to time and a superimposed double dot implies that a quantity is differentiated twice with respect to time, which means that  $\ddot{\mathbf{u}}$  is the acceleration vector. The first term on the left-hand side denotes the divergence of the stress vector  $\boldsymbol{\tau}$ , and the second term on the left refers to the internal body forces. The term on the right-hand side denotes the acceleration force.

In actually measured dynamic responses of structures dissipation of energy is observed during vibration. In practice the element damping parameters are difficult to find, in particular because the damping properties are frequency dependent. For this reason, the damping matrix is in general constructed using the mass and stiffness matrix of the complete element assemblage together with experimental results on the amount of damping.

Although, in our case mechanical damping is of less interest, for the transient heat transfer analysis the 'thermal damping' matrix consists of the heat capacity of the material, which certainly is of interest. It determines the rate of heat adsorption or heat loss, for example of the aircraft skin during take-off after an initial heat-up due to solar radiation, and will be further discussed in Section 5.3.4.

### 5.3.2 The weak formulation of the mechanical system

The description of the motion of the body in Eq. (5.1) is given in a strong sense. By applying the principle of virtual work a weak form of the equation can be obtained, by setting

$$\int_V \delta \mathbf{u}^T [\operatorname{div} \boldsymbol{\tau} - \rho \ddot{\mathbf{u}} + \rho \mathbf{g}] dV = 0, \quad (5.2)$$

in which  $\delta$  denotes the variation of a given quantity. The principle idea is to replace the equation of motion by a virtual work equation in which a residual force integrated over the volume of the body equals zero. With aid of Green's theorem

$$\int_V \delta \mathbf{u}^T \operatorname{div} \boldsymbol{\tau} dV = - \int_V \delta \boldsymbol{\epsilon}^T \boldsymbol{\tau} dV + \int_S \delta \mathbf{u}^T \boldsymbol{\tau} \bar{\mathbf{n}} dS, \quad (5.3)$$

Eq. (5.2) can be transformed into

$$\int_V \delta \mathbf{u}^T \rho \ddot{\mathbf{u}} dV + \int_V \delta \boldsymbol{\epsilon}^T \boldsymbol{\tau} dV = \int_V \delta \mathbf{u}^T \rho \mathbf{g} dV + \int_S \delta \mathbf{u}^T \mathbf{t} dS, \quad (5.4)$$

where we used the fact that at the boundary  $S$  the traction is required that either

$$\mathbf{t} - \boldsymbol{\tau} \bar{\mathbf{n}} = 0, \quad (5.5)$$

with  $\mathbf{t}$  the boundary traction and  $\bar{\mathbf{n}}$  the outward normal to the surface of the body, or

$$\mathbf{u}_{\bar{\mathbf{n}}} = \mathbf{u}_s, \quad (5.6)$$

with  $\mathbf{u}_{\bar{\mathbf{n}}}$  the displacements at the boundary and  $\mathbf{u}_s$  the prescribed displacements. The second term on the left-hand side of Eq. (5.4) is the internal virtual work,  $\delta W_{\text{int}}$ , and the right-hand side is the external virtual work,  $\delta W_{\text{ext}}$ . The equations up to this point have been derived with reference to the deformed configuration. The Eulerian strains in this case read:

$$\boldsymbol{\epsilon} = \frac{1}{2} \left( \frac{\partial \mathbf{u}}{\partial \mathbf{x}} + \left( \frac{\partial \mathbf{u}}{\partial \mathbf{x}} \right)^T \right). \quad (5.7)$$

To obtain all quantities with respect to the undeformed configuration a Total Lagrange approach is applied. The Cauchy stress tensor is transformed into this reference configuration via

$$\boldsymbol{\tau} = \frac{\rho}{\rho_0} \mathbf{F} \boldsymbol{\sigma} \mathbf{F}^T, \quad (5.8)$$



where  $\boldsymbol{\sigma}$  denotes the second Piola-Kirchhoff stress tensor which represents the stresses in the undeformed configuration, and  $\mathbf{F}$  is the deformation gradient tensor, defined as

$$\mathbf{F} = \frac{\partial \mathbf{x}}{\partial \mathbf{X}} = \frac{\partial (\mathbf{X} + \mathbf{u})}{\partial \mathbf{X}} = \mathbf{I} + \frac{\partial \mathbf{u}}{\partial \mathbf{X}}. \quad (5.9)$$

In this equation the vector  $\mathbf{X}$  refers to the position of a material point in the undeformed state of the structure,  $\mathbf{x}$  refers to the deformed state, and  $\mathbf{u}$  is the displacement of the same material point, where all vectors are defined in an ortho-normal frame of coordinates. By the fact that there is mass conservation we can write

$$\rho dV = \rho_0 dV_0, \quad (5.10)$$

where  $\rho_0$  and  $V_0$  refer to the undeformed state. The internal virtual work can thus be written as

$$\delta W_{\text{int}} = \int_{V_0} \delta \boldsymbol{\epsilon}^T \mathbf{F} \boldsymbol{\sigma} \mathbf{F}^T dV_0. \quad (5.11)$$

The strains can be expressed with respect to the undeformed reference configuration as well by introducing the Green-Lagrange strain tensor:

$$\boldsymbol{\gamma} = \frac{1}{2} (\mathbf{F}^T \mathbf{F} - \mathbf{I}). \quad (5.12)$$

Together with Eq. (5.12) the virtual Eulerian strain tensor  $\delta \boldsymbol{\epsilon}$  in Eq. (5.11) can be replaced by

$$\delta \boldsymbol{\epsilon}^T \mathbf{F} \mathbf{F}^T = \delta \boldsymbol{\gamma}^T. \quad (5.13)$$

The total virtual work equation can finally be written as a function of the second Piola-Kirchhoff stress tensor and the corresponding conjugate Green's strain tensor:

$$\int_{V_0} \delta \mathbf{u}^T \rho_0 \ddot{\mathbf{u}} dV_0 + \int_{V_0} \delta \boldsymbol{\gamma}^T \boldsymbol{\sigma} dV_0 = \int_{V_0} \delta \mathbf{u}^T \rho_0 \mathbf{g} dV_0 + \int_{S_0} \delta \mathbf{u}^T \mathbf{t} dS_0. \quad (5.14)$$

In order to obtain the finite element representation the virtual work equation given in Eq. 5.14 must be discretised.

### 5.3.3 Discretisation of the mechanical system

The finite element representation of the virtual work equation for the dynamic motion can be obtained by dividing the body into a number of finite elements. For each element the displacement field  $\mathbf{u}^e$  can be interpolated by

$$\mathbf{u}^e = \mathbf{H}^e \hat{\mathbf{u}}^e; \quad \dot{\mathbf{u}}^e = \mathbf{H}^e \dot{\hat{\mathbf{u}}}^e; \quad \text{and} \quad \ddot{\mathbf{u}}^e = \mathbf{H}^e \ddot{\hat{\mathbf{u}}}^e, \quad (5.15)$$

and the relation between the strains and the nodal displacements is obtained as

$$\boldsymbol{\gamma}^e = \mathbf{B}^e \hat{\mathbf{u}}^e; \quad \text{and} \quad \dot{\boldsymbol{\gamma}}^e = \mathbf{B}^e \dot{\hat{\mathbf{u}}}^e. \quad (5.16)$$

The matrix  $\mathbf{B}^e$  and  $\mathbf{H}^e$  map the displacements  $\hat{\mathbf{u}}^e$  at the nodes of the element onto the strains  $\boldsymbol{\gamma}^e$  and displacements  $\mathbf{u}^e$  for each element  $e$  respectively. Decomposing the integrals in the virtual work equation into a sum of integrals over the volume  $V_0^e$  and surface area  $S_0^e$  of a number of  $k$  finite elements gives

$$\begin{aligned} \sum_{e=1}^k \int_{V_0^e} \delta \hat{\mathbf{u}}^{eT} \rho_0^e \mathbf{H}^{(e)T} \mathbf{H}^e \ddot{\hat{\mathbf{u}}}^e dV_0^n + \sum_{e=1}^k \int_{V_0^e} \delta \hat{\mathbf{u}}^{(e)T} \mathbf{B}^{(e)T} \boldsymbol{\sigma}^e dV_0^e = \\ \sum_{e=1}^k \int_{V_0^e} \delta \hat{\mathbf{u}}^{(e)T} \rho_0^e \mathbf{H}^{(e)T} \mathbf{g} dV_0^e + \sum_{e=1}^k \int_{S_0^e} \delta \hat{\mathbf{u}}^{(e)T} \mathbf{H}^{(e)T} \mathbf{t}^e dS_0^e. \end{aligned} \quad (5.17)$$

The mass matrix of the structure can be written as the summation of the mass of each individual element  $\mathbf{M}^m$ :

$$\mathbf{M} = \sum_{e=1}^k \int_{V_0^e} \rho_0^e \mathbf{H}^{(e)T} \mathbf{H}^e dV_0^e. \quad (5.18)$$

The element body forces and element surface forces can be assembled in the external load vector  $\mathbf{f}_{\text{ext}}$ :

$$\mathbf{f}_{\text{ext}} = \sum_{e=1}^k \int_{V_0^e} \rho_0^e \mathbf{H}^{(e)T} \mathbf{g} dV_0^e + \sum_{e=1}^k \int_{S_0^e} \mathbf{H}^{(e)T} \mathbf{t}^e dS_0^e. \quad (5.19)$$

The internal forces of the element can likewise be assembled in the internal force vector  $\mathbf{f}_{\text{int}}$ :

$$\mathbf{f}_{\text{int}} = \sum_{e=1}^k \int_{V_0^e} \rho_0^e \mathbf{B}^{(e)T} \boldsymbol{\sigma}^e dV_0^e. \quad (5.20)$$

The general equilibrium equations governing the dynamic response of a mechanical system of finite elements as given in Eq. (5.17), for example a beam in vibration due to a sudden load application, must hold for any admissible  $\delta\hat{\mathbf{u}}$  and thus can be written as follows:

$$\mathbf{M}\ddot{\hat{\mathbf{u}}} = \mathbf{f}_{\text{ext}} - \mathbf{f}_{\text{int}}. \quad (5.21)$$

The effect of energy dissipation in the dynamic response of the mechanical system can be taken into account by introducing velocity-dependent damping forces. According to (Bathe 1996), these forces can be added as additional contributions to the body forces:

$$\mathbf{f}_{\text{ext}} = \sum_{e=1}^k \int_{V_0^e} \rho_0^e \mathbf{H}^{(e)T} [\mathbf{g} - \kappa^e \mathbf{H} \dot{\hat{\mathbf{u}}}] dV_0^e + \sum_{e=1}^k \int_{S_0^e} \mathbf{H}^{(e)T} \mathbf{t}^e dS_0^e. \quad (5.22)$$

Where  $\kappa^m$  denotes the damping property parameter of element  $m$ . In this case we find for the total system

$$\mathbf{M}\ddot{\hat{\mathbf{u}}} + \mathbf{C}\dot{\hat{\mathbf{u}}} = \mathbf{f}_{\text{ext}} - \mathbf{f}_{\text{int}}. \quad (5.23)$$

where the damping matrix  $\mathbf{C}^m$  of each element is written for the total damping of the finite element assembly as follows:

$$\mathbf{C} = \sum_{e=1}^k \int_{V_0^e} \kappa^e \mathbf{H}^{(e)T} \mathbf{H}^e dV_0^e. \quad (5.24)$$

Beside the inertia and stiffness forces, as present in Eq. 5.21, Eq. 5.23 also includes the damping forces on the left-hand side of the equation.

In the derivations no specification of the finite element itself has been given. The virtual strains  $\delta\gamma^e$  and virtual displacements  $\delta\mathbf{u}^e$  of the material point in each element are described by the Eqs. (5.15) and (5.16) as a function of the virtual nodal displacements  $\delta\hat{\mathbf{u}}^e$  of the finite element. Therefore, still a large number of formulations for the matrices  $\mathbf{B}^e$  and  $\mathbf{H}^e$  are possible. In Chapter 6 the Eqs. (5.15) and (5.16) will be derived for the thermo-mechanical solid-like shell element. Here the element type, the order of approximation of the displacement field and the shape of the element will be described.

### 5.3.4 The thermal system of equations

The thermal system of equations is calculated with the general heat transfer equations from the first law of thermodynamics:

$$\rho_0 \dot{\epsilon} + \text{Div } \mathbf{q} = \boldsymbol{\sigma} \cdot \dot{\mathbf{F}} + \rho_0 r, \quad (5.25)$$

where  $\dot{\epsilon}$  and  $\dot{\mathbf{F}}$  denote the material time derivative of the internal energy and the deformation gradient respectively,  $\rho_0$  is the mass density in the undeformed reference configuration, and  $\boldsymbol{\sigma}$  is the Cauchy stress tensor. Further, the vector  $\mathbf{q}$  represents the heat flux due to conduction and the scalar  $r$  the heat supply due to external sources, such as radiation. Thus, the first term on the left gives the internal energy of the body, and the second term the heat conduction. The terms on the right-hand side are the stress power, which can be regarded as the internal energy production, and the external energy supply.

In the further derivation we will only consider solids for which we can assume that the material particles of the body are at rest. The deformations of the structure are assumed not to generate heat and a corresponding change in the temperature field, which can for example be found in metal forming processes. The heat transfer conditions are considered as being decoupled from the stress conditions. Phase changes in the material will not be considered either. The latent heat in case of a phase transition of the material (i.e. for example melting or solidification) should be taken into account if the temperature rises above the phase transition point. The material parameters can be temperature-dependent in the following derivation. With Gibbs relation for elastic materials as given by (Liu 2002),

$$\theta\dot{\eta} = \dot{\epsilon} - \frac{1}{\rho_0} \boldsymbol{\sigma} \cdot \dot{\mathbf{F}}, \quad (5.26)$$

the energy balance given in Eq. 5.25 can be written as follows:

$$\rho_0\theta\dot{\eta} + \text{Div } \mathbf{q} = \rho_0 r. \quad (5.27)$$

Thus, the stress power, i.e. the work done by the internal stress, does not dissipate energy in case of an elastic material. Moreover, also for inelastic materials that for example exhibit a strain hardening behaviour, as discussed in Chapter 7, we will assume that the amount of heat produced due to deformation can be neglected.

To derive an expression for the entropy  $\eta$  we introduce the following definition for the specific heat  $c$ , see (Liu 2002):

$$c \equiv -\frac{\partial^2 \Psi}{\partial \theta^2} \theta, \quad (5.28)$$

where  $\Psi$  is the Helmholtz or free energy. When the specific heat is assumed to be constant, i.e. independent of the temperature, the entropy can be found directly upon integration,

$$\eta \equiv -\frac{\partial \Psi}{\partial \theta} = \int_{\theta_0}^{\theta} \frac{\partial^2 \Psi}{\partial \tilde{\theta}^2} d\tilde{\theta} = c \ln \frac{\theta}{\theta_0}, \quad (5.29)$$

where the scalar  $\theta_0$  denotes the reference temperature of the body. From Eq. 5.29 it follows that the material time derivative of the entropy  $\dot{\eta}$  can be written as

$$\dot{\eta} = c \left( \frac{\dot{\theta}}{\theta} \right), \quad (5.30)$$

where  $\dot{\theta}$  is the temperature flux. When the thermal conductivity is assumed to be independent of the temperature the classical Fourier's law of heat conduction is found,

$$\mathbf{q} = -\mathbf{k}\nabla\theta, \quad (5.31)$$

where  $\mathbf{k}$  is the thermal conductivity tensor and the temperature distribution  $\nabla\theta$  is defined as

$$\nabla\theta = \left[ \frac{\partial\theta}{\partial x} \quad \frac{\partial\theta}{\partial y} \quad \frac{\partial\theta}{\partial z} \right], \text{ or in compact notation: } \nabla\theta = \left[ \theta_{,x} \quad \theta_{,y} \quad \theta_{,z} \right]. \quad (5.32)$$

The thermal conductivity matrix  $\mathbf{k}$  can be orientation-dependent and the exact form depends on the material class. For an orthotropic material it reads:

$$\mathbf{k} = \begin{bmatrix} k_{xx} & 0 & 0 \\ 0 & k_{yy} & 0 \\ 0 & 0 & k_{zz} \end{bmatrix}. \quad (5.33)$$

In case of an isotropic material all diagonal terms are equal to each other. There are more material classes, see (Carslaw and Jaeger 2003) for a detailed overview, but only the isotropic and orthotropic cases will be used in this thesis. With the above mentioned specific models for the entropy  $\eta$  and the heat flux  $\mathbf{q}$ , the thermal system of equation reads

$$\rho_0 c \dot{\theta} + \text{Div } \mathbf{q} = \rho_0 r. \quad (5.34)$$

With the equations the effect of a certain heat source on the temperature distribution can be determined. The rate of change in temperature, the dynamic response, is in this case determined by the thermal conduction and the heat capacity of the material, i.e. the amount of heat the material can 'store' or 'dispose' as a function of time. Using similar descriptions as in the mechanical system of equations we can denote  $\rho_0 r$  as the external thermal loading,  $\mathbf{k}$  as the thermal equivalent of the elastic stiffness in the mechanical system, and  $\rho c$  as the thermal 'damping' term. Further on we will see that this is important for combining and solving the mechanical and thermal system of equations simultaneously.

### 5.3.5 The weak formulation of the thermal system

To obtain the finite element solution the principle of virtual temperatures is applied similar to the principle of virtual displacements. All procedures are directly applicable, however in this case the equation is solved for the scalar of unknown temperature:

$$\int_{V_0} \delta\theta[\rho_0 c \dot{\theta} + \text{Div } \mathbf{q} - \rho_0 r] dV_0 = 0. \quad (5.35)$$

Rewriting the second term between the brackets according to the algebraic rule given below

$$\int_{V_0} \text{Div}(\delta\theta \mathbf{q}) dV_0 = \int_{V_0} \nabla \delta\theta \cdot \mathbf{q} dV_0 + \int_{V_0} \delta\theta \text{Div } \mathbf{q} dV_0, \quad (5.36)$$

the following expression for Eq. 5.35 is found

$$\int_{V_0} \delta\theta \rho_0 c \dot{\theta} dV_0 - \int_{V_0} \nabla \delta\theta \cdot \mathbf{q} dV_0 = \int_{V_0} \text{Div}(\delta\theta \mathbf{q}) dV_0 + \int_{V_0} \rho_0 r dV_0. \quad (5.37)$$

By applying the divergence theorem we arrive at

$$\int_{V_0} \delta\theta \rho_0 c \dot{\theta} dV_0 - \int_{V_0} \nabla \delta\theta \cdot \mathbf{q} dV_0 = \int_{S_0} \delta\theta \mathbf{q} \cdot \mathbf{n} dS_0 + \int_{V_0} \rho_0 r dV_0. \quad (5.38)$$

The heat flux  $\mathbf{q}$  has been defined in Eq. 5.31 with Fourier's law of heat conduction. Further on, there are several boundary conditions encountered in the heat transfer analysis. The temperature and heat flow can be prescribed at specific points and surfaces of the body. Thus, we can state the following boundary conditions at the surface of the body that must be satisfied:

$$\theta = \theta^S \quad \text{on } S_\theta, \quad (5.39)$$

and

$$k_n \nabla \theta \cdot \mathbf{n} = q^S \quad \text{on } S_q, \quad (5.40)$$

where  $\theta^S$  is the known surface temperature on  $S_\theta$ ,  $k_n$  is the thermal conductivity of the body,  $n$  denotes the coordinate axis in the direction of the unit normal vector  $\mathbf{n}$  (pointing outward) to the surface. Further on,  $q^S$  is the prescribed heat flux input on the surface  $S_q$  of the body, with  $S_\theta \cup S_q = S$ , and  $S_\theta \cap S_q = 0$ . Eq. 5.38 can thus be written as

$$\int_{V_0} \delta\theta \rho c \dot{\theta} dV_0 + \int_{V_0} \nabla \delta\theta \mathbf{k} \nabla \theta dV_0 = \int_{S_q} \delta\theta q^S dS + \int_{V_0} \delta\theta q^B dV_0, \quad (5.41)$$

where  $q^B = \rho_0 r$  is the internally generated heat (excluding the heat capacity effect) due to an external heat source. Together both terms on the right-hand side are generally denoted by  $Q$ , the heat flow input.

In order to be complete, though not implemented in the model, it is shown below that radiation can be treated as a heat flux acting on the surface similar to convection. Thus both convection and radiation can be included in  $q^S$ . For convection a medium is required as a heat transport carrier. A distinction between free and forced convection can be made. Free convection can only take place in a gravitation field and is therefore not found in space. An example is the air in a specific region which warms up and rises due to the lower density. Forced convection takes place when a fluid is moved by external forces and thereby brings about the heat transport. In many cases the heat transport between a solid with temperature  $\theta^S$  and its fluid environment with temperature  $\theta_{\text{env}}$  is considered.

The heat flow due to convection  $q^S$  is modelled according to Newton's law and is given by

$$q^S = h_c(\theta_{\text{env}} - \theta^S), \quad (5.42)$$

in which  $h_c$  is the heat transfer coefficient for convection, which may be temperature-dependent. In contrast to heat conduction and convection no medium or temperature difference between two bodies or a body and its environment is required for heat radiation. Equilibrium exist in case that both bodies generate and absorb radiation in equal quantity. However, the temperature of the body and its surface condition have a strong influence on the outgoing radiation.

Radiation can be subdivided in radiation interchange between two bodies and between a body and its environment. In the latter case the temperature of the external radiative source  $\theta_r$  is assumed to be known. The heat flow due to radiation is modelled according to the Stefan-Boltzmann law and is given by

$$q^S = \psi \sigma_B (\theta_r^4 - \theta^{(S)4}), \quad (5.43)$$

where  $\sigma_B$  is the Stefan-Boltzmann constant, and  $\psi$  incorporates the emissivity of the radiant and absorbing materials and the geometric view factors of the considered surfaces. By factoring  $\theta_r^4 - \theta^{(S)4}$  Eq. (5.43) can be written similar to the convection Eq. (5.42),

$$q^S = h_r(\theta_r - \theta^S), \quad (5.44)$$

where for  $h_r$  the following expression is found:

$$h_r = \psi \sigma_B (\theta_r^2 + \theta^{(S)2})(\theta_r + \theta^S). \quad (5.45)$$

The Kirchhoff assumption can be applied, which states that the emission and absorption of radiation are equal to each other. This assumption holds true if the temperature is not too high, and is for example not valid anymore for space re-entry vehicles. For the surface heat flow we can write with the previously derived formulations for convection and radiation:

$$\int_{S_q} \delta\theta q^S dS = \int_{S_c} \delta\theta h_c(\theta_{\text{env}} - \theta^S) dS + \int_{S_r} \delta\theta h_r(\theta_r - \theta^S) dS. \quad (5.46)$$

### 5.3.6 Discretisation of the thermal system

The governing heat transfer equations can be discretised as follows for an element  $m$ ;

$$\theta^e = \mathbf{H}^e \hat{\boldsymbol{\theta}}; \quad (5.47)$$

$$\dot{\theta}^e = \mathbf{H}^e \dot{\hat{\boldsymbol{\theta}}}; \quad (5.48)$$

$$\theta^{S(e)} = \mathbf{H}^{S(e)} \hat{\boldsymbol{\theta}}; \quad (5.49)$$

$$\nabla\theta^e = \mathbf{B}^e \hat{\boldsymbol{\theta}}, \quad (5.50)$$

where  $\hat{\boldsymbol{\theta}}$  is the vector of nodal point temperatures and  $\mathbf{H}^e$  and  $\mathbf{B}^e$  are the element temperature and temperature-gradient interpolation matrices respectively. The matrix  $\mathbf{H}^{S(e)}$  is the surface temperature interpolation matrix. The derived thermal system of equations can be used in transient nonlinear analysis. The system is solved using an iterative solution procedure, for example the Newton-Raphson method.

It is important to notice that in the convection and radiation surface heat flow both contain the unknown surface temperature  $\theta^S$ . When for a given time-step  $t + \Delta t$  the nodal point temperatures at the end of iteration  $i$  are written as

$${}^{t+\Delta t}\boldsymbol{\theta}^i = {}^{t+\Delta t}\boldsymbol{\theta}^{(i-1)} + \Delta\boldsymbol{\theta}^i. \quad (5.51)$$

The incremental change in convection and radiation heat flow can be taken together with the conduction term on the left-hand side. For convenience we will leave out the superscript  $t + \Delta t$  in the following equations. With the division of the temperature in the temperature at the previous iteration and the incremental temperature change, Eq. (5.41) can be rewritten as

$$\mathbf{C}^i \dot{\boldsymbol{\theta}}^i + (\mathbf{K}^{k(i-1)} + \mathbf{K}^{c(i-1)} + \mathbf{K}^{r(i-1)}) \Delta\boldsymbol{\theta}^i = \mathbf{Q} - \mathbf{Q}^{k(i-1)}, \quad (5.52)$$



where the heat capacity matrix  $\mathbf{C}$  is denoted as

$$\mathbf{C}^i = \sum_{e=1}^k \int_{V^e} (\rho c_p)^{(e)i} \mathbf{H}^{(e)T} \mathbf{H}^e dV^e ; \quad (5.53)$$

the conductivity matrix  $\mathbf{K}^{k(i-1)}$  as

$$\mathbf{K}^{k(i-1)} = \sum_{e=1}^k \int_{V^e} \mathbf{B}^{(e)T} \mathbf{k}^{(e)(i-1)} \mathbf{B}^e dV^e ; \quad (5.54)$$

the convection matrix  $\mathbf{K}^{c(i-1)}$  as

$$\mathbf{K}^{c(i-1)} = \sum_{e=1}^k \int_{S_c^e} h_c^{(e)(i-1)} \mathbf{H}^{S(e)T} \mathbf{H}^{S(e)} dS^e ; \quad (5.55)$$

and the radiation matrix  $\mathbf{K}^{r(i-1)}$  as given below:

$$\mathbf{K}^{r(i-1)} = \sum_{e=1}^k \int_{S_r^e} h_r^{(e)(i-1)} \mathbf{H}^{S(e)T} \mathbf{H}^{S(e)} dS^e . \quad (5.56)$$

The heat conduction in the previous iteration is defined as

$$\mathbf{Q}^{k(i-1)} = \sum_{e=1}^k \int_{V^e} \mathbf{B}^{(e)T} \mathbf{k}^{(e)(i-1)} \mathbf{B}^e \boldsymbol{\theta}^{(i-1)} dV^e , \quad (5.57)$$

and the heat flow input  $\mathbf{Q}$  is determined as

$$\mathbf{Q}^{B(i)} + \mathbf{Q}^{c(i-1)} + \mathbf{Q}^{r(i-1)} , \quad (5.58)$$

where  $\mathbf{Q}^B$ , without the rate of heat stored within the material, is given by

$$\mathbf{Q}^{B(i)} = \sum_{e=1}^k \int_{V^e} \mathbf{H}^{(e)T} q^{B(e)} dV^e , \quad (5.59)$$

the convection heat flow by

$$\mathbf{Q}^{c(i-1)} = \sum_{e=1}^k \int_{S_c^e} h_c^{(e)(i-1)} \mathbf{H}^{S(e)T} \mathbf{H}^{S(e)} (\boldsymbol{\theta}_{\text{env}} - \boldsymbol{\theta}^{(i-1)}) dS^e , \quad (5.60)$$

and the radiation heat flow as

$$\mathbf{Q}^{r(i-1)} = \sum_{e=1}^k \int_{S_r^e} h_r^{(e)(i-1)} \mathbf{H}^{S(e)T} \mathbf{H}^{S(e)} (\boldsymbol{\theta}_r - \boldsymbol{\theta}^{(i-1)}) dS^e . \quad (5.61)$$

When no convection and radiation conditions are considered, in linear transient analysis the thermal system of equations reduces to

$$\mathbf{C}\dot{\boldsymbol{\theta}} + \mathbf{K}^k\boldsymbol{\theta} = \mathbf{Q}. \quad (5.62)$$

The matrices  $\mathbf{C}$  and  $\mathbf{K}^k$  in this case are not time-dependent. For a steady-state situation the heat transfer equations further reduce to the following model:

$$\mathbf{K}^k\boldsymbol{\theta} = \mathbf{Q}. \quad (5.63)$$

The matrix formulation of the complete dynamic thermo-mechanical model in general form can be presented as

$$\begin{bmatrix} \mathbf{M}_u & 0 \\ 0 & 0 \end{bmatrix} \begin{bmatrix} \ddot{\hat{\mathbf{u}}} \\ \ddot{\hat{\boldsymbol{\theta}}} \end{bmatrix} + \begin{bmatrix} \mathbf{C}_u & \\ & \mathbf{C}_\theta \end{bmatrix} \begin{bmatrix} \dot{\hat{\mathbf{u}}} \\ \dot{\hat{\boldsymbol{\theta}}} \end{bmatrix} + \begin{bmatrix} \mathbf{K}_u & \\ & \mathbf{K}_\theta \end{bmatrix} \begin{bmatrix} \hat{\mathbf{u}} \\ \hat{\boldsymbol{\theta}} \end{bmatrix} = \begin{bmatrix} \mathbf{F} \\ \mathbf{Q} \end{bmatrix}. \quad (5.64)$$

Through the off-diagonal terms in the stiffness-conductivity matrix a coupling between the temperature and the displacements due to thermal expansion can be made. This will be further detailed when deriving the governing equations in specific for the solid-like shell element in Chapter 6. In case of a dynamic system of equations an implicit time-integration procedure is used to obtain the solution of the (total) system. This will be shown in Section 5.4.1. The general procedure to solve (nonlinear) steady-state problems is outlined in Section 5.4.2. The solution procedure is further specified in Section 5.4.3 with the Newton-Raphson incremental-iterative method. In this method the load is applied in a number of load increments to assure accuracy and proper convergence.

## 5.4 Analysis and solution procedure

### 5.4.1 Transient analysis

The (nonlinear) equations of motion derived in the previous section take into account the dynamic behaviour, that is the acceleration and velocity, of the structure. In this way the most complete and accurate model is obtained, however it also requires more complicated solving techniques than linear static problems. Here we will describe a specific implicit time-integration solver called Park's method [(Park 1975a), (Park 1975b), and (Hughes 2000)]. The method has been implemented in the finite element platforms Stags (Rankin, Brogan, Loden, and Cabiness 1997) and B2000

(Remmers 1998) and is a linear multi-step method, in which the term 'linear' denotes the form in which the method is expressed. The second order differential Eqs. (5.23) can namely be rewritten as first order differential equations by means of Jensen's transformation algorithm, (Jensen 1974) as follows:

$$\dot{\mathbf{v}} = \mathbf{f}_{\text{ext}} - \mathbf{f}_{\text{int}}, \quad (5.65)$$

where the vector  $\mathbf{v}$ , called the generalised momentum auxiliary vector, is defined as

$$\mathbf{v} = \mathbf{M}\dot{\hat{\mathbf{u}}} + \mathbf{d}(\hat{\mathbf{u}}), \quad (5.66)$$

where  $\mathbf{d}$  is the damping operator, which can be defined as

$$\mathbf{d}(\hat{\mathbf{u}}) = \alpha\mathbf{M}\dot{\hat{\mathbf{u}}} + \beta\mathbf{f}_{\text{int}}(\hat{\mathbf{u}}) + \gamma\bar{\mathbf{C}}\hat{\mathbf{u}}, \quad (5.67)$$

where  $\alpha$ ,  $\beta$ , the Rayleigh damping factors, and  $\gamma$  are scalars and  $\bar{\mathbf{C}}$  is a matrix. If we choose the scalars to be zero, the matrix  $\bar{\mathbf{C}}$  coincides with our previously denoted damping matrix  $\mathbf{C}$  and we can write

$$\mathbf{v} = \mathbf{M}\dot{\hat{\mathbf{u}}} + \mathbf{C}\hat{\mathbf{u}}. \quad (5.68)$$

The general time integration procedure that has been used in the present thesis is Park's Method. In the procedure it is assumed that a solution is known at time-step  $n-1$  and that the history vectors for the displacements  $\mathbf{h}_{n-1}^{\mathbf{u}}$  and the generalised momentum  $\mathbf{h}_{n-1}^{\mathbf{v}}$  exist. The aim of the procedure is to advance the solution at time-step  $n-1$  to time-step  $n$ , thus  $\Delta t = t_n - t_{n-1}$ . First  $\dot{\mathbf{v}}$  is calculated directly from the external and internal load vector at time-step  $n-1$ :

$$\dot{\mathbf{v}}_{n-1} = \mathbf{f}_{\text{ext}}(t_{n-1}) - \mathbf{f}_{\text{int}}(\hat{\mathbf{u}}_{n-1}). \quad (5.69)$$

In case  $n=0$  the generalised momentum is

$$\mathbf{v} = \mathbf{M}\dot{\hat{\mathbf{u}}} + \mathbf{C}\hat{\mathbf{u}}, \quad (5.70)$$

else the equation reads:

$$\mathbf{v}_{n-1} = \mathbf{h}_{n-1}^{\mathbf{v}} + t_{\beta}\dot{\mathbf{v}}_{n-1}, \quad (5.71)$$

where  $\mathbf{h}_{n-1}^{\mathbf{v}}$  is the history vector of the generalised momentum and  $t_{\beta} = \Delta t\beta_0$  is the modified time-step. The history vectors  $\mathbf{h}_n^{\mathbf{v}}$  and  $\mathbf{h}_n^{\mathbf{u}}$  at time-step  $n$  are determined as follows:

$$\mathbf{h}_n^{\mathbf{v}} = \Delta t\mathbf{b}_n^{\dot{\mathbf{v}}} - \mathbf{a}_n^{\mathbf{v}}; \text{ and } \mathbf{h}_n^{\mathbf{u}} = \Delta t\mathbf{b}_n^{\dot{\mathbf{u}}} - \mathbf{a}_n^{\mathbf{u}}, \quad (5.72)$$

where the history vectors  $\mathbf{a}_n^u$  and  $\mathbf{a}_n^v$  are computed as

$$\mathbf{a}_n^u = \sum_{i=1}^{m_\alpha} \alpha_i \mathbf{u}_{n-i}; \text{ and } \mathbf{a}_n^v = \sum_{i=1}^{m_\alpha} \alpha_i \mathbf{v}_{n-i}. \quad (5.73)$$

The history vectors  $\mathbf{b}_n^{\dot{u}}$  and  $\mathbf{b}_n^{\dot{v}}$  are computed as

$$\mathbf{b}_n^{\dot{u}} = \sum_{i=1}^{m_\beta} \beta_i \dot{\mathbf{u}}_{n-i}; \text{ and } \mathbf{b}_n^{\dot{v}} = \sum_{i=1}^{m_\beta} \beta_i \dot{\mathbf{v}}_{n-i}, \quad (5.74)$$

with the integration formulas

$$\sum_{i=0}^{m_\alpha} \alpha_i \mathbf{u}_{n-i} = \Delta t \sum_{i=0}^{m_\beta} \beta_i \dot{\mathbf{u}}_{n-i}; \text{ and } \sum_{i=0}^{m_\alpha} \alpha_i \mathbf{v}_{n-i} = \Delta t \sum_{i=0}^{m_\beta} \beta_i \dot{\mathbf{v}}_{n-i}. \quad (5.75)$$

In the formulas above  $\alpha_i$  and  $\beta_i$  are integration constants, and  $m_\alpha$  and  $m_\beta$  determine the starting procedure to build the history vectors  $\mathbf{h}_n^u$  and  $\mathbf{h}_n^v$ . Once the history vectors are determined the equation of motion can be solved for  $\mathbf{u}_n$  via an iterative procedure, for example a Newton-Raphson method, in which a trial  $\mathbf{u}_n$  is used. The Newton-Raphson method will be discussed in Section 5.4.3. The equation of motion becomes

$$\mathbf{g}(\mathbf{u}_n) = \mathbf{M}\mathbf{u}_n + t_\beta \mathbf{C}\hat{\mathbf{u}}_n + t_\beta^2 \mathbf{f}_{\text{int}}(\hat{\mathbf{u}}_n) - \mathbf{M}\mathbf{h}_n^u - t_\beta \mathbf{h}_n^v - t_\beta^2 \mathbf{f}_{\text{ext}}(t) = 0, \quad (5.76)$$

and from this  $\dot{\mathbf{u}}_n$  can be calculated via

$$\dot{\mathbf{u}}_n = (\mathbf{u}_n - \mathbf{h}_n^u)/t_\beta, \quad (5.77)$$

and the step number can be advanced from  $n$  to  $n + 1$ , the vectors  $\mathbf{u}_n$ ,  $\dot{\mathbf{u}}_n$ ,  $\mathbf{h}_n^v$ , and  $\mathbf{h}_n^u$  are stored. The time-step is incremented from  $t$  to  $t + \Delta t$ , and if  $t < t_{\text{max}}$  the whole loop is repeated. To build the history vectors  $\mathbf{h}_n^v$  and  $\mathbf{h}_n^u$  in Eqs. (5.76) and (5.77) a starting procedure is needed in the integration procedure. For the Park formula,  $m_\alpha = 3$ , so that two starting algorithms are required. The parameters for the first two steps and for the full Park method are given in Table 5.1. Park's method combines the Gear's 2 and 3 step methods, see (Gear 1971), with equal weight to obtain an unconditionally stable method with less damping as a result. The starting algorithms have a worse accuracy compared to the full Park method, but the stability level is the same.

Method	$\beta_0$	$\beta_1$	$\alpha_1$	$\alpha_2$	$\alpha_3$
Park (1 <sup>st</sup> step)	$\frac{6}{10}$	$\frac{4}{10}$	-1		
Park (2 <sup>nd</sup> step)	$\frac{6}{10}$	$\frac{2}{10}$	$-\frac{12}{10}$	$\frac{2}{10}$	
Park (full)	$\frac{6}{10}$		$-\frac{15}{10}$	$\frac{6}{10}$	$-\frac{1}{10}$

Table 5.1: Linear multi-step scheme for Park's method, including 1<sup>st</sup> and 2<sup>nd</sup> step.

### 5.4.2 Nonlinear static analysis

In case only static problems are considered, the acceleration vector  $\ddot{\mathbf{u}}$  and velocity vector  $\dot{\mathbf{u}}$  are zero. Static problems can be divided into linear and nonlinear problems. For a linear elastic problem the constitutive relation can be written as

$$\boldsymbol{\sigma}^m = \mathbf{D}^m \boldsymbol{\gamma}^m = \mathbf{D}^m \mathbf{B}^m \hat{\mathbf{u}}^m, \quad (5.78)$$

and thus for the linear elastic stiffness matrix  $\mathbf{K}$  we can write

$$\mathbf{K} = \sum_{m=1}^k \int_{V_0^m} \mathbf{B}^{mT} \mathbf{D}^m \mathbf{B}^m dV_0^m. \quad (5.79)$$

The virtual internal energy from Eq. (5.23) then becomes

$$\mathbf{f}_{\text{int}} = \mathbf{K} \hat{\mathbf{u}}. \quad (5.80)$$

The system of equations is solved by minimising the residual function  $\Psi$ :

$$\Psi = \mathbf{f}_{\text{ext}} - \mathbf{f}_{\text{int}}. \quad (5.81)$$

In case of physically nonlinear material behaviour there is no linear stress-strain relation. The stress increment  $\Delta \boldsymbol{\sigma}$  depends nonlinearly on the strain increment  $\Delta \boldsymbol{\gamma}$ . The strain increment in turn can be a nonlinear function of the continuous displacement field  $\Delta \mathbf{u}$ , and for the stress increment we can thus write

$$\Delta \boldsymbol{\sigma} = f(\Delta \boldsymbol{\gamma}(\Delta \mathbf{u})). \quad (5.82)$$

The stress increment  $\Delta \boldsymbol{\sigma}$  can be linearised as

$$\Delta \boldsymbol{\sigma} = \left( \frac{\partial \boldsymbol{\sigma}}{\partial \boldsymbol{\gamma}} \right) \left( \frac{\partial \boldsymbol{\gamma}}{\partial \hat{\mathbf{u}}} \right) \Delta \mathbf{u}. \quad (5.83)$$

At a specific time in the loading process the material tangent stiffness matrix is

$$\mathbf{D}_i = \left( \frac{\partial \boldsymbol{\sigma}}{\partial \boldsymbol{\gamma}} \right). \quad (5.84)$$

From the virtual internal work equation the derivative  $\partial \gamma / \partial \mathbf{u}$  can be identified as the differential operator  $\mathbf{L}$ . Together with the fact that  $\Delta \mathbf{u}$  can be written as  $\mathbf{H} \Delta \hat{\mathbf{u}}$  we arrive at

$$\Delta \boldsymbol{\sigma} = \mathbf{D}_i \mathbf{L} \mathbf{H} \Delta \hat{\mathbf{u}} = \mathbf{D}_i \mathbf{B} \Delta \hat{\mathbf{u}}. \quad (5.85)$$

The stress at time  $t + \Delta t$  can be written as

$$\boldsymbol{\sigma}^{t+\Delta t} = \boldsymbol{\sigma}^t + \Delta \boldsymbol{\sigma}. \quad (5.86)$$

Since static problems are considered, it should be noted that "time" is used here to order events in the mechanical process and has no physical meaning. When we substitute this into the virtual work Eq. (5.17) we obtain

$$\sum_{e=1}^k \int_{V_0^e} \delta \hat{\mathbf{u}}^{(e)T} \mathbf{B}^{(e)T} \boldsymbol{\sigma}^{tm} dV_0^e + \sum_{e=1}^k \int_{V_0^e} \delta \hat{\mathbf{u}}^{(e)T} \mathbf{B}^{(e)T} \Delta \boldsymbol{\sigma} dV_0^e = \mathbf{f}_{\text{ext}}. \quad (5.87)$$

Rewriting this equation using the expression for the external virtual work  $\mathbf{f}_{\text{ext}}$  and the expression for the stress increment  $\Delta \boldsymbol{\sigma}$  gives

$$\begin{aligned} & \sum_{e=1}^k \int_{V_0^e} \delta \hat{\mathbf{u}}^{(e)T} \mathbf{B}^{(e)T} \boldsymbol{\sigma}^{t(e)} dV_0^e + \sum_{e=1}^k \int_{V_0^e} \delta \hat{\mathbf{u}}^{(e)T} \mathbf{B}^{(e)T} \mathbf{D}_i^t \mathbf{B}^e \Delta \hat{\mathbf{u}}^e dV_0^e = \\ & \sum_{e=1}^k \int_{V_0^e} \delta \hat{\mathbf{u}}^{(e)T} \rho_0^n \mathbf{H}^{(e)T} \mathbf{g}^{t+\Delta t} dV_0^e + \sum_{e=1}^k \int_{S_0^e} \delta \hat{\mathbf{u}}^{(e)T} \mathbf{H}^{(e)T} \mathbf{t}^{t+\Delta t(e)} dS_0^e. \end{aligned} \quad (5.88)$$

Thus, in an iterative procedure, the system of equations can be solved for the unknown displacements. To obtain an accurate method and to assure proper convergence, an incremental-iterative procedure is proposed in the next section.

### 5.4.3 The incremental-iterative solution procedure

With the system of equations derived in the previous section, Eq. 5.88, the deformation of the structure can be described. To solve the system for the nodal displacements, a Newton-Raphson procedure can generally be

used. In the incremental-iterative solution method the load is applied in a number of load increments. In general the structure shows a geometrically nonlinear behaviour, which means that there are large deformations that consequently require a suitable measure. Also a physically nonlinear behaviour can be present, where the stress is related to the strain via a nonlinear function. A properly converged solution is difficult to obtain for large loading steps. The response of inelastic materials is path-dependent, which means that the value of the stress depends on the followed strain path. To predict the structural behaviour accurately small strain increments are necessary. To solve for the new displacements Eq. (5.81) is linearised. The error which is caused by the linearisation is corrected via a number of  $i$  equilibrium iterations. Thus for each load increment the change of the displacements  $d\hat{\mathbf{u}}_{n+1}^{i+1}$  is calculated via

$$d\hat{\mathbf{u}}_{n+1}^{i+1} = \mathbf{K}_t^{-1}(\mathbf{f}_{\text{ext}}^{t+\Delta t} - \mathbf{f}_{\text{int},n}). \quad (5.89)$$

Applying

$$\mathbf{K}_t = \sum_{e=1}^k \int_{V_0^e} \mathbf{B}^{(e)T} \mathbf{D}_i^t \mathbf{B}^e dV_0^e, \quad (5.90)$$

gives

$$\mathbf{K}_t \Delta \hat{\mathbf{u}} = \mathbf{f}_{\text{ext}}^{t+\Delta t} - \mathbf{f}_{\text{int}}^t, \quad (5.91)$$

where the matrix  $\mathbf{K}_t$  represents the tangent stiffness of the structure to a small load increment. Upon summation over all iterations, the total change of the displacements per load increment  $\Delta \hat{\mathbf{u}}_{n+1}$  is calculated:

$$\Delta \hat{\mathbf{u}}_{n+1}^{i+1} = \sum_{j=1}^{i+1} d\hat{\mathbf{u}}_{n+1}^j. \quad (5.92)$$

From this, the total displacements  $\hat{\mathbf{u}}_{n+1}^{i+1}$  are determined:

$$\hat{\mathbf{u}}_{n+1}^{i+1} = \hat{\mathbf{u}}_n + \Delta \hat{\mathbf{u}}_{n+1}^{i+1}, \quad (5.93)$$

and the residual Eq. (5.81) can be written as

$$\Psi = \sum_{e=1}^k \int_{V_0^e} (\mathbf{B}^e \hat{\mathbf{u}}_{n+1}^{i+1})^T (\boldsymbol{\sigma}^n)_{n+1}^{i+1} dV_0^e - \mathbf{f}_{n+1}). \quad (5.94)$$

The iterations are carried out up to the point that the residual reaches a user-defined convergence criterion. The stress update  $\boldsymbol{\sigma}_{n+1}^{i+1}$  is calculated

from the stress  $\sigma_n$  and nodal displacements  $\hat{\mathbf{u}}_n$  of the previous equilibrium state  $n$  via

$$(\sigma^e)_{n+1}^{i+1} = (\sigma^e)_n + \Delta\sigma^e(\Delta\gamma^e(\hat{\mathbf{u}}_n, \Delta\hat{\mathbf{u}}_{n+1}^{i+1})), \quad (5.95)$$

where the stress increment  $\Delta\sigma$  is a (nonlinear) function of the strain increment  $\Delta\gamma$ , which is itself a function of the displacement history and the displacement increment. The stress is updated with the total increment, and not after each iteration to avoid spurious unloading in case of elasto-plastic calculations. The matrix  $\mathbf{K}_t$  is the tangent stiffness matrix and can be calculated as

$$\mathbf{K}_t = \sum_{e=1}^k \mathbf{H}^{(e)T} \mathbf{K}_t^e \mathbf{H}^e. \quad (5.96)$$

This matrix consists of two contributions which both are functions of the nodal displacements  $\hat{\mathbf{u}}^e$ :

$$\mathbf{K}_t^e = \mathbf{K}_\sigma^e + \mathbf{K}_0^e = \sum_{e=1}^k \int_{V_0^e} \mathbf{B}^{(e)T} \sigma^e dV_0^e + \sum_{e=1}^k \int_{V_0^e} \mathbf{B}^{(e)T} \left( \frac{\partial\sigma}{\partial\gamma} \right) \left( \frac{\partial\gamma}{\partial\hat{\mathbf{u}}} \right) dV_0^e, \quad (5.97)$$

where the matrix  $\mathbf{K}_\sigma^e$  is dependent on the current state of stress and the matrix  $\mathbf{K}_0^e$  is a function of the material tangent stiffness  $(\partial\sigma/\partial\gamma)$ . In case of elasto-plastic calculations, that is for physically nonlinear behaviour, the total derivative  $(d\sigma/d\gamma)$  must be applied. In Chapter 6 the matrices  $\mathbf{K}_\sigma^e$  and  $\mathbf{K}_0^e$  will be described for the solid-like shell element.

In the description of the Newton-Raphson method the structure was assumed to be loaded incrementally by an external force vector. Thus, the solution procedure has been described for load-control conditions. However, in the procedure also a displacement-control can be followed. In this case the prescribed deformation at certain points of the structure is used to determine the corresponding internal force vector, which can be regarded as the initially applied load.

The Newton-Raphson procedure described in this section is in general adequate. However, the procedure is not very efficient and fails at limit points when strong physical nonlinearities are present. Displacement-control can be solution, but in case of snap-back phenomena also fails. A path-following technique as introduced by (Riks 1970) can be used. The method is amongst others described by Hashagen and is not described in this thesis.



## 5.5 Physical nonlinearities

The relation between the stresses and strains can be nonlinear in case of strain hardening or damage, which will be discussed in detail in Chapters 7 and 8 respectively. For both the strain hardening and the damage model a loading function is used to describe the occurrence of plasticity or damage. The advantage of the 3D solid-like shell herein is the straightforward way the physically nonlinear models can be included.

### 5.5.1 Strain hardening

As shown in Eq. (5.95) the stress-strain relation can be written as

$$\boldsymbol{\sigma}_{n+1}^{i+1} = \boldsymbol{\sigma}_n + \Delta\boldsymbol{\sigma}(\Delta\boldsymbol{\gamma}(\hat{\mathbf{u}}_n, \Delta\hat{\mathbf{u}}_{n+1}^{i+1})), \quad (5.98)$$

where for an elastic material  $\Delta\boldsymbol{\sigma}$  is a linear function of the strain  $\Delta\boldsymbol{\gamma}$ :

$$\Delta\boldsymbol{\sigma}_{n+1}^{i+1} = \mathbf{D}\Delta\boldsymbol{\gamma}_{n+1}^{i+1}, \quad (5.99)$$

with  $\mathbf{D}$  the linear elastic stiffness operator. However, the materials used in fibre-metal laminates, fibre-composites and metals, in general show a nonlinear stress-strain behaviour due to strain hardening or damage. To capture these phenomena a loading or yield function is introduced that bounds all possible stress states in a material point. Stress states inside the contour specified by the yield function only cause elastic deformations, while stress states on this yield surface give rise to elasto-plastic deformations. By definition stress states outside this yield contour are not possible.

The loading function can be either be expressed as a function of strain or stress as will be used for the strain hardening model:

$$f(\boldsymbol{\sigma}, \kappa) = \tilde{\sigma}(\boldsymbol{\sigma}) - \bar{\sigma}(\kappa) \leq 0, \quad (5.100)$$

where  $\kappa$  is the hardening parameter which determines the yield strength scalar  $\bar{\sigma}$  by a so-called hardening law. The equivalent stress  $\tilde{\sigma}$  is a function of the current stress state  $\boldsymbol{\sigma}$ . The hardening parameter  $\kappa$  memorises the largest value attained during the loading history and can therefore only increase. This means that the rate of strain hardening  $\dot{\kappa}$  must be non-negative. If the loading function is negative, unloading occurs and there is no strain hardening. If the loading function is zero, further loading can take place and the rate of the plastic multiplier  $\dot{\lambda} \geq 0$ . Loading or unloading in any material point can be formalised by applying the Kuhn-Tucker conditions:

$$f \leq 0 \quad , \quad \dot{\lambda} \geq 0 \quad , \quad f\dot{\lambda} = 0, \quad (5.101)$$

The inelastic strains are irreversible and remain after removal of the load. The total strain  $\dot{\gamma}$  can be decomposed into an elastic component  $\dot{\epsilon}^{el}$  and an inelastic component  $\dot{\epsilon}^{pl}$ , respectively

$$\dot{\gamma} = \dot{\epsilon}^{el} + \dot{\epsilon}^{pl}. \quad (5.102)$$

The elastic strain rate  $\dot{\epsilon}^{el}$  is related to the stress rate  $\dot{\sigma}$  via the elastic stiffness matrix:

$$\dot{\sigma} = \mathbf{D}\dot{\epsilon}^{el}. \quad (5.103)$$

The plastic strain rate  $\dot{\epsilon}^{pl}$  can be written as a product of the magnitude of the plastic flow  $\dot{\lambda}$  and the direction of the plastic flow  $\mathbf{m}$ :

$$\dot{\epsilon}^{pl} = \dot{\lambda}\mathbf{m}. \quad (5.104)$$

In general we can write for the direction of the flow

$$\mathbf{m} = \frac{\partial g}{\partial \boldsymbol{\sigma}}, \quad (5.105)$$

where  $g(\boldsymbol{\sigma}, \kappa)$  is called the plastic potential. When the function  $g$  coincides with the strain hardening function  $f$  the flow direction is orthogonal to the yield surface. In that case we speak of an associated flow rule, otherwise of a non-associated flow rule, and we can write

$$\dot{\epsilon}^{pl} = \dot{\lambda} \frac{\partial f}{\partial \boldsymbol{\sigma}}. \quad (5.106)$$

The value of the multiplier  $\dot{\lambda}$  can be determined from the requirement that during plastic flow the stresses remain bounded. In Chapter 7 this is further discussed for the Von Mises yield function in which an associated flow rule is applied.

The hardening parameter is integrated along the loading path via

$$\kappa = \int \dot{\kappa} dt. \quad (5.107)$$

There are several hardening hypotheses available in the literature to define the rate of the hardening parameter  $\dot{\kappa}$ . The strain hardening hypothesis reads:

$$\dot{\kappa} = \sqrt{\frac{2}{3}(\dot{\epsilon}^{pl})^T \mathbf{T} \dot{\epsilon}^{pl}}, \quad (5.108)$$

where  $\mathbf{T}$  is a diagonal matrix defined as  $\mathbf{T} = \text{diag}[1, 1, 1, 1/2, 1/2, 1/2]$ , which takes into account that the shear strains in the vector  $\boldsymbol{\epsilon}$  are in fact the double engineering shear strains.

### 5.5.2 The return-mapping algorithm

In the elasto-plastic analysis a return-mapping algorithm is used to determine the stress state which satisfies the Kuhn-Tucker conditions of Eq. (5.101) at each point of the applied loading path. Starting from a given state  $n$  for which the stress  $\boldsymbol{\sigma}^n$ , the total strain  $\boldsymbol{\gamma}^n$ , and the hardening parameter  $\kappa^n$  are known, the new total strain is determined from

$$\boldsymbol{\gamma}_{n+1}^{i+1} = \boldsymbol{\gamma}_n + \Delta\boldsymbol{\gamma}_{n+1}^{i+1}, \quad (5.109)$$

where the strain increment  $\Delta\boldsymbol{\gamma}_{n+1}^{i+1}$  follows from the displacement increment  $\Delta\hat{\boldsymbol{\gamma}}$ . With this strain increment an estimation of the new stress, the so-called trial stress, is made:

$$\boldsymbol{\sigma}_{\text{trial}} = \boldsymbol{\sigma}_n + \mathbf{D}\Delta\boldsymbol{\gamma}. \quad (5.110)$$

If the yield condition given in Eq. (5.100) is satisfied for this trial stress there will be only elastic deformations. When the yield condition is violated, that is when  $f(\boldsymbol{\sigma}_{\text{trial}}, \kappa) > 0$ , the stress state lies outside the yield surface and a return-mapping algorithm is applied to map back the stress onto the yield surface. At the same time the plastic strains and hardening parameter increase.

To obtain an unconditionally stable algorithm, a fully implicit Euler backward method is applied in which all stress-dependent quantities are determined at  $\boldsymbol{\sigma} = \boldsymbol{\sigma}_{n+1}$  and  $\kappa = \kappa_{n+1}$ . The new stress  $\boldsymbol{\sigma}_{n+1}$  is calculated with

$$\boldsymbol{\sigma}_{n+1} = \boldsymbol{\sigma}_{\text{trial}} - \mathbf{D}\Delta\boldsymbol{\epsilon}^{pl}|_{n+1}, \quad (5.111)$$

where we used the decomposition of the total strain increment into an elastic and a plastic part, similar to Eq. (5.102). In accordance with Eq. (5.106), the incremental plastic strain is given by

$$\Delta\boldsymbol{\epsilon}^{pl}|_{n+1} = \Delta\lambda_{n+1} \frac{\partial f}{\partial \boldsymbol{\sigma}}|_{n+1}. \quad (5.112)$$

The method is called implicit since neither  $\Delta\lambda_{n+1}$  nor  $\boldsymbol{\sigma}_{n+1}$  (and correspondingly the normal to the yield surface  $\mathbf{n}$  and the flow direction  $\mathbf{m}$ ) can be calculated directly. An additional equation is required, which comes from the compliance with the yield function at the end of the load step:

$$f(\boldsymbol{\sigma}_{n+1}, \kappa_{n+1}) = 0, \quad (5.113)$$

or, since  $\kappa_{n+1} = \kappa_{n+1}(\lambda_{n+1})$ , Eq. (5.113) can also be written as

$$f(\boldsymbol{\sigma}_{n+1}, \lambda_{n+1}) = 0. \quad (5.114)$$

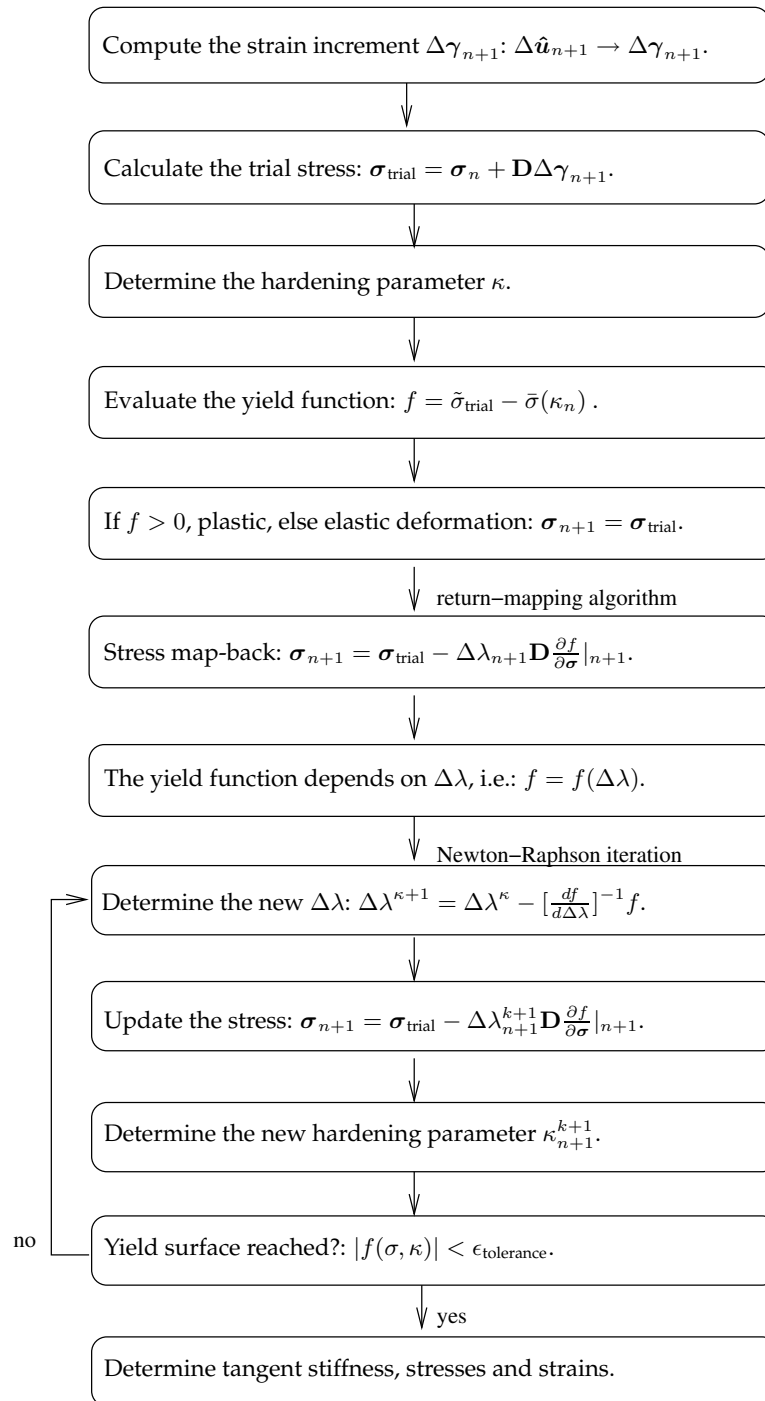


Figure 5.2: Algorithmic procedure for the strain hardening analysis. For each iteration and at each integration point the listed operations need to be performed.

Eqs. (5.111) and (5.114) in total form seven equations with seven unknowns, viz. the six stress components of  $\boldsymbol{\sigma}_{n+1}$  and  $\lambda_{n+1}$ . The nonlinear system of equations is solved via a Newton-Raphson procedure. First Eq. (5.111) is re-casted in a similar form as equation Eq. (5.114):

$$\mathbf{g}(\boldsymbol{\sigma}_{n+1}, \kappa_{n+1}) = \boldsymbol{\sigma}_{n+1} - \boldsymbol{\sigma}_{\text{trial}} + \mathbf{D}\Delta\boldsymbol{\epsilon}^{pl}|_{n+1} = \mathbf{0}. \quad (5.115)$$

The system is now solved as

$$\begin{bmatrix} \boldsymbol{\sigma}_{n+1}^{k+1} \\ \lambda_{n+1}^{k+1} \end{bmatrix} = \begin{bmatrix} \boldsymbol{\sigma}_{n+1}^k \\ \lambda_{n+1}^k \end{bmatrix} - \mathbf{J}^{-1} \begin{bmatrix} \mathbf{g}(\boldsymbol{\sigma}_{n+1}^k, \lambda_{n+1}^k) \\ f(\boldsymbol{\sigma}_{n+1}^k, \lambda_{n+1}^k) \end{bmatrix}, \quad (5.116)$$

with  $k$  the iteration counter of the local Newton-Raphson iteration and the matrix  $\mathbf{J}$  represents the Jacobian of the system:

$$\mathbf{J} = \begin{bmatrix} \frac{\partial \mathbf{g}}{\partial \boldsymbol{\sigma}} & \frac{\partial \mathbf{g}}{\partial \gamma} \\ \frac{\partial f}{\partial \boldsymbol{\sigma}} & \frac{\partial f}{\partial \gamma} \end{bmatrix}. \quad (5.117)$$

The procedure for the strain hardening analysis is summarised in Figure 5.2.

### 5.5.3 The consistent tangent stiffness matrix

As described in Section 5.4.3, the nonlinear system of equations is linearised in the finite element formulation. The linearised system is solved in an iterative Newton-Raphson procedure until convergence is reached. A consistent linearisation of the tangent stiffness matrix is important for the performance of the Newton-Raphson iteration, which is expressed in the computation time and robustness of the method. In a full Newton-Raphson procedure the use of a consistent tangent stiffness matrix, in which the effects of plastic flow on the stiffness are included, is very advantageous compared to a conventional tangent stiffness matrix. It can typically reduce the number of iterations necessary to obtain a converged solution by a factor of two, as indicated by (de Borst and Sluys 1999). To obtain the consistency, the linearisation must be consistent with the stress update in the return-mapping algorithm. The consistent tangent stiffness matrix can be derived by differentiating Eq. (5.111) with respect to  $\Delta\lambda$ ,  $\Delta\kappa$ , and  $\gamma$ :

$$\frac{d\boldsymbol{\sigma}}{d\gamma} = \frac{\partial \boldsymbol{\sigma}}{\partial \Delta\gamma} + \frac{\partial \boldsymbol{\sigma}}{\partial \Delta\lambda} \frac{\partial \Delta\lambda}{\partial \Delta\gamma} + \frac{\partial \boldsymbol{\sigma}}{\partial \Delta\kappa} \frac{\partial \Delta\kappa}{\partial \Delta\gamma} = \frac{\partial \boldsymbol{\sigma}}{\partial \Delta\gamma} + \begin{bmatrix} \frac{\partial \boldsymbol{\sigma}}{\partial \Delta\lambda} & \frac{\partial \boldsymbol{\sigma}}{\partial \Delta\kappa} \end{bmatrix} \begin{bmatrix} \frac{\partial \Delta\lambda}{\partial \Delta\gamma} \\ \frac{\partial \Delta\kappa}{\partial \Delta\gamma} \end{bmatrix},$$

$$(5.118)$$

where we used the fact that  $\gamma$  can be decomposed into a constant part  $\gamma_n$  and a non-constant, strain increment  $\Delta\gamma_{n+1}$ . The residuals defined in Eqs. (5.114) and (5.115) must be zero when convergence in the local return-mapping is obtained. When these residuals are collected in the residual vector  $\mathbf{r} = (f, \mathbf{g})$ , a total differentiation of  $\mathbf{r}$  with respect to  $\Delta\gamma$  can be written as

$$\left[ \frac{\partial \Delta\lambda}{\partial \Delta\gamma}, \frac{\partial \Delta\kappa}{\partial \Delta\gamma} \right] = -\mathbf{J}^{-1} \left( \frac{\partial \mathbf{r}}{\partial \boldsymbol{\sigma}} \right) \left( \frac{\partial \boldsymbol{\sigma}}{\partial \Delta\gamma} \right), \quad (5.119)$$

where  $\mathbf{J}$  is the Jacobian given in Eq. (5.117). The Jacobian is obtained for the values  $\Delta\lambda_{n+1}$  and  $\Delta\kappa_{n+1}$  that lead to convergence in the local return-mapping algorithm. When Eq. (5.119) is applied in Eq. (5.118) the consistent tangent stiffness operator can finally be written as

$$\frac{d\boldsymbol{\sigma}}{d\gamma} = \frac{\partial \boldsymbol{\sigma}}{\partial \Delta\gamma} - \left[ \frac{\partial \boldsymbol{\sigma}}{\partial \Delta\lambda}, \frac{\partial \boldsymbol{\sigma}}{\partial \Delta\kappa} \right] \mathbf{J}^{-1} \left( \frac{\partial \mathbf{r}}{\partial \boldsymbol{\sigma}} \right) \left( \frac{\partial \boldsymbol{\sigma}}{\partial \Delta\gamma} \right). \quad (5.120)$$

It should be noted that the consistent tangent stiffness matrix is only useful in a full Newton-Raphson procedure, since then the stiffness matrix is updated during iteration and the plastic flow is included.

### 5.5.4 Damage growth

In damage mechanics the degradation of the material due to the development of microcracks is accounted for by one or more scalar or tensor-valued internal damage variables, see (Lemaître and Chaboche 1990). As in standard plasticity, the influence of the material history on the stress evolution is incorporated via a number of internal variables. Unloading, however, occurs elastically in plasticity models, whereas in damage mechanics the degradation of the elastic stiffness is taken into account. Simple elasticity-based damage formulations give a secant unloading to a stress-free and strain-free state in the origin. The damage variables are defined by the ratio of the cracked volume over the total volume of a piece of material.

The degradation of the material can be taken into account through the principle of equivalent stress or equivalent strain. In the first case the strain in a damaged material will be higher at equal stress than in a undamaged material. In the latter case the stress in the damaged material is lower than in the undamaged material at equal strain. Since the classical

finite element method starts from the assumption of known strains in the integration points and the stresses are calculated from these strains, the principle of equivalent strain is used.

In the material model the damage is taken into account as a reduction of the stiffness of the material. In the case of an isotropic material this damage parameter can be represented by a single scalar variable, in which all damage effects are added and reflected. The constitutive relation can be written as

$$\boldsymbol{\sigma} = (1 - \omega)\mathbf{D}\boldsymbol{\gamma}, \quad (5.121)$$

in which  $\boldsymbol{\sigma}$  and  $\boldsymbol{\gamma}$  are the stresses and strains in the integration point respectively, and  $\mathbf{D}$  is the virgin isotropic elastic stiffness matrix, either expressed in terms of bulk modulus  $\kappa$  and shear modulus  $\mu$  or in terms of Young's modulus  $E$  and Poisson's ratio  $\nu$ . The damage parameter of the material is given by  $\omega$ .

For anisotropic materials a scalar damage variable is no longer sufficient to describe the occurrence of damage in the different directions. (Cordebois and Sideroff 1982) proposed to take a damage matrix in these situations. The constitutive relation then changes to

$$\boldsymbol{\sigma} = (\mathbf{I} - \boldsymbol{\Omega})\mathbf{D}\boldsymbol{\gamma}, \quad (5.122)$$

where  $\mathbf{I}$  is the unit matrix and  $\boldsymbol{\Omega}$  the damage matrix. For continuum elements with a non-zero Poisson's ratio there is an indirect coupling between the degradation of the stiffnesses in the individual directions. The individual damage parameters of the ply are therefore difficult to determine. A simple model for anisotropic damage can be used where the damage matrix depends on a single scalar parameter  $\omega$ , i.e.  $\boldsymbol{\Omega} = \boldsymbol{\Omega}(\omega)$ .

Matrix damage growth is controlled by the damage loading function

$$f(\tilde{\gamma}, \kappa) = \tilde{\gamma} - \kappa, \quad (5.123)$$

where  $\kappa$  is a history-dependent parameter, which reflects the loading history and  $\tilde{\gamma}$  is the equivalent strain. From an initial value  $\kappa_0$  it grows and memorises the largest value ever attained by the equivalent strain  $\tilde{\gamma}$ . If the loading function is negative, unloading occurs and the history-dependent parameter does not increase, i.e.,  $\dot{\kappa} = 0$ . If the loading function is zero, further loading can take place and the history-dependent parameter increases,  $\dot{\kappa} \geq 0$ . Damage will occur if the value of the loading function exceeds a threshold value. The threshold value is then adjusted to the new situation and growth of damage is determined by exceeding this new

value in next steps. This structure can be formalised in the same way as for plasticity with the Kuhn-Tucker conditions:

$$f \leq 0 \quad , \quad \dot{\kappa} \geq 0 \quad , \quad f\dot{\kappa} = 0. \quad (5.124)$$

Similar to plasticity models, the damage theory is completed by defining an evolution law for the damage variable  $\omega$  as a function of the history-dependent parameter  $\kappa$ :

$$\omega = \omega(\kappa). \quad (5.125)$$

As in the one-dimensional case  $0 \leq \omega \leq 1$ , the initial value  $\omega = 0$  representing the state of the fully intact material, and the final value  $\omega = 1$  representing the state where there is a total loss of coherence.

The solution procedure in the damage analysis looks as follows. Similar to the strain hardening analysis we start from a given state  $n$  for which the stress  $\sigma^n$ , the total strain  $\gamma^n$ , and the damage parameter  $\kappa^n$  are known. The new total strain is determined from

$$\gamma_{n+1}^{i+1} = \gamma_n + \Delta\gamma_{n+1}^{i+1}, \quad (5.126)$$

where the strain increment  $\Delta\gamma_{n+1}^{i+1}$  follows from the displacement increment  $\Delta\hat{\gamma}$ . By evaluating the damage loading function, Eq. 5.123, the new damage parameter  $\kappa^{n+1}$  can be determined. In case there is loading  $\kappa^{n+1}$  is:

$$\kappa^{n+1} = \tilde{\gamma}. \quad (5.127)$$

With the new damage parameter, the damage variable  $\omega$  can be updated, the new damage matrix  $\Omega(\omega)$  can be determined, and the new stresses can be calculated, i.e.,

$$\omega_{j+1} = \omega(\kappa_{j+1}), \quad (5.128)$$

$$\Omega_{j+1} = \Omega(\omega_{j+1}), \quad (5.129)$$

and

$$\sigma_{j+1} = (\mathbf{I} - \Omega_{j+1})\mathbf{D}\gamma_{j+1}. \quad (5.130)$$

However, as we will observe in Chapter 8, these relationships are interdependent and need to be solved simultaneously in an implicit solution



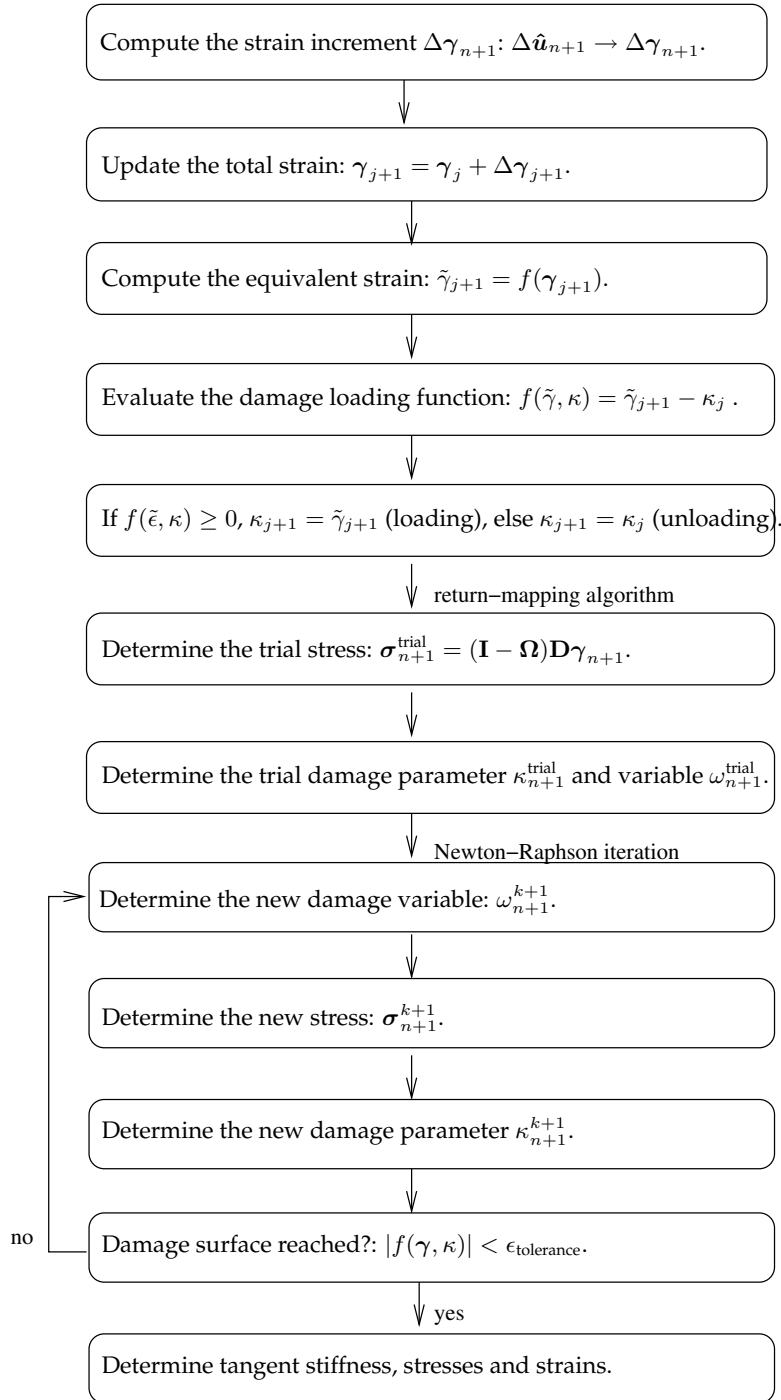


Figure 5.3: Algorithmic procedure for the damage analysis. For each iteration and at each integration point the listed operations need to be performed.

procedure. When we write the three equations in similar form as the damage loading function, we obtain:

$$f(\omega_{n+1}, \kappa_{n+1}) = \tilde{\gamma}(\omega) - \kappa = 0, \quad (5.131)$$

$$g(\boldsymbol{\sigma}_{n+1}, \omega_{n+1}) = \boldsymbol{\sigma} - (\mathbf{I} - \boldsymbol{\Omega}(\omega))\mathbf{D}\boldsymbol{\gamma} = 0, \quad (5.132)$$

$$h(\kappa_{n+1}, \omega_{n+1}) = \omega - \omega(\kappa) = 0. \quad (5.133)$$

Eqs. (5.131) and (5.133) in total form eight equations with eight unknowns, the six stress components of  $\boldsymbol{\sigma}_{n+1}$ ,  $\omega_{n+1}$ , and  $\kappa_{n+1}$ . The nonlinear system of equations is solved via a Newton-Raphson procedure.

$$\begin{bmatrix} \kappa_{n+1}^{k+1} \\ \boldsymbol{\sigma}_{n+1}^{k+1} \\ \omega_{n+1}^{k+1} \end{bmatrix} = \begin{bmatrix} \kappa_{n+1}^k \\ \boldsymbol{\sigma}_{n+1}^k \\ \omega_{n+1}^k \end{bmatrix} - \mathbf{J}^{-1} \begin{bmatrix} f(\boldsymbol{\sigma}_{n+1}^k, \omega_{n+1}^k, \kappa_{n+1}^k) \\ \mathbf{g}(\boldsymbol{\sigma}_{n+1}^k, \omega_{n+1}^k) \\ h(\boldsymbol{\sigma}_{n+1}^k, \omega_{n+1}^k, \kappa_{n+1}^k) \end{bmatrix}, \quad (5.134)$$

with  $k$  the iteration counter of the local Newton-Raphson iteration and the matrix  $\mathbf{J}$  represents the Jacobian of the system:

$$\mathbf{J} = \begin{bmatrix} \frac{\partial f}{\partial \boldsymbol{\sigma}} & \frac{\partial f}{\partial \omega} & \frac{\partial f}{\partial \kappa} \\ \frac{\partial \mathbf{g}}{\partial \boldsymbol{\sigma}} & \frac{\partial \mathbf{g}}{\partial \omega} & \frac{\partial \mathbf{g}}{\partial \kappa} \\ \frac{\partial h}{\partial \boldsymbol{\sigma}} & \frac{\partial h}{\partial \omega} & \frac{\partial h}{\partial \kappa} \end{bmatrix}. \quad (5.135)$$

The solution procedure now looks similar to the return-mapping algorithm discussed in Section 5.5.2. The complete procedure for the damage analysis is shown in Figure 5.3.

Thus in the damage analysis first the state of deformation is determined and the occurrence of damage is evaluated. If damage occurs the stiffness matrix is adapted and the new damage parameter is determined, which sets the new damage threshold. An incremental iterative procedure, such as for example the Newton-Raphson method, is required to perform the analysis. In this procedure the derivative of the constitutive relation is necessary, which for the constitutive relation with anisotropic material behaviour is given by

$$\dot{\boldsymbol{\sigma}} = (\mathbf{I} - \boldsymbol{\Omega})\mathbf{D}\dot{\boldsymbol{\gamma}} - \dot{\boldsymbol{\Omega}}\mathbf{D}\boldsymbol{\gamma}, \quad (5.136)$$

in which  $\dot{\Omega}$  is the derivative of the damage matrix with respect to a virtual time. For the derivation of a consistent tangent stiffness matrix it is necessary that this derivative is written as a function of the derivatives of the deformations  $\dot{\Omega}\gamma = \Omega^*\dot{\gamma}$ , leading to

$$\dot{\sigma} = (\mathbf{I} - \Omega)\mathbf{D}\dot{\gamma} - \dot{\Omega}\mathbf{D}\gamma = (\mathbf{I} - \Omega)\mathbf{D}\dot{\gamma} - \Omega^*\mathbf{D}\dot{\gamma} = \mathbf{D}_t\dot{\gamma}. \quad (5.137)$$

Whether this tangent stiffness matrix is symmetrical depends on the formulation of the damage growth law. In Chapter 8 the derivation of an orthotropic damage model is discussed in detail following the general outline given above.

## 5.6 The Jem/Jive numerical software

Numerical software is necessary to solve the thermo-mechanical system of equations for a specific structure. In some standard finite element packages, such as Marc or Abaqus, special user-defined subroutines, for example the strain hardening behaviour of a material, can often be introduced. However, these packages still only allow for the use of pre-defined elements. Open-source packages, such as Diana or B2000, give more freedom to the user, though within the limits of the numerical framework. Two C++ toolkits, named Jem and Jive, have been developed by the company (Habener 2005), which provide the necessary tools while maintaining the flexibility. The Jem toolkit provides the basis for robust and modular software, while Jive is used to transform a partial differential equation into a system of equations and solve it subsequently. The thermo-mechanical element described in Chapter 6 has been included in a tailor-made program in which the transient and nonlinear static analysis can be performed.

## 5.7 Summary

In this chapter the thermo-mechanical system of equations have been derived from the fundamental laws of mechanics and thermodynamics. The finite element method is applied to solve the system in a numerically efficient way.

To do so, the considered body or structure is divided into a number of finite elements and the weak formulation of the governing thermo-mechanical equations is discretised. Depending on the type of analysis we want to perform, i.e. static or dynamic, the final system of equations and solution procedure is obtained. Since the thermo-mechanical equations are nonlinear an incremental iterative solution procedure, the Newton-Raphson method, is required.

To include physical nonlinearities, such as strain hardening or damage growth, a loading function is introduced to bound all states of stress into a material point. In case of strain hardening a return-mapping algorithm is used to project the stress back onto the surface of the loading function (i.e. the yield surface) when the stress state violates the loading function.

For damage growth, the damage parameter affects the tangent stiffness matrix and the new stress state can directly be determined. With the general framework given, the next important step in the application of the finite element method is the formulation of the element itself, which is done in the next chapter. In Chapters 7 and 8 the hardening law and respectively the damage growth law will be given together with the specific loading functions.

# Chapter 6

## The thermo-mechanical solid-like shell element

### 6.1 Introduction

Aerospace structures, especially in the fuselage sections, are thin-walled structures. In these parts metal fatigue due to pressurisation and depressurisation of the fuselage is a serious threat to the structure, as indicated in Section 2.1. The fuselage skin is also the first barrier against fire penetration. Fibre metal laminates could be very suitable materials in the fuselage due to the previous mentioned factors.

However, the use of different constituents also raises new questions especially regarding the thermo-mechanical properties. Differences in thermal expansion coefficients of the fibres and the aluminium cause residual stresses after curing of the laminate. The aluminium layers are loaded in tension, the fibres are loaded in compression after the curing process. In service, when the temperature can vary between  $-55$  up to  $70$  °C due to solar radiation and convection, (varying) internal stresses can be expected as well. This influences the fatigue crack initiation and can lead to secondary bending for asymmetric lay-ups. The effect of temperature on the static and dynamic properties of fibre metal laminates is more complex than for monolithic aluminium and must be quantified.

The use of standard continuum elements to model thin-walled structures, as the fuselage skin, may lead to problems. They tend to show Poisson-thickness locking when their aspect ratios (i.e. the ratio of element length over its width) are too high. As a result, the elements become overly stiff. (Rolfes, Noack, and Taeschner 1999) showed the un-coupled thermo-mechanical 3D-analysis process of composite structures which uses a shell

finite element model throughout. The mechanical part in their research consists of to the thermally induced stresses, which are also calculated in transverse direction, see also (Rolfes, Tessmer, and Rohwer 2003).

An alternative is the so-called solid-like shell element given by (Parisch 1995), which can describe the behaviour of fibre metal laminates in a fully three-dimensional state and which can handle failure mechanisms like cracking and delamination in connection with interface elements. In this chapter the construction of a thermo-mechanical solid-like shell element including thermal expansion and heat transfer is described. The combined thermo-mechanical system of equations is solved simultaneously.

## 6.2 Element definitions

The use of standard continuum elements to numerically model thin-walled structures, as the fuselage skin, may lead to problems. Since the kinematic relations of standard continuum elements do not account for variations of the strain in thickness direction, they tend to show Poisson-thickness locking when their aspect ratios (i.e. the ratio of element length over its width) are too high. As a result, the elements become overly stiff, (Bischoff and Ramm 1997). For fibre metal laminates the thickness of the individual layers is even smaller and the effect of Poisson-thickness locking thus more present.

An alternative is the so-called solid-like shell element as derived by (Parisch 1995). This element consists of 8 or 16 external nodes, each with three translational degrees of freedom, see Figure 6.1. Four internal degrees of freedom are used to add a quadratic term to the displacement field in the thickness direction (the so-called internal 'stretch' of the element). Hence, the strain varies linearly over the thickness instead of being constant and Poisson-thickness locking is avoided. This implies that the element can also be used in thin applications.

A solid-like shell element was used by (Hashagen 1995) to describe the behaviour of fibre metal laminates in a fully three-dimensional state and to be able to model failure mechanisms and delamination (in connection with interface elements). (Remmers and de Borst 2001) showed that a combination of delamination buckling and delamination growth could be modelled with the solid-like shell element as well.

The 8 or 16 external nodes have three degrees of freedom in the case of only mechanical loading, since only the displacements are considered. For the thermo-mechanical solid-like shell element each external node has four degrees of freedom, the three displacements,  $\hat{u}_x$ ,  $\hat{u}_y$ , and  $\hat{u}_z$ , and the

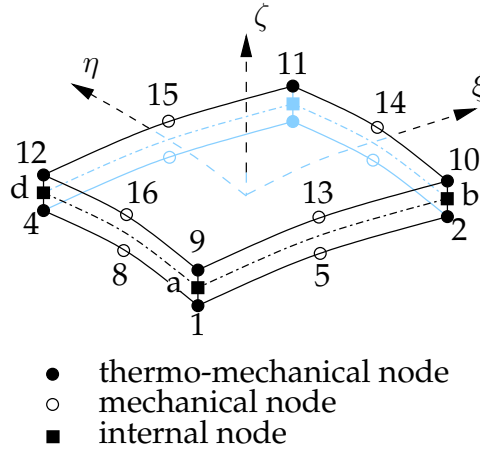


Figure 6.1: Geometry of the sixteen-noded thermo-mechanical solid-like shell element. Each geometrical node  $I$  contains at least three degrees of freedom, and a fourth degree of freedom at the corner nodes  $[\hat{u}_x, \hat{u}_y, \hat{u}_z, \hat{\theta}]_I$ . Each internal node  $J$  has one degree of freedom:  $\hat{w}_J$ .

temperature at the node  $\hat{\theta}$ . By adding the temperature degree of freedom only at the corner nodes of the sixteen-noded element eventual numerical instability, due to a difference in order for mechanical and thermal strain, can be avoided, see Section 6.2.4.

### 6.2.1 Geometry and kinematical description

Consider the thick shell shown in Figure 6.2. The position of a material point in the shell in the undeformed configuration can be written as a function of the three curvilinear coordinates  $[\xi, \eta, \zeta]$ :

$$\mathbf{X}(\xi, \eta, \zeta) = \mathbf{X}_0(\xi, \eta) + \zeta \mathbf{D}(\xi, \eta), \quad (6.1)$$

where  $\mathbf{X}_0(\xi, \eta)$  is the projection of the point on the mid-surface of the shell and  $\mathbf{D}(\xi, \eta)$  is the thickness director in this point:

$$\mathbf{X}_0(\xi, \eta) = \frac{1}{2} [\mathbf{X}_t(\xi, \eta) + \mathbf{X}_b(\xi, \eta)]; \quad (6.2)$$

$$\mathbf{D}(\xi, \eta) = \frac{1}{2} [\mathbf{X}_t(\xi, \eta) - \mathbf{X}_b(\xi, \eta)]. \quad (6.3)$$

The subscripts  $(\cdot)_t$  and  $(\cdot)_b$  denote the projections of the variable onto the top and bottom surface, respectively. The position of the material point

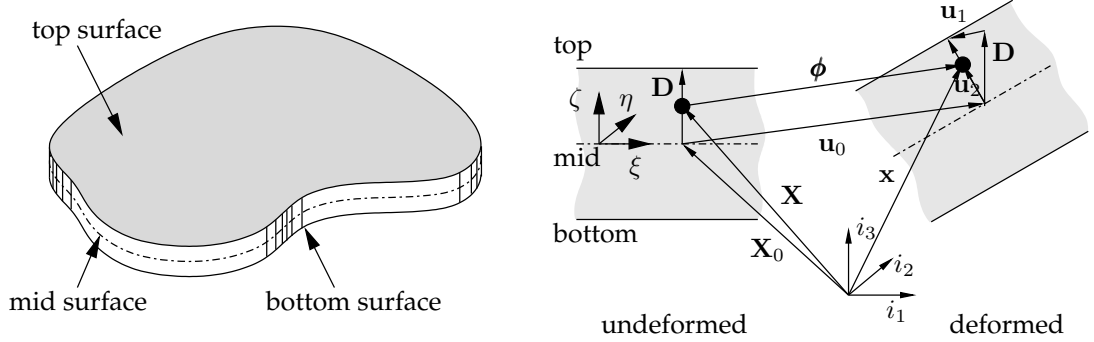


Figure 6.2: Kinematic relations of the regular solid-like shell element in undeformed and deformed position. The dash-dotted line denotes the mid-surface of the shell.

in the deformed configuration  $\mathbf{x}(\xi, \eta, \zeta)$  is related to  $\mathbf{X}(\xi, \eta, \zeta)$  via the displacement field  $\phi(\xi, \eta, \zeta)$  according to:

$$\mathbf{x}(\xi, \eta, \zeta) = \mathbf{X}(\xi, \eta, \zeta) + \phi(\xi, \eta, \zeta), \quad (6.4)$$

where

$$\phi(\xi, \eta, \zeta) = \mathbf{u}_0(\xi, \eta) + \zeta \mathbf{u}_1(\xi, \eta) + (1 - \zeta^2) \mathbf{u}_2(\xi, \eta). \quad (6.5)$$

In this relation,  $\mathbf{u}_0$  and  $\mathbf{u}_1$  are the displacements of  $\mathbf{X}_0$  on the shell mid-surface, and the thickness director  $\mathbf{D}$ , respectively:

$$\mathbf{u}_0(\xi, \eta) = \frac{1}{2} [\mathbf{u}_t(\xi, \eta) + \mathbf{u}_b(\xi, \eta)]; \quad (6.6)$$

$$\mathbf{u}_1(\xi, \eta) = \frac{1}{2} [\mathbf{u}_t(\xi, \eta) - \mathbf{u}_b(\xi, \eta)], \quad (6.7)$$

and  $\mathbf{u}_2(\xi, \eta)$  denotes the internal stretching of the element, which is colinear with the thickness director in the deformed configuration and is a function of an additional 'stretch' parameter  $w$ :

$$\mathbf{u}_2(\xi, \eta) = w(\xi, \eta) [\mathbf{D} + \mathbf{u}_1(\xi, \eta)]. \quad (6.8)$$

In the remainder, we will consider the displacement field  $\phi$  as a function of two kinds of variables; the ordinary displacement field  $\mathbf{u}$ , which will be split in a displacement of the top and bottom surfaces  $\mathbf{u}_t$  and  $\mathbf{u}_b$ , respectively, and the internal stretch parameter  $w$ :

$$\phi = \phi(\mathbf{u}_t, \mathbf{u}_b, w). \quad (6.9)$$



### 6.2.2 The base vectors and the metric matrices

The base vectors at the material point in undeformed configuration  $\mathbf{G}_i$  can be found by differentiating the position vector  $\mathbf{X}$  with respect to the isoparametric coordinates  $\Theta^i = [\xi, \eta, \zeta]$ :

$$\mathbf{G}_\kappa = \frac{\partial \mathbf{X}}{\partial \Theta^\kappa} = \mathbf{E}_\kappa + \zeta \mathbf{D}_{,\kappa}; \quad \kappa = 1, 2; \quad (6.10)$$

$$\mathbf{G}_3 = \frac{\partial \mathbf{X}}{\partial \Theta^3} = \mathbf{D}, \quad (6.11)$$

where  $(\cdot)_{,\kappa}$  denotes the partial derivative with respect to  $\Theta^\kappa$ .  $\mathbf{E}_\kappa$  is the covariant surface vector, which is the projection of the base-vector  $\mathbf{G}_\kappa$  on the mid-surface and is defined as

$$\mathbf{E}_\kappa = \frac{\partial \mathbf{X}_0}{\partial \Theta^\kappa}. \quad (6.12)$$

The base vectors of the shell in the deformed configuration  $\mathbf{g}_i$  are found in a similar fashion:

$$\mathbf{g}_\kappa = \frac{\partial \mathbf{x}}{\partial \Theta^\kappa} = \mathbf{E}_\kappa + \mathbf{u}_{0,\kappa} + \zeta \mathbf{D}_{,\kappa} + \zeta \mathbf{u}_{1,\kappa} + \text{h.o.t.}, \quad (6.13)$$

$$\mathbf{g}_3 = \frac{\partial \mathbf{x}}{\partial \Theta^3} = \mathbf{D} + \mathbf{u}_1 - 2\zeta \mathbf{u}_2 + \text{h.o.t.}. \quad (6.14)$$

The higher order terms (h.o.t.) in Eqs. (6.13) and (6.14) contain terms up to the fourth order in the thickness coordinate  $\zeta$  and the derivatives of the stretch parameter  $\mathbf{u}_2$  with respect to  $\xi$  and  $\eta$ . In the remainder, these terms will be neglected without a significant loss of accuracy of the kinematic model (Parisich 1995).

The metric tensors  $\mathbf{G}$  and  $\mathbf{g}$  can be determined by using the base vectors  $\mathbf{G}_i$  and  $\mathbf{g}_i$  in Eqs. (6.10) - (6.14):

$$G_{ij} = \mathbf{G}_i \cdot \mathbf{G}_j; \quad g_{ij} = \mathbf{g}_i \cdot \mathbf{g}_j. \quad (6.15)$$

Elaboration of the expressions yields the following components of the metric tensor in the undeformed configuration:

$$G_{\kappa\lambda} = \mathbf{E}_\kappa \cdot \mathbf{E}_\lambda + \zeta [\mathbf{E}_\kappa \cdot \mathbf{D}_{,\lambda} + \mathbf{E}_\lambda \cdot \mathbf{D}_{,\kappa}]; \quad (6.16)$$

$$G_{\kappa 3} = \mathbf{E}_\kappa \cdot \mathbf{D} + \zeta \mathbf{D}_{,\kappa} \cdot \mathbf{D}; \quad (6.17)$$

$$G_{33} = \mathbf{D} \cdot \mathbf{D}, \quad (6.18)$$

and in the deformed configuration (again neglecting the terms which are quadratic in thickness direction):

$$g_{\kappa\lambda} = (\mathbf{E}_\kappa + \mathbf{u}_{0,\kappa}) \cdot (\mathbf{E}_\lambda + \mathbf{u}_{0,\lambda}) + \zeta [(\mathbf{E}_\kappa + \mathbf{u}_{0,\kappa}) \cdot (\mathbf{D}_{,\lambda} + \mathbf{u}_{1,\lambda}) + (\mathbf{E}_\lambda + \mathbf{u}_{0,\lambda}) \cdot (\mathbf{D}_{,\kappa} + \mathbf{u}_{1,\kappa})]; \quad (6.19)$$

$$g_{\kappa 3} = (\mathbf{E}_\kappa + \mathbf{u}_{0,\kappa}) \cdot (\mathbf{D} + \mathbf{u}_1) + \zeta [(\mathbf{D} + \mathbf{u}_1) \cdot (\mathbf{D}_{,\kappa} + \mathbf{u}_{1,\kappa}) - 2(\mathbf{E}_\kappa + \mathbf{u}_{0,\kappa}) \cdot \mathbf{u}_2]; \quad (6.20)$$

$$g_{33} = (\mathbf{D} + \mathbf{u}_1) \cdot (\mathbf{D} + \mathbf{u}_1) - \zeta 4(\mathbf{D} + \mathbf{u}_1) \cdot \mathbf{u}_2. \quad (6.21)$$

We can rewrite these relations as

$$G_{ij} = G_{ij}^0 + \zeta G_{ij}^1; \quad (6.22)$$

$$g_{ij} = g_{ij}^0 + \zeta g_{ij}^1, \quad (6.23)$$

where  $G_{ij}^0$  and  $g_{ij}^0$  correspond to the constant terms in Eqs. (6.16) - (6.21), whereas  $G_{ij}^1$  and  $g_{ij}^1$  correspond to the terms that vary linearly with respect to the thickness  $\zeta$ . For the derivation of the Green strains also the so-called contravariant triad  $\mathbf{G}^j$  is applied. It can be calculated with the covariant triad in the following manner:

$$\mathbf{G}^j = (G_{ij})^{-1} \mathbf{G}_i. \quad (6.24)$$

The contravariant base vector  $\mathbf{G}^j$  is related to the contravariant surface vector  $\mathbf{E}^k$  via the so-called shell tensor  $\mu_k^j$ , (Ogden 1984):

$$\mathbf{G}^j = \mu_k^j \mathbf{E}^k; \quad \mu_k^j = (\delta_k^j - \zeta \bar{G}_k^j) \mathbf{E}^k. \quad (6.25)$$

In Eq. (6.25),  $\bar{G}_k^j$  denotes the mixed variant metric tensor which is calculated with the contravariant and the covariant tensor components as follows, see Eq. (6.22) (Parisich 1995):

$$\bar{G}_k^j = G^{0jm} G_{1mk}. \quad (6.26)$$

### 6.2.3 Green-Lagrange and thermal strain field

The Green-Lagrange strain tensor  $\gamma^{GL}$ , which defines the mechanical strains, is written conventionally in terms of the deformation gradient  $\mathbf{F}$ :

$$\gamma^{GL} = \frac{1}{2}(\mathbf{F}^T \mathbf{F} - \mathbf{I}). \quad (6.27)$$

The deformation gradient  $\mathbf{F}$  can be written as a function of the covariant base vector in the deformed configuration  $\mathbf{g}_i$  and the contravariant base vector in the undeformed reference configuration  $\mathbf{G}^i$ :

$$\mathbf{F} = \mathbf{g}_i \otimes \mathbf{G}^i. \quad (6.28)$$

Inserting this relation in Eq. (6.27) we can write the Green-Lagrange strain tensor in terms of the contravariant basis  $\mathbf{G}^j$ :

$$\boldsymbol{\gamma}^{GL} = \gamma_{ij}^{GL} \mathbf{G}^i \otimes \mathbf{G}^j; \quad (6.29)$$

where:

$$\gamma_{ij}^{GL} = \frac{1}{2}(g_{ij} - G_{ij}). \quad (6.30)$$

Substituting Eq. (6.25) in this relation yields

$$2\boldsymbol{\gamma}^{GL} = (g_{ij} - G_{ij})(\delta_k^i - \zeta \bar{G}_k^i)(\delta_l^j - \zeta \bar{G}_l^j) \mathbf{E}^k \otimes \mathbf{E}^l. \quad (6.31)$$

After some manipulations, the strain tensor can be written in terms of the membrane mid-surface strain  $\epsilon_{ij}$  and the bending strain  $\rho_{ij}$  according to

$$2\boldsymbol{\gamma}^{GL} = (\epsilon_{ij} + \zeta \rho_{ij}) \mathbf{E}^i \otimes \mathbf{E}^j. \quad (6.32)$$

The components can be calculated as follows, (Parisich 1995):

$$2\epsilon_{\kappa\lambda} = \mathbf{E}_\kappa \cdot \mathbf{u}_{,\lambda}^0 + \mathbf{u}_{,\kappa}^0 \cdot \mathbf{E}_\lambda + \mathbf{u}_{,\kappa}^0 \cdot \mathbf{u}_{,\lambda}^0; \quad (6.33)$$

$$2\epsilon_{\kappa 3} = \mathbf{E}_\kappa \cdot \mathbf{u}^1 + \mathbf{u}_{,\kappa}^0 \cdot \mathbf{D} + \mathbf{u}_{,\kappa}^0 \cdot \mathbf{u}^1; \quad (6.34)$$

$$2\epsilon_{33} = \mathbf{u}^1 \cdot \mathbf{D} + \mathbf{D} \cdot \mathbf{u}^1 + \mathbf{u}^1 \cdot \mathbf{u}^1; \quad (6.35)$$

$$\begin{aligned} 2\rho_{\kappa\lambda} = & \mathbf{D}_{,\kappa} \cdot \mathbf{u}_{,\lambda}^0 + \mathbf{u}_{,\kappa}^1 \cdot \mathbf{E}_\lambda + \mathbf{u}_{,\kappa}^1 \cdot \mathbf{u}_{,\lambda}^0 + \mathbf{D}_{,\lambda} \cdot \mathbf{u}_{,\kappa}^0 + \mathbf{u}_{,\lambda}^1 \cdot \mathbf{E}_\kappa + \mathbf{u}_{,\lambda}^1 \cdot \mathbf{u}_{,\kappa}^0 \\ & - [\mathbf{E}_\tau \cdot \mathbf{u}_{,\lambda}^0 + \mathbf{u}_{,\tau}^0 \cdot \mathbf{E}_\lambda + \mathbf{u}_{,\tau}^0 \cdot \mathbf{u}_{,\lambda}^0] \bar{G}_\kappa^\tau \\ & - [\mathbf{E}_\kappa \cdot \mathbf{u}_{,\nu}^0 + \mathbf{u}_{,\kappa}^0 \cdot \mathbf{E}_\nu + \mathbf{u}_{,\kappa}^0 \cdot \mathbf{u}_{,\nu}^0] \bar{G}_\lambda^\nu; \end{aligned} \quad (6.36)$$

$$2\rho_{\kappa 3} = \mathbf{D}_{,\kappa} \cdot \mathbf{u}^1 + \mathbf{u}_{,\kappa}^1 \cdot \mathbf{D} + \mathbf{u}_{,\kappa}^1 \cdot \mathbf{u}^1; \quad (6.37)$$

$$2\rho_{33} = -4\mathbf{d} \cdot \mathbf{w}. \quad (6.38)$$

The virtual strain components of Eqs. (6.33) - (6.38) read:

$$2\delta\epsilon_{\kappa\lambda} = \mathbf{e}_\lambda \cdot \delta\mathbf{u}_{,\kappa}^0 + \mathbf{e}_\kappa \cdot \delta\mathbf{u}_{,\lambda}^0; \quad (6.39)$$

$$2\delta\epsilon_{\kappa 3} = \delta\mathbf{u}_{,\kappa}^0 \cdot \mathbf{d} + \mathbf{e}_\kappa \cdot \delta\mathbf{u}^1; \quad (6.40)$$

$$2\delta\epsilon_{33} = 2\mathbf{d} \cdot \delta\mathbf{u}^1; \quad (6.41)$$

$$\begin{aligned} 2\delta\rho_{\kappa\lambda} &= \delta\mathbf{u}_{,\kappa}^0 \cdot \mathbf{e}_\lambda + \mathbf{d}_{,\kappa} \cdot \delta\mathbf{u}_{,\lambda}^1 + \delta\mathbf{u}_{,\lambda}^1 \cdot \mathbf{e}_\kappa + \mathbf{d}_{,\lambda} \cdot \delta\mathbf{u}_{,\kappa}^0 \\ &\quad - [\delta\mathbf{u}_{,\tau}^0 \cdot \mathbf{e}_\lambda + \mathbf{e}_\tau \cdot \delta\mathbf{u}_{,\lambda}^0] \bar{G}_\kappa^\tau \\ &\quad - [\delta\mathbf{u}_{,\kappa}^0 \cdot \mathbf{e}_\nu + \mathbf{e}_\kappa \cdot \delta\mathbf{u}_{,\nu}^0] \bar{G}_\lambda^\nu; \end{aligned} \quad (6.42)$$

$$2\delta\rho_{\kappa 3} = \mathbf{d} \cdot \delta\mathbf{u}_{,\kappa}^1 + \mathbf{d}_{,\kappa} \cdot \delta\mathbf{u}^1; \quad (6.43)$$

$$2\delta\rho_{33} = -4[2\mathbf{w} \cdot \delta\mathbf{u}^1 + \mathbf{d} \cdot \mathbf{d}\delta w]. \quad (6.44)$$

The thermal expansion strain tensor  $\gamma^\alpha$  can also be written in terms of the contravariant basis  $\mathbf{G}^j$ :

$$\gamma^\alpha = \gamma_{ij}^\alpha \mathbf{G}^i \otimes \mathbf{G}^j, \quad (6.45)$$

where

$$\gamma_{ij}^\alpha = \theta G_{ij}, \quad (6.46)$$

and  $\theta$  is the relative temperature. In shell theory small strains are considered and therefore the expansion strains are derived with reference to the undeformed configuration. This implies that there is no coupling between the thermal expansion and the deformation, the expansion is stress-free. Substituting Eq. (6.25) in the thermal strain field relation yields

$$\gamma^\alpha = \theta G_{ij} (\delta_k^i - \zeta \bar{G}_k^i) (\delta_l^j - \zeta \bar{G}_l^j) \mathbf{E}^k \otimes \mathbf{E}^l. \quad (6.47)$$

Similar to the Green-Lagrange strain tensor, the thermal strain tensor can be written in terms of the membrane mid-surface strain  $\epsilon_{ij}$  and the bending strain  $\rho_{ij}$  according to

$$\gamma^\alpha = (\epsilon_{ij} + \zeta \rho_{ij}) \mathbf{E}^i \otimes \mathbf{E}^j, \quad (6.48)$$

where in this case we find

$$\epsilon_{\kappa\lambda}^\alpha = \theta \mathbf{E}_\kappa \cdot \mathbf{E}_\lambda; \quad (6.49)$$

$$\epsilon_{\kappa 3}^\alpha = \theta \mathbf{E}_\kappa \cdot \mathbf{D}; \quad (6.50)$$

$$\epsilon_{33}^\alpha = \theta \mathbf{D} \cdot \mathbf{D}; \quad (6.51)$$

$$\begin{aligned} \rho_{\kappa\lambda}^\alpha &= \theta [\mathbf{E}_{\kappa} \cdot \mathbf{D}_{,\lambda} + \mathbf{E}_\lambda \cdot \mathbf{D}_{,\kappa}] \\ &\quad - \theta [\bar{G}_\kappa^\tau \cdot \mathbf{E}_\nu + \bar{G}_\lambda^\nu \cdot \mathbf{E}_\tau]; \end{aligned} \quad (6.52)$$

$$\rho_{\kappa 3}^\alpha = \theta \mathbf{D}_{,\kappa} \cdot \mathbf{D}; \quad (6.53)$$

$$\rho_{33}^\alpha = 0. \quad (6.54)$$

The components of the strain tensor  $\epsilon_{ij}$ ,  $\rho_{ij}$  refer to the in general non-orthogonal triplet  $\mathbf{E}^i$  spanned at the material point in the undeformed reference configuration. For composite materials it is convenient to define the strains in a local ortho-normal reference system  $\mathbf{l}_j$  provided by the characteristic material direction (e.g. fibre orientation) of the individual layer. The strain tensor can be transformed to the local reference frame as follows:

$$\gamma_{ij} = (\epsilon_{ij} + \zeta \rho_{ij}) t_k^i t_l^j; \quad t_k^i = \mathbf{E}^i \cdot \mathbf{l}_k. \quad (6.55)$$

For the finite element implementation the variation of the thermal strain field  $\delta\gamma^\alpha$  is derived:

$$\delta\epsilon_{\kappa\lambda}^\alpha = \delta\theta \mathbf{E}_\kappa \cdot \mathbf{E}_\lambda; \quad (6.56)$$

$$\delta\epsilon_{\kappa 3}^\alpha = \delta\theta \mathbf{E}_\kappa \cdot \mathbf{D}; \quad (6.57)$$

$$\delta\epsilon_{33}^\alpha = \delta\theta \mathbf{D} \cdot \mathbf{D}; \quad (6.58)$$

$$\delta\rho_{\kappa\lambda}^\alpha = \delta\theta [\mathbf{E}_\kappa \cdot \mathbf{D}_{,\lambda} + \mathbf{E}_\lambda \cdot \mathbf{D}_{,\kappa}] - \delta\theta [\bar{G}_\kappa^\tau \cdot \mathbf{E}_\nu + \bar{G}_\lambda^\nu \cdot \mathbf{E}_\tau]; \quad (6.59)$$

$$\delta\rho_{\kappa 3}^\alpha = \delta\theta \mathbf{D}_{,\kappa} \cdot \mathbf{D}; \quad (6.60)$$

$$\delta\rho_{33}^\alpha = 0. \quad (6.61)$$

The thermal strain increment  $\Delta\gamma^\alpha$  is normally needed in an iterative solution scheme. It can be derived as

$$\Delta\epsilon_{\kappa\lambda}^\alpha = \Delta\theta \mathbf{E}_\kappa \cdot \mathbf{E}_\lambda; \quad (6.62)$$

$$\Delta\epsilon_{\kappa 3}^\alpha = \Delta\theta \mathbf{E}_\kappa \cdot \mathbf{D}; \quad (6.63)$$

$$\Delta\epsilon_{33}^\alpha = \Delta\theta \mathbf{D} \cdot \mathbf{D}; \quad (6.64)$$

$$\Delta\rho_{\kappa\lambda}^\alpha = \Delta\theta [\mathbf{E}_\kappa \cdot \mathbf{D}_{,\lambda} + \mathbf{E}_\lambda \cdot \mathbf{D}_{,\kappa}] - \Delta\theta [\bar{G}_\kappa^\tau \cdot \mathbf{E}_\nu + \bar{G}_\lambda^\nu \cdot \mathbf{E}_\tau]; \quad (6.65)$$

$$\Delta\rho_{\kappa 3}^\alpha = \Delta\theta \mathbf{D}_{,\kappa} \cdot \mathbf{D}; \quad (6.66)$$

$$\Delta\rho_{33}^\alpha = 0. \quad (6.67)$$

Due to the symmetry of the shear components of the Green's strain tensor, the engineering strain components can be collected in the vector  $\gamma^{GL}$ . The vector  $\gamma^{GL(E)}$  is applied since  $\epsilon_{ij}$  and  $\rho_{ij}$  refer to the covariant components of the Green's strain:

$$\partial\gamma^{GL(E)} = \begin{bmatrix} \delta\epsilon_{11} + \zeta\delta\rho_{11} \\ \delta\epsilon_{22} + \zeta\delta\rho_{22} \\ \delta\epsilon_{33} + \zeta\delta\rho_{33} \\ \delta 2\epsilon_{12} + \zeta\delta 2\rho_{12} \\ \delta 2\epsilon_{23} + \zeta\delta 2\rho_{23} \\ \delta 2\epsilon_{31} + \zeta\delta 2\rho_{31} \end{bmatrix} = \mathbf{H}_0 \begin{bmatrix} \delta u_x^0 \\ \delta u_y^0 \\ \delta u_z^0 \\ \delta u_x^1 \\ \delta u_y^1 \\ \delta u_z^1 \\ \delta w \end{bmatrix}_{\epsilon+\rho} + \mathbf{H}_1 \begin{bmatrix} \delta u_{x,1}^0 \\ \delta u_{y,1}^0 \\ \delta u_{z,1}^0 \\ \delta u_{x,1}^1 \\ \delta u_{y,1}^1 \\ \delta u_{z,1}^1 \\ \delta w_{,1} \end{bmatrix} + \mathbf{H}_2 \begin{bmatrix} \delta u_{x,2}^0 \\ \delta u_{y,2}^0 \\ \delta u_{z,2}^0 \\ \delta u_{x,2}^1 \\ \delta u_{y,2}^1 \\ \delta u_{z,2}^1 \\ \delta w_{,2} \end{bmatrix}. \quad (6.68)$$

For the thermal strain tensor we find:

$$\partial\gamma^{\alpha(E)} = \begin{bmatrix} \delta\epsilon_{11}^{\alpha} + \zeta\delta\rho_{11}^{\alpha} \\ \delta\epsilon_{22}^{\alpha} + \zeta\delta\rho_{22}^{\alpha} \\ \delta\epsilon_{33}^{\alpha} + \zeta\delta\rho_{33}^{\alpha} \\ \delta\epsilon_{12}^{\alpha} + \zeta\delta\rho_{12}^{\alpha} \\ \delta\epsilon_{23}^{\alpha} + \zeta\delta\rho_{23}^{\alpha} \\ \delta\epsilon_{31}^{\alpha} + \zeta\delta\rho_{31}^{\alpha} \end{bmatrix} = \mathbf{H}_0^{\alpha} \begin{bmatrix} \delta\theta^0 \\ \delta\theta^1 \end{bmatrix}_{\alpha}; \quad (6.69)$$

with the matrices  $\mathbf{H}_0$ ,  $\mathbf{H}_0^{\alpha}$ ,  $\mathbf{H}_1$  and  $\mathbf{H}_2$ :

$$\mathbf{H}_0 = \begin{bmatrix} 0 & 0 & 0 \\ 0 & 0 & 0 \\ 0 & \mathbf{d}^T & 0 \\ 0 & 0 & 0 \\ 0 & \mathbf{e}_2^T & 0 \\ 0 & \mathbf{e}_1^T & 0 \end{bmatrix} + \zeta \begin{bmatrix} 0 & 0 & 0 \\ 0 & 0 & 0 \\ 0 & -4w\mathbf{d}^T & -2\mathbf{d}^T\mathbf{d} \\ 0 & 0 & 0 \\ 0 & \mathbf{d}_{,2}^T & 0 \\ 0 & \mathbf{d}_{,1}^T & 0 \end{bmatrix} = \mathbf{H}_0^{\epsilon} + \zeta\mathbf{H}_0^{\rho}; \quad (6.70)$$

$$\mathbf{H}_0^{\alpha} = \begin{bmatrix} \mathbf{E}_1^T\mathbf{E}_1 & 0 \\ \mathbf{E}_2^T\mathbf{E}_2 & 0 \\ \mathbf{D}^T\mathbf{D} & 0 \\ \mathbf{E}_1^T\mathbf{E}_2 & 0 \\ \mathbf{E}_2^T\mathbf{D} & 0 \\ \mathbf{D}^T\mathbf{E}_1 & 0 \end{bmatrix} + \zeta \begin{bmatrix} 0 & 2\mathbf{E}_1^T[\mathbf{D}_{,1} - \bar{G}_1^1] \\ 0 & 2\mathbf{E}_2^T[\mathbf{D}_{,2} - \bar{G}_2^2] \\ 0 & 0 \\ 0 & \mathbf{E}_1^T[\mathbf{D}_{,2} - \bar{G}_2^2] + \mathbf{E}_2^T[\mathbf{D}_{,1} - \bar{G}_1^1] \\ 0 & \mathbf{D}_{,2}\mathbf{D} \\ 0 & \mathbf{D}^T\mathbf{D}_{,1} \end{bmatrix} = \mathbf{H}_0^{\alpha} + \zeta\mathbf{H}_0^{\alpha}; \quad (6.71)$$

$$\mathbf{H}_1 = \begin{bmatrix} \mathbf{e}_1^T & 0 & 0 \\ 0 & 0 & 0 \\ 0 & 0 & 0 \\ \mathbf{e}_2^T & 0 & 0 \\ 0 & 0 & 0 \\ \mathbf{d}^T & 0 & 0 \end{bmatrix} + \zeta \begin{bmatrix} \mathbf{d}_{,1}^T - [2\mathbf{e}_1^T\bar{G}_1^1 + \mathbf{e}_2^T\bar{G}_1^2] & \mathbf{e}_1^T & 0 \\ -\mathbf{e}_2^T\bar{G}_1^1 & 0 & 0 \\ 0 & 0 & 0 \\ \mathbf{d}_{,2}^T - [\mathbf{e}_2^T\bar{G}_1^1 + 2\mathbf{e}_1^T\bar{G}_2^1 + \mathbf{e}_2^T\bar{G}_2^2] & \mathbf{e}_2^T & 0 \\ 0 & 0 & 0 \\ 0 & \mathbf{d}^T & 0 \end{bmatrix} = \mathbf{H}_1^{\epsilon} + \zeta\mathbf{H}_1^{\rho}; \quad (6.72)$$

$$\mathbf{H}_2 = \begin{bmatrix} 0 & 0 & 0 \\ \mathbf{e}_2^T & 0 & 0 \\ 0 & 0 & 0 \\ \mathbf{e}_1^T & 0 & 0 \\ \mathbf{d}^T & 0 & 0 \\ 0 & 0 & 0 \end{bmatrix} + \zeta \begin{bmatrix} -\mathbf{e}_1^T \bar{G}_2^1 & 0 & 0 \\ \mathbf{d}_{,2}^T - [\mathbf{e}_1^T \bar{G}_2^2 + 2\mathbf{e}_2^T \bar{G}_2^2] & \mathbf{e}_2^T & 0 \\ 0 & 0 & 0 \\ \mathbf{d}_{,1}^T - [\mathbf{e}_1^T \bar{G}_1^1 + 2\mathbf{e}_2^T \bar{G}_1^2 + \mathbf{e}_1^T \bar{G}_2^2] & \mathbf{e}_1^T & 0 \\ 0 & \mathbf{d}^T & 0 \\ 0 & 0 & 0 \end{bmatrix} = \mathbf{H}_2^\epsilon + \zeta \mathbf{H}_2^\rho. \quad (6.73)$$

The matrices  $\mathbf{H}_0$ ,  $\mathbf{H}_0^\alpha$ ,  $\mathbf{H}_1$  and  $\mathbf{H}_2$  contain the vectors  $\mathbf{e}_i$ ,  $\mathbf{d}$ ,  $\mathbf{d}_{,i}$ . These vectors consist of a part which is independent on  $\mathbf{u}$  and a part which is dependent on  $\mathbf{u}$ . Thus, also  $\mathbf{H}_0$ ,  $\mathbf{H}_0^\alpha$ ,  $\mathbf{H}_1$  and  $\mathbf{H}_2$  consist of a  $\mathbf{u}$ -independent and a  $\mathbf{u}$ -dependent contribution.

## 6.2.4 Constitutive relations

The stress tensor consists of a mechanical induced part and a thermal expansion part. The mechanical stress tensor can be written as the relation between the second Piola-Kirchhoff stress and the Green-Lagrange strain tensor. The thermal stress tensor is written in a similar way with the thermal strain tensor. Thus:

$$\boldsymbol{\sigma} = \mathbf{D}^{GL} \boldsymbol{\gamma}^{GL} - \mathbf{D}^\alpha \boldsymbol{\gamma}^\alpha, \quad (6.74)$$

where  $\mathbf{D}^{GL}$  is the tangent stiffness matrix for the Green-Lagrange strains and  $\mathbf{D}^\alpha$  is the thermal expansion matrix, which consists of the thermal expansion coefficients times the bulk modulus:

$$\mathbf{D}^\alpha = \begin{bmatrix} \alpha_1 D_{11} & 0 & 0 & 0 & 0 & 0 \\ 0 & \alpha_2 D_{22} & 0 & 0 & 0 & 0 \\ 0 & 0 & \alpha_3 D_{33} & 0 & 0 & 0 \\ 0 & 0 & 0 & 0 & 0 & 0 \\ 0 & 0 & 0 & 0 & 0 & 0 \\ 0 & 0 & 0 & 0 & 0 & 0 \end{bmatrix}. \quad (6.75)$$

The thermal expansion in composites is in general orthotropic; the expansion is different in fibre direction and transverse to the fibre direction. The thermal strain tensor  $\delta \boldsymbol{\gamma}_{ij}^\alpha$  is a function of the virtual temperature field in the element and will be derived similar to the derivation of the virtual Green tensor  $\delta \boldsymbol{\gamma}_{ij}^{GL}$  as function of the virtual displacement  $\delta \hat{\mathbf{u}}$  as performed by (Hashagen 1998). The thermal expansion provides the coupling between the temperature field and the displacement field. Vice versa, strong

deformations could cause thermal heat in the structure. However in the current derivation this effect is not considered as it plays a minor role in an aircraft structure.

For the 16 node element only at the 8 corner nodes the temperature is included. For the displacement field second-order shape functions are thus used and for the temperature field first-order functions. In this way both the mechanical strain, due to mechanical loading, and the thermal strain, due to expansion, are of the same order. The mechanical strain follows from the displacement variation and the thermal strain follows directly from the temperature distribution times the thermal expansion coefficient in a given direction. Hence, both the displacements due to mechanical loading and due to thermal loading have a constant distribution over the element. Same order shape functions for the temperature and displacement field can lead to slightly different values at the integration points within one element, and causes a so called "checkerboard" pattern in the calculation field which can lead to a non-convergent solution. With the different order in shape functions this problem is avoided.

The internal degrees of freedom, which are used to add a quadratic term to the displacement field in the thickness direction, are not able to support an external loading and are eliminated on element level by condensation as suggested by (Parisich 1995).

### 6.2.5 The temperature field

The thermal system of equations, neglecting the deformation energy, was given by Eq. 5.34 as derived in Section 5.3.4:

$$\rho_0 c \dot{\theta} + \text{Div } \mathbf{q} = \rho_0 r. \quad (6.76)$$

where  $\rho_0$  is the mass density,  $c$  is the specific heat,  $\theta$  is the temperature,  $\mathbf{q}$  is the thermal conductivity, and  $r$  is the external heat flow input. Or written with the principle of virtual temperatures, according to Eq. 5.41:

$$\int_{V_0} \delta \theta \rho c \dot{\theta} dV_0 + \int_{V_0} \nabla \delta \theta \mathbf{k} \nabla \theta dV_0 = \int_{S_q} \delta \theta q^S dS + \int_{V_0} \delta \theta q^B dV_0, \quad (6.77)$$

where  $\nabla \theta$  is defined as

$$\nabla \theta = \begin{bmatrix} \theta_{,x} & \theta_{,y} & \theta_{,z} \end{bmatrix}, \quad (6.78)$$



and the thermal conductivity matrix  $\mathbf{k}$  in case of an orthotropic material is

$$\mathbf{k} = \begin{bmatrix} k_{xx} & 0 & 0 \\ 0 & k_{yy} & 0 \\ 0 & 0 & k_{zz} \end{bmatrix}. \quad (6.79)$$

To add the temperature field calculation in the solid-like shell element it is convenient to use the same approach as for the displacement field. The temperature field is also fully three-dimensional. we can write the (change in) temperature field  $\psi(\xi, \eta, \zeta)$  as a function of mid-surface (change in) temperature and the thickness coordinate  $\zeta$  in the same way as for the displacement (although it has no physical meaning here):

$$\psi(\xi, \eta, \zeta) = \boldsymbol{\theta}^0(\xi, \eta) + \zeta \boldsymbol{\theta}^1(\xi, \eta). \quad (6.80)$$

The components  $\boldsymbol{\theta}^0$  and  $\boldsymbol{\theta}^1$  describe the change in temperature of the mid-surface  $\mathbf{X}^0$  and the shell thickness director  $\mathbf{D}$ , respectively. When  $\boldsymbol{\theta}_t$  and  $\boldsymbol{\theta}_b$  denote the change in temperature of top and bottom surface, respectively, the change in temperature can be calculated via

$$\boldsymbol{\theta}_0(\xi, \eta) = \frac{1}{2} [\boldsymbol{\theta}_t(\xi, \eta) + \boldsymbol{\theta}_b(\xi, \eta)], \quad (6.81)$$

$$\boldsymbol{\theta}_1(\xi, \eta) = \frac{1}{2} [\boldsymbol{\theta}_t(\xi, \eta) - \boldsymbol{\theta}_b(\xi, \eta)]. \quad (6.82)$$

Similar to the virtual Green-Lagrange strains and thermal strains the virtual temperature change can be collected in the vector  $\delta \mathbf{q}^{(E)}$  in the covariant basis:

$$\delta \mathbf{q}^{(E)} = \begin{bmatrix} \delta q_{11} \\ \delta q_{22} \\ \delta q_{33} \end{bmatrix} = \begin{bmatrix} \delta \theta_{,1}^0 + \zeta \delta \theta_{,1}^1 \\ \delta \theta_{,2}^0 + \zeta \delta \theta_{,2}^1 \\ \delta \theta^1 \end{bmatrix} = \mathbf{H}_0^\theta \begin{bmatrix} \delta \theta^0 \\ \delta \theta^1 \end{bmatrix} + \mathbf{H}_1^\theta \begin{bmatrix} \delta \theta_{,1}^0 \\ \delta \theta_{,1}^1 \end{bmatrix} + \mathbf{H}_2^\theta \begin{bmatrix} \delta \theta_{,2}^0 \\ \delta \theta_{,2}^1 \end{bmatrix}; \quad (6.83)$$

where the matrices  $\mathbf{H}_0^\theta$ ,  $\mathbf{H}_1^\theta$  and  $\mathbf{H}_2^\theta$  are

$$\mathbf{H}_0^\theta = \begin{bmatrix} 0 & 0 \\ 0 & 0 \\ 0 & 1 \end{bmatrix} \quad \mathbf{H}_1^\theta = \begin{bmatrix} 1 & \zeta \\ 0 & 0 \\ 0 & 0 \end{bmatrix} \quad \mathbf{H}_2^\theta = \begin{bmatrix} 0 & 0 \\ 1 & \zeta \\ 0 & 0 \end{bmatrix}. \quad (6.84)$$

## 6.3 Finite element implementation

### 6.3.1 The shape functions

The shape functions must be determined to map the virtual nodal displacements and temperatures onto the virtual displacements in each material point. The strains  $\epsilon_{ij}$  and  $\rho_{ij}$ , measured with respect to  $\mathbf{E}^i$ , are mapped onto the local system  $\mathbf{l}_j$ . The value of the displacement  $\mathbf{u}$  and the temperature  $\theta$  are approximated by the value at the nodes of the element and the shape functions:

$$\begin{bmatrix} \delta u_x^0 \\ \delta u_y^0 \\ \delta u_z^0 \\ \delta u_x^1 \\ \delta u_y^1 \\ \delta u_z^1 \\ \delta w \end{bmatrix}_{\epsilon+\rho} = \begin{bmatrix} \mathbf{\Pi}^0 & 0 & 0 & 0 \\ 0 & \mathbf{\Pi}^0 & 0 & 0 \\ 0 & 0 & \mathbf{\Pi}^0 & 0 \\ \mathbf{\Pi}^1 & 0 & 0 & 0 \\ 0 & \mathbf{\Pi}^1 & 0 & 0 \\ 0 & 0 & \mathbf{\Pi}^1 & 0 \\ 0 & 0 & 0 & \mathbf{\Pi}^w \end{bmatrix} \delta \hat{\mathbf{u}} = \mathbf{\Lambda} \delta \hat{\mathbf{u}}; \quad (6.85)$$

$[7 \times (3N+4)]$

$$\begin{bmatrix} \delta u_x^0 \\ \delta u_y^0 \\ \delta u_z^0 \\ \delta u_x^1 \\ \delta u_y^1 \\ \delta u_z^1 \end{bmatrix}_{\alpha} = \begin{bmatrix} \mathbf{\Pi}_{\alpha}^0 & 0 \\ \mathbf{\Pi}_{\alpha}^0 & 0 \\ \mathbf{\Pi}_{\alpha}^0 & 0 \\ 0 & \mathbf{\Pi}_{\alpha}^1 \\ 0 & \mathbf{\Pi}_{\alpha}^1 \\ 0 & \mathbf{\Pi}_{\alpha}^1 \end{bmatrix} \delta \hat{\theta} = \mathbf{\Lambda}_{\alpha} \delta \hat{\theta}; \quad (6.86)$$

$[6 \times (2N)]$

$$\begin{bmatrix} \delta u_{x,\kappa}^0 \\ \delta u_{y,\kappa}^0 \\ \delta u_{z,\kappa}^0 \\ \delta u_{x,\kappa}^1 \\ \delta u_{y,\kappa}^1 \\ \delta u_{z,\kappa}^1 \\ \delta w_{,\kappa} \end{bmatrix} = \begin{bmatrix} \mathbf{\Pi}_{,\kappa}^0 & 0 & 0 & 0 \\ 0 & \mathbf{\Pi}_{,\kappa}^0 & 0 & 0 \\ 0 & 0 & \mathbf{\Pi}_{,\kappa}^0 & 0 \\ \mathbf{\Pi}_{,\kappa}^1 & 0 & 0 & 0 \\ 0 & \mathbf{\Pi}_{,\kappa}^1 & 0 & 0 \\ 0 & 0 & \mathbf{\Pi}_{,\kappa}^1 & 0 \\ 0 & 0 & 0 & \mathbf{\Pi}_{,\kappa}^w \end{bmatrix} \delta \hat{\mathbf{u}} = \mathbf{\Lambda}_{,\kappa} \delta \hat{\mathbf{u}}, \quad (6.87)$$

$[7 \times (3N+4)]$

and;

$$\begin{bmatrix} \delta \theta_{,\kappa}^0 \\ \delta \theta_{,\kappa}^1 \end{bmatrix} = \begin{bmatrix} \mathbf{\Pi}_{,\kappa}^0 & 0 \\ 0 & \mathbf{\Pi}_{,\kappa}^1 \end{bmatrix} \delta \hat{\theta} = \mathbf{\Lambda}_{,\kappa} \delta \hat{\theta}, \quad (6.88)$$

$[2 \times (2N)]$

where the vector of the virtual nodal displacements is written as follows:

$$\delta \hat{\mathbf{u}}^T = (\delta u_x^1, \dots, \delta u_x^N, \delta u_y^1, \dots, \delta u_y^N, \delta u_z^1, \dots, \delta u_z^N, \delta w_1, \dots, \delta w_4), \quad (6.89)$$

and the first  $3N$  components represent the displacement of the nodes in the directions  $i_1$ ,  $i_2$ , and  $i_3$  of the global reference  $\mathbf{i}$  and the last four components represent the internal degrees of freedom. The parameter  $N$  is sixteen in case of a sixteen-noded element. The vector of the virtual nodal temperatures can be written as

$$\delta \hat{\boldsymbol{\theta}}^T = (\delta \theta^1, \dots, \delta \theta^N). \quad (6.90)$$

The vectors  $\boldsymbol{\Pi}^0$ ,  $\boldsymbol{\Pi}^1$ ,  $\boldsymbol{\Pi}^w$ ,  $\boldsymbol{\Pi}_{,\kappa}^0$ ,  $\boldsymbol{\Pi}_{,\kappa}^1$ , and  $\boldsymbol{\Pi}_{,\kappa}^w$  are composed of the iso-parametric shape functions for a eight-noded shell element. The eight biquadratic shape functions for an eight-noded shell element are denoted by  $\psi_i(\xi, \eta)$ , and the vectors  $\boldsymbol{\Pi}^i$  ( $i = 0, 1$ ) can be composed as follows for the sixteen-noded element:

$$\boldsymbol{\Pi}^0 = \frac{1}{2}(\psi_1, \dots, \psi_8, \psi_1, \dots, \psi_8); \quad (6.91)$$

$$\boldsymbol{\Pi}^1 = \frac{1}{2}(-\psi_1, \dots, -\psi_8, \psi_1, \dots, \psi_8); \quad (6.92)$$

$$\boldsymbol{\Pi}_{,\kappa}^0 = \frac{1}{2}(\psi_{1,\kappa}, \dots, \psi_{8,\kappa}, \psi_{1,\kappa}, \dots, \psi_{8,\kappa}); \quad (6.93)$$

$$\boldsymbol{\Pi}_{,\kappa}^1 = \frac{1}{2}(-\psi_{1,\kappa}, \dots, \psi_{8,\kappa}, \psi_{1,\kappa}, \dots, \psi_{8,\kappa}). \quad (6.94)$$

The vectors  $\boldsymbol{\Pi}_\alpha^0$  and  $\boldsymbol{\Pi}_\alpha^1$  are composed of four bilinear shape functions for a four-noded shell element denoted by  $\phi_i(\xi, \eta)$ . These vectors account for the thermal expansion for which only the eight corner nodes of the sixteen-noded solid-like shell element can be used to obtain a linear temperature distribution and thus a linear thermal strain contribution. In this way the mechanical strain and the thermal expansion strain are of the same order and a checkerboard pattern in the solution field is avoided.

$$\boldsymbol{\Pi}_\alpha^0 = \frac{1}{2}(\phi_1, \dots, \phi_4, \phi_1, \dots, \phi_4); \quad (6.95)$$

$$\boldsymbol{\Pi}_\alpha^1 = \frac{1}{2}(-\phi_1, \dots, -\phi_4, \phi_1, \dots, \phi_4). \quad (6.96)$$

The vectors  $\boldsymbol{\Pi}^w$  and  $\boldsymbol{\Pi}_{,\kappa}^w$  are also composed of bilinear shape functions  $\phi_i(\xi, \eta)$ :

$$\boldsymbol{\Pi}^w = (\phi_1, \phi_2, \phi_3, \phi_4); \quad (6.97)$$

$$\boldsymbol{\Pi}_{,\kappa}^w = (\phi_{1,\kappa}, \phi_{2,\kappa}, \phi_{3,\kappa}, \phi_{4,\kappa}). \quad (6.98)$$

### 6.3.2 Stress independent part of the stiffness matrix

The virtual Green's strain vector  $\delta\gamma^{(E)}$  can be rewritten by substitution of the matrices  $\mathbf{H}_0$ ,  $\mathbf{H}_1$  and  $\mathbf{H}_2$ :

$$\delta\gamma^{(E)} = (\mathbf{H}_0\boldsymbol{\Lambda} + \mathbf{H}_0^\alpha\boldsymbol{\Lambda}_\alpha + \mathbf{H}_1\boldsymbol{\Lambda}_{,1} + \mathbf{H}_2\boldsymbol{\Lambda}_{,2})\delta\hat{\mathbf{u}} = \mathbf{B}^{(E)}\delta\hat{\mathbf{u}}. \quad (6.99)$$

To set up the constitutive relation the strains  $\delta\gamma^{(E)}$  have to be transformed to the local system  $\mathbf{l}_j$ . With the factor  $\lambda_{kl}^{ij}$ :

$$\lambda_{kl}^{ij} = t_k^i t_l^j; \quad \text{with:} \quad t_k^i = \mathbf{E}^i \cdot \mathbf{l}_k, \quad (6.100)$$

the physical engineering components of the strains  $\delta\gamma^{(l)}$  in the local frame of reference  $\mathbf{l}_j$  are obtained. The matrix  $\mathbf{B}^{(E)}$ , which relates the displacements to the strains in the general non-orthogonal triplet  $\mathbf{E}^i$ , can be transformed to the matrix  $\mathbf{B}^{(l)}$ , which relates the displacements to the physical engineering strains in the local system  $\mathbf{l}_j$ :

$$\delta\gamma^{(l)} = \mathbf{B}^{(l)}\delta\hat{\mathbf{u}}. \quad (6.101)$$

The gradient  $\partial\gamma/\partial\hat{\mathbf{u}}$ , which is also required to set up the stiffness matrix, differentiates the strains with respect to the displacement field:

$$\frac{\partial\gamma}{\partial\hat{\mathbf{u}}} = \mathbf{B}^{(l)}. \quad (6.102)$$

In the iterative Newton-Raphson solution procedure the tangent stiffness matrix  $\mathbf{K}_t$  is used to calculate the change of the displacements  $d\mathbf{a}$ . It can be calculated via

$$\mathbf{K}_t = \sum_{e=1}^k (\mathbf{H}^e)^T \mathbf{K}_t^e \mathbf{H}^e. \quad (6.103)$$

The matrix  $\mathbf{K}_t^e$  can be derived from the internal force vector  $\mathbf{p}^e$ . In principle,  $\mathbf{p}^e$  consists of two parts, namely  $\mathbf{B}^e$  and  $\boldsymbol{\sigma}^e$ . Both contributions are functions of the nodal displacements  $\hat{\mathbf{u}}^e$ . Applying the chain rule for the differentiation of the residual  $\Psi$  the matrix  $\mathbf{K}_t^e$  consists of two parts, a stress-independent part and a stress-dependent part, and reads:

$$\mathbf{K}_t^e = \mathbf{K}_0^e + \mathbf{K}_\sigma^e = \int_{V_0^e} \mathbf{B}^{eT} \frac{\partial\boldsymbol{\sigma}^e}{\partial\gamma} \frac{\partial\gamma^e}{\partial\hat{\mathbf{u}}} dV_0^e + \mathbf{K}_\sigma^e. \quad (6.104)$$

The matrix  $\mathbf{K}_\sigma^e$  is dependent on the current state of stress and the matrix  $\mathbf{K}_0^e$  is a function of the material tangent stiffness ( $\partial\boldsymbol{\sigma}/\partial\gamma$ ). However for

elasto-plastic situations the total derivative  $d\boldsymbol{\sigma}/d\boldsymbol{\gamma}$  instead of the partial derivative must be applied. The first part of the stiffness matrix equals

$$\mathbf{K}_0^e = \int_{V_0} \mathbf{B}^T \mathbf{D} \mathbf{B} (\sqrt{\det G_{ij}}) d\xi d\eta d\zeta. \quad (6.105)$$

The integration over the volume is carried out via Gauss integration. The integration in the thickness direction is split up into a number  $n_l$  of sub-integrations over the different layers. Then, the strains and stresses are calculated with respect to the material directions of the different layers.

### 6.3.3 Stress dependent part of the stiffness matrix

The evaluation of the second part of the stiffness matrix, the stress dependent part  $\mathbf{K}_\sigma^e$  of Eq. (5.96), is essentially not different for the thermo-mechanical solid-like shell element compared to the purely mechanical element, since the incremental change of the virtual thermal expansion strain is zero. For completeness the derivation of the stress dependent of the stiffness matrix is given here, which starts with the calculation of the incremental change  $d$  of the virtual strains

$$2d(\delta\epsilon_{\kappa\lambda}) = \delta\mathbf{u}_{,\kappa}^0 \cdot d\mathbf{u}_{,\lambda}^0 + \delta\mathbf{u}_{,\lambda}^0 \cdot d\mathbf{u}_{,\kappa}^0; \quad (6.106)$$

$$2d(\delta\epsilon_{\kappa 3}) = \delta\mathbf{u}_{,\kappa}^0 \cdot d\mathbf{u}^1 + \delta\mathbf{u}^1 \cdot d\mathbf{u}_{,\kappa}^0; \quad (6.107)$$

$$2d(\delta\epsilon_{33}) = 2d\mathbf{u}^1 \cdot \delta\mathbf{u}^1; \quad (6.108)$$

$$\begin{aligned} 2d(\delta\rho_{\kappa\lambda}) &= \delta\mathbf{u}_{,\kappa}^1 \cdot d\mathbf{u}_{,\lambda}^0 + \delta\mathbf{u}_{,\lambda}^0 \cdot d\mathbf{u}_{,\kappa}^1 + \delta\mathbf{u}_{,\lambda}^1 \cdot d\mathbf{u}_{,\kappa}^0 + \delta\mathbf{u}_{,\kappa}^0 \cdot d\mathbf{u}_{,\lambda}^1 \\ &\quad - [\delta\mathbf{u}_{,\tau}^0 \cdot d\mathbf{u}_{,\lambda}^0 + \delta\mathbf{u}_{,\lambda}^0 \cdot d\mathbf{u}_{,\tau}^0] \bar{G}_{\kappa}^{\tau} \\ &\quad - [\delta\mathbf{u}_{,\kappa}^0 \cdot d\mathbf{u}_{,\tau}^0 + \delta\mathbf{u}_{,\tau}^0 \cdot d\mathbf{u}_{,\kappa}^0] \bar{G}_{\lambda}^{\tau}; \end{aligned} \quad (6.109)$$

$$2d(\delta\rho_{\kappa 3}) = \delta\mathbf{u}_{,\kappa}^1 \cdot d\mathbf{u}^1 + \delta\mathbf{u}^1 \cdot d\mathbf{u}_{,\kappa}^1; \quad (6.110)$$

$$2d(\delta\rho_{33}) = -8[\delta\mathbf{u}^1 \cdot d\mathbf{w} + \delta\mathbf{w} \cdot d\mathbf{u}^1 + w\delta\mathbf{u}^1 \cdot d\mathbf{u}^1]. \quad (6.111)$$

When the following matrices are introduced:

$$\boldsymbol{\Omega}^{\mu} = \begin{bmatrix} \boldsymbol{\Pi}^{\mu} & 0 & 0 & 0 \\ 0 & \boldsymbol{\Pi}^{\mu} & 0 & 0 \\ 0 & 0 & \boldsymbol{\Pi}^{\mu} & 0 \end{bmatrix}; \quad \boldsymbol{\Omega}_{\tau}^{\mu} = \begin{bmatrix} \boldsymbol{\Pi}_{,\tau}^{\mu} & 0 & 0 & 0 \\ 0 & \boldsymbol{\Pi}_{,\tau}^{\mu} & 0 & 0 \\ 0 & 0 & \boldsymbol{\Pi}_{,\tau}^{\mu} & 0 \end{bmatrix}; \quad (6.112)$$

$$\boldsymbol{\Omega}^w = \begin{bmatrix} 0 & 0 & 0 & \boldsymbol{\Pi}^w \end{bmatrix}; \quad (6.113)$$

$$\mathbf{C}_{\tau} = \bar{G}_{\tau}^1 \boldsymbol{\Omega}_{,1}^0 + \bar{G}_{\tau}^2 \boldsymbol{\Omega}_{,2}^0; \quad \text{with: } \tau = \kappa, \lambda \quad \text{and} \quad \mu = 0, 1; \quad (6.114)$$

Then, the incremental change of virtual strains can be written as a function of the nodal displacements

$$2d(\delta\epsilon_{\kappa\lambda}) = \delta\hat{\mathbf{u}}^T(\boldsymbol{\Omega}_{,\kappa}^0)^T\boldsymbol{\Omega}_{,\lambda}^0d\hat{\mathbf{u}} + \delta\hat{\mathbf{u}}^T(\boldsymbol{\Omega}_{,\kappa}^0)^T\boldsymbol{\Omega}_{,\lambda}^0d\hat{\mathbf{u}}; \quad (6.115)$$

$$2d(\delta\epsilon_{\kappa 3}) = \delta\hat{\mathbf{u}}^T(\boldsymbol{\Omega}_{,\kappa}^0)^T\boldsymbol{\Omega}^1d\hat{\mathbf{u}} + \delta\hat{\mathbf{u}}^T(\boldsymbol{\Omega}^1)^T\boldsymbol{\Omega}_{,\kappa}^0d\hat{\mathbf{u}}; \quad (6.116)$$

$$2d(\delta\epsilon_{33}) = 2\delta\hat{\mathbf{u}}^T(\boldsymbol{\Omega}^1)^T\boldsymbol{\Omega}^1d\hat{\mathbf{u}}^1; \quad (6.117)$$

$$\begin{aligned} 2d(\delta\rho_{\kappa\lambda}) &= \delta\hat{\mathbf{u}}^T(\boldsymbol{\Omega}_{,\kappa}^1)^T\boldsymbol{\Omega}_{,\lambda}^0d\hat{\mathbf{u}} + \delta\hat{\mathbf{u}}^T(\boldsymbol{\Omega}_{,\lambda}^0)^T\boldsymbol{\Omega}_{,\kappa}^1d\hat{\mathbf{u}} \\ &\quad + \delta\hat{\mathbf{u}}^T(\boldsymbol{\Omega}_{,\lambda}^1)^T\boldsymbol{\Omega}_{,\kappa}^0d\hat{\mathbf{u}} + \delta\hat{\mathbf{u}}^T(\boldsymbol{\Omega}_{,\kappa}^0)^T\boldsymbol{\Omega}_{,\lambda}^1d\hat{\mathbf{u}} \\ &\quad - \delta\hat{\mathbf{u}}^T(\mathbf{C}_{\kappa})^T\boldsymbol{\Omega}_{,\lambda}^0d\hat{\mathbf{u}} - \delta\hat{\mathbf{u}}^T(\mathbf{C}_{\lambda})^T\boldsymbol{\Omega}_{,\kappa}^0d\hat{\mathbf{u}} \\ &\quad - \delta\hat{\mathbf{u}}^T(\boldsymbol{\Omega}_{,\kappa}^0)^T\mathbf{C}_{\lambda}d\hat{\mathbf{u}} - \delta\hat{\mathbf{u}}^T(\boldsymbol{\Omega}_{,\lambda}^0)^T\mathbf{C}_{\kappa}d\hat{\mathbf{u}}; \end{aligned} \quad (6.118)$$

$$2d(\delta\rho_{\kappa 3}) = \delta\hat{\mathbf{u}}_{,\kappa} \cdot d\mathbf{u}^1 + \delta\mathbf{u}^1 \cdot d\hat{\mathbf{u}}_{,\kappa}; \quad (6.119)$$

$$\begin{aligned} 2d(\delta\rho_{33}) &= -8[\delta\hat{\mathbf{u}}(\boldsymbol{\Omega}^1)^T\mathbf{d}\boldsymbol{\Omega}^w d\hat{\mathbf{u}} + \delta\hat{\mathbf{u}}^T(\boldsymbol{\Omega}^w)^T\mathbf{d}^T\boldsymbol{\Omega}^1d\hat{\mathbf{u}} \\ &\quad + w\delta\hat{\mathbf{u}}^T(\boldsymbol{\Omega}^1)^T\boldsymbol{\Omega}^1d\hat{\mathbf{u}}]. \end{aligned} \quad (6.120)$$

The incremental change of virtual strains refer to the covariant components, while the stress components refer to the local system  $\mathbf{l}_j$ . Therefore the factor  $\omega^{mn}$  is introduced for the set-up of the stress dependent part of the stiffness matrix:

$$\omega^{mn} = t_k^m t_l^n \sigma_{kl}; \quad \text{with: } t_i^j = \mathbf{E}^j \cdot \mathbf{l}_i. \quad (6.121)$$

By applying Eqs. (6.115) - (6.120) and Eq. (6.121) in Eq. (5.96) the nonlinear contribution of the stiffness matrix can be written as

$$\begin{aligned} \mathbf{K}_{\sigma}^e &= \int_{V_0} \left[ \omega^{11}(\boldsymbol{\Omega}_{,1}^0)^T\boldsymbol{\Omega}_{,1}^0 + \omega^{22}(\boldsymbol{\Omega}_{,2}^0)^T\boldsymbol{\Omega}_{,2}^0 \right. \\ &\quad + \omega^{33}(\boldsymbol{\Omega}^1)^T\boldsymbol{\Omega}^1 + \omega^{12} \left( (\boldsymbol{\Omega}_{,1}^0)^T\boldsymbol{\Omega}_{,2}^0 + (\boldsymbol{\Omega}_{,2}^0)^T\boldsymbol{\Omega}_{,1}^0 \right) \\ &\quad + \omega^{23} \left( (\boldsymbol{\Omega}_{,2}^0)^T\boldsymbol{\Omega}^1 + (\boldsymbol{\Omega}^1)^T\boldsymbol{\Omega}_{,2}^0 \right) + \omega^{31} \left( (\boldsymbol{\Omega}_{,1}^0)^T\boldsymbol{\Omega}^1 + (\boldsymbol{\Omega}^1)^T\boldsymbol{\Omega}_{,1}^0 \right) \\ &\quad + \zeta\omega^{11} \left( (\boldsymbol{\Omega}_{,1}^1)^T\boldsymbol{\Omega}_{,1}^0 + (\boldsymbol{\Omega}_{,1}^0)^T\boldsymbol{\Omega}_{,1}^1 - (\mathbf{C}_1)^T\boldsymbol{\Omega}_{,1}^0 - (\boldsymbol{\Omega}_{,1}^0)^T\mathbf{C}_1 \right) \\ &\quad + \zeta\omega^{22} \left( (\boldsymbol{\Omega}_{,2}^1)^T\boldsymbol{\Omega}_{,2}^0 + (\boldsymbol{\Omega}_{,2}^0)^T\boldsymbol{\Omega}_{,2}^1 - (\mathbf{C}_2)^T\boldsymbol{\Omega}_{,2}^0 - (\boldsymbol{\Omega}_{,2}^0)^T\mathbf{C}_2 \right) \\ &\quad - \zeta\omega^{33} \left( 4w(\boldsymbol{\Omega}^1)^T\boldsymbol{\Omega}^1 + 4(\boldsymbol{\Omega}^1)^T\mathbf{d}\boldsymbol{\Omega}^w + 4(\boldsymbol{\Omega}^w)^T\mathbf{d}^T\boldsymbol{\Omega}^1 \right) \\ &\quad \left. + \zeta\omega^{23} \left( (\boldsymbol{\Omega}_{,2}^1)^T\boldsymbol{\Omega}^1 + (\boldsymbol{\Omega}^1)^T\boldsymbol{\Omega}_{,2}^1 \right) + \zeta\omega^{31} \left( (\boldsymbol{\Omega}_{,1}^1)^T\boldsymbol{\Omega}^1 + (\boldsymbol{\Omega}^1)^T\boldsymbol{\Omega}_{,1}^1 \right) \right] \end{aligned}$$

$$\begin{aligned}
& + \zeta \omega^{12} \left( (\boldsymbol{\Omega}_{,1}^1)^T (\boldsymbol{\Omega}_{,2}^1)^T \boldsymbol{\Omega}_{,1}^0 + (\boldsymbol{\Omega}_{,1}^1)^T \boldsymbol{\Omega}_{,2}^1 + (\boldsymbol{\Omega}_{,2}^0)^T \boldsymbol{\Omega}_{,1}^1 - (\mathbf{C}_1)^T \boldsymbol{\Omega}_{,2}^0 \right) \\
& - (\mathbf{C}_2)^T \boldsymbol{\Omega}_{,1}^0 - (\boldsymbol{\Omega}_{,1}^0)^T \mathbf{C}_2 - (\boldsymbol{\Omega}_{,2}^0)^T \mathbf{C}_1 \left] (\sqrt{\det(G_{ij})}) d\xi d\eta d\zeta. \quad (6.122)
\end{aligned}$$

Integration of the volume is carried out via Gauss integration.

### 6.3.4 The strain increment and internal force vector

With  $\mathbf{K}_\sigma^e$  and  $\mathbf{K}_0^e$  the tangent stiffness  $\mathbf{K}_t^e$  of the solid-like shell element is fully defined. However, to solve for the displacements of the structure also the internal force vector  $\mathbf{p}^e(\hat{\mathbf{u}})$  must be evaluated. This can be accomplished by calculating the stress increment  $\Delta\boldsymbol{\sigma}$ . Based on the strain definition, the strain increment can be calculated in the following manner:

$$2\Delta\epsilon_{\kappa\lambda} = \mathbf{e}_\lambda \cdot \Delta\mathbf{u}_{,\kappa}^0 + \mathbf{e}_\kappa \cdot \Delta\mathbf{u}_{,\lambda}^0 + \Delta\mathbf{u}_{,\kappa}^0 \cdot \Delta\mathbf{u}_{,\lambda}^0 + 2\Delta\theta \mathbf{E}_\kappa \cdot \mathbf{E}_\lambda; \quad (6.123)$$

$$2\Delta\epsilon_{\kappa 3} = \mathbf{e}_\kappa \cdot \Delta\mathbf{u}^1 + \mathbf{d} \cdot \Delta\mathbf{u}_{,\kappa}^0 + \Delta\mathbf{u}_{,\kappa}^0 \cdot \Delta\mathbf{u}^1 + 2\Delta\theta \mathbf{E}_\kappa \cdot \mathbf{D}; \quad (6.124)$$

$$2\Delta\epsilon_{33} = 2\mathbf{d} \cdot \Delta\mathbf{u}^1 + \Delta\mathbf{u}^1 \cdot \Delta\mathbf{u}^1 + 2\Delta\theta \mathbf{D} \cdot \mathbf{D}; \quad (6.125)$$

$$\begin{aligned}
2\Delta\rho_{\kappa\lambda} = & \mathbf{e}_\lambda \cdot \Delta\mathbf{u}_{,\kappa}^1 + \mathbf{d}_{,\kappa} \cdot \Delta\mathbf{u}_{,\lambda}^0 + \Delta\mathbf{u}_{,\kappa}^1 \cdot \Delta\mathbf{u}_{,\lambda}^0 \\
& + \mathbf{e}_\kappa \cdot \Delta\mathbf{u}_{,\lambda}^1 + \mathbf{d}_{,\lambda} \cdot \Delta\mathbf{u}_{,\kappa}^0 + d\mathbf{u}_{,\lambda}^1 \cdot \Delta\mathbf{u}_{,\kappa}^0 \\
& - [\mathbf{e}_\lambda \cdot \Delta\mathbf{u}_{,\lambda}^0 + \mathbf{e}_\lambda \cdot \Delta\mathbf{u}_{,\lambda}^0 + \Delta\mathbf{u}_{,\lambda}^0 \cdot \Delta\mathbf{u}_{,\lambda}^0] \bar{G}_\kappa^\lambda \\
& - [\mathbf{e}_\kappa \cdot \Delta\mathbf{u}_{,\tau}^0 + \mathbf{e}_\tau \cdot \Delta\mathbf{u}_{,\kappa}^0 + \Delta\mathbf{u}_{,\kappa}^0 \cdot \Delta\mathbf{u}_{,\tau}^0] \bar{G}_\lambda^\tau \\
& + 2\Delta\theta [\mathbf{E}_\kappa \cdot \mathbf{D}_{,\lambda} + \mathbf{E}_\lambda \cdot \mathbf{D}_{,\kappa}] - 2\Delta\theta [\bar{G}_\kappa^\tau \cdot \mathbf{E}_\nu + \bar{G}_\lambda^\nu \cdot \mathbf{E}_\tau]; \quad (6.126)
\end{aligned}$$

$$2\Delta\rho_{\kappa 3} = \mathbf{d}_{,\kappa} \cdot \Delta\mathbf{u}^1 + \mathbf{d} \cdot \Delta\mathbf{u}_{,\kappa}^1 + \Delta\mathbf{u}_{,\kappa}^1 \cdot \Delta\mathbf{u}_{,\kappa}^1 + 2\Delta\theta \mathbf{D}_{,\kappa} \cdot \mathbf{D}; \quad (6.127)$$

$$2\Delta\rho_{33} = -8w\mathbf{d} \cdot \Delta\mathbf{u}^1 - 4\mathbf{d} \cdot \mathbf{d}\Delta w - 4\Delta w \mathbf{d} \cdot \Delta\mathbf{u}^1 - 4w\Delta\mathbf{u}^1 \cdot \Delta\mathbf{u}^1. \quad (6.128)$$

Using the matrices defined in Eq. (6.112) and after transformation into the local system  $\mathbf{l}_j$  the physical engineering strain increment can be calculated as a function of the nodal displacement increment  $\Delta\hat{\mathbf{u}}$ . Subsequently, the stress increment  $\Delta\boldsymbol{\sigma}$  is calculated by premultiplying the strain increment with the linear elastic stiffness matrix  $\mathbf{D}$ . The new total stress is calculated via:

$$(\boldsymbol{\sigma}^e)_{n+1}^{i+1} = (\boldsymbol{\sigma}^e)_n + \Delta\boldsymbol{\sigma}^e(\Delta\boldsymbol{\gamma}^e(\hat{\mathbf{u}}_n, \Delta\hat{\mathbf{u}}_{n+1}^{i+1})), \quad (6.129)$$

in which  $\boldsymbol{\sigma}_n$  and  $\hat{\mathbf{u}}_n$  represent the stress and the nodal displacements of the previous equilibrium state  $n$ . When physically nonlinearities are considered the stress increment is obtained via the return-mapping algorithm. The new stress  $\boldsymbol{\sigma}$  is premultiplied with the matrix  $\mathbf{B}^{(l)}$  to obtain the internal force vector  $\mathbf{p}^e$ .

### 6.3.5 Modifications of the stiffness matrix

Two modifications of the stiffness matrix, described by (Hashagen 1998), are given here as well in order to be complete. The first is the condensation of the element stiffness matrix  $\mathbf{K}_t$  due to the fact that the internal degrees of freedom are not used explicitly to obtain the equilibrium equation 5.81. The second modification is related to the problem of shear locking for the eight-noded solid-like shell element, which is solved by an assumed shear strain approximation.

#### Condensation of internal degrees of freedom

The condensation of the internal degrees of freedom is performed only for the mechanical system of equations and not for the heat transfer. As shown in Eq. 5.92, within every iteration the displacement increment  $\Delta \hat{\mathbf{u}}^{i+1}$  is determined:

$$\Delta \hat{\mathbf{u}}^{i+1} = \Delta \hat{\mathbf{u}}^i + d\hat{\mathbf{u}}^{i+1}. \quad (6.130)$$

where the vector  $d\hat{\mathbf{u}}^{i+1}$  is calculated through the evaluation of the linearised system:

$$\left[ \mathbf{K}_0 + \mathbf{K}_\sigma \right] \begin{bmatrix} d\hat{\mathbf{u}}^{i+1} \\ d\hat{\mathbf{w}}^{i+1} \end{bmatrix} = \begin{bmatrix} \mathbf{K}_{uu}^i & \mathbf{K}_{uw}^i \\ \mathbf{K}_{wu}^i & \mathbf{K}_{ww}^i \end{bmatrix} \begin{bmatrix} d\hat{\mathbf{u}}^{i+1} \\ d\hat{\mathbf{w}}^{i+1} \end{bmatrix} = \begin{bmatrix} \mathbf{p}_u^i \\ \mathbf{p}_w^i \end{bmatrix} - \begin{bmatrix} \mathbf{f}^i \\ 0 \end{bmatrix}. \quad (6.131)$$

And therefore, the change in the displacements of the internal degrees of freedom is determined as

$$d\hat{\mathbf{w}}^{i+1} = -\mathbf{K}_{ww}^{-1} \Big|_w^i [\mathbf{K}_{wu}^i d\hat{\mathbf{u}}^{i+1} - \mathbf{p}_w^i]. \quad (6.132)$$

When the latter formulation of  $d\hat{\mathbf{w}}^{i+1}$  in Eq.6.132 is used in Eq.6.131, the following expression for  $\mathbf{K}_t^e$ , Eq. 5.97, is found:

$$\mathbf{K}_t^e = -\mathbf{K}_{uu}^i - \mathbf{K}_{uw}^i \mathbf{K}_{ww}^{-1} \Big|_w^i \mathbf{K}_{wu}^i. \quad (6.133)$$

The internal force vector of the element  $\mathbf{p}^e$  can be written as

$$\mathbf{p}^e = [\mathbf{p}_u^i - \mathbf{K}_{uw}^i \mathbf{K}_{ww}^{-1} \Big|_w^i \mathbf{p}_w^i]. \quad (6.134)$$



### Assumed natural strains

The concept of the assumed natural strains is used to overcome the locking phenomenon, which has been observed for the four-noded shell element (Andelfinger 1991) and for the eight-noded solid-like shell element as well (Parisch 1995). The eight-noded solid-like shell element belongs to the same class as the four-noded shell element when the order of the element is considered. The reason of the locking, namely the overestimation of the shear strains, has been treated by (Bathe and Dvorkin 1986) through the introduction of so-called assumed shear strains.

The transverse shear strains  $\epsilon_{\kappa 3}$  are calculated with the following approximation:

$$\epsilon_{23} = f_C \epsilon_{23}^C + f_A \epsilon_{23}^A; \quad (6.135)$$

$$\epsilon_{13} = f_B \epsilon_{13}^B + f_D \epsilon_{13}^D. \quad (6.136)$$

The quantities  $\epsilon_{\kappa 3}^S$  in Eqs. 6.135 and 6.136 represent the transverse shear strains in the four sampling points A through D, which are located on the mid-surface and the four sides of the eight-noded element as shown in Figure 6.3. The coordinates of the sampling points are given in Table 6.1.

The virtual shear strains in the sampling point  $\epsilon_{\kappa 3}^S$  are calculated with

$$2\delta\epsilon_{\kappa 3}^S = \frac{1}{4} [(\mathbf{e}_\kappa - \mathbf{d}), (-\mathbf{e}_\kappa + \mathbf{d}), (\mathbf{e}_\kappa + \mathbf{d}), (-\mathbf{e}_\kappa + \mathbf{d})]^S \begin{bmatrix} \delta\mathbf{u}^J \\ \delta\mathbf{u}^K \\ \delta\mathbf{u}^L \\ \delta\mathbf{u}^M \end{bmatrix}, \quad (6.137)$$

where

$$\mathbf{e}_\kappa^S = \frac{1}{4} [-\mathbf{x}^J - \mathbf{x}^K + \mathbf{x}^L + \mathbf{x}^M]; \text{ and: } \mathbf{d}^S = \frac{1}{4} [\mathbf{x}^J - \mathbf{x}^K + \mathbf{x}^L - \mathbf{x}^M]. \quad (6.138)$$

The superscripts  $J, K, L, M$  in Eqs. 6.137 and 6.138 represent the nodes of the side on which the sampling point  $S$  is located, as given in Table 6.1. In case of the eight-noded element two rows of the matrix  $\mathbf{B}^{(E)}$  (Eq. 6.99),  $2\delta\epsilon_{23}$  and  $2\delta\epsilon_{13}$ , are replaced by Eqs. 6.135 and 6.136. From the latter equations also the nonlinear contributions to the stiffness matrix can be calculated, and the terms corresponding to  $\omega^{13}$  and  $\omega^{23}$  in Eq. 6.122 are replaced by

$$\mathbf{K}_\sigma^{\text{ANS}} = \int \omega^{23} [f_D \bar{\mathbf{D}}_{23}^D + f_B \bar{\mathbf{D}}_{23}^B] + \omega^{13} [f_A \bar{\mathbf{D}}_{13}^A + f_C \bar{\mathbf{D}}_{13}^C] dV_0. \quad (6.139)$$

Sampling point	Coordinates		Nodes			
	$\xi$	$\eta$	J	K	L	M
A	0.0	-1.0	5	1	6	2
B	1.0	0.0	6	2	7	3
C	0.0	1.0	8	4	7	3
D	-1.0	0.0	5	1	8	4

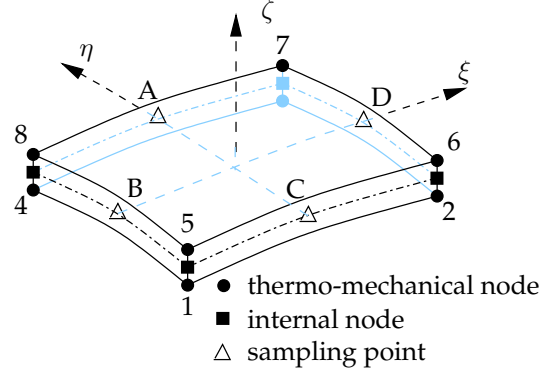


Table 6.1: Sampling points where the transverse shear strains  $\epsilon_{\kappa 3}^S$  are determined in the assumed shear strain concept.

Figure 6.3: Geometry and location of the sampling points A-D of the eight-noded thermo-mechanical solid-like shell element.

The quantities  $\bar{\mathbf{D}}_{\kappa 3}^S$  are the mapping matrices, which perform the correct multiplication of the nodal displacements, that are obtained when the non-linear contributions of the assumed shear strains are set up as follows:

$$d(\delta\epsilon_{\kappa 3}^S) = \frac{1}{8} [(d\mathbf{u}^M - d\mathbf{u}^J), -(d\mathbf{u}^L - d\mathbf{u}^K), (d\mathbf{u}^L - d\mathbf{u}^K), -(d\mathbf{u}^M - d\mathbf{u}^J)] \begin{bmatrix} \delta\mathbf{u}^J \\ \delta\mathbf{u}^K \\ \delta\mathbf{u}^L \\ \delta\mathbf{u}^M \end{bmatrix}. \quad (6.140)$$

Eq. 6.140 can be rewritten in matrix form as

$$d(\delta\epsilon_{\kappa 3}^S) = (\delta\mathbf{u}^J, \delta\mathbf{u}^K, \delta\mathbf{u}^L, \delta\mathbf{u}^M) \mathbf{D}_{\kappa 3}^S \begin{bmatrix} d\mathbf{u}^J \\ d\mathbf{u}^K \\ d\mathbf{u}^L \\ d\mathbf{u}^M \end{bmatrix}, \quad (6.141)$$

where the mapping matrices  $\mathbf{D}_{\kappa 3}^S$  in the sampling points are given as

$$\mathbf{D}_{\kappa 3}^S = \frac{1}{8} \begin{bmatrix} -\mathbf{I}_3 & \mathbf{0} & \mathbf{0} & \mathbf{I}_3 \\ \mathbf{0} & \mathbf{I}_3 & -\mathbf{I}_3 & \mathbf{0} \\ \mathbf{0} & -\mathbf{I}_3 & \mathbf{I}_3 & \mathbf{0} \\ \mathbf{I}_3 & \mathbf{0} & \mathbf{0} & -\mathbf{I}_3 \end{bmatrix}. \quad (6.142)$$

The matrix  $\bar{\mathbf{D}}_{\kappa 3}^S$  is obtained by expanding  $\mathbf{D}_{\kappa 3}^S$  using all displacements of the element, since the matrix  $\mathbf{D}_{\kappa 3}^S$  is defined with the displacements of the four nodes  $J, K, L,$  and  $M$ .

## 6.4 Benchmark tests

In this section a number of examples is presented to demonstrate the performance of the thermo-mechanical solid-like shell element. In the first two examples a strip is considered which is subjected to a heat source. The analysis is performed with an eight-noded element in both cases. The aspect ratio  $S = l/h$  is high,  $S = 100$  in example 1 and  $S = 100/236$  in example 2. The third example is a thick-walled cylinder with a different temperature on the inside and the outside. For all examples analytical solutions are available and presented as well.

### 6.4.1 Strip subjected to a heat source

Consider the aluminium 2024-T3 strip depicted in Figure 6.4, which is clamped at one end and free to expand at the other end. The right end of the strip is subjected to a equally distributed heat source  $Q$  equal to 0.275 W. The thermal conductivity  $k$  according to Section 3.5.2 is  $0.1222 \text{ Wmm}^{-1}\text{C}^{-1}$ . The height of the strip  $h$  is 0.3 mm, the length  $l$  is 300 mm, and the width  $w$  is 30 mm. The thermal expansion coefficient  $\alpha$  is  $22.4 \cdot 10^{-6} \text{ }^\circ\text{C}^{-1}$  and the equally distributed heat source  $Q$  can be collected in the point heat sources  $Q/4$  that act on the corner nodes. The strip is numerically modelled with 10 elements and the aspect ratio of each element is therefore  $S = l/h = 100$ .

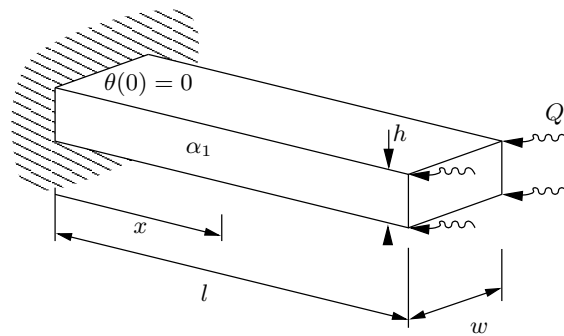


Figure 6.4: Strip subjected to a heat source.

The relative temperature is set to zero at the clamped side (temperature boundary condition):

$$\theta(0) = 0. \quad (6.143)$$

The temperature due to the heat source will rise linearly with respect to the distance from the clamped side where  $x = 0$ . The temperature at distance  $x$  can be calculated analytically as:

$$\theta(x) = \frac{Qx}{kA}, \quad (6.144)$$

where  $Q$  is the heat source,  $k$  is the thermal conductivity and  $A$  is the cross-sectional area of the strip. The distributed temperature over the strip causes free expansion at the right end, which can be calculated analytically as

$$\epsilon_\alpha = \alpha \int \theta(x) dx, \quad (6.145)$$

and

$$u_\alpha = \epsilon_\alpha l, \quad (6.146)$$

where  $\epsilon_\alpha$  is the expansion strain,  $\theta$  is the distributed temperature over the strip and  $u_\alpha$  is the total expansion. If we fill in the given values, at the free edge the following relative temperature, expansion strain and total expansion are found:

$$\begin{aligned} \theta(l) &= 75.0 \text{ }^\circ\text{C}, \\ \epsilon_\alpha &= 8.4 \cdot 10^{-4}, \\ u_\alpha &= 0.25 \text{ mm}. \end{aligned} \quad (6.147)$$

Numerically the same values are found.

## 6.4.2 Bi-material strip subjected to a heat source

Now a bi-material strip is considered, where two strips with different thermal expansion coefficient are bonded together, see Figure 6.5. The strip is subjected to a constant temperature  $\theta$  of  $2.5 \text{ }^\circ\text{C}$  in this case. An aluminium 2024-T3 strip of 0.3 mm on top of a glass-fibre epoxy layer of 0.127 mm will be considered here, with the fibre orientation in the length of the strip. The other dimensions are taken similar as in the previous example, 300 mm for the length  $l$ , and 30 mm for the width  $w$ . In this case two times 10 elements are used to model both strips numerically.

The thermal expansion coefficients  $\alpha_1$  for the aluminium and  $\alpha_2$  for the glass-fibre epoxy are respectively  $22.4 \cdot 10^{-6} \text{ }^\circ\text{C}^{-1}$  and  $3.9 \cdot 10^{-6} \text{ }^\circ\text{C}^{-1}$ , which are taken from Sections 3.5.2 and 3.3.3 respectively. The aluminium

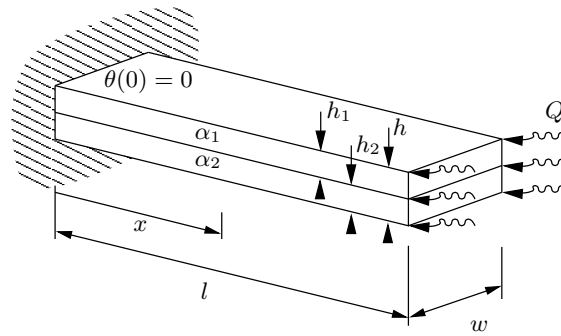


Figure 6.5: Bi-material strip subjected to a heat source.

stiffness is  $72.4 \cdot 10^3 \text{ N/mm}^2$  and the stiffness of the glass-fibre epoxy layer is  $50.6 \cdot 10^3 \text{ N/mm}^2$  in fibre direction, as can be found in Chapter 3 as well. The temperature boundary condition is set to a zero relative temperature at the clamped side:

$$\theta(0) = 0. \quad (6.148)$$

The relation between the curvature  $\kappa$  and stiffness of the two materials, and the difference in their thermal expansivity is given by (Clyne 1996):

$$\kappa = 6E_1E_2(h_1 + h_2)h_1h_2(\alpha_1 - \alpha_2)\theta/C, \quad (6.149)$$

where,

$$C = (E_1^2h_1^4 + 4E_1E_2h_1^3h_2 + 6E_1E_2h_1^2h_2^2 + 4E_1E_2h_1h_2^3 + E_2^2h_2^4), \quad (6.150)$$

and  $E$  is the Young's modulus,  $h$  is the thickness,  $\theta$  is the relative temperature and the subscripts 1 and 2 refer to the first and second component of the bi-material strip.

To derive the maximum deflection  $v$  at the edge, the curvature  $\kappa$  must be integrated twice over the length of the strip, since:

$$\kappa = \frac{d^2v}{dx^2}. \quad (6.151)$$

Integrating and substituting the boundary conditions yields the deflection. At the edge, where  $x = l$ , the maximum deflection is found, and with the given input values we find:

$$v_{max} = 5.54 \text{ mm}. \quad (6.152)$$

Numerically a value of 5.53 mm is found for the maximum deflection. The results are in good agreement.

### 6.4.3 Thick-walled cylinder subjected to temperature

An infinitely long, thick-walled cylindrical tube is subjected to a different temperature at the inside and the outside wall. This will lead to a non-linear temperature field over the thickness. The cylinder will expand and this will introduce stresses. The cylinder with inside radius,  $a$ , and outside radius,  $b$ , has an inside wall temperature,  $\theta_a$ , and an outside wall temperature,  $\theta_b$ , relative to the reference temperature,  $\theta_o$ .

The problem can be treated as an axisymmetric problem with a two-dimensional deformation field. The strain, in this case, is symmetric with respect to the axis of rotation and the shear strains are zero. The problem is independent of the angle  $\phi$ , and all quantities are functions of  $r$  only. The numerical solution is obtained with the thermo-mechanical solid-like shell element. The derivation of the analytical solution is described in Appendix A.

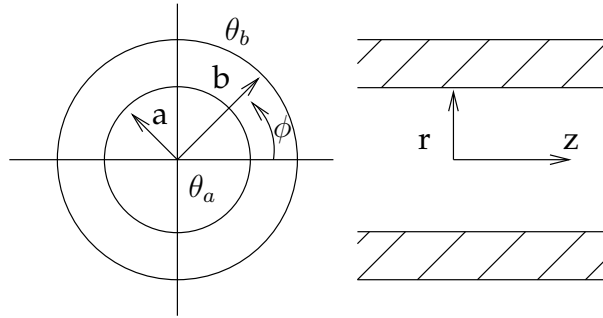


Figure 6.6: Thick-walled cylinder subjected to temperature.

The analytical solution for the temperature field in radial direction is given by Eq. (A.14),

$$\theta(r) = \frac{1}{\ln b/a} (\theta_a \ln \frac{b}{r} + \theta_b \ln \frac{r}{a}). \quad (6.153)$$

For the displacement field in radial direction the following expression has been derived, Eq. (A.33),

$$u_r = D_1 r + D_2 r \ln r + D_3 \frac{1}{r}. \quad (6.154)$$

For the radial and circumferential strains and stresses the expressions,

found in Eqs. (A.34) - (A.35) and Eq. (A.36) - (A.37), read

$$\epsilon_r = D_1 + D_2(1 + \ln r) - D_3 \frac{1}{r^2}, \quad (6.155)$$

$$\epsilon_\phi = D_1 + D_2 \ln r + D_3 \frac{1}{r^2}, \quad (6.156)$$

$$\sigma_r = 2(\lambda + G)D_1 + (\lambda + 2G)D_2 + 2(\lambda + G)D_2 \ln r - 2GD_3 \frac{1}{r^2} - \kappa\alpha\Delta\theta, \quad (6.157)$$

$$\sigma_\phi = 2(\lambda + G)D_1 + \lambda D_2 + 2(\lambda + G)D_2 \ln r + 2GD_3 \frac{1}{r^2} - \kappa\alpha\Delta\theta. \quad (6.158)$$

The integration constants are determined from the boundary conditions for the radial stress  $\sigma_r = 0$  when  $r = a$  or  $r = b$ , and can be found in Eqs. (A.38) - (A.40).

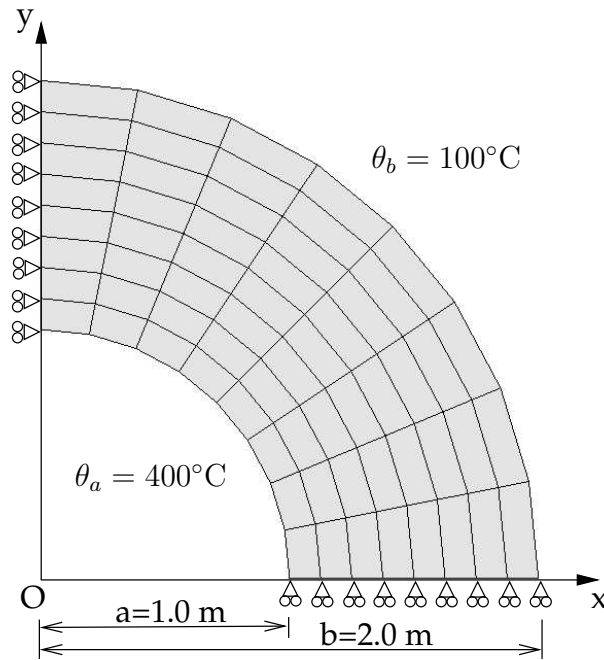


Figure 6.7: Numerical model for the thick-walled cylinder.

For the numerical solution the Jem/Jive finite element package and the 8-node thermo-mechanical solid-like shell element has been used to calculate the temperature and displacement field. The thermo-mechanical coupling consists of the thermal expansion, due to the difference in temperature at the nodes. The cylinder is axial symmetric for both the x-axis

and the y-axis, and only a quarter of the cylinder needs to be modelled. At the y-axis the boundary conditions prevent the movement in x-direction, and at the x-axis the movement in y-direction is prevented. The number of elements in radial (and circumferential) direction is doubled in each sequential calculation from 1 to 8 elements. The results of the analytical and numerical solution are listed for the example below.

### Example

Let  $a = 1.0$  m,  $b = 2.0$  m,  $\theta_a = 400^\circ\text{C}$ , and  $\theta_b = 100^\circ\text{C}$ . Further more for the material parameters we choose  $E = 1.0$  (MPa),  $\nu = 0.0$ , and  $\alpha = 20.0 \cdot 10^{-6} \text{ }^\circ\text{C}^{-1}$ . The following parameters can be determined with this data;

$$\lambda = \frac{\nu E}{(1 + \nu)(1 - 2\nu)} = 0, \quad (6.159)$$

$$G = \frac{E}{2(1 + \nu)} = 0.5, \text{ and} \quad (6.160)$$

$$\kappa = \frac{E}{1 - 2\nu} = 1.0. \quad (6.161)$$

And for the analytical solution the following integration constants are found with Eqs. (A.38) - (A.40);  $D_1 = 8.328 \cdot 10^{-3}$ ,  $D_2 = -4.328 \cdot 10^{-3}$ , and  $D_3 = -4.0 \cdot 10^{-3}$ . With Eq. (6.153), and Eqs. (6.154) - (6.158) the temperature, displacement, strains, and stresses at each point in the cylinder can be calculated. In Table 6.2 the values at the inner wall, where  $r = a = 1.0$  m and  $\theta_a = 400^\circ\text{C}$ , and at the outer wall, where  $r = b = 2.0$  m and  $\theta_b = 100^\circ\text{C}$ , are listed.

Property	Formula	Units	Inner wall ( $r=a=1.0$ m and $\theta_a=400^\circ\text{C}$ )	Outer wall ( $r=b=2.0$ m and $\theta_b=100^\circ\text{C}$ )
$u_r$	$D_1 r + D_2 r \ln r + D_3 \frac{1}{r}$	[m]	$4.3281 \cdot 10^{-3}$	$8.6562 \cdot 10^{-3}$
$\epsilon_r$	$D_1 + D_2(1 + \ln r) - D_3 \frac{1}{r^2}$	[-]	$8.0 \cdot 10^{-3}$	$2.0 \cdot 10^{-3}$
$\epsilon_\phi$	$D_1 + D_2 \ln r + D_3 \frac{1}{r^2}$	[-]	$4.3281 \cdot 10^{-3}$	$4.3281 \cdot 10^{-3}$
$\sigma_r$	$(\lambda + 2G)\epsilon_r + \lambda\epsilon_\phi - \kappa\alpha\Delta\theta$	[MPa]	0.0	0.0
$\sigma_\phi$	$\lambda\epsilon_r + (\lambda + 2G)\epsilon_\phi - \kappa\alpha\Delta\theta$	[MPa]	$-3.6719 \cdot 10^{-3}$	$2.3281 \cdot 10^{-3}$

Table 6.2: Values of the displacement, strain, and stress in radial and circumferential direction at the inner and outer wall of the cylinder.

The results of the analytical and numerical temperature and displacement calculation can be found in the Figures 6.9 and 6.10 below. In Figure 6.11 and 6.12 the analytically determined strain and stress field are



given. From Figure 6.13 and 6.14 give the convergence rate can be obtained, where the error is determined for each step in mesh-refinement (from 2 and 4 elements towards 8 elements).

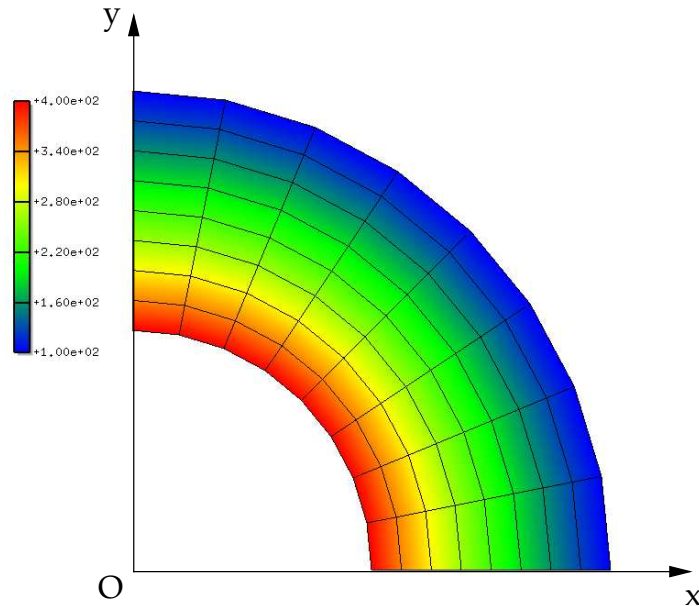


Figure 6.8: Numerically determined temperature distribution for the thick-walled cylinder.

By taking four elements in radial direction, the temperature field and displacement field can already be calculated quite accurately. The order of the error is near the value of 2 in both cases. This means that the error reduces by a factor 4 when the mesh-refinement is doubled.

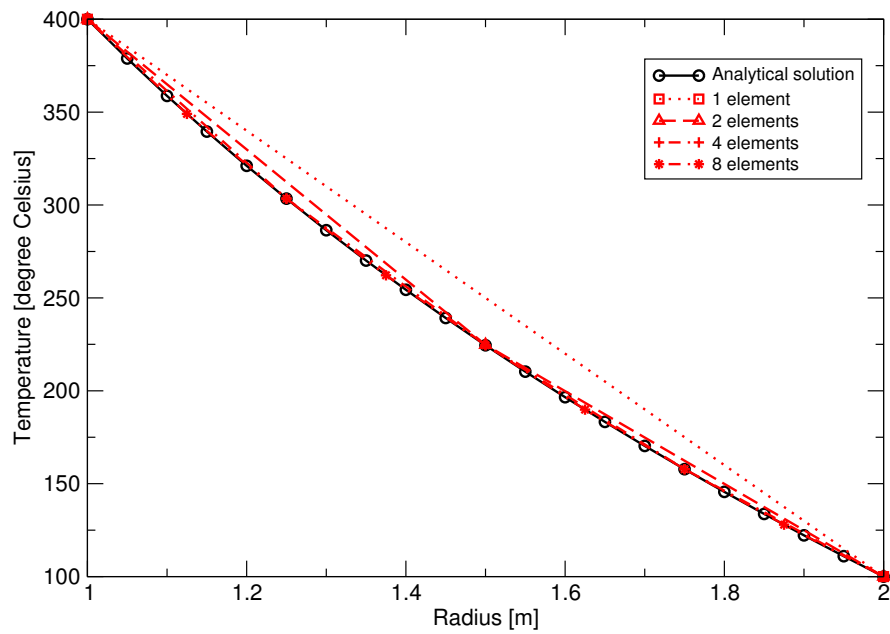


Figure 6.9: Analytically and numerically determined temperature field in radial direction.

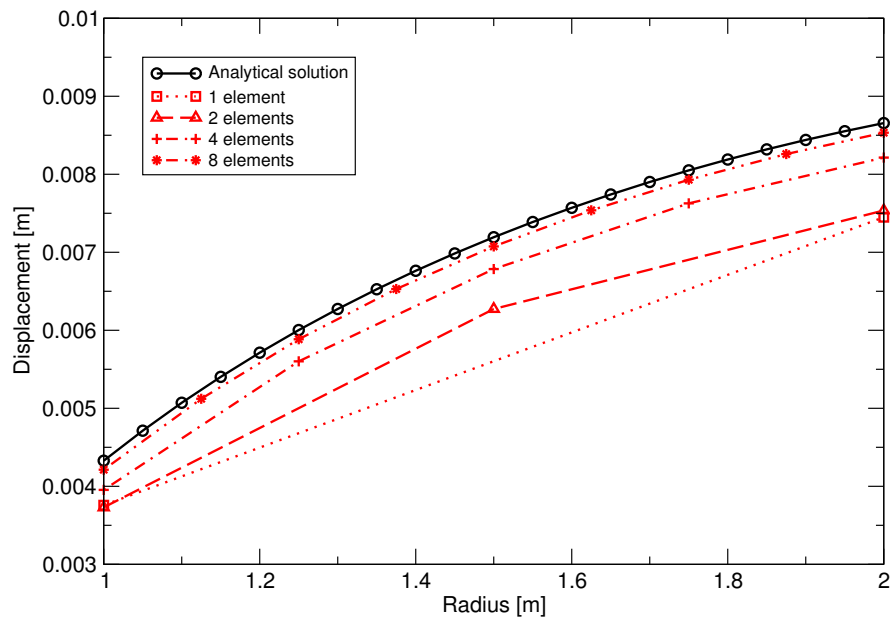


Figure 6.10: Analytically and numerically determined displacement field in radial direction.

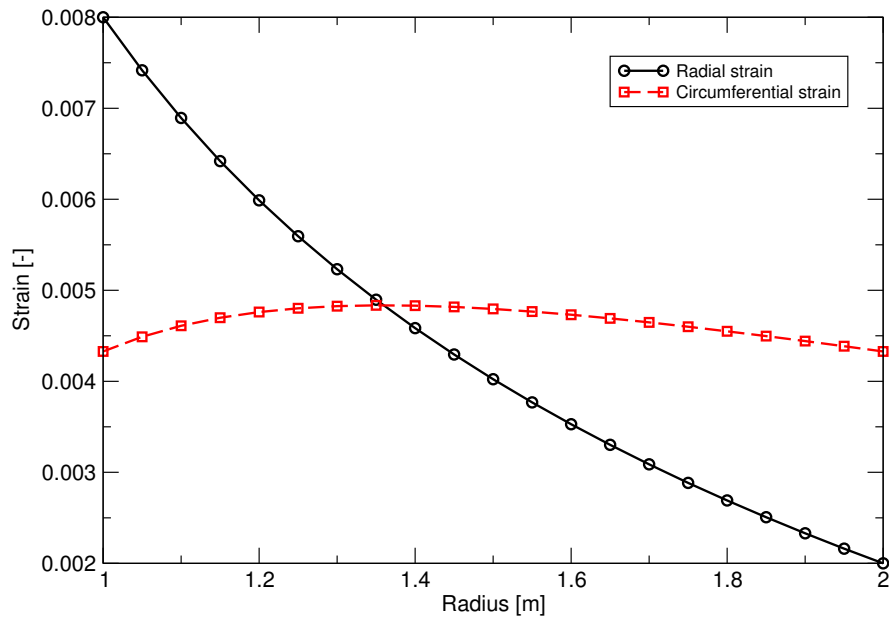


Figure 6.11: Strain in radial and circumferential direction.

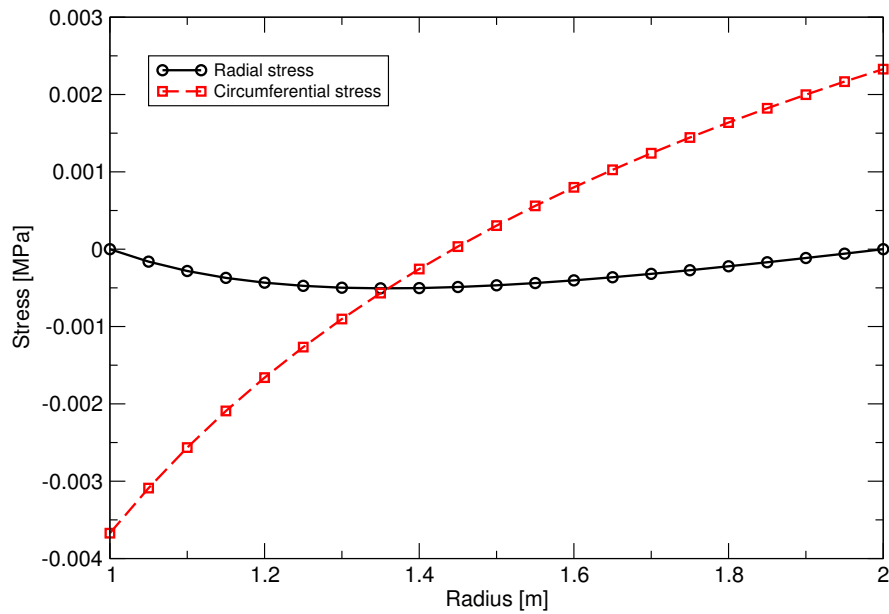


Figure 6.12: Stress in radial and circumferential direction. When the Poisson's ratio  $\nu$  is taken zero and stiffness  $E \neq 1$ , values can directly be multiplied with  $E$  to obtain the stresses in that case.

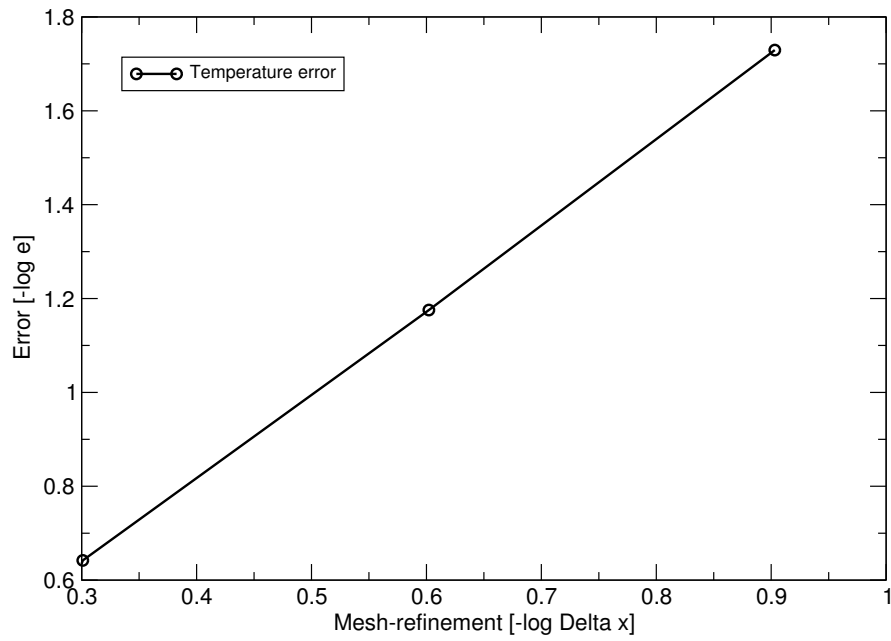


Figure 6.13: Error determination for the temperature.

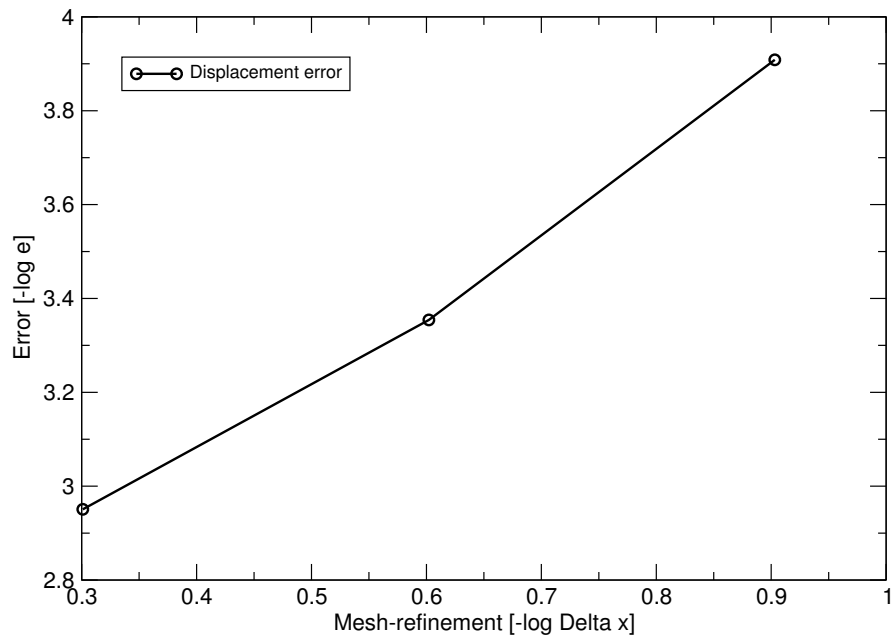


Figure 6.14: Error determination for the displacement.

## 6.5 Summary

Experiments on Glare showed the excellent fatigue and fire resistance of this fibre metal laminate, which could mean a major improvement in aircraft safety. To understand and calculate the effect of temperature on the material the solid-like shell element developed in earlier research is extended to include thermal expansion and heat transfer. With the thermo-mechanical solid-like shell element finite element simulations can be performed to investigate the thermal effects for Glare in detail. The simulation will be used to analyse the material behaviour for in-service temperature conditions (-55 up to 70 °C). Two examples (performed for aluminium 2024-T3 and glass-fibre epoxy) show the good agreement between analytically and numerically determined expansion and deflection of a long, thin strip consisting of a homogeneous material or two materials with different thermal expansion.



# Chapter 7

## The isotropic hardening model

In the thermo-mechanical solid-like shell element description in Chapter 6 geometrically nonlinear behaviour is included. Beside geometrical nonlinearities also physical nonlinearities, such as strain hardening and damage growth, can be observed when loading fibre metal laminates. The strain hardening behaviour of aluminium will be modelled in this chapter using an isotropic Von Mises plasticity formulation. The three-dimensional state description of the solid-like shell allows for a straightforward implementation. The strain hardening model is used in a number of blunt notch simulations and compared with experimental test results.

### 7.1 Introduction

For aluminium, as in general for most metals, the inelastic response is characterised by a strain hardening behaviour. In Figure 3.17 of Chapter 3 the aluminium stress-strain behaviour in tension has been shown. In this chapter we will derive a plasticity model for multi-dimensional stress-states.

In general, aluminium can be regarded as an isotropic material. However, due to the rolling process especially in thin sheet the grains obtain a preferred direction, which causes anisotropy in the mechanical properties. The difference between the stress-strain behaviour in rolling direction and the transverse direction can be substantial, as indicated by Figure 3.18. In (Hashagen 1998) the anisotropic aluminium behaviour is taken into account using a Hoffman yield function.

In the current chapter however, we will use an isotropic Von Mises yield function for several reasons. One reason is that the difference between the rolling and transverse direction is overshadowed by the scat-

ter in aluminium stress-strain curves obtained by different sources, as can be clearly observed from Figure 3.18. Thus, the value of a more detailed model depends on the accuracy of the input data. Moreover, the complexity of the more detailed anisotropic Hoffman model is increased over an isotropic model and is therefore known to be less robust. The general solution procedure for the system of equations including hardening has been described in Chapter 5.

The isotropic hardening model will be calibrated with the experimental test results for aluminium 2024-T3 given in Chapter 3. Thus, the aluminium stress-strain behaviour for an arbitrary loading condition can be determined. In combination with the glass-fibre epoxy properties, the blunt notch behaviour of standard and special Glare laminates will be simulated in several benchmark tests.

## 7.2 The aluminium hardening behaviour

### 7.2.1 The Von Mises yield criterion

In the general numerical framework described in Chapter 5, the concept of a loading or yield function was introduced to bound all possible stress states in a material point. Stress states inside the contour specified by the yield function only cause elastic deformations, while stress states on this yield surface give rise to elasto-plastic deformations.

Many yield functions have been proposed to capture the isotropic or anisotropic plasticity behaviour, but here the commonly used pressure-independent Von Mises plasticity formulation is used. This formulation is the classical smooth approximation of the Tresca yield function to ascertain the unique definition of the gradient to the yield surface and thus avoid difficulties in the incremental stress-strain relation. Starting from the general form of the yield function as given in Eq. 5.100:

$$f(\boldsymbol{\sigma}, \kappa) = \tilde{\sigma}(\boldsymbol{\sigma}) - \bar{\sigma}(\kappa) \leq 0, \quad (7.1)$$

where  $\tilde{\sigma}(\boldsymbol{\sigma})$  defines the Von Mises yield contour, see for example (de Borst and Sluys 1999), according to

$$\tilde{\sigma}(\boldsymbol{\sigma}) = \sqrt{1/2[(\sigma_I - \sigma_{II})^2 + (\sigma_{II} - \sigma_{III})^2 + (\sigma_{III} - \sigma_I)^2]}, \quad (7.2)$$

where  $\sigma_I$ ,  $\sigma_{II}$ , and  $\sigma_{III}$  are the principal stresses. The Von Mises yield contour can also be written, by using the second deviatoric stress invariant  $J_2$  in Eq. 7.2, as

$$\tilde{\sigma}(\boldsymbol{\sigma}) = \sqrt{3J_2}. \quad (7.3)$$



The flow theory of plasticity in this case utilises the Von Mises yield contour and is therefore also named the  $J_2$ -flow theory. The definition of the second deviatoric stress invariant  $J_2$  is

$$J_2 = 1/2 \boldsymbol{\sigma}^T \mathbf{P} \boldsymbol{\sigma}, \quad (7.4)$$

where the matrix  $\mathbf{P}$  is written as follows:

$$\mathbf{P} = \begin{bmatrix} 2/3 & -1/3 & -1/3 & 0 & 0 & 0 \\ -1/3 & 2/3 & -1/3 & 0 & 0 & 0 \\ -1/3 & -1/3 & 2/3 & 0 & 0 & 0 \\ 0 & 0 & 0 & 2 & 0 & 0 \\ 0 & 0 & 0 & 0 & 2 & 0 \\ 0 & 0 & 0 & 0 & 0 & 2 \end{bmatrix}. \quad (7.5)$$

The yield function can thus be rewritten as

$$f(\boldsymbol{\sigma}, \kappa) = \sqrt{3/2 \boldsymbol{\sigma}^T \mathbf{P} \boldsymbol{\sigma}} - \bar{\sigma}(\kappa) \leq 0, \quad (7.6)$$

The advantage of the factor  $3/2$  becomes clear in pure uniaxial tension when the yield function simply reduces to the uniaxial yield strength  $\bar{\sigma}$ . If during loading the yield function becomes equal to zero, plastic deformation will take place. If, during unloading, the yield function becomes less than zero, a purely elastic behaviour is retrieved. Thus, unloading or reloading up to yield is a purely elastic process.

### 7.2.2 The hardening law

The yield strength  $\bar{\sigma}$  is a function of the hardening parameter  $\kappa$  in Eq. 7.6. The following exponentially saturating hardening law is assumed for  $\bar{\sigma}$ :

$$\bar{\sigma}(\kappa) = \bar{\sigma}_0 + (\bar{\sigma}_u - \bar{\sigma}_0)(1 - e^{-\xi\kappa}), \quad (7.7)$$

where  $\bar{\sigma}_0$  is the initial yield stress,  $\bar{\sigma}_u$  is the ultimate stress, and  $\xi$  is the hardening rate. The hardening parameter  $\kappa$  is typically dependent on the strain history via invariants of the plastic strain tensor  $\boldsymbol{\epsilon}^{pl}$ . Here, the strain hardening hypothesis is used, i.e., the evolution of the hardening parameter is assumed to be related to the second invariant of the strain tensor as follows (see also Eq. 5.108):

$$\dot{\kappa} = \sqrt{2/3 (\dot{\boldsymbol{\epsilon}}^{pl})^T \mathbf{T} \dot{\boldsymbol{\epsilon}}^{pl}}. \quad (7.8)$$

The value of  $\kappa$  is obtained upon integration over the loading path. The loading history of the yield function only depends on the scalar-valued hardening parameter, which means that the yield surface can only expand or shrink. Thus, an isotropic hardening behaviour is found in this way.

When we use an associative flow rule, i.e. the plastic flow is written as  $\mathbf{m} = \mathbf{n} = \partial f / \partial \boldsymbol{\sigma}$ , and apply the Von Mises yield function of Eq. 7.6 in Eq. 5.106 the plastic strain rate reads:

$$\begin{bmatrix} \dot{\epsilon}_1^{pl} \\ \dot{\epsilon}_2^{pl} \\ \dot{\epsilon}_3^{pl} \end{bmatrix} = \frac{\dot{\lambda}}{2\bar{\sigma}} \begin{bmatrix} 2\sigma_1 - \sigma_2 - \sigma_3 \\ 2\sigma_2 - \sigma_3 - \sigma_1 \\ 2\sigma_3 - \sigma_1 - \sigma_2 \end{bmatrix}. \quad (7.9)$$

This expression can now be used in Eq. 7.8 to determine  $\dot{\kappa}$ , which leads to

$$\dot{\kappa} = \frac{\dot{\lambda}}{\bar{\sigma}} \sqrt{1/6[2\sigma_1 - \sigma_2 - \sigma_3]^2 + (2\sigma_2 - \sigma_3 - \sigma_1)^2 + (2\sigma_3 - \sigma_1 - \sigma_2)^2}, \quad (7.10)$$

which after reworking leads to

$$\dot{\kappa} = \dot{\lambda}. \quad (7.11)$$

The rate of the plastic flow  $\dot{\lambda}$  is thus equal to the strain hardening rate  $\dot{\kappa}$ .

### 7.2.3 The uniaxial stress-strain curve

When we consider a test in uniaxial tension,  $(\sigma_1, \sigma_2, \sigma_3) = (\sigma, 0, 0)$ , a general experimental approach to determine the hardening diagram for metals, the associated flow rule according to Eq. 7.9 gives

$$\dot{\epsilon}_1^{pl} = \frac{1}{2} \dot{\lambda} [2, -1, -1]^T. \quad (7.12)$$

Thus,  $\dot{\epsilon}_1^{pl} = \dot{\lambda}$ , or by using Eq. 7.11  $\dot{\epsilon}_1^{pl} = \dot{\kappa}$ , i.e. the uniaxial plastic strain in loading direction coincides with the hardening parameter. The hardening model for aluminium 2024-T3 can therefore directly be obtained from the uniaxial tensile test given in Figure 3.17 of Chapter 3, and is given by

$$\bar{\sigma}(\kappa) = 335.0 + (471.0 - 335.0)(1 - e^{-21.57\kappa}), \quad (7.13)$$

The experimental and simulated uniaxial stress-strain curve for aluminium 2024-T3 with the derived hardening law are depicted in Figure 7.1. From this figure it can be seen that the hardening law used in the model gives a good agreement with the experimental aluminium stress-strain curve over the whole strain range. The model, however, predicts a sharper transition from the elastic to the plastic region compared to the experimental curve.

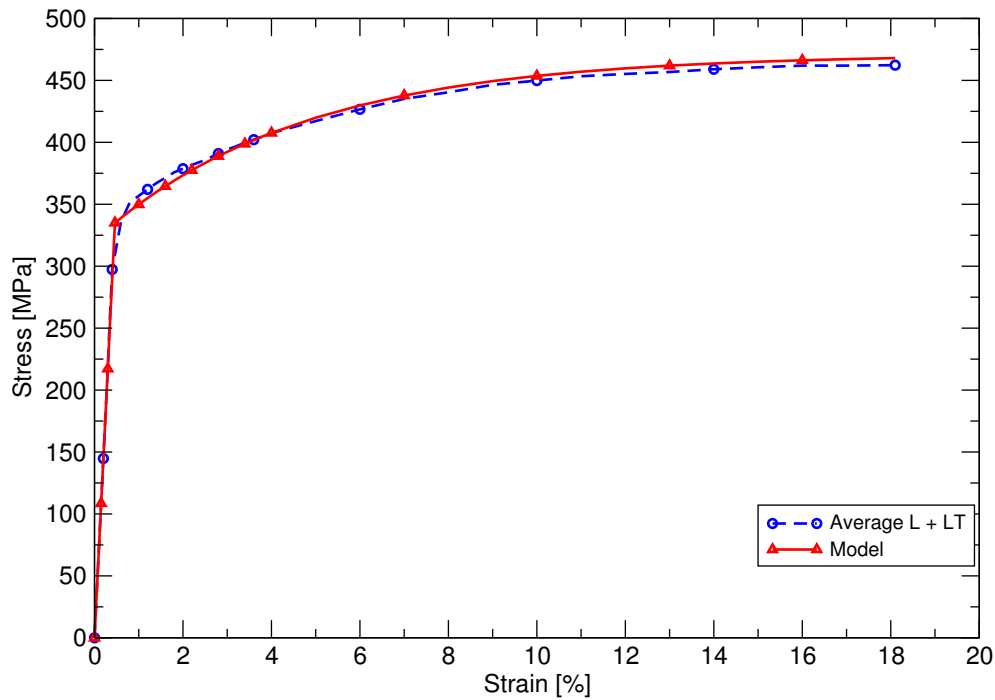


Figure 7.1: The aluminium 2024-T3 stress-strain curve (average of longitudinal and transverse direction), together with the model based on an exponentially saturating hardening law.

## 7.3 Benchmark tests

In this section a number of benchmark tests are performed on Glare laminates to demonstrate the hardening model presented in this chapter. The Glare laminates consist of aluminium layers, for which the hardening model is used to describe the elasto-plastic behaviour, and glass-fibre-epoxy layers, in which damage plays a role. For consistency with the experiments, a damage model is used for the glass-fibre epoxy layers. The damage model will be discussed in detail in Chapter 8.

In the first example a Glare3-3/2-0.4 blunt notch simulation is compared with experimental data and a simulation found in the literature. The second example considers the blunt notch test simulation for the special Glare laminates previously discussed in Section 4.2.3. All layers are defined in one (or two) elements, though by taking one element for each layer the model can become more accurate in thickness direction, see (Hashagen 1998).

### 7.3.1 Blunt notch test on a standard Glare laminate

A Glare3-3/2-0.4 laminate was tested by (Meziere 2000) to determine the starting point of different failure mechanisms, such as matrix damage, delamination and fibre breakage. A number of specimens were used and loaded up to several stages of the ultimate load. A finite element analysis was performed by (Schipperen 2001b) on this laminate to compare the failure starting points and the load-displacement curve. Thus, the numerical blunt notch simulation performed in this section can directly be compared with the experimental results obtained by (Meziere 2000) and the numerical results obtained by (Schipperen 2001b) for the Glare3-3/2-0.4 laminate.

The Glare3-3/2-0.4 specimen has a length of 200 mm, a width of 50 mm, and a notch size of 5.0 mm, of which only a quarter is modelled for reasons of symmetry. The specimen has a nominal thickness of 1.708 mm (0.127 mm for each fibre layer) and is tested in the longitudinal direction. In Figure 7.2 the finite element mesh for the quarter model of the specimen is shown. The model consists of 816 eight-noded elements.

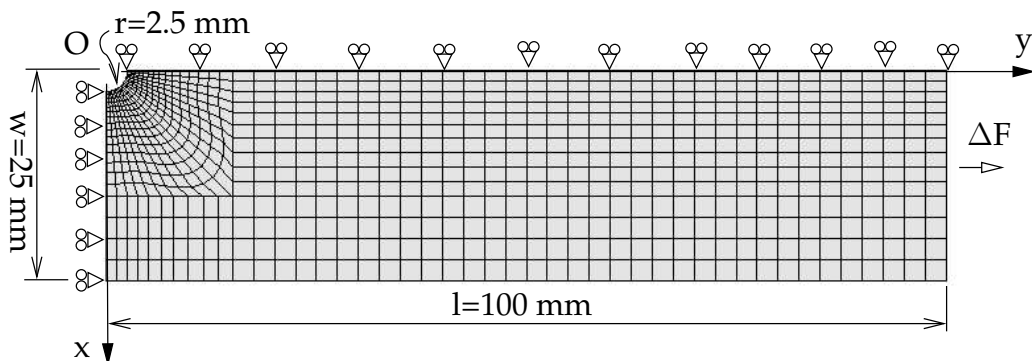


Figure 7.2: Finite element mesh for the the Glare3-3/2-0.4 blunt notch specimen (quarter model).

In Figure 7.3 the numerically obtained stress-strain curve for the Glare3-3/2-0.4 blunt notch specimen is given together with the experimental and numerical results found in the literature. The points of first and 76% matrix damage, and fibre breakage obtained numerically by (Schipperen 2001b) are given as an indication as well. The numerical analysis performed by (Schipperen 2001b) was done using two different aluminium models, indicated by "high" and "low" in the figure, derived from two different experimental sources, as shown in Figure 3.18. From the figure it can be seen that the agreement between the numerical simulation and

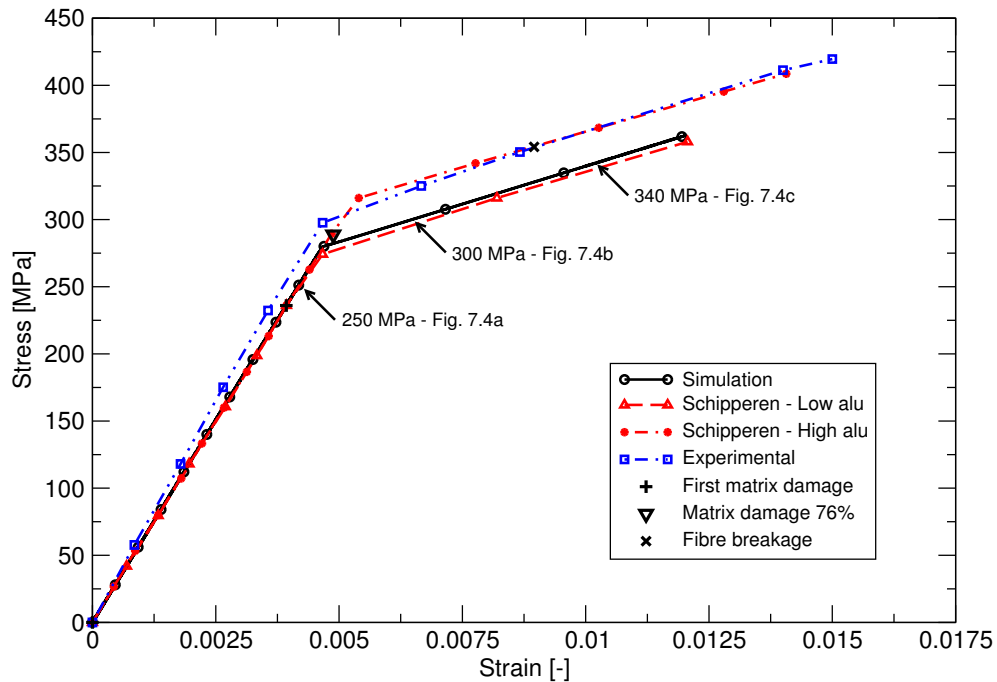


Figure 7.3: Comparison between the stress-strain curve obtained from the numerical Glare3-3/2-0.4 blunt notch simulation and the resulting curves obtained from experimental and numerical data in the literature.

both the experimental and numerical stress-strain curves from the literature is good and corresponding to the analysis with the "low"-aluminium of (Schipperen 2001b).

In Figure 7.4 the Von Mises stress distribution in the aluminium layer(s) of the Glare3-3/2-0.4 laminate is given. The plots are determined at three different Von Mises stress levels in the undisturbed (free field) region of the blunt notch specimen, viz.  $\sigma_0$  equals 250, 300, and 340 MPa. From this figure it can be seen that the plasticity region starts at the right edge of the notch, due to local stress concentrations, and gradually spreads over the whole specimen upon continued loading.

In the figure the stress distribution in the fibre layers at the cross-section can also be seen. The Von Mises stress is plotted here as well, which however approximately equals the stress in loading direction due to the small contribution of the other directions.

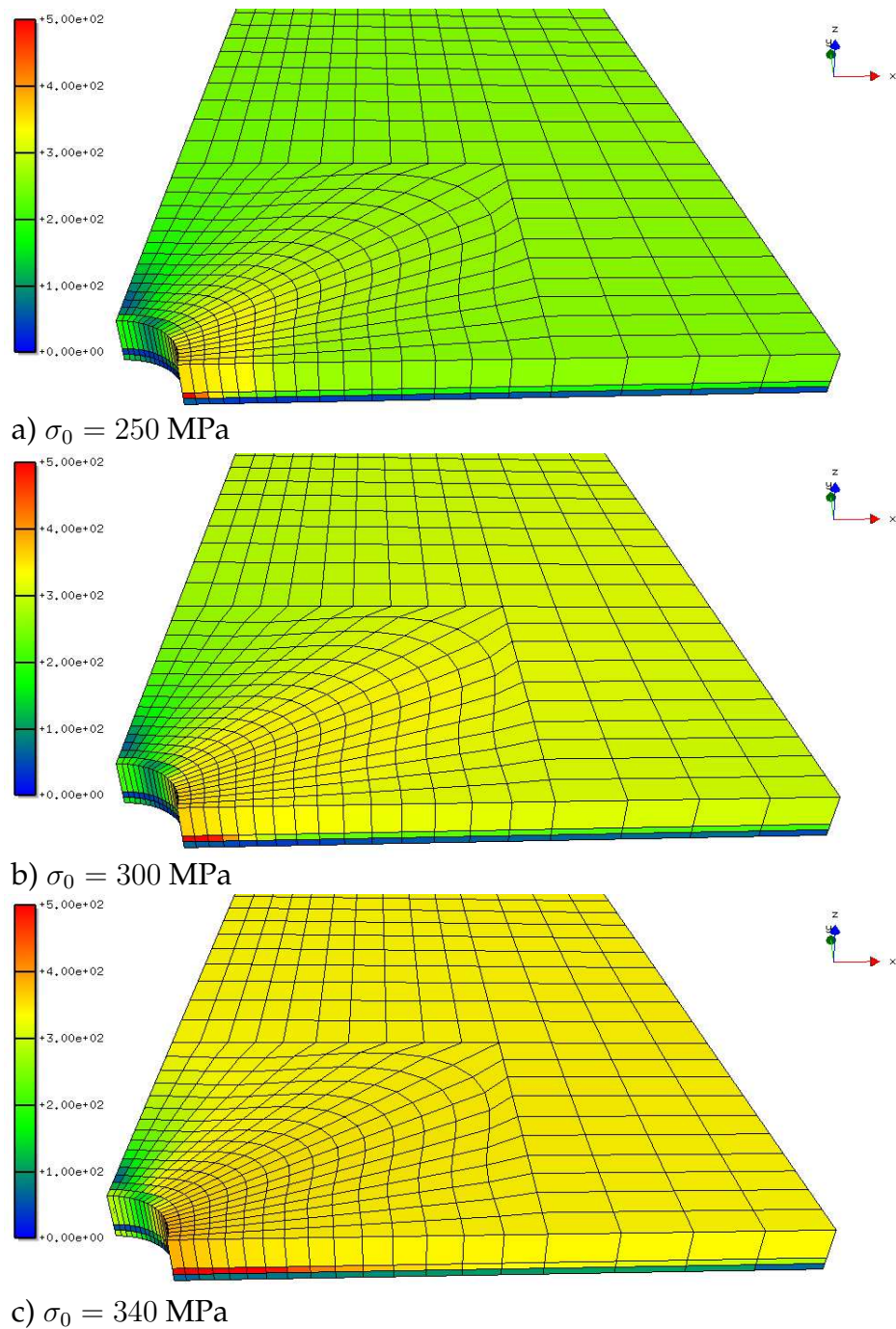


Figure 7.4: The numerically determined Von Mises stress distribution in the aluminium layer(s) of the Glare3-3/2-0.4 laminate. The indicated Von Mises stress levels  $\sigma_0$  are the values in the undisturbed region of the blunt notch specimen.

### 7.3.2 Blunt notch tests on special Glare laminates

Experimental blunt notch results for special Glare laminates have been discussed in Section 4.2.3. In this second benchmark test, blunt notch simulations are performed on this special Glare laminate with 0, 45, 67.5, and 90° off-axis angles. The obtained stress-strain curves are compared in this section with the experimental curves obtained by (Hagenbeek 2002b).

The dimensions of the special Glare specimen are 200 mm for the length, a width of 30 mm, and a notch size of 6.35 mm. In this case a full model is necessary due to the asymmetric lay-up. In Figure 7.5 the finite element mesh for the full specimen model, which consists of 2560 eight-noded elements, is shown. In thickness direction two elements are chosen with a condensed but overall symmetric lay-up. Thus, secondary bending is not considered for which the exact representation of the lay-up would be required.

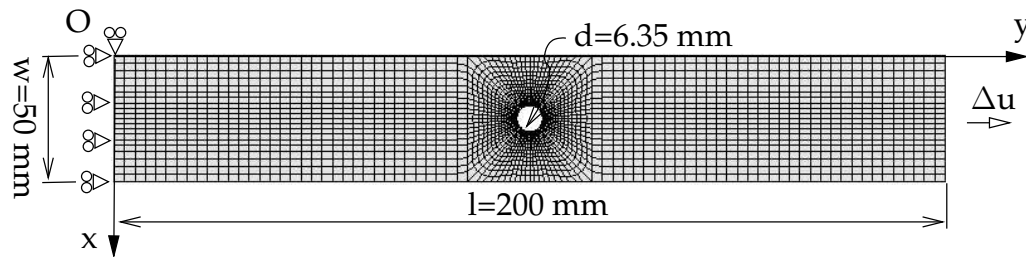


Figure 7.5: Finite element mesh for the special Glare blunt notch specimen (full model).

In Figures 7.6 and 7.8 the numerically obtained stress-strain curves for the special Glare blunt notch specimen are given at respectively room temperature and 80 °C together with the experimental results obtained by (Hagenbeek 2002b). From Figure 7.6 it can be seen that the agreement between the numerical simulation and the experimental stress-strain curves is very good in case of the 0 and 90° off-axis angles. The blunt notch simulation for the 45 and especially the 67.5° off-axis angle, depicted in Figure 7.8, show more deviation from the experimental results, though still a good agreement is found.

It should however be noted that the maximum strain found in all the simulations is more than twice as large compared to the experimental results. This might be caused by the secondary bending in the experimental test specimens, which is neglected in the simulations.

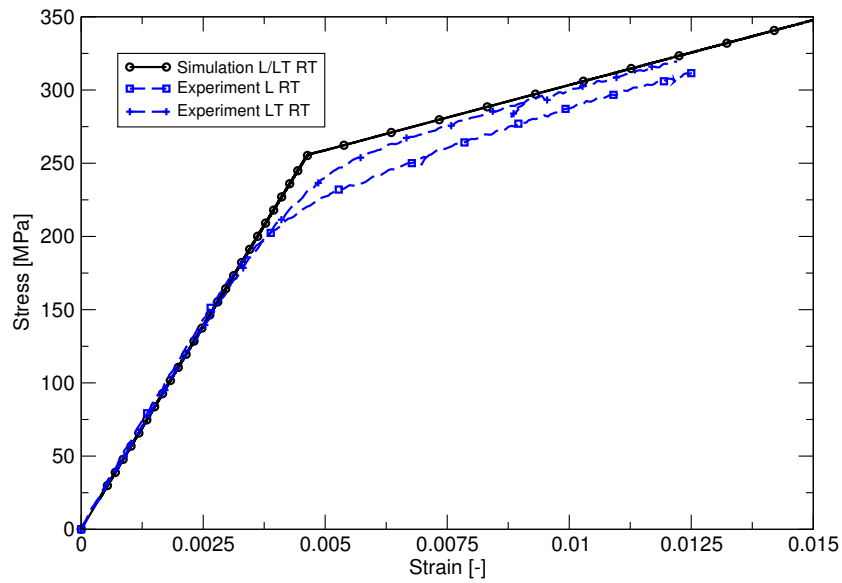


Figure 7.6: Comparison between the numerical (up to 3.2% strain) and experimental stress-strain curves obtained for the special Glare blunt notch specimens tested at 0 and 90° off-axis angles at room temperature.

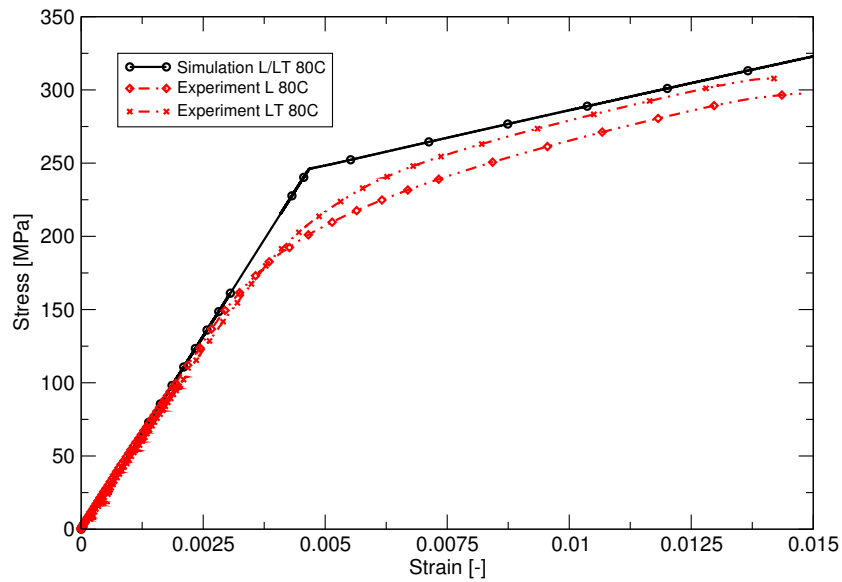


Figure 7.7: Comparison between the numerical and experimental stress-strain curves obtained for the special Glare blunt notch specimens tested at 0 and 90° off-axis angles at 80°C. The simulation runs up to 3.2% strain.



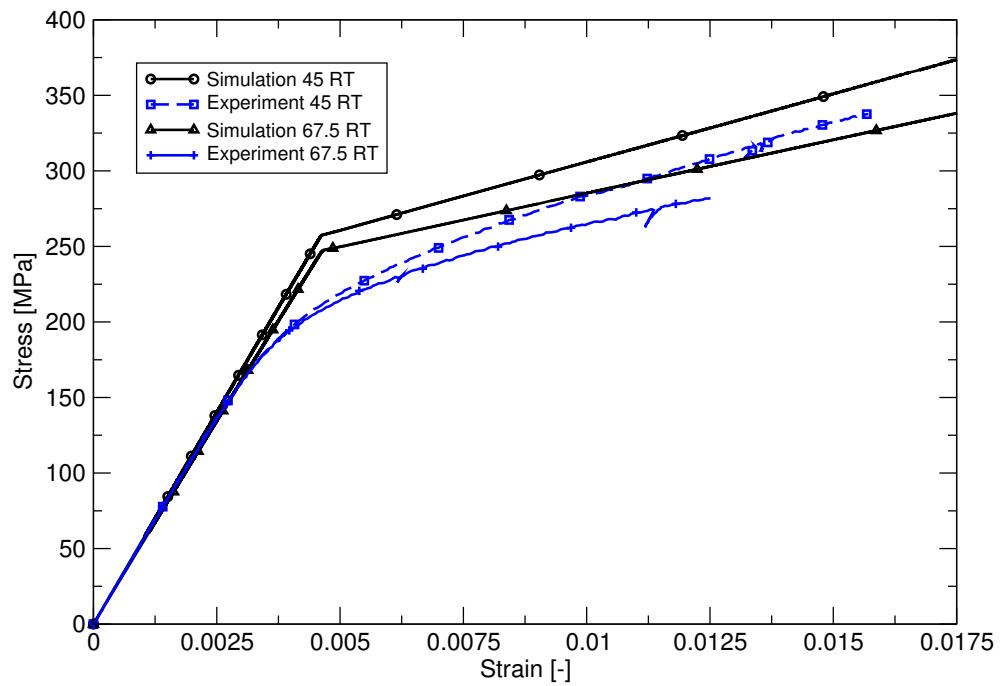


Figure 7.8: Comparison between the numerical and experimental stress-strain curves obtained for the special Glare blunt notch specimens tested at 45 and 67.5° off-axis angles. Simulations run up to 2.3 and 3.4% strain in case of the 45 and 67.5° off-axis angle respectively.

## 7.4 Summary

In this chapter the strain hardening behaviour of aluminium has been modelled. The yield function is based on an isotropic Von Mises plasticity formulation. The three-dimensional state description of the solid-like shell allows for a straightforward implementation.

The orthotropy in aluminium sheet material due to the rolling process can be substantial, but has not been taken into account since the difference between the rolling and transverse direction is overshadowed by the scatter in aluminium stress-strain curves from different literature sources. Moreover, the complexity of the more detailed anisotropic Hoffman model is increased over an isotropic model and is therefore known to be less robust.

The yield strength  $\bar{\sigma}$  is a function of the hardening parameter  $\kappa$  and an exponentially saturating hardening law has been assumed for  $\bar{\sigma}$ . Due to the associative flow rule, it is found that  $\dot{\kappa} = \dot{\lambda}$ , and the hardening model for aluminium 2024-T3 can therefore directly be obtained from the uniaxial tensile test given in Figure 3.17 of Chapter 3. The hardening law used in the simulations gives a good agreement with the experimental aluminium 2024-T3 stress-strain curve.

Benchmark tests have been performed on a Glare3-3/2-0.4 blunt notch specimen and on the special Glare laminate (tested at 0, 45, 67.5, and 90° off-axis angle, at room temperature and 80 °C ) previously discussed in Section 4.2.3. The simulations showed a good agreement with the results found in the literature. The maximum strains reached in the simulations is however twice as large compared to the experimental results, which might be due to the non-included effect of secondary bending.

# Chapter 8

## The orthotropic damage model

### 8.1 Introduction

To capture the damage and failure behaviour of the glass-fibre epoxy, a damage model will be included. In this chapter the modelling of matrix damage and fibre failure is described for the unidirectional glass-fibre epoxy ply at room temperature and at 80°C. From this elementary ply all possible laminate lay-ups are determined and the failure behaviour can directly be related to the material testing performed for the unidirectional glass-fibre epoxy in Chapter 3.

For the material model the concept of continuum damage mechanics is used, which is described in detail by (Lemaître and Chaboche 1990) and (de Borst and Sluys 1999) amongst others. The concept was introduced by (Kachanov 1958) to describe creep failure in metals. Failure was characterised by a scalar damage variable, that represents the ratio of the damaged material to the initial, undamaged material. (Lemaître and Chaboche 1978), amongst others, extended the concept to other types of loading and failure by using tensor-valued damage variables. More recently, the approach is increasingly used in the failure analysis of laminated composites in combination also with temperature. (Allix, Bahlouli, Cluzel, and Perret 1996) modelled the temperature dependent mechanical behaviour of carbon-epoxy laminates with strain energy based damage mechanics. Anisotropy and thermal residual stresses are taken into account by (McCartney 1998) who described the transverse crack formation in cross-ply laminates.

A straightforward and accurate orthotropic damage model is given by (Schipperen 2001a) for transverse matrix cracking. The occurrence and growth of damage in this reference is governed by a strain measure, which

is determined from the Hoffman plasticity model in a strain-based formulation. It is emphasised that other failure criteria could be used, e.g. Hashin-Rotem, Tsai-Hill or Puck-Schneider, of which many have been evaluated by (Sun, Quinn, Tao, and Oplinger 1996). The damage parameters are directly implemented into the stiffness matrix. The same approach will be followed here with some modifications to include fibre failure and to assure a good correspondence with the material test data.

## 8.2 The glass-fibre epoxy damage behaviour

The general outline for the damage modelling has been given in Section 5.5.4 and shown in Figure 5.3. Thus, an implicit incremental-iterative solution procedure will be applied. The equivalent strain measure, the damage growth laws, and the damage matrix will be detailed in this section. Specific material models for the unidirectional glass-fibre epoxy layer will be given as well, based on the experimental test data derived in Chapter 3.

### 8.2.1 The equivalent strain

For the definition of the equivalent strain  $\tilde{\gamma}$  a constitutive assumption is needed, which can be, similar to plasticity, any invariant measure of the total strains or of the elastic energy per unit mass. Thus the equivalent strain  $\tilde{\gamma}$  can also be obtained by rewriting the yield function of the orthotropic Hoffman plasticity model in a strain-based format. For a continuum material the Hoffman yield function with isotropic softening is given by

$$\Phi(\tilde{\sigma}, \bar{\sigma}) = \tilde{\sigma} - \bar{\sigma} = 0, \quad (8.1)$$

where the equivalent stress  $\tilde{\sigma}$  is defined as

$$\tilde{\sigma} = \sqrt{1/2 \boldsymbol{\sigma}^T \mathbf{P} \boldsymbol{\sigma} + \boldsymbol{\sigma}^T \mathbf{q}}, \quad (8.2)$$

with the following definitions for  $\mathbf{P}$  and  $\mathbf{q}$ ,

$$\mathbf{P} = \begin{bmatrix} 2(\alpha_4 + \alpha_6) & -2\alpha_4 & -2\alpha_6 & 0 & 0 & 0 \\ -2\alpha_4 & 2(\alpha_4 + \alpha_5) & -2\alpha_5 & 0 & 0 & 0 \\ -2\alpha_6 & -2\alpha_5 & 2(\alpha_6 + \alpha_5) & 0 & 0 & 0 \\ 0 & 0 & 0 & 6\alpha_7 & 0 & 0 \\ 0 & 0 & 0 & 0 & 6\alpha_8 & 0 \\ 0 & 0 & 0 & 0 & 0 & 6\alpha_9 \end{bmatrix}, \quad (8.3)$$

$$\mathbf{q}^T = (\alpha_1, \alpha_2, \alpha_3, 0, 0, 0), \quad (8.4)$$

and the stress tensor  $\boldsymbol{\sigma}$ ,

$$\boldsymbol{\sigma}^T = (\sigma_{11}, \sigma_{22}, \sigma_{33}, \sigma_{12}, \sigma_{23}, \sigma_{31}). \quad (8.5)$$

The softening of the model is represented by the softening parameter  $\bar{\sigma}$ , while the parameters  $\alpha_i$  depend on the yield values of the material according to

$$\begin{aligned} \alpha_1 &= \bar{\sigma}_0^2 \left[ \frac{\bar{\sigma}_{11}^c - \bar{\sigma}_{11}^t}{\bar{\sigma}_{11}^c \bar{\sigma}_{11}^t} \right]; & \alpha_4 &= \frac{\bar{\sigma}_0^2}{2} \left[ \frac{1}{\bar{\sigma}_{11}^c \bar{\sigma}_{11}^t} + \frac{1}{\bar{\sigma}_{22}^c \bar{\sigma}_{22}^t} - \frac{1}{\bar{\sigma}_{33}^c \bar{\sigma}_{33}^t} \right]; \\ \alpha_2 &= \bar{\sigma}_0^2 \left[ \frac{\bar{\sigma}_{22}^c - \bar{\sigma}_{22}^t}{\bar{\sigma}_{22}^c \bar{\sigma}_{22}^t} \right]; & \alpha_5 &= \frac{\bar{\sigma}_0^2}{2} \left[ \frac{1}{\bar{\sigma}_{22}^c \bar{\sigma}_{22}^t} + \frac{1}{\bar{\sigma}_{33}^c \bar{\sigma}_{33}^t} - \frac{1}{\bar{\sigma}_{11}^c \bar{\sigma}_{11}^t} \right]; \\ \alpha_3 &= \bar{\sigma}_0^2 \left[ \frac{\bar{\sigma}_{33}^c - \bar{\sigma}_{33}^t}{\bar{\sigma}_{33}^c \bar{\sigma}_{33}^t} \right]; & \alpha_6 &= \frac{\bar{\sigma}_0^2}{2} \left[ \frac{1}{\bar{\sigma}_{33}^c \bar{\sigma}_{33}^t} + \frac{1}{\bar{\sigma}_{11}^c \bar{\sigma}_{11}^t} - \frac{1}{\bar{\sigma}_{22}^c \bar{\sigma}_{22}^t} \right]; \\ \alpha_7 &= \frac{\bar{\sigma}_0^2}{3\bar{\sigma}_{12}^2}; & \alpha_8 &= \frac{\bar{\sigma}_0^2}{3\bar{\sigma}_{23}^2}; & \alpha_9 &= \frac{\bar{\sigma}_0^2}{3\bar{\sigma}_{13}^2}. \end{aligned} \quad (8.6)$$

The parameters  $\bar{\sigma}_{ii}^t$ ,  $\bar{\sigma}_{ii}^c$ , and  $\bar{\sigma}_{ij}$  are the yield values in tension, compression and shear respectively, which in case of hardening do not remain constant but depend on the hardening parameter. The strain hardening models for unidirectional glass-fibre epoxy have been derived from the experimental test results of Section 3.3.2 together with the relation between  $\kappa$  and both  $\gamma_{22}$  and  $\gamma_{12}$ . Simulations of a test with loading perpendicular to the fibres and a simple shear test at room temperature and at 80°C, depicted in Figures 8.2 and 8.3, are used to obtain a (linear) calibration between  $\kappa$  and both  $\gamma_{22}$  and  $\gamma_{12}$  at  $\kappa_0 = 0.045$ . The resulting hardening models as a function of  $\kappa$  are given in Table 8.1. Since the UD glass-fibre epoxy is transversely isotropic  $\bar{\sigma}_{33t} = \bar{\sigma}_{22t}$  and  $\bar{\sigma}_{23} = \bar{\sigma}_{13} = \bar{\sigma}_{12}$ , and further the values in compression are taken similar as in tension. In case there is no strain hardening, than the parameter  $\bar{\sigma}_0 = \bar{\sigma} = \bar{\sigma}_{11}^t$  in Eq. 8.6.

To obtain the equivalent strain of the damage formulation, the yield function is rewritten with the help of Hooke's law into a strain-based formulation. The stiffness can be reduced due to the presence of damage, and therefore a tensor  $\mathbf{D}^\omega$  is used which will be further detailed in Section 8.2.2. The damage loading function in terms of the equivalent strain is thus

$$f(\tilde{\gamma}, \kappa) = \frac{1}{D_{11}} \sqrt{1/2 \boldsymbol{\gamma}^T \mathbf{D}^{\omega T} \mathbf{P} \mathbf{D}^\omega \boldsymbol{\gamma} + \boldsymbol{\gamma}^T \mathbf{D}^{\omega T} \mathbf{q}} - \kappa. \quad (8.7)$$

The tensor  $\mathbf{P}$  and the vector  $\mathbf{q}$  are the same as in the plasticity formulation, except for the softening parameter  $\bar{\sigma}_0$  which is substituted by the equivalent strain threshold  $\kappa_0$ .

Property	Values in different ranges of $\kappa$ [MPa]			
	at room temperature		at 80°C	
$\bar{\sigma}_{11t} =$ $\bar{\sigma}_{11c} = \bar{\sigma}_{11t}$	2277.0		1984.5	
$\bar{\sigma}_{22t} =$ $\bar{\sigma}_{22c} = \bar{\sigma}_{22t}$ $\bar{\sigma}_{33t} = \bar{\sigma}_{22t}$ $\bar{\sigma}_{33c} = \bar{\sigma}_{22t}$	$\kappa < 0.045$ 15.94	$\kappa \geq 0.045$ $-1.372 \cdot 10^3 \kappa^2 + 4.311 \cdot 10^2 \kappa$	$\kappa < 0.045$ 1.0	$\kappa \geq 0.045$ $-1.010 \cdot 10^3 \kappa^2 + 1.253 \cdot 10^2 \kappa$
$\bar{\sigma}_{12} =$  $\bar{\sigma}_{23} = \bar{\sigma}_{12}$ $\bar{\sigma}_{13} = \bar{\sigma}_{12}$	$\kappa < 0.045$ 15.94	$\kappa \geq 0.045$ $-8.183 \cdot 10^3 \kappa^6 + 1.974 \cdot 10^4 \kappa^5$ $-1.920 \cdot 10^4 \kappa^4 + 9.678 \cdot 10^3 \kappa^3$ $-2.705 \cdot 10^3 \kappa^2 + 4.190 \cdot 10^2 \kappa$	$\kappa < 0.045$ 1.0	$\kappa \geq 0.045$ $3.894 \cdot 10^4 \kappa^3 - 3.951 \cdot 10^3 \kappa^2$ $+1.860 \cdot 10^2 \kappa$

Table 8.1: The modelled strain hardening curves for unidirectional glass-fibre epoxy at room temperature and at 80°C based on the experimental test results of Section 3.3.2.

The damage loading function determines if damage growth will occur, as mentioned in Section 5.5.4. If so, the damage parameters are updated via a damage growth law and the constitutive relation between the stress and strain is affected. Beside this, the damage surface is also expanded similar to the strain hardening concept in the plasticity model.

The experimental curves of the UD glass-fibre epoxy tested in transverse direction at room temperature and 80°C, depicted in Figure 8.2, show instantaneous failure and corresponding drop in stress after the ultimate stress is reached. However, from a numerical point of view it is better to avoid a discontinuity in the material model, since it can lead to numerical instability in the calculation process. Therefore, after the ultimate stress is reached in the strain hardening branch a consecutive softening branch is introduced in the numerical damage model. The equivalent strain measure of Eq. 8.7, as given by (Schipperen 2001a), is modified as follows to ascertain a monotonically increasing  $\kappa$ :

$$\kappa = \int \dot{\kappa} dt, \quad (8.8)$$

where

$$f(\dot{\gamma}, \dot{\kappa}) = \frac{1}{D_{11}} \sqrt{1/2 \dot{\gamma}^T \mathbf{D}^T \mathbf{P} \mathbf{D} \dot{\gamma} + \dot{\gamma}^T \mathbf{D}^T \mathbf{q}} - \dot{\kappa}. \quad (8.9)$$

### 8.2.2 The effect of damage on the stiffness matrix

The constitutive relation between the stress and strain for an orthotropic damage model was given in Section 5.5.4 as  $\boldsymbol{\sigma} = (\mathbf{I} - \boldsymbol{\Omega})\mathbf{D}\boldsymbol{\gamma}$ . However, this formulation can cause an undesirable influence of the damage parameter in one direction on the other directions through the off-diagonal terms in the elastic stiffness matrix. To avoid this effect, the damage parameters are directly implemented into the stiffness matrix, which yields

$$\mathbf{D}^\omega = \begin{bmatrix} (1 - \omega_f)D_{11} & (1 - \omega)D_{12} & (1 - \alpha\omega)D_{13} & 0 & 0 & 0 \\ (1 - \omega)D_{12} & (1 - \omega)D_{22} & (1 - \omega)D_{23} & 0 & 0 & 0 \\ (1 - \alpha\omega)D_{13} & (1 - \omega)D_{23} & D_{33} & 0 & 0 & 0 \\ 0 & 0 & 0 & (1 - \alpha\omega)D_{44} & 0 & 0 \\ 0 & 0 & 0 & 0 & (1 - \alpha\omega)D_{55} & 0 \\ 0 & 0 & 0 & 0 & 0 & D_{66} \end{bmatrix} \quad (8.10)$$

Matrix cracking in the unidirectional glass-fibre epoxy layer is covered in the model by the damage parameter  $\omega$ . The factor  $\alpha$  determines the degree of damage of the less influenced directions with respect to the damage parameter. The stiffness in fibre direction  $D_{11}$  is not affected by the matrix cracking and has its own damage parameter  $\omega_f$ . Nonlinearities in fibre direction could be taken into account with this parameter, though (since the glass-fibre epoxy behaves linearly elastic in this direction) it will be used here to include ultimate fibre failure.

### 8.2.3 The damage growth laws

The damage parameters are controlled in general by a damage growth law which depends on the damage-history parameter  $\kappa$  (that equals the equivalent strain in case of damage growth). For matrix cracking an exponentially decaying law is chosen, given by

$$\omega = 1 - e^{-\xi(\kappa - \kappa_0)^2}, \quad (8.11)$$

where  $\kappa_0$  is the damage threshold and  $\xi$  is the damage growth rate. Since matrix cracking affects the stiffness in more directions it is important to choose the damage growth law such that the material behaviour in all loading directions is correctly predicted.

The experimental test results at room temperature and 80°C, for the tests loaded perpendicular to the fibres and in shear as listed in Section 3.3.2,

are used to calibrate the model. In Table 8.2 the damage growth laws for fibre and matrix damage in unidirectional glass-fibre epoxy are given (with the factor  $\alpha = 0.7$ ). Below the threshold value  $\kappa_0$  the damage parameters  $\omega_f$  and  $\omega$  are zero (or equal to the maximum attained value in a previous loading condition). Beyond the threshold, matrix damage starts to increase according to the given exponential law and finally reaches the value of 1.0. This value is reached beyond the point of ultimate failure and allows for the softening branch in the stress-strain curve. For fibre damage a

Property	Values in different ranges of $\epsilon_{11}$ or $\kappa$ [-]		
	at RT / 80°C	at room temperature	at 80°C
$\omega_f =$	$\epsilon_{11} < 0.045$	$\epsilon_{11} \geq 0.045$	$\epsilon_{11} \geq 0.045$
	0.0	$0.939 - 0.939 \cdot \exp^{-500 \cdot (\epsilon_{11} - 0.045)}$	$0.99 - 0.99 \cdot \exp^{-500 \cdot (\epsilon_{11} - 0.045)}$
$\omega =$	$\kappa < 0.045$	$\kappa \geq 0.045$	$\kappa \geq 0.045$
	0.0	$1 - \exp^{-300.0 \cdot (\kappa - 0.045)^2}$	$1 - \exp^{-300.0 \cdot (\kappa - 0.045)^2}$

Table 8.2: The damage growth laws for fibre and matrix damage in unidirectional glass-fibre epoxy at room temperature and 80°C based on the experimental test results of Section 3.3.2.

maximum strain criterion is used for the strain in fibre direction. Beyond this point of ultimate fibre failure an exponentially decaying function is chosen to avoid numerical instabilities.

### 8.3 The tangent stiffness matrix with damage

In the general outline of the damage model as described in Section 5.5.4 the stress is evaluated from the given strain. For an efficient computational procedure, the tangent stiffness matrix can be derived by a consistent linearisation of the stress-strain relation. The derivative of the chosen exponential damage growth law of Eq. 8.11 is given by

$$\dot{\omega} = 2\xi(\kappa - \kappa_0)e^{-\xi(\kappa - \kappa_0)^2} \dot{\kappa}, \quad (8.12)$$

where the derivative of  $\kappa$  has components in all strain directions, and is written as

$$\dot{\kappa} = \frac{\partial \kappa}{\partial \gamma} \dot{\gamma} = \frac{1}{2\kappa D_{11}} (D_{ji}^\omega P_{jk} D_{kl}^\omega \gamma_l + D_{ji}^\omega q_j) \dot{\gamma}_{ii}. \quad (8.13)$$

The total derivation of the first row of the tangent stiffness matrix can be determined from the stress-strain relation in this direction, as can also be



found in (Schipperen 2001a):

$$\sigma_1 = (1 - \omega_f)D_{11}\gamma_{11} + (1 - \omega)D_{12}\gamma_{22} + (1 - \alpha\omega)D_{13}\gamma_{33}, \quad (8.14)$$

$$\begin{aligned} \dot{\sigma}_1 &= (1 - \omega_f)D_{11}\dot{\gamma}_{11} + (1 - \omega)D_{12}\dot{\gamma}_{22} - \dot{\omega}D_{12}\gamma_{22} + (1 - \alpha\omega)D_{13}\dot{\gamma}_{33} \\ &\quad - \alpha\dot{\omega}D_{13}\gamma_{33}, \end{aligned} \quad (8.15)$$

Thus, the terms of the tangent stiffness matrix read:

$$D_{11t}^\omega = \frac{\partial \dot{\sigma}_1}{\dot{\gamma}_{11}} = (1 - \omega_f)D_{11} - b_{11}^*D_{12}\gamma_{22} - \alpha b_{11}^*D_{13}\gamma_{33}, \quad (8.16a)$$

$$D_{12t}^\omega = \frac{\partial \dot{\sigma}_1}{\dot{\gamma}_{22}} = (1 - \omega)D_{12} - b_{22}^*D_{12}\gamma_{22} - \alpha b_{22}^*D_{13}\gamma_{33}, \quad (8.16b)$$

$$D_{13t}^\omega = \frac{\partial \dot{\sigma}_1}{\dot{\gamma}_{33}} = (1 - \alpha\omega)D_{13} - b_{33}^*D_{12}\gamma_{22} - \alpha b_{33}^*D_{13}\gamma_{33}, \quad (8.16c)$$

$$D_{14t}^\omega = \frac{\partial \dot{\sigma}_1}{\dot{\gamma}_{12}} = -b_{12}^*D_{12}\gamma_{22} - \alpha b_{12}^*D_{13}\gamma_{33}, \quad (8.16d)$$

$$D_{15t}^\omega = \frac{\partial \dot{\sigma}_1}{\dot{\gamma}_{23}} = -b_{23}^*D_{12}\gamma_{22} - \alpha b_{23}^*D_{13}\gamma_{33}, \quad (8.16e)$$

$$D_{16t}^\omega = \frac{\partial \dot{\sigma}_1}{\dot{\gamma}_{31}} = -b_{31}^*D_{12}\gamma_{22} - \alpha b_{31}^*D_{13}\gamma_{33}, \quad (8.16f)$$

where the following abbreviation has been used for ease of formulation:

$$b_{ii}^* = 2\xi(\kappa - \kappa_0)e^{-\xi(\kappa - \kappa_0)^2} \left( \frac{1}{2\kappa D_{11}} (D_{ji}^\omega P_{jk} D_{kl}^\omega \gamma_l + D_{ji}^\omega q_j) \right) \dot{\gamma}_{ii}. \quad (8.17)$$

The other terms of the tangent stiffness matrix have been derived in a similar manner, the resulting formulation is given below:

$$D_{21t}^\omega = (1 - \omega)D_{12} - b_{11}^*D_{12}\gamma_{11} - b_{11}^*D_{22}\gamma_{22} - b_{11}^*D_{23}\gamma_{33}, \quad (8.18a)$$

$$D_{22t}^\omega = (1 - \omega)D_{22} - b_{22}^*D_{12}\gamma_{11} - b_{22}^*D_{22}\gamma_{22} - b_{22}^*D_{23}\gamma_{33}, \quad (8.18b)$$

$$D_{23t}^\omega = (1 - \omega)D_{23} - b_{33}^*D_{12}\gamma_{11} - b_{33}^*D_{22}\gamma_{22} - b_{33}^*D_{23}\gamma_{33}, \quad (8.18c)$$

$$D_{24t}^\omega = -b_{12}^*D_{12}\gamma_{11} - b_{12}^*D_{22}\gamma_{22} - b_{12}^*D_{23}\gamma_{33}, \quad (8.18d)$$

$$D_{25t}^\omega = -b_{23}^*D_{12}\gamma_{11} - b_{23}^*D_{22}\gamma_{22} - b_{23}^*D_{23}\gamma_{33}, \quad (8.18e)$$

$$D_{26t}^\omega = -b_{31}^*D_{12}\gamma_{11} - b_{31}^*D_{22}\gamma_{22} - b_{31}^*D_{23}\gamma_{33}, \quad (8.18f)$$

$$D_{31t}^\omega = (1 - \alpha\omega)D_{13} - \alpha b_{11}^*D_{13}\gamma_{11} - b_{11}^*D_{23}\gamma_{22}, \quad (8.19a)$$

$$D_{32t}^\omega = (1 - \omega)D_{23} - \alpha b_{22}^*D_{13}\gamma_{11} - b_{22}^*D_{23}\gamma_{22}, \quad (8.19b)$$

$$D_{33t}^\omega = D_{33} - \alpha b_{33}^*D_{13}\gamma_{11} - b_{33}^*D_{23}\gamma_{22}, \quad (8.19c)$$

$$D_{34t}^\omega = -\alpha b_{12}^*D_{13}\gamma_{11} - b_{12}^*D_{23}\gamma_{22}, \quad (8.19d)$$

$$D_{35t}^\omega = -\alpha b_{23}^*D_{13}\gamma_{11} - b_{23}^*D_{23}\gamma_{22}, \quad (8.19e)$$

$$D_{36t}^\omega = -\alpha b_{31}^*D_{13}\gamma_{11} - b_{31}^*D_{23}\gamma_{22}, \quad (8.19f)$$

$$D_{4it}^\omega = -\alpha b_{ii}^* D_{44} \gamma_{12} \quad \text{for } i = 1, 2, 3, \quad (8.20a)$$

$$D_{44t}^\omega = D_{44} - \alpha b_{12}^* D_{44} \gamma_{12}, \quad (8.20b)$$

$$D_{45t}^\omega = -\alpha b_{23}^* D_{44} \gamma_{12}, \quad (8.20c)$$

$$D_{46t}^\omega = -\alpha b_{31}^* D_{44} \gamma_{12}, \quad (8.20d)$$

$$D_{5it}^\omega = -\alpha b_{ii}^* D_{55} \gamma_{23} \quad \text{for } i = 1, 2, 3, \quad (8.21a)$$

$$D_{54t}^\omega = -\alpha b_{12}^* D_{55} \gamma_{23}, \quad (8.21b)$$

$$D_{55t}^\omega = D_{55} - \alpha b_{23}^* D_{55} \gamma_{23}, \quad (8.21c)$$

$$D_{56t}^\omega = -\alpha b_{31}^* D_{55} \gamma_{23}, \quad (8.21d)$$

$$D_{6it}^\omega = 0 \quad \text{for } i = 1, 2, 3, 4, 5, \quad (8.22a)$$

$$D_{66t}^\omega = D_{66}. \quad (8.22b)$$

It should be noted that the tangent stiffness matrix is non-symmetric in this case.

## 8.4 Simulated and experimental stress-strain curves

In the previous sections the damage model has been described and calibrated with the experimental data at room temperature and 80°C. The simulated and experimental stress-strain curves are given in this section to indicate the accuracy of the calibration.

### Fibre damage

In Figure 8.1 the simulated and experimental tensile stress-strain curve in fibre direction are shown for unidirectional glass-fibre epoxy at room temperature and 80°C. The overview of the experimental test results for the Glare constituents can be found in Chapter 3 and further details are mentioned by (Hagenbeek 2004b).

It should be noted that the experimental curve is a modelled average curve from a number of individual tests and the fibre failure is indicated as a sudden and instantaneous drop to a zero stress level. The aim in the damage model is to capture the behaviour up to failure and to avoid numerical instabilities afterwards, rather than to give an exact description of the failure behaviour (which shows variation over the individual tests). The exponential decaying law defined in 8.2.3 to avoid the numerical instabilities after fibre failure can be clearly observed in Figure 8.1. The

simulation is performed with a single (eight-noded) element, which is restrained on one end and with a prescribed displacement on the other end (in fibre direction).

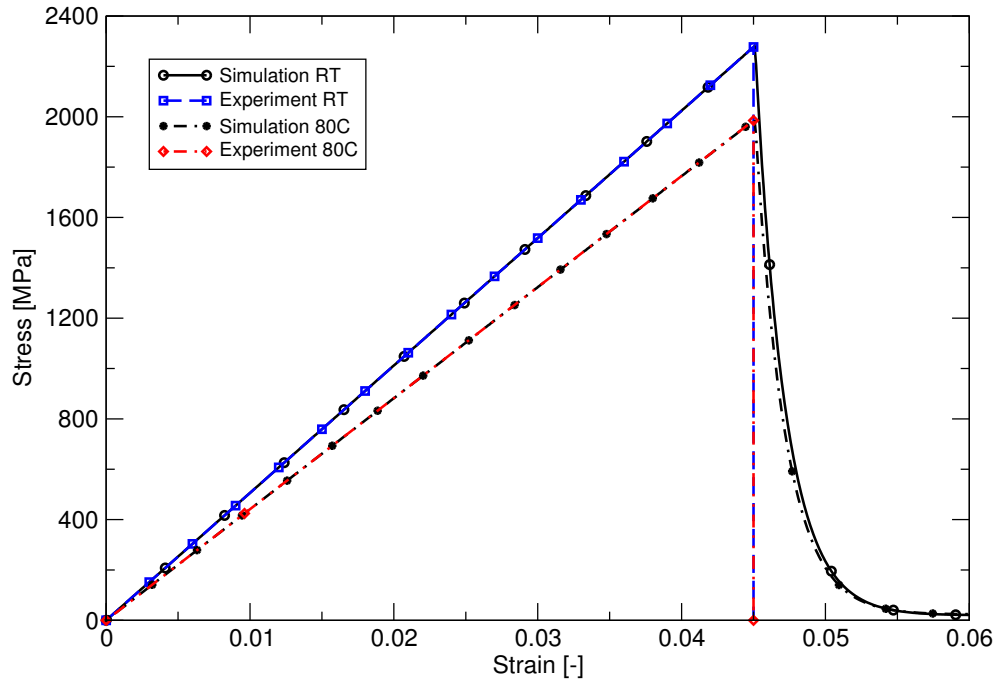


Figure 8.1: The simulated and experimental tensile stress-strain curve in fibre direction for unidirectional glass-fibre epoxy at room temperature and 80°C.

### Matrix damage

Figure 8.2 gives the simulated and experimental tensile stress-strain curve perpendicular to the fibre direction for UD glass-fibre epoxy at room temperature and 80°C. As described for the fibre failure above, the failure is indicated as a sudden and instantaneous drop to a zero stress level. In this case numerical instabilities are avoided by introducing a softening branch, as mentioned in Section 8.2.3. A faster softening of the material would probably better describe the physics, but is difficult to obtain with the current model. The difficulty is related to the large difference in stiffness and failure strain between the glass-fibres and the epoxy matrix (compare, e.g., the scales in Figures 8.1 and 8.2). The rate  $\dot{\kappa}$  decreases due to a decreasing stiffness and counteracts the damage growth. The simulation is performed

with a single (eight-noded) element, which is restrained on one end and with a prescribed displacement on the other end (in transverse direction).

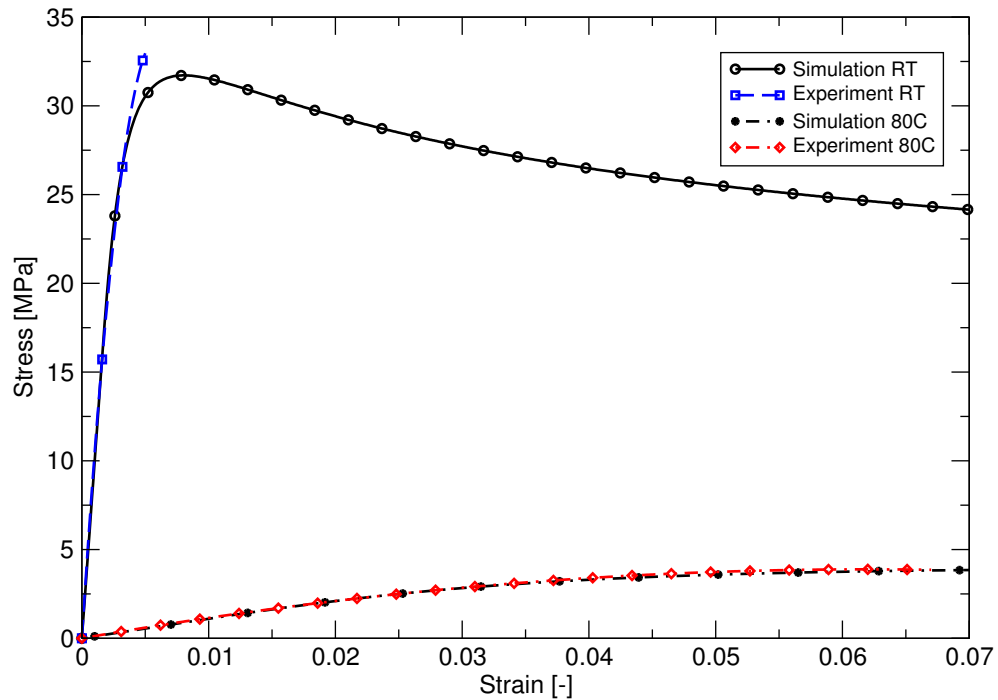


Figure 8.2: The simulated and experimental tensile stress-strain curve perpendicular to the fibre direction for unidirectional glass-fibre epoxy at room temperature and 80°C.

In Figure 8.3 the simulated and experimental shear stress-strain curve (loaded in fibre direction) are shown for UD glass-fibre epoxy at room temperature and 80°C. At room temperature, the simulation agrees fairly well with the experimental curve up to 2% strain, then starts to deviate more considerably. The simulation in this case is a simple shear test, performed with a single (eight-noded) element. In transverse direction all nodes are restrained, in fibre direction one side is restrained and the other side has a prescribed displacement.

The damage model is thus able to capture the UD glass-fibre epoxy behaviour at room temperature and 80°C and in the different directions with reasonable accuracy. In the next section, a number of benchmark tests will be performed to demonstrate the behaviour of the damage model for composite and Glare laminates.

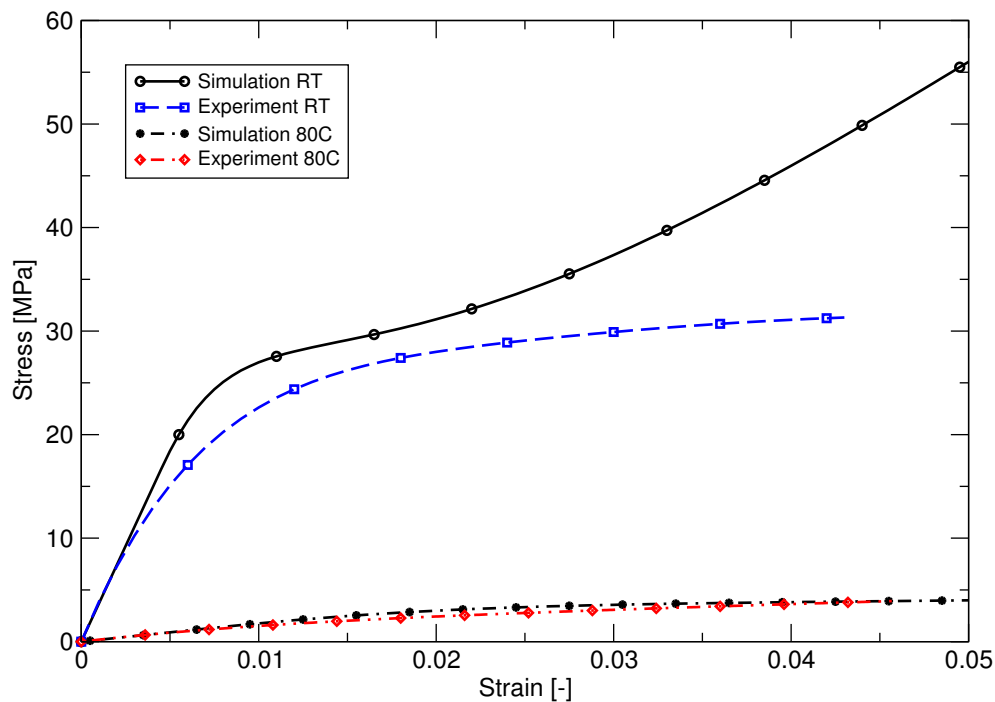


Figure 8.3: The simulated and experimental shear stress-strain curve for unidirectional glass-fibre epoxy at room temperature and 80°C.

## 8.5 Benchmark tests

### 8.5.1 Off-axis tests on 0/90 cross-ply glass-fibre epoxy

A first benchmark test to demonstrate the performance of the damage model is the simulation of a 0/90 composite with tensile loadings under different off-axis angles. The test specimens mentioned in Section 3.4 have a length of 150 mm (without the clamped area) and a width of 25 mm, see (Hagenbeek 2004a). In the numerical model, 150 elements are used and one end is restrained in the loading direction and the other end is unrestrained in both the loading and perpendicular to the loading direction, as shown in Figure 8.4. The off-axis angles are 0, 7.5, 15, 22.5, and 45°.

The simulated and experimental tensile stress-strain curves are shown in Figure 8.5. From this figure it can be seen that up to 1% strain all simulations closely match the experimental results. Beyond this strain the simulation for 0 and 45° off-axis angle still show a good agreement with the experimental curves, but the simulations for 7.5, 15, 22.5° start to deviate from the experimentally found curves.

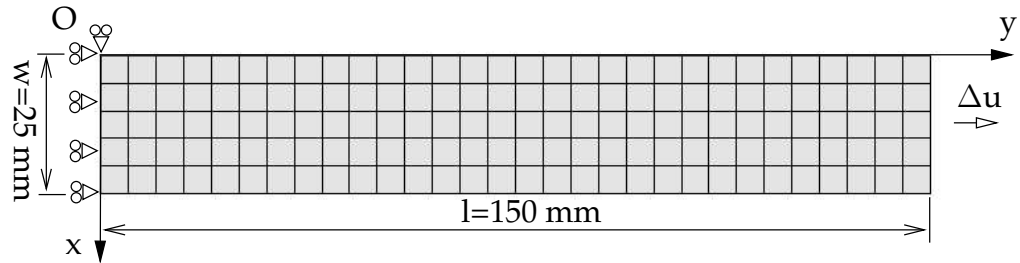


Figure 8.4: Finite element mesh for the simulation of the 0/90 composite test specimen which is tested for several off-axis angles.

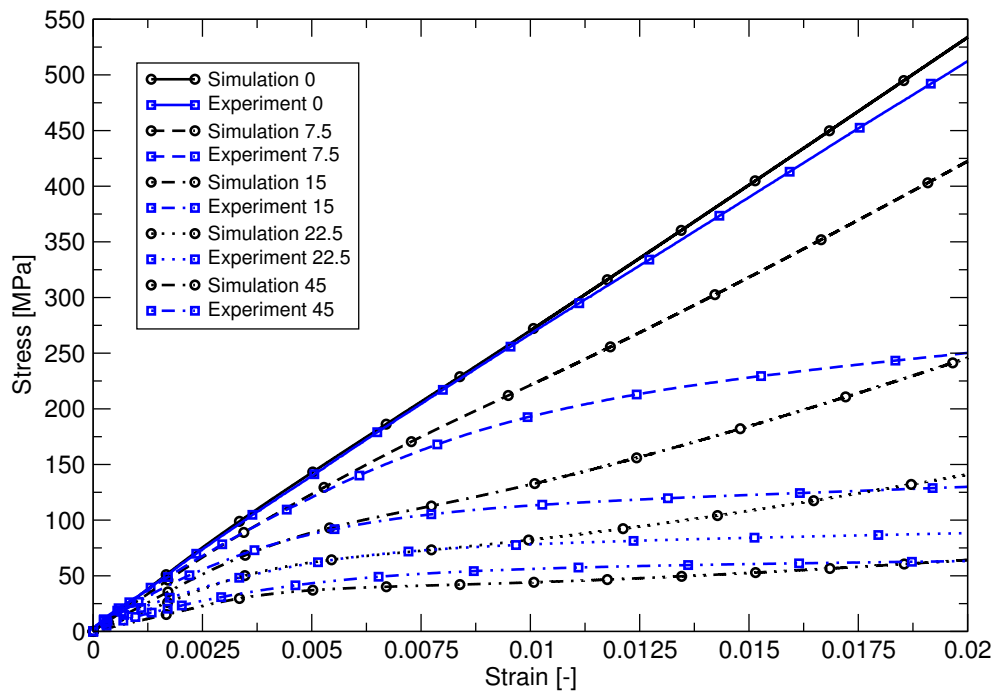


Figure 8.5: The simulated and experimental tensile stress-strain curves for a 0/90 glass-fibre epoxy composite tested with 0, 7.5, 15, 22.5, and 45° off-axis angle.

The absence of a further stiffness reduction after 1% can be explained by the implementation of the UD glass-fibre epoxy in the damage model, as given in Section 8.4. However, in the experimental tests the layers might already show damage due to fibre shearing (which is not covered in the model). This phenomenon becomes visible in the test specimens at larger strains.

### 8.5.2 Tensile tests on standard Glare laminates

In the second benchmark test the simulated and experimental tensile stress-strain curves are compared for three different Glare grades with an equal number and thickness of aluminium layers: viz. Glare2-3/2-0.3, Glare3-3/2-0.3, and Glare4-3/2-0.3. The differences between the simulation of each Glare grade can thus directly be related to the glass-fibre prepreg lay-up in between the aluminium layers.

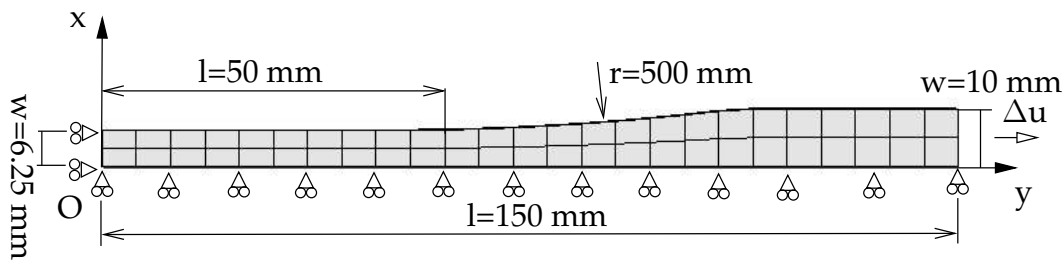


Figure 8.6: Finite element mesh of the tensile test specimen (quarter model).

For the aluminium layers, the hardening model presented in Chapter 7 is taken. The stress-strain curves for each Glare grade are considered in the longitudinal (L) direction and the longitudinal transverse (LT) direction. The simulations are performed at room temperature, for which experimental stress-strain curves from the literature are available, and at 80°C, which are used to indicate the change in stress-strain behaviour of the specific laminates.

On the Glare2-3/2-0.3 in longitudinal transverse (LT) direction a small mesh-refinement study has been carried out with meshes of 2x25, 4x50, 4x100, and 8x200 elements. A limited mesh-dependency has been found, only the first step in the refinement gives some minor difference, as shown in Figure 8.7. The major source of mesh-dependency is localisation, which can for example be dealt with by a gradient method, see (de Borst and

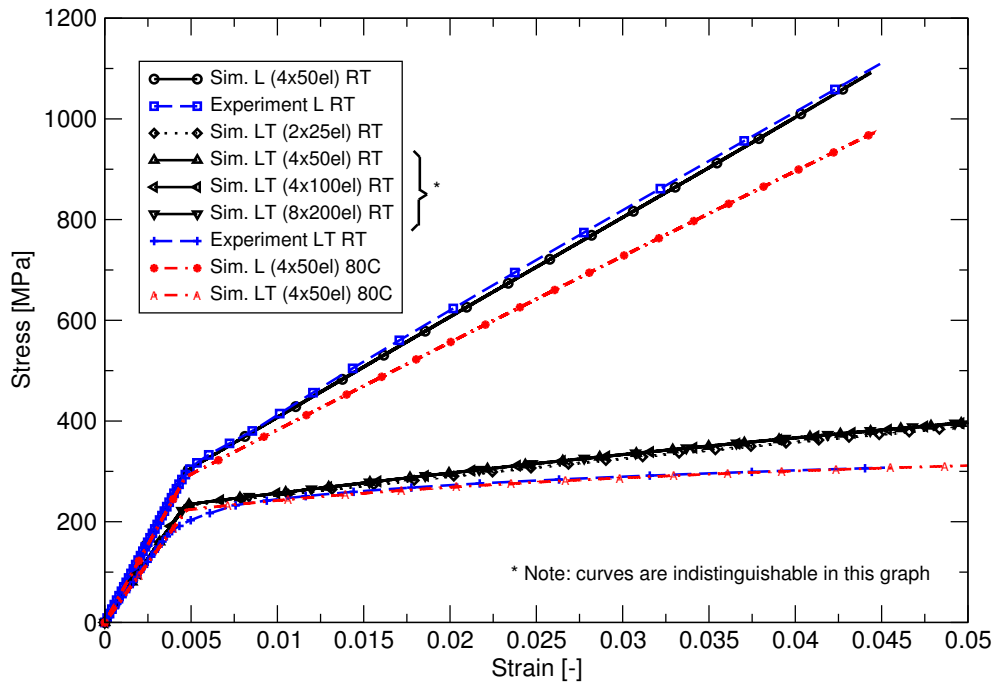


Figure 8.7: The simulated and experimental tensile stress-strain curve for Glare2-3/2-0.3 in L and LT direction.

Muhlhaus 1992) for plasticity and (Peerlings, de Borst, Brekelmans, and de Vree 1996) in case of damage. A quarter model of the tensile test specimen with 200 (4x50) eight-noded elements, as depicted in Figure 8.6, is therefore used to perform the rest of the simulations.

From Figure 8.7 it can be seen that for Glare2-3/2-0.3 the agreement between the simulated and experimental tensile stress-strain curve in the longitudinal (L) direction (at room temperature) is excellent. Up to 2% strain, the behaviour in longitudinal transverse (LT) direction is captured accurately as well.

In the hardening model a distinct transition at the yield point has been chosen in order to obtain an accurate fit of the whole aluminium 2024-T3 stress-strain curve. For this reason and due to the fact that we have an isotropic hardening model, the initial yield region in LT direction is not captured. Beyond the 2% strain, the contribution of the glass-fibre epoxy matrix is still present and can explain the deviation between simulation and experiment.

For Glare3-3/2-0.3 the agreement between the simulated and experimental tensile stress-strain curve (at room temperature) is very good as



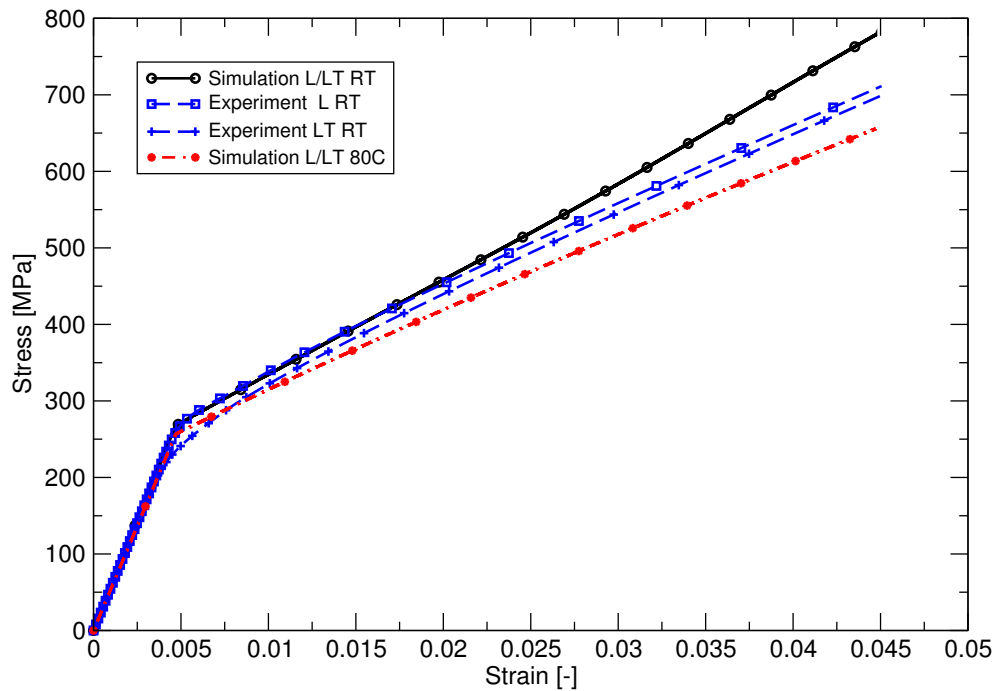


Figure 8.8: The simulated and experimental tensile stress-strain curve for Glare3-3/2-0.3 in L and LT direction.

well. In the simulation the L and the LT direction are identical. Again the aluminium yield behaviour in LT direction is not captured by the isotropic hardening model and beyond 2% strain the deviation between simulation and experiment increases to about 12.5% at the ultimate strain.

Similar results as for Glare3-3/2-0.3 are found for Glare4-3/2-0.3. In L direction the deviation between the ultimate stress in the simulation and the experimental test is 7.0%, which is less than found for Glare3-3/2-0.3, and in LT direction the deviation is larger, namely 14.5%. These results confirm the fact that the deviation beyond 2% strain is caused by the contribution of the glass-fibre epoxy matrix that is still largely intact.

As indicated by all figures, the damage and hardening model are able to capture the behaviour (at room temperature) of the three given Glare grades very accurately, especially up to 2% strain. It should be noted that no additional tuning (beside the glass-fibre epoxy and aluminium description) of the model has been performed, which confirms the accuracy of the gathered input data.

In the next section the tensile stress-strain curves of a special Glare laminate tested under various off-axis angles are considered. In this laminate

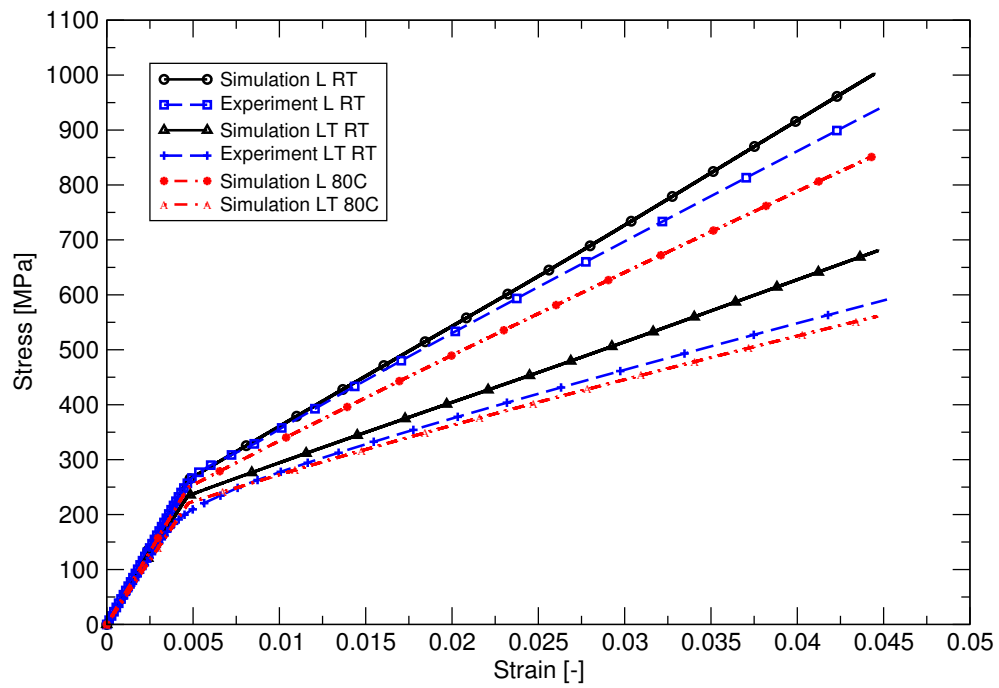


Figure 8.9: The simulated and experimental tensile stress-strain curve for Glare4-3/2-0.3 in L and LT direction.

glass-fibre epoxy layers in  $+45$  and  $-45^\circ$  direction, so called doublers, are added to a Glare3 baseline laminate.

### 8.5.3 Tensile tests on special Glare laminates

In Section 4.2 the tensile test results on a special Glare laminate are shown, as given by (Hagenbeek 2002b). In the same reference the tensile stress-strain curves are found for 0, 45, 67.5, and 90° off-axis angle, which are compared in this section with simulations at room temperature and 80°C. As mentioned in Section 4.2, the special laminate has a Glare3 baseline laminate and in addition doublers with fibre layers in +45 and -45° direction. In this case a full model of the tensile test specimen with 1600 (8x200) eight-noded elements, as depicted in Figure 8.10, is used to perform the simulation. In the simulation, a prescribed displacement is used, which rules out any secondary bending of the asymmetric lay-up.

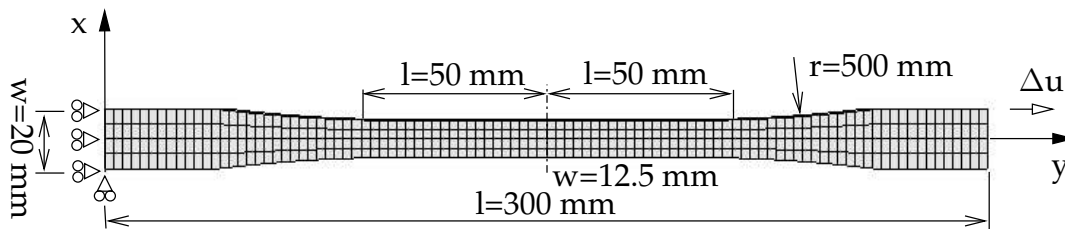


Figure 8.10: Finite element mesh of the tensile test specimen (full model).

The agreement between the simulated and experimental tensile stress-strain curve of the special Glare laminate in the L and LT direction is very good at room temperature, especially up to 2% strain, and at 80°C, as can be seen in Figures 8.11 and 8.12. In the simulation there is no difference between the L and LT direction, due to the isotropic aluminium model and the given fibre lay-up. Similar to the results of the simulations for the standard Glare laminates in Section 8.5.2, beyond 2% strain the deviation increases to about 8.5% when the experimental test specimen shows failure. The difference in failure strain between the experiment and the simulation, which shows failure at 4.5%, is most likely due to secondary bending in the experimental test specimen.

In Figure 8.13 the simulated and experimental tensile stress-strain curve are given for the 45 and 67.5° off-axis angle at room temperature and 80°C. The experimental curves with 45 and 67.5° off-axis angle are well captured by the simulations, though again failure is found earlier in the experiment.

The benchmark tests for the special Glare laminate show that the model can capture the behaviour of more complex build-up laminates very well. Similar to the results for the standard Glare laminates beyond 2% strain

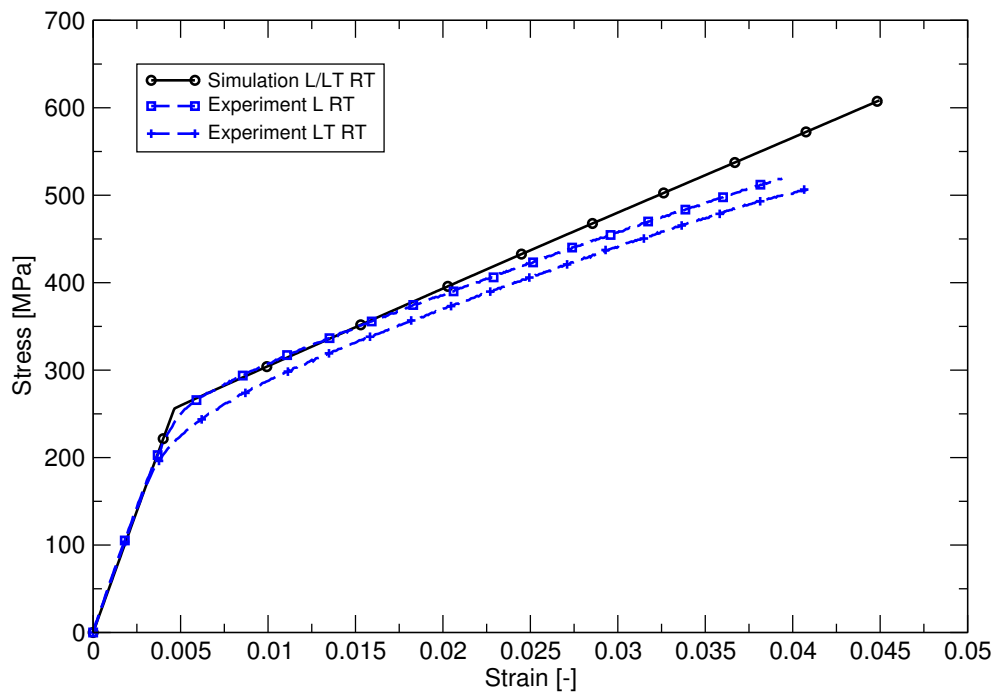


Figure 8.11: The simulated and experimental tensile stress-strain curves of a special Glare laminate in L and LT direction at room temperature.

the deviation between simulation and experiment increases due to the glass-fibre epoxy matrix contribution that is still largely intact and the orthotropy of the aluminium sheet is not covered.

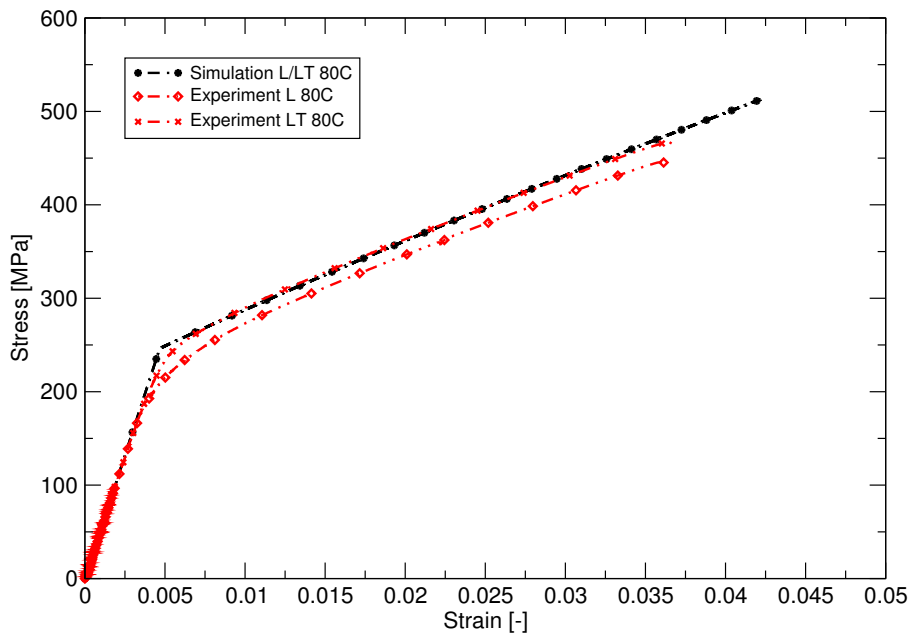


Figure 8.12: The simulated and experimental tensile stress-strain curves of a special Glare laminate in L and LT direction at 80°C.

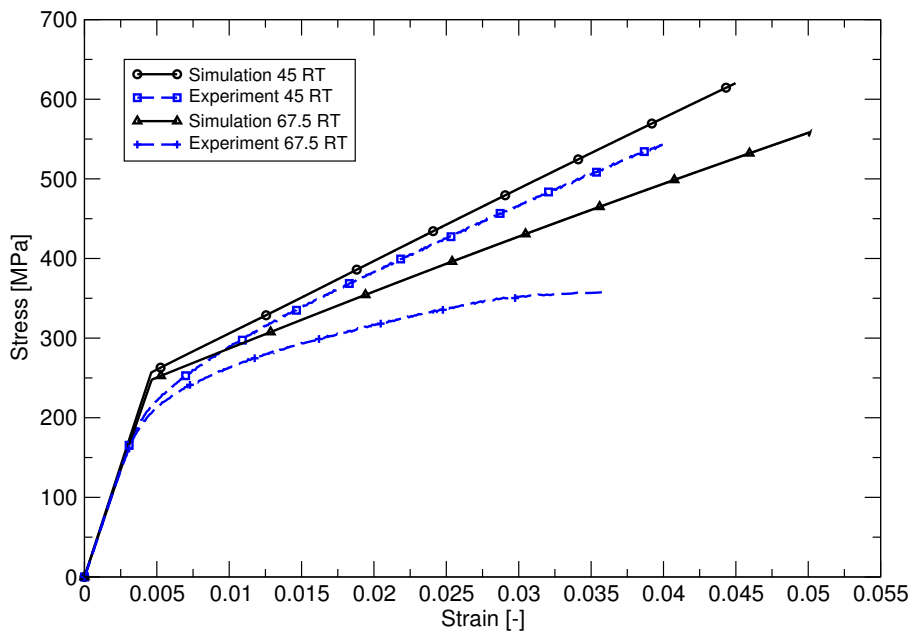


Figure 8.13: The simulated and experimental tensile stress-strain curves of a special Glare laminate for 45 and 67.5° off-axis angle.

## 8.6 Summary

In this chapter the damage model for the UD glass-fibre epoxy behaviour has been described. The model uses the concept of continuum damage mechanics, where a damage variable is used to denote the ratio between the damaged and the undamaged area. For fibre and matrix damage a separate damage parameter is taken. The equivalent strain measure is obtained by rewriting the yield function of the orthotropic Hoffman plasticity model into a strain-based format.

The damage parameters are directly implemented into the stiffness matrix to be able to avoid an undesirable influence of the damage parameter in one direction on the other directions. In the model not only expansion but also shrinkage of the damage surface is allowed by calculating the damage-history parameter  $\kappa$  incrementally. Thus, beside strain hardening also a softening branch can be modelled for the glass-fibre epoxy, which is especially useful to avoid numerical instability.

The experimental data for the UD glass-fibre epoxy at room temperature and 80°C, given in Section 3.3.2, is used to calibrate the damage model. The simulations of the shear and tensile test in transverse direction show a good fit with the experimental curves, though only a slow softening branch could be obtained in transverse direction.

The benchmark tests to simulate the off-axis tensile tests on a 0/90 composite, tensile tests on standard glare, and off-axis tensile tests on special glare laminates (at room temperature and 80°C) with extra fibre layers in -45 and 45° direction, show a very good agreement with the experimental results. The slow softening branch found in transverse direction for the UD glass-fibre epoxy can explain the deviation at room temperature between the simulated and experimental stress-strain curves at larger strains (beyond 2% for the Glare tests). However, the ultimate strengths found in the Glare simulations are never more than 15% off from the experimental values.

# Chapter 9

## The transient model

In this chapter the transient model, described in general in Chapter 5, is further detailed. This model allows us to investigate the response of the structure in time due to dynamic thermo-mechanical loadings. A transient analysis can for example be performed to determine the rate at which the aircraft skin is heated up due to an external heat source, or to study mechanical vibrations due to an impact.

Two benchmark tests are presented to demonstrate the performance of the thermo-mechanical solid-like shell element and the transient solver. In the first test a vibration due to a mechanical, thermal and combined thermo-mechanical loading is considered to validate the element. In the second test the ability of the transient solver is demonstrated for the snap-through of a cylindrical panel subjected to a concentrated load. The resulting deflection is compared with numerical solutions obtained with Park's method for different time steps, and with results for another transient algorithm given by (Kuhl and Ramm 1996).

### 9.1 Introduction

Since temperature can largely affect the properties of especially the glass-fibre epoxy, see Chapter 3, it is important to determine the temperature field that is reached in the structure. This can be done by taking the rate at which heat is stored in the structure into account in the model. This will provide the development of the temperature distribution (also in thickness direction), the stress distribution due to differences in temperature as well as expansion, and the ultimate temperatures or steady state reached within a specific time. The simulations can be used to investigate the thermo-mechanical behaviour of the laminate in time and to found for

example the choice of a worst case temperature used in design.

The mechanical behaviour of the structure can also depend on time, for example due to impact. If the loads are applied rapidly, with respect to the natural frequencies of the system, inertial forces need to be considered; i.e. a truly dynamic problem needs to be solved. Since in actually measured responses of structures it is observed that energy is dissipated during vibration, which in vibration analysis is usually taken into account by introducing velocity-dependent damping forces.

Another reason to perform a transient analysis could be the fact that the material properties are time-dependent. The stiffness, damping or even the mass matrix are dependent on the temperature, since these matrices consist of material properties such as the Young's and shear modulus, and the mass density. In the same way the heat capacity and heat conduction matrix depend on the temperature, and therefore on its turn depend on time before a steady state temperature is reached.

To include the temperature-dependency into the model would mean that we have to determine the derivatives of all the mentioned matrices, such as stiffness, heat capacity, etc. The advantage of doing so is however small, since in general the main interest will lie in the structural behaviour for a given temperature (field) and less in the process in which this is reached. Moreover the effort to implement such temperature-dependency into the model would be very large. Thus, if we are interested in the effect of temperature on the structure, the thermo-mechanical material properties at this temperature will simply be used.

## 9.2 Dynamic system response

In order to calculate the dynamic response of the structure due to thermo-mechanical loadings, Eq. 5.64 has to be solved:

$$\begin{bmatrix} \mathbf{M}_u & \\ & 0 \end{bmatrix} \begin{bmatrix} \ddot{\hat{\mathbf{u}}} \\ \ddot{\hat{\boldsymbol{\theta}}} \end{bmatrix} + \begin{bmatrix} \mathbf{C}_u & \\ & \mathbf{C}_\theta \end{bmatrix} \begin{bmatrix} \dot{\hat{\mathbf{u}}} \\ \dot{\hat{\boldsymbol{\theta}}} \end{bmatrix} + \begin{bmatrix} \mathbf{K}_u & \mathbf{K}_{u\theta} \\ & \mathbf{K}_\theta \end{bmatrix} \begin{bmatrix} \hat{\mathbf{u}} \\ \hat{\boldsymbol{\theta}} \end{bmatrix} = \begin{bmatrix} \mathbf{F} \\ \mathbf{Q} \end{bmatrix}. \quad (9.1)$$

Where through the off-diagonal terms in the stiffness-conductivity matrix  $\mathbf{K}_{u\theta}$  a coupling between the temperature and the displacements due to thermal expansion has been made as described in Section 6.2.4. The solution technique described in Section 5.4.1 for transient analysis, called Park's method, can be used to solve the system of equations. This method has been implemented in the Jem/Jive numerical software, described in Section 5.6. Corresponding to Eq. 9.1 we therefore need to construct the mass and damping matrices for each element, beside the stiffness matrix.



## 9.3 Benchmark tests

In this section two benchmark tests are presented to demonstrate the performance of the thermo-mechanical solid-like shell element and the transient solver. In the first example a single element is subjected to either a heat source, a mechanical loading, or a combination of both. The application of the thermal loading will result in a gradual increase in temperature when a transient analysis is performed where the heat capacity is taken into account. But it will also result in a mechanical vibration induced by the thermal expansion.

In the second example the ability of the transient solver is demonstrated. In this case, the snap-through of a cylindrical panel subjected to a concentrated vertex load is simulated. The resulting deflection is compared with numerical solutions obtained with Park's method at different time steps and with results for the Constraint Energy Momentum Algorithm (CEMA), another transient algorithm, given by (Kuhl and Ramm 1996).

### 9.3.1 Dynamic response to thermo-mechanical loadings

A single eight-noded shell element is respectively subjected to a heat source, a mechanical load and a combination of both loadings. The element is clamped at one end and free to expand at the other end. The numbers in this example are chosen such that the thermally and mechanically induced vibration are of the same order of amplitude and wavelength.

The equally distributed heat source  $Q$  at the right end is equal to 10560 W and the thermal conductivity  $k$  is  $2200 \text{ Wmm}^{-1}\text{K}^{-1}$ . The equally distributed mechanical load  $F$  is 1.0 N. Further more an elastic material with a stiffness  $E$  of  $2.0 \cdot 10^6 \text{ Pa}$  is taken. The Poisson's ratio is assumed to be zero. The dimensions of the element are 1.0 mm for the height  $h$ , the length  $l$ , and the width  $w$ . The thermal expansion coefficient  $\alpha$  is  $1.0 \cdot 10^{-6} \text{ }^\circ\text{C}^{-1}$ .

The relative temperature is set to zero at the clamped side (temperature boundary condition):

$$\theta(0) = 0. \quad (9.2)$$

The steady-state temperature due to the heat source has a linear distribution over the length of the element. The temperature at distance  $x$  can be calculated analytically as:

$$\theta(x) = \frac{Qx}{kA}, \quad (9.3)$$

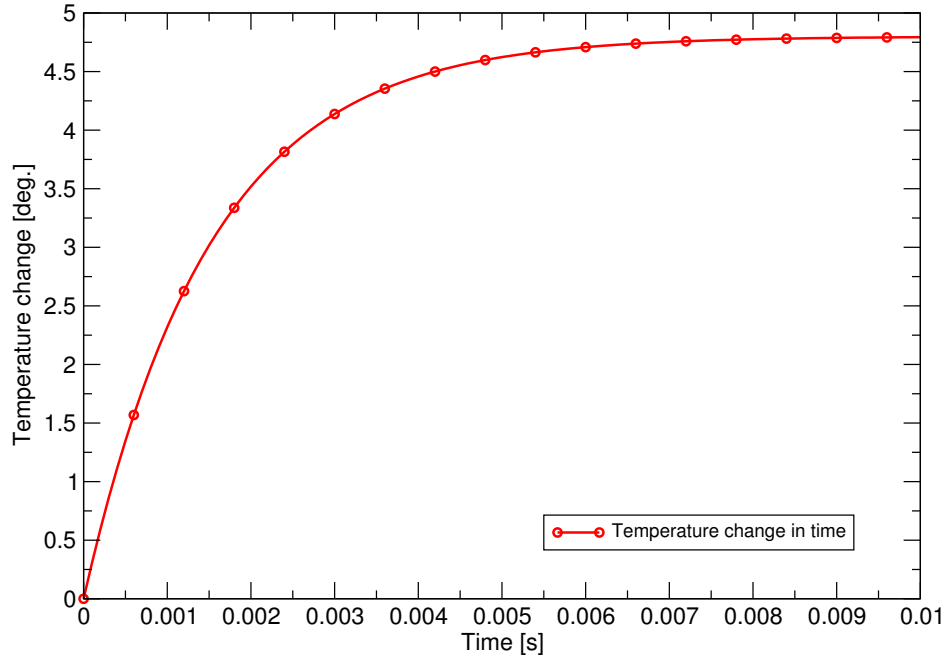


Figure 9.1: The temperature change with respect to time.

where  $Q$  is the heat source,  $k$  is the thermal conductivity and  $A$  is the cross-sectional area. The distributed temperature over the strip causes free expansion at the right end, which can be calculated analytically as

$$\epsilon_{\alpha} = \alpha \int \theta(x) dx, \quad (9.4)$$

and;

$$u_{\alpha} = \epsilon_{\alpha} l, \quad (9.5)$$

where  $\epsilon_{\alpha}$  is the expansion strain,  $\theta$  is the distributed temperature and  $u_{\alpha}$  is the total expansion. At the free edge the following relative steady-state temperature, expansion strain and total expansion are found:

$$\begin{aligned} \theta(l) &= 4.8^{\circ}\text{C}, \\ \epsilon_{\alpha} &= 2.4 \cdot 10^{-6}, \\ u_{\alpha} &= 2.4 \cdot 10^{-6} \text{ mm}. \end{aligned} \quad (9.6)$$

In the transient analysis the element reaches this steady-state temperature distribution after approximately eight milliseconds with a chosen specific heat  $C_p$  of  $10.0 \text{ J/g}^{\circ}\text{C}$  and a mass density  $\rho$  of  $1.0 \text{ g/mm}^3$ , as shown

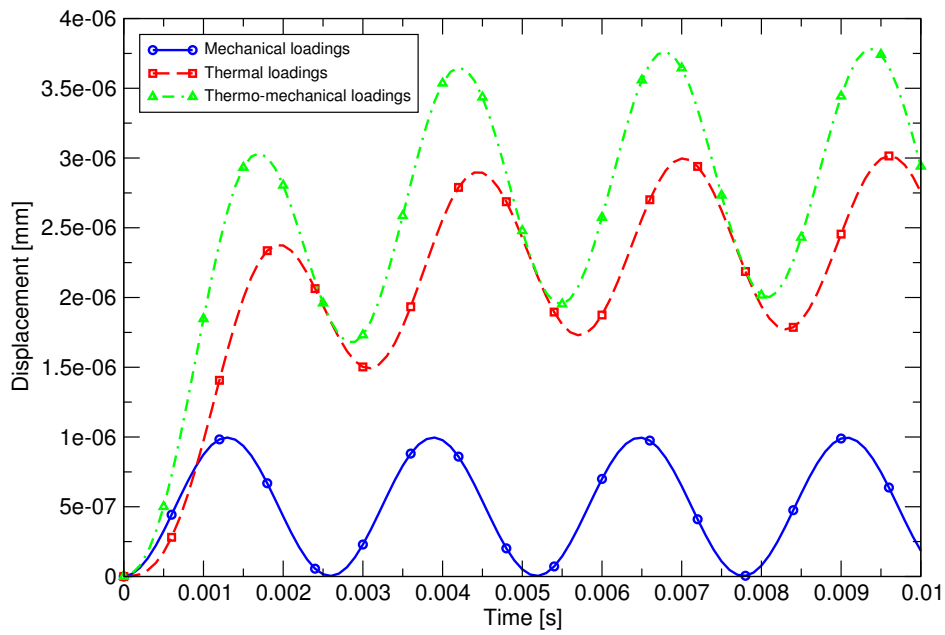


Figure 9.2: The effect of thermal and mechanical loadings on the dynamic behaviour without damping.

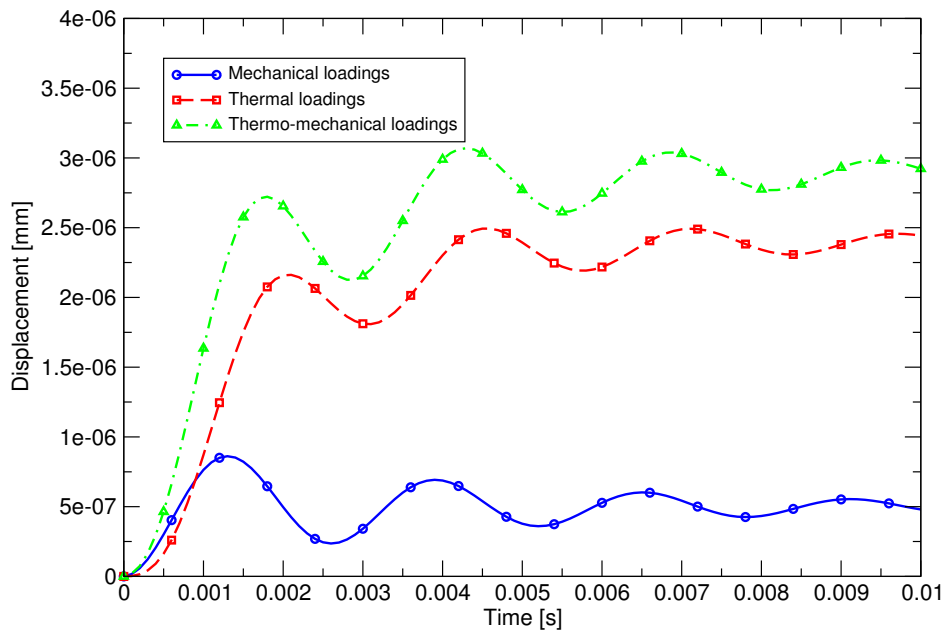


Figure 9.3: The effect of thermal and mechanical loadings on the dynamic behaviour with damping.

in Figure 9.1. The expansion which is a result of this temperature field increases gradually in time and causes a vibration. In Figure 9.2 the vibration due to the thermal loading is depicted together with the vibration due to a mechanical and a combined thermo-mechanical loading. From this figure it can be seen that the thermo-mechanical curve is a superposition of the thermal and the mechanical curve. In Figure 9.3 the results are shown in case damping is taken into account with a damping coefficient of 500.0.

### 9.3.2 Cylindrical panel subjected to a concentrated load

To demonstrate the ability of the transient solver, a snap-through of a cylindrical panel subjected to a concentrated vertex load is considered. In Figure 9.4 the geometry, material properties and boundary/loading conditions for the cylindrical panel are shown. In the first 200 milliseconds the concentrated load increases to its maximum value of  $50 \cdot 10^6$  Newton and is kept constant at this value up to 300 milliseconds. Due to symmetry only one quarter of the panel has to be modelled, which is done with 64 eight-noded elements. The example has been treated in a paper by (Kuhl and Ramm 1996) for shell elements. The choice was made to constrain the bottom-side (instead of the top-side) of the solid-like shell at the edges where rotation is allowed. Constraining the top-side however would give different results. To be able to capture the deflection of the panel at the concentrated vertex load accurately the time step has to be chosen below the wave time. The wave time is the time necessary for the stress wave to travel through the material. There are two types of waves that can be distinguished, the shear wave:

$$v_s = \sqrt{\frac{\mu}{\rho}}, \quad (9.7)$$

and the pressure wave:

$$v_p = \sqrt{\frac{2\mu + \lambda}{\rho}}, \quad (9.8)$$

where  $\lambda$  and  $\mu$  are the Lamé elastic constants defined as:

$$\mu = \frac{E}{2(1 + \nu)}, \quad (9.9)$$

and the pressure wave:

$$\lambda = \frac{\nu E}{(1 + \nu)(1 - 2\nu)}, \quad (9.10)$$

With the values for the properties, shown in Figure 9.4, a shear and pressure wave speed of 4899 m/s is found, which means that the smallest (critical) wave time is

$$t^* = \frac{h}{v} = 2.04 \cdot 10^{-5}. \quad (9.11)$$

In Figure 9.5 the snap-through of the panel, at 150 ms, is shown. The deflections of the panel at the concentrated vertex load are compared in Figure 9.6 with Park's method for five different time steps. The first three are below the determined critical wave time, viz. 0.005, 0.01, and 0.02 ms and indicate that Park's method gives a clear convergence in the results. The two extra time steps for which the simulation is performed are 0.5 and 1.0 ms, which shows that the accuracy of the obtained solution is lost and that there is numerical damping in the method.

The results of the deflection of the panel at the concentrated vertex load for Park's method (for time steps 0.02 ms, 0.5 ms and 1.0 ms) is compared in Figure 9.6 with the Constraint Energy Momentum Algorithm (CEMA) mentioned by (Kuhl and Ramm 1996) (with time step 1.0 ms).

It is emphasised that the CEMA method of (Kuhl and Ramm 1996) is applied in combination with shell elements. The results of the simulation with the solid-like shell can therefore not directly be compared, but are used as an indication of the trend in the deflection and the ability of the transient solver. The sixteen-noded solid-like shell elements would have the same order for the interpolation functions as the eight-noded shell elements, but the results will still be influenced by the different boundary conditions.

A similar snap-through behaviour of the eight-noded solid-like shell as for the eight-noded shells is found. The CEMA method, with time step of 1.0 ms, shows a remarkably good correspondence with the vibration of the panel after snap-through found with Park's method and a time step of 0.02 ms. The CEMA method thus shows much less numerical damping than Park's method at a time step much larger than the critical time step.

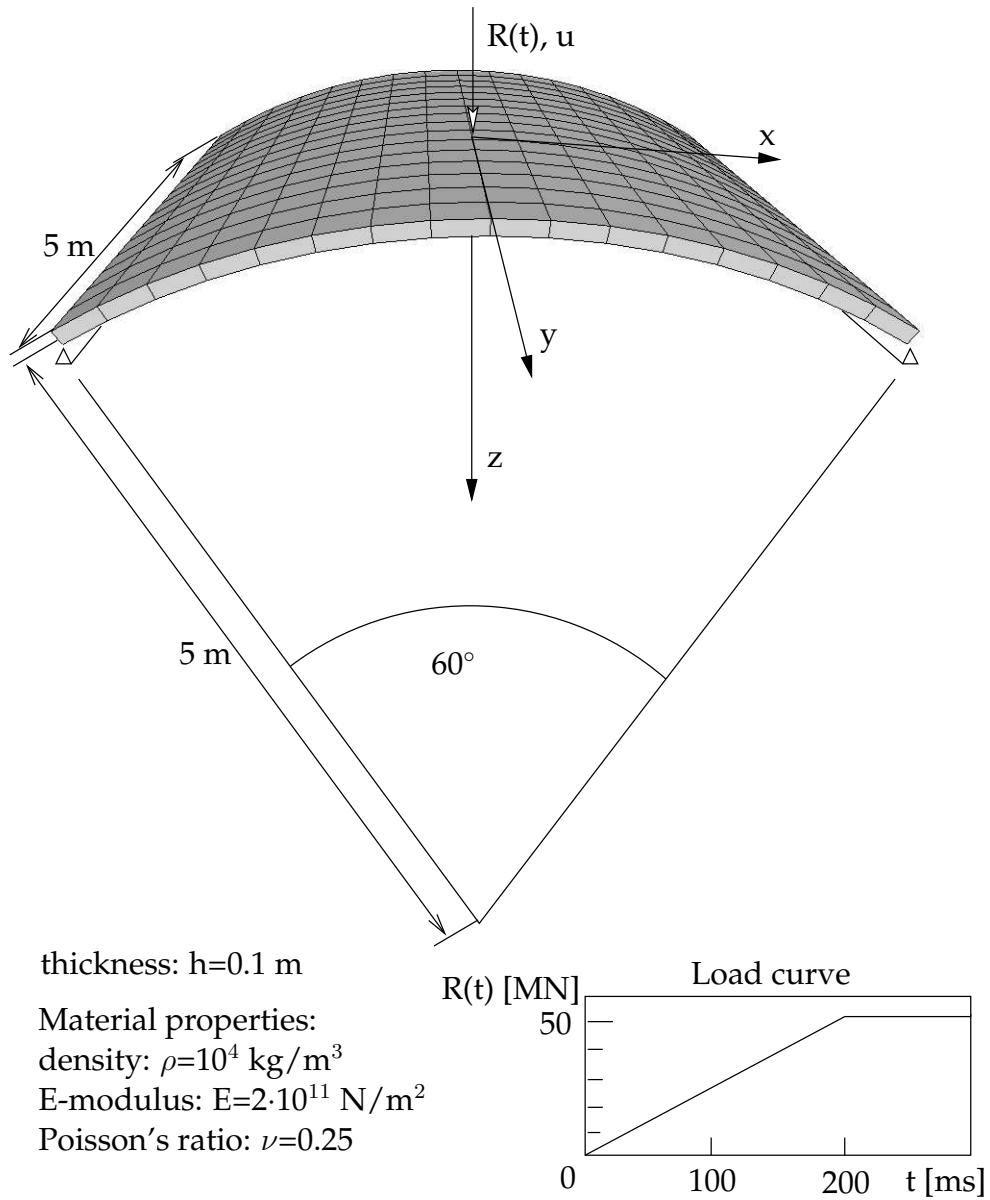


Figure 9.4: Geometry, finite element mesh, material properties, and boundary/loading conditions for the cylindrical panel subjected to a concentrated vertex load.

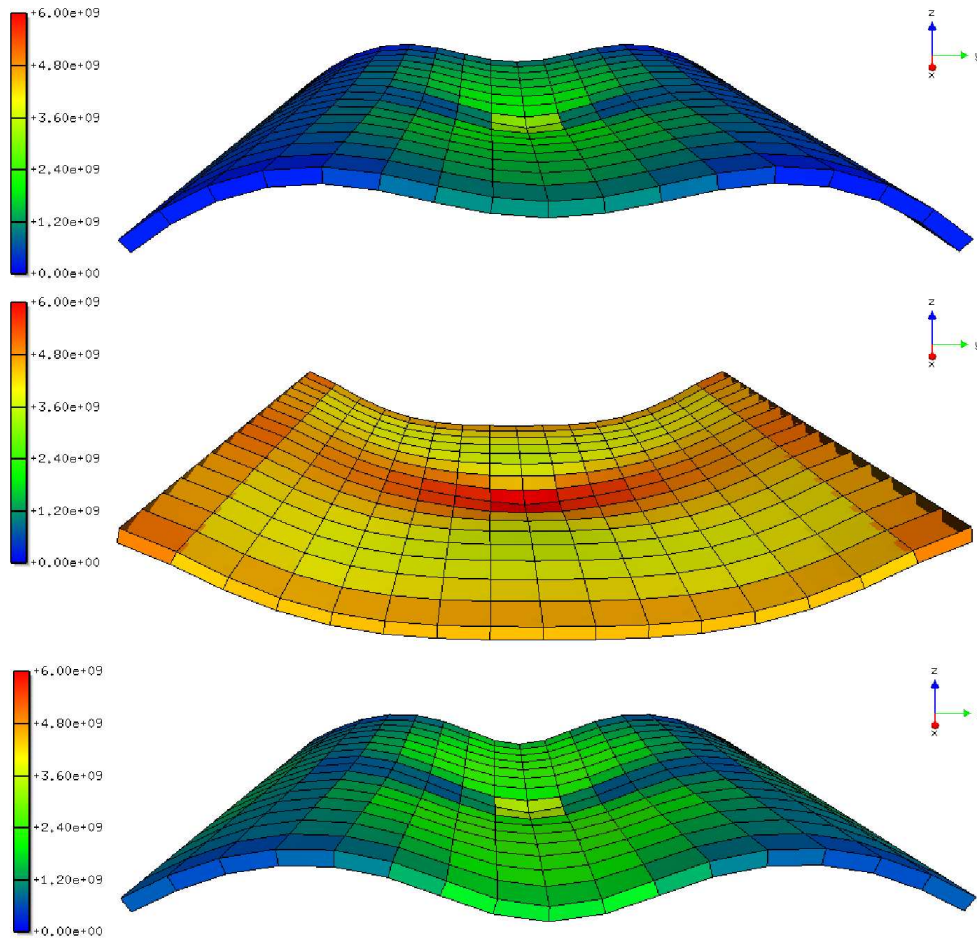


Figure 9.5: Snap-through, at 150 ms (top), 165 ms (middle), 180 ms (bottom picture) of the cylindrical panel subjected to a concentrated vertex load. The colours indicate the Von Mises stresses in the panel.

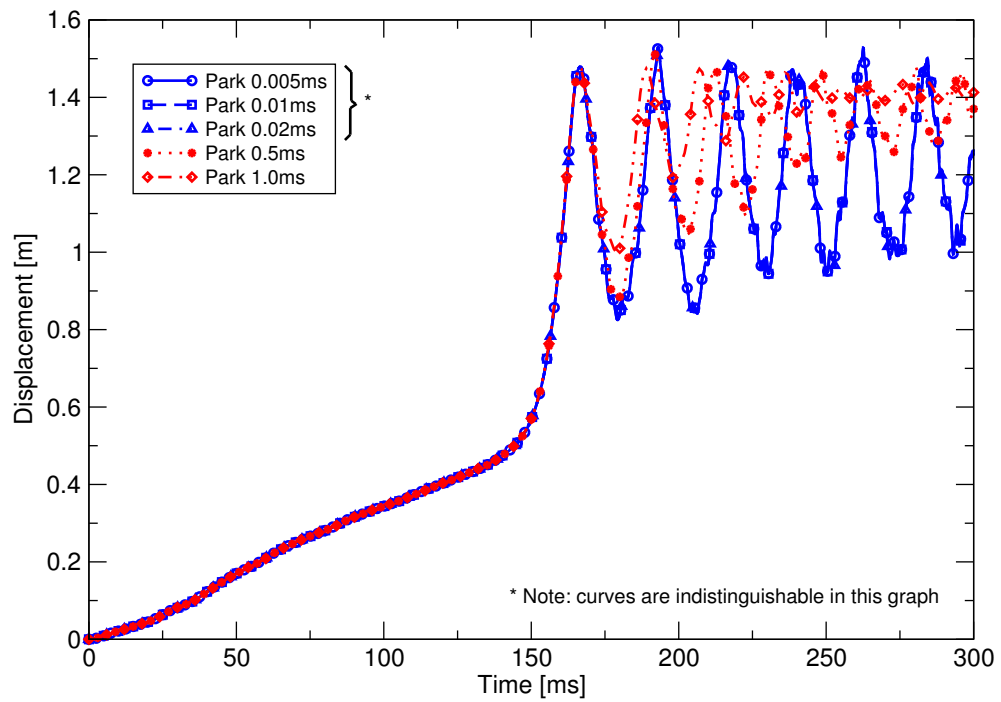


Figure 9.6: Time-history for the snap-through of the cylindrical panel in case of Park's method presented in this thesis (in combination with eight-noded solid-like shells) for five different time steps.



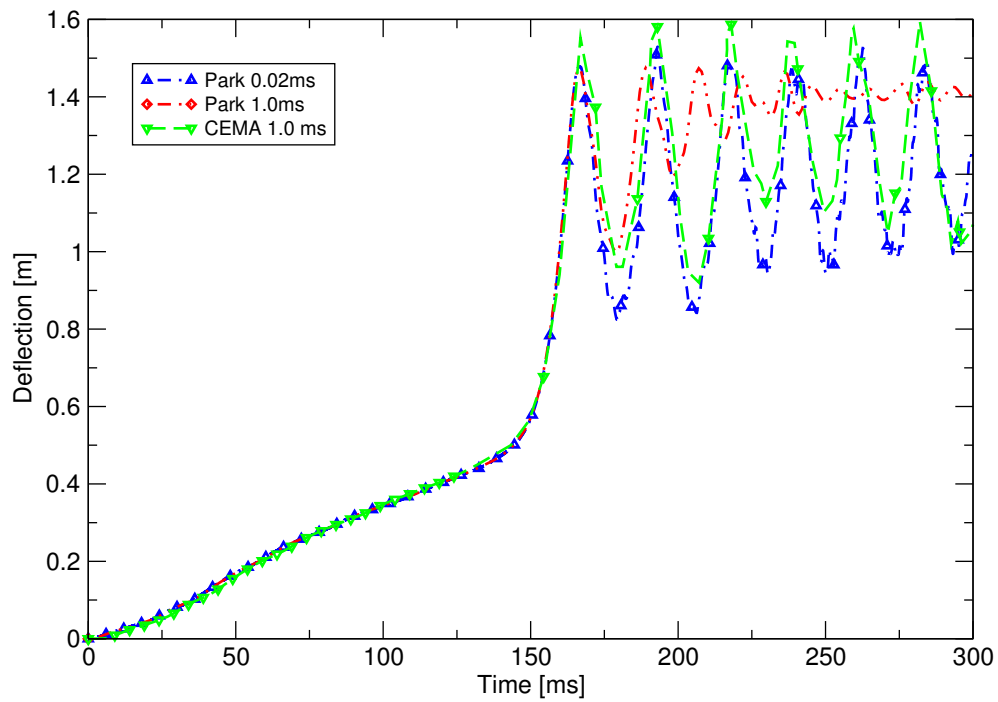


Figure 9.7: Time-history for the snap-through of the cylindrical panel in case of the CEMA method mentioned in (Kuhl and Ramm 1996) (together with eight-noded shell elements) and Park's method presented in this thesis (in combination with eight-noded solid-like shells) for different time steps.

## 9.4 Summary

In this chapter the transient model, which has been described in general in Chapter 5, has been detailed. Since temperature can largely affect the properties of especially the glass-fibre epoxy, see Chapter 3, it is important to determine the temperature field that is reached in the structure.

This can be done by taking the rate at which heat is stored in the structure into account in the model. The thermo-mechanical system of equations in the transient analysis is solved with Park's method as described in Section 5.4.1. The analysis can thus provide the development of the temperature distribution, the stress distribution due to differences in temperature as well as expansion, and the ultimate temperatures or steady state reached within a specific time.

The mechanical behaviour of the structure can also depend on time, for example due to impact. If the loads are applied rapidly, with respect to the natural frequencies of the system, inertial forces need to be considered; i.e. a truly dynamic problem needs to be solved. The dissipation of energy during vibration, which is observed in actually measured responses of structures, is usually taken into account by introducing velocity-dependent damping forces.

Two benchmark tests have been presented to demonstrate the performance of the thermo-mechanical solid-like shell element and the transient solver. A thermo-mechanical transient analysis on a single element has been performed, which shows a gradual increase in temperature and a mechanical vibration. In a second example the ability of the transient solver, based on Park's algorithm, and the performance of the solid-like shell element have been demonstrated for the snap-through of a cylindrical panel subjected to a concentrated load. The resulting deflection shows a similar trend as the numerical solution obtained for shell elements with the constraint energy momentum algorithm (CEMA), given by (Kuhl and Ramm 1996). The latter shows less numerical damping than Park's method at time steps larger than the critical time step.

# Chapter 10

## Conclusions

The thermo-mechanical finite element model developed in this thesis represents a very powerful simulation tool. The model is based on a solid-like shell element, which can have multiple layers in one element and allows for high aspect ratios without showing Poisson-thickness locking, which occurs in standard continuum elements. Therefore, the element is very suitable for the thin-walled aerospace structures where Glare is applied.

The three-dimensional state description of the solid-like shell allows for a straightforward implementation of the hardening and damage model.

A good fit of the hardening and damage model with the experimental curves for aluminium 2024-T3 and the UD glass-fibre epoxy could be obtained, though for the latter only a slow softening branch, included to avoid numerical instability, was obtained in transverse direction.

Off-axis stiffness calculations, based on the experimental UD glass-fibre epoxy results and the Classical Laminate Theory, on the tension and shear stiffness at room temperature and 80 °C of three different composite laminate lay-ups,  $[0/90]_{4s}$ ,  $[0/90/0]_{3s}$ , and  $[0/90/\pm 45]_{2s}$ , showed a good agreement with experimental tests results.

The transient thermo-mechanical behaviour can be captured by the model using Park's method to solve the dynamic system of equations. The good performance of the thermo-mechanical solid-like shell element and the transient solver have been demonstrated in benchmark tests.

The experimental test results for the special lay-up Glare show that a strong account must be given to the possible strength and stiffness reductions due to off-axis loading and/or temperature. Simulations and tests show a reduction of 24% in ultimate strength at room temperature due to off-axis loading and a further reduction of 17% at 80 °C temperature.

Blunt notch test simulations have been performed on Glare3-3/2-0.4 and on the special Glare laminate (tested at 0, 45, 67.5, and 90° off-axis an-

gle). Furthermore, (off-axis) tensile tests were simulated for a 0/90 composite, standard Glare laminates, and special Glare laminates with additional fibre layers in  $-45$  and  $45^\circ$  direction. All benchmark tests showed a good agreement with experimental results.

# Appendix A

## Analytical solution for the thick-walled cylinder

In Section 6.4.3 the example is given of an infinitely long, thick-walled cylindrical tube subjected to a different temperature at the inside,  $\theta_a$ , and the outside wall,  $\theta_b$ , relative to the reference temperature,  $\theta_o$ . This will lead to a non-linear temperature field over the thickness. The tube will expand and this will introduce stresses. In this appendix the analytical solution for the temperature distribution and displacement in radial direction are derived. Further more the expressions for the strains and stresses in radial and circumferential direction are determined.

The problem can be treated as an axisymmetric problem with a two-dimensional deformation field. The strain, in this case, is symmetric with respect to the axis of rotation and the shear strains are zero. The problem is independent of the angle  $\phi$ , and all quantities are functions of  $r$  only. The cylindrical tube has an inside radius,  $a$ , and outside radius,  $b$ , as depicted in Figure 6.6. If body forces are zero, the only equilibrium equation, which is in the radial direction, becomes

$$\frac{\partial \sigma_r}{\partial r} + \frac{\sigma_r - \sigma_\phi}{r} = 0. \quad (\text{A.1})$$

The strain-displacement equations in polar coordinates are

$$\epsilon_\phi = \frac{u_r}{r}; \quad \epsilon_r = \frac{\partial u_r}{\partial r}; \quad \epsilon_z = \frac{\partial u_z}{\partial z}, \quad (\text{A.2})$$

which can be written as a function of the stresses

$$\epsilon_\phi = \frac{1}{E}[\sigma_\phi - \nu(\sigma_r + \sigma_z)] + \alpha\Delta\theta, \quad (\text{A.3})$$

$$\epsilon_r = \frac{1}{E}[\sigma_r - \nu(\sigma_\phi + \sigma_z)] + \alpha\Delta\theta, \quad (\text{A.4})$$

$$\epsilon_z = \frac{1}{E}[\sigma_z - \nu(\sigma_r + \sigma_\phi)] + \alpha\Delta\theta. \quad (\text{A.5})$$

The term  $\alpha\Delta\theta$  denote the strain due to thermal expansion where the difference in temperature  $\Delta\theta$  is determined as follows

$$\Delta\theta = \theta(r) - \theta_o. \quad (\text{A.6})$$

The general heat transfer equations, as listed in Eq. (5.34), are

$$\rho_0 c \dot{\theta} + \text{Div } \mathbf{q} = \rho_0 r. \quad (\text{A.7})$$

The first and second term on the left-hand side of the equation represents the temperature change for the material and for thermal conduction respectively. The right-hand side denotes the heat flow input, including convection and radiation from the surface. For a stationary and source-free temperature field and assuming Fourier's law of heat conduction, the heat balance equation reduces to

$$\mathbf{k}\nabla^2\theta = 0, \text{ where } \nabla \text{ is defined as } \nabla = \frac{\partial}{\partial x} + \frac{\partial}{\partial y} + \frac{\partial}{\partial z}. \quad (\text{A.8})$$

Since the temperature is a function of  $r$  only,  $\theta = \theta(r)$ , and by assuming an isotropic heat conduction, the equation becomes, in polar coordinates,

$$\frac{\partial^2\theta}{\partial r^2} + \frac{1}{r}\frac{\partial\theta}{\partial r} \equiv \frac{1}{r}\frac{\partial}{\partial r}\left(r\frac{\partial\theta}{\partial r}\right) = 0. \quad (\text{A.9})$$

After integrating twice the solution for  $\theta(r)$  is

$$\theta(r) = A_1(\ln r + A_2), \quad (\text{A.10})$$

The integration constants  $A_1$  and  $A_2$  are determined from the boundary conditions

$$\theta_o + \theta(r) = \theta_{\text{in}a} \quad \text{for } r = a \quad (\text{A.11})$$

$$\theta_o + \theta(r) = \theta_{\text{in}b} \quad \text{for } r = b \quad (\text{A.12})$$

Where  $\theta_o$  is the uniform reference temperature. With  $\theta(a) = \theta_{in a} - \theta_o = \theta_a$  and  $\theta(b) = \theta_{in b} - \theta_o = \theta_b$ , the constants are

$$A_1 = \frac{\theta_b - \theta_a}{\ln b/a}; \quad A_2 = \frac{\theta_a \ln b - \theta_b \ln a}{\theta_b - \theta_a}, \quad (\text{A.13})$$

and the solution for the temperature field in radial direction becomes

$$\theta(r) = \frac{1}{\ln b/a} (\theta_a \ln \frac{b}{r} + \theta_b \ln \frac{r}{a}). \quad (\text{A.14})$$

Since the tube is considered to be long, the plain strain conditions apply and hence  $\epsilon_z = 0$ .

$$\epsilon_z = \frac{1}{E} [\sigma_z - \nu(\sigma_r + \sigma_\phi)] + \alpha \Delta \theta = 0, \quad (\text{A.15})$$

And for  $\sigma_z$  we can derive

$$\sigma_z = \nu(\sigma_r + \sigma_\phi) - E \alpha \Delta \theta, \quad (\text{A.16})$$

Substituting Eq. (A.16) into Eqs. (A.3) and (A.4) gives

$$\epsilon_\phi = \frac{1}{E} [\sigma_\phi - \nu(\sigma_r + \nu(\sigma_r + \sigma_\phi) - E \alpha \Delta \theta)] + \alpha \Delta \theta, \quad (\text{A.17})$$

$$\epsilon_r = \frac{1}{E} [\sigma_r - \nu(\sigma_\phi + \nu(\sigma_r + \sigma_\phi) - E \alpha \Delta \theta)] + \alpha \Delta \theta. \quad (\text{A.18})$$

Thus, after multiplying with  $E$ , the stress  $\sigma_r$  can be expressed as

$$\sigma_r = \frac{1}{1 - \nu^2} E \epsilon_r + \frac{\nu(1 + \nu)}{1 - \nu^2} \sigma_\phi - \frac{1 + \nu}{1 - \nu^2} E \alpha \Delta \theta, \quad (\text{A.19})$$

And by filling in Eq. (A.19) into Eq. (A.18) the stress  $\sigma_\phi$  can be written in terms of strains and after some elaboration we find,

$$\sigma_\phi = \left[ \frac{\nu E}{(1 + \nu)(1 - 2\nu)} + \frac{E}{(1 + \nu)} \right] \epsilon_\phi + \frac{\nu E}{(1 + \nu)(1 - 2\nu)} \epsilon_r - \frac{E}{(1 - 2\nu)} \alpha \Delta \theta. \quad (\text{A.20})$$

The stresses  $\sigma_r$  and  $\sigma_\phi$  can be listed shortly as

$$\sigma_r = (\lambda + 2G) \epsilon_r + \lambda \epsilon_\phi - \kappa \alpha \Delta \theta, \quad (\text{A.21})$$

$$\sigma_\phi = \lambda \epsilon_r + (\lambda + 2G) \epsilon_\phi - \kappa \alpha \Delta \theta, \quad (\text{A.22})$$

where

$$\lambda = \frac{\nu E}{(1 + \nu)(1 - 2\nu)}; \quad G = \frac{E}{2(1 + \nu)}; \quad \kappa = \frac{E}{1 - 2\nu}. \quad (\text{A.23})$$

Substituting  $\epsilon_\phi = \frac{u_r}{r}$  and  $\epsilon_r = \frac{\partial u_r}{\partial r}$ ,

$$\sigma_r = (\lambda + 2G) \frac{\partial u_r}{\partial r} + \lambda \frac{u_r}{r} - \kappa \alpha \Delta \theta, \quad (\text{A.24})$$

$$\sigma_\phi = \lambda \frac{\partial u_r}{\partial r} + (\lambda + 2G) \frac{u_r}{r} - \kappa \alpha \Delta \theta, \quad (\text{A.25})$$

Substituting these expressions in Eq. (A.1) gives, after some elaboration.

$$\frac{\partial}{\partial r} \left[ \frac{\partial u_r}{\partial r} + \frac{u_r}{r} - \frac{\kappa \alpha}{(\lambda + 2G)} \Delta \theta \right] = 0, \quad (\text{A.26})$$

After integrating once and filling in Eq. (A.14) for  $\theta$ , which is a function of  $r$  as well, we obtain

$$\frac{\partial u_r}{\partial r} + \frac{u_r}{r} = B_1 + \frac{\kappa \alpha}{(\lambda + 2G)} (A_1 A_2 - \theta_o) + \frac{\kappa \alpha}{(\lambda + 2G)} A_1 \ln r, \quad (\text{A.27})$$

where  $A_1$  and  $A_2$  can be found in Eq. (A.13). The equation can be rewritten in a simplified form

$$\frac{\partial u_r}{\partial r} + \frac{u_r}{r} = \frac{1}{r} \frac{\partial}{\partial r} (r u_r) = C_1 + C_2 \ln r, \quad (\text{A.28})$$

where

$$C_1 = B_1 + \frac{(A_1 A_2 - \theta_o) \kappa \alpha}{(\lambda + 2G)}; \quad C_2 = \frac{A_1 \kappa \alpha}{(\lambda + 2G)}. \quad (\text{A.29})$$

Integrating this equation yields

$$u_r = \frac{1}{r} \int [C_1 r + C_2 r \ln r] dr = \frac{1}{4} (2C_1 - C_2) r + \frac{1}{2} C_2 r \ln r + C_3 \frac{1}{r}, \quad (\text{A.30})$$

where partial integration has been used

$$\int r \ln r dr = \frac{1}{2} r^2 \ln r - \int \frac{1}{2} r^2 \frac{1}{r} dr = \frac{1}{2} r^2 \ln r - \frac{1}{4} r^2 + C. \quad (\text{A.31})$$

With the following notations,

$$D_1 = \frac{1}{4} (2C_1 - C_2); \quad D_2 = \frac{1}{2} C_2; \quad D_3 = C_3. \quad (\text{A.32})$$



Eq. (A.30) can be rewritten as

$$u_r = D_1 r + D_2 r \ln r + D_3 \frac{1}{r}. \quad (\text{A.33})$$

Only  $C_1$  and  $C_3$  are unknown constants, thus  $D_1$  and  $D_3$  must be determined. Using Eq. (A.2) we obtain

$$\epsilon_r = D_1 + D_2(1 + \ln r) - D_3 \frac{1}{r^2}, \quad (\text{A.34})$$

$$\epsilon_\phi = D_1 + D_2 \ln r + D_3 \frac{1}{r^2}. \quad (\text{A.35})$$

Substituting the expressions for  $\epsilon_\phi$  and  $\epsilon_r$  into Eqs. (A.21) and (A.22) gives

$$\sigma_r = 2(\lambda + G)D_1 + (\lambda + 2G)D_2 + 2(\lambda + G)D_2 \ln r - 2GD_3 \frac{1}{r^2} - \kappa\alpha\Delta\theta, \quad (\text{A.36})$$

$$\sigma_\phi = 2(\lambda + G)D_1 + \lambda D_2 + 2(\lambda + G)D_2 \ln r + 2GD_3 \frac{1}{r^2} - \kappa\alpha\Delta\theta, \quad (\text{A.37})$$

and from the boundary conditions for the radial stress  $\sigma_r = 0$  when  $r = a$  or  $r = b$ , the integration constants can be determined,

$$D_1 = \frac{1}{2(\lambda + G)} \frac{1}{b^2 - a^2} \left[ - \frac{(\lambda + G)A_1\kappa\alpha}{(\lambda + 2G)} (b^2 \ln b - a^2 \ln a) + \kappa\alpha(b^2\theta_b - a^2\theta_a) \right] - \frac{A_1\kappa\alpha}{4(\lambda + G)} \quad (\text{A.38})$$

$$D_2 = \frac{1}{2} \frac{A_1\kappa\alpha}{(\lambda + 2G)} \quad (\text{A.39})$$

$$D_3 = - \frac{1}{2G} \frac{a^2 b^2}{a^2 - b^2} \left[ - \frac{(\lambda + G)A_1\kappa\alpha}{(\lambda + 2G)} \ln b/a + \kappa\alpha(\theta_b - \theta_a) \right] \quad (\text{A.40})$$



# References

- Alderliesten, R. (2001). Fatigue. In A. Vlot and J. W. Gunnink (Eds.), *Fibre Metal Laminates an Introduction*, Dordrecht, The Netherlands, pp. 155–171. Kluwer Academic Publishers.
- Allix, O., N. Bahlouli, C. Cluzel, and L. Perret (1996). Modelling and identification of temperature-dependent mechanical behaviour of the elementary ply. *Composites Science and Technology* 56, 883–888.
- Aluminum Association (1982). *Aluminum standards and data*. Washington D.C.: Seventh edition.
- Andelfinger, U. (1991). *Untersuchung zur Zuverlässigkeit hybridgemischter Finiter Elemente für Flächentragwerke*. Ph. D. thesis, Universität Stuttgart, Stuttgart, Germany.
- ASTM-1269E (2001). Standard test method for determining specific heat capacity by differential scanning calorimetry. Technical report, American Society for Testing and Materials.
- ASTM-D-5379 (1999). Standard test method for shear properties of composite materials by the v-notched beam method. Technical report, American Society for Testing and Materials.
- ASTM-D3039 (2000). Standard test method for tensile properties of polymer matrix composite materials. Technical report, American Society for Testing and Materials.
- Bär, H. (1992). Verifikation und Ergänzung von Berechnungsmethoden für die statische und dynamische Auslegung von Glare-Strukturen. Technical Report MBB TN-TK536-5/95, Institut für Flugzeugbau der Universität Stuttgart.
- Bathe, K. (1996). *Finite element procedures*. Upper Saddle River, New Jersey: Prentice-Hall, Inc.
- Bathe, K. and E. Dvorkin (1986). A formulation of general shell elements - the use of mixed interpolation of tensorial components. *International Journal of Numerical Methods in Engineering* 22, 698–722.

- Behrens, E. (1968). Thermal conductivities of composite materials. *Journal of composite materials* 2,number 1, 2–17.
- Bischoff, M. and E. Ramm (1997). Shear deformable shell elements for large strains and rotations. *International Journal for Numerical Methods in Engineering* 40, 4427–4449.
- Boeing (2005). Boeing 787 Dreamliner. Program Fact Sheet. <http://www.boeing.com/commercial/7e7>.
- Boertien, M. (1996). Strength of Glare after exposure to moisture. Master thesis, Delft University of Technology, Faculty of Aerospace Engineering, Delft, The Netherlands.
- Borgonje, B. (2000). The influence of elevated temperature on Glare after exposure to moisture. Master thesis, Delft University of Technology, Faculty of Aerospace Engineering, Delft, The Netherlands.
- Borgonje, B. and W. van der Hoeven (2001). Long-term behaviour. In A. Vlot and J. W. Gunnink (Eds.), *Fibre Metal Laminates an Introduction*, Dordrecht, The Netherlands, pp. 53–68. Kluwer Academic Publishers.
- Carslaw, H. and J. Jaeger (2003). *Conduction of heat in solids*. New York: Oxford University Press.
- CBS (2005, April). Centraal Bureau voor de Statistiek (CBS). PB05-053. <http://www.cbs.nl>.
- Clyne, T. (1996). Residual stresses in surface coatings and their effects on interfacial debonding. *Key Engineering Materials* 116/7, 307–330.
- Cordebois, J. and F. Sideroff (1982). Endommagement anisotrope en élasticité et plasticité. *Journal de Mécanique Théorique et Appliquée* 45-60 Num. Spécial, 311–321.
- Cytec Engineered Materials (2000). FM94 modified epoxy film. Technical Datasheet available, page 6, document no. 05/97 (040102). <http://www.cytec.com>.
- de Borst, R. and H. Muhlhaus (1992). Gradient-dependent plasticity - Formulation and algorithmic aspects. *International Journal for Numerical Methods in Engineering* 35, 521–539.
- de Borst, R. and L. Sluys (1999). Computational methods in non-linear solid mechanics. Technical Report CTme5142, Delft University of Technology, Faculty of Civil Engineering and Geosciences, Delft, The Netherlands.

- Dop, P. (2002). Improvement of Glare off-axis properties, Investigation of alternative laminates. Master thesis, Delft University of Technology, Faculty of Aerospace Engineering, Delft, The Netherlands.
- Evancho, J. (2001). Secondary applications. In A. Vlot and J. W. Gunnink (Eds.), *Fibre Metal Laminates an Introduction*, Dordrecht, The Netherlands, pp. 309–324. Kluwer Academic Publishers.
- Gear, C. (1971). *Numerical initial value problems in ordinary differential equations*. Upper Saddle River, New Jersey: Prentice-Hall, Inc.
- Graafmans, G. (1995). Thermal behaviour of fiber metal laminates, thermal conductivity of and the effect of thermal fatigue on Glare. Master thesis, Delft University of Technology, Faculty of Aerospace Engineering, Delft, The Netherlands.
- Gunnink, J., A. Vlot, T. de Vries, and W. van der Hoeven (2002). Glare technology development 1997-2000. *Journal of Applied Composite Materials* 9, 201–219.
- Gürdal, Z., T. Haftka, and P. Hajela (1998). *Design and Optimization of Laminated Composite Materials*. University of Florida, Rensselaer Polytechnic Institute: Virginia Polytechnic Institute and State University.
- Habanera (2005). The Jem/Jive C++ toolkits. Habanera numerical software. <http://www.habanera.com>.
- Hagenbeek, M. (1999). Impact of ice, Impact properties of Glare. Technical Report B2v-98-15, Delft University of Technology, Faculty of Aerospace Engineering, Delft, The Netherlands.
- Hagenbeek, M. (2001). Impact properties. In A. Vlot and J. W. Gunnink (Eds.), *Fibre Metal Laminates an Introduction*, Dordrecht, The Netherlands, pp. 409–426. Kluwer Academic Publishers.
- Hagenbeek, M. (2002a). The feasibility of static tests on realistic door corner lay-up. Technical Report Report B2v-02-10, Delft University of Technology, Faculty of Aerospace Engineering, Delft, The Netherlands.
- Hagenbeek, M. (2002b). Off-axis tests on realistic door corner lay-up. Technical Report Report B2v-02-41, Delft University of Technology, Faculty of Aerospace Engineering, Delft, The Netherlands.
- Hagenbeek, M. (2004a). Off-axis properties of glass-fibre epoxy composites, test report for 0/90, 0/90/0, and 0/90/±45 laminates. Tech-

- nical Report B2v-04-04, Delft University of Technology, Faculty of Aerospace Engineering, Delft, The Netherlands.
- Hagenbeek, M. (2004b). Thermal and mechanical properties of UD glass-fibre epoxy. Technical Report Report B2v-04-01, Delft University of Technology, Faculty of Aerospace Engineering, Delft, The Netherlands.
- Hagenbeek, M., C. van Hengel, O. Bosker, and C. Vermeeren (2003). Static properties of Fibre Metal Laminates. *Applied Composite Materials* 10, 207–222.
- Hashagen, F. (1995). A geometrically and physically nonlinear layered solid-like shell element. Technical Report TU Delft nr.: 03-21-0-31-22, Delft University of Technology.
- Hashagen, F. (1998). *Numerical Analysis of Failure Mechanisms in Fibre Metal Laminates*. Ph. D. thesis, Delft University of Technology, Delft, The Netherlands.
- Hatch, J. (Ed.) (1983). *Aluminium properties and physical metalurgy*. Metals Park, Ohio: American Society for Metals.
- Homan, J. (1984). Crack opening in Arall as a consequence of adhesive deformation. Master thesis, Delft University of Technology, Faculty of Aerospace Engineering, Delft, The Netherlands.
- Hooijmeijer, P. and P. Kuijpers (1999). Fire testing and properties of Glare material: A literature survey. Technical Report B2v-99-25, GTO sub-project 5.1.2.1, Delft University of Technology.
- Horst, P. (1995). Methods Fibre Metal Laminates (subtask 5.1), brite/euram-2040. Technical Report MBB TN-TK536-5/95, DBAA.
- Hughes, T. (2000). *The finite element method; Linear static and dynamic finite element analysis*. Mineola, New York: Dover Publications Inc.
- Hyer, M. (1998). *Stress analysis of fiber-reinforced composite materials*. New York: McGraw-Hill.
- IATA (2005, March). The International Air Transport Association (IATA). 2004-The safest ever for air transport. <http://www.iata.org>.
- ISO-11359-2 (1999). Plastics - Thermomechanical analysis (TMA) - Part 2: Determination of coefficient of linear thermal expansion and glass transition temperature. Technical report, International Organisation for Standardization.

- ISO-14126 (1999). Fibre-reinforced plastic composites - determination of compressive properties in the in-plane direction. Technical report, International Organisation for Standardization.
- ISO-527-5 (1997). Plastics-determination of tensile properties-Part 5: Test conditions for unidirectional fibre-reinforced plastic composites. Technical report, International Organisation for Standardization.
- Jensen, P. (1974). Transient analysis of structures by stiffly stable methods. *Computers and Structures* 4, 615–626.
- Jones, R. (1999). *Mechanics of Composite Materials*. Second Edition, Taylor & Francis.
- Kachanov, L. (1958). On the time to failure under creep conditions (in russian). *Izv. Akad. Nauk SSSR* 8, 26–31.
- Kuhl, D. and E. Ramm (1996). Constraint energy momentum algorithm and its application to non-linear dynamics of shells. *Computer methods in applied mechanics and engineering* 136, 293–315.
- Lemaître, J. and J.-L. Chaboche (1978). Aspect phénoménologique de la rupture par endommagement. *Journal de Mécanique Appliquée* 2, No. 3, 317–365.
- Lemaître, J. and J.-L. Chaboche (1990). *Mechanics of solid materials*. Cambridge: Cambridge University Press.
- Liu, I. (2002). *Continuum Mechanics*. Heidelberg, Germany: Springer-Verlag.
- Marissen, R. (1988). *Fatigue crack growth in Arall a hybrid aluminium-aramid composite material*. Ph. D. thesis, Delft University of Technology, Delft, The Netherlands.
- Matweb (2004). The online materials information resource. Automation Creations Inc. <http://www.matweb.com>.
- McCarthy, M., J. Xiao, C. McCarthy, A. Kamoulakos, J. Ramos, J. Gallard, and V. Melito (2004). Modelling of bird strike on an aircraft wing leading edge made from fibre metal laminates - Part 2: Modelling of impact with SPH bird model. *Applied Composite Materials* 11, 317–340.
- McCarthy, M., J. Xiao, N. Petrinic, A. Kamoulakos, and V. Melito (2004). Modelling of bird strike on an aircraft wing leading edge made from fibre metal laminates - Part 1: Material modelling. *Applied Composite Materials* 11, 295–315.

- McCartney, L. (1998). Predicting transverse crack formation in cross-ply laminates. *Composites Science and Technology* 58, 1069–1081.
- Meziere, Y. (2000). Experimental project to assess the failure mechanisms during blunt notch of Glare. Technical Report B2v-00-47, Delft University of Technology, Faculty of Aerospace Engineering, Delft, The Netherlands.
- Military Handbook (1998). Metallic materials and elements for aerospace vehicle structures. Technical Report MIL-HDBK-5H, Department of Defence, USA.
- Military Handbook (2002). Composite materials handbook. Technical Report MIL-HDBK-17, Department of Defence, USA.
- Ogden, R. (1984). *Non-linear Elastic Deformations*. Ellis Horwood Limited.
- Out, B. and M. Hagenbeek (2002). Mechanical properties of cured cross-ply prepreg. Technical Report B2V-01-31, Delft University of Technology, Faculty of Aerospace Engineering, Delft, The Netherlands.
- Parisch, H. (1995). A continuum-based shell theory for non-linear applications. *International Journal for Numerical Methods in Engineering* 38 (11), 1855–1883.
- Park, K. (1975a). Evaluating time integration methods for nonlinear dynamic analysis. In T. Belytschko, J. Osias, and P. Marcal (Eds.), *Finite Element Analysis of Transient Non-linear Behavior*, New York, USA, pp. 35–58. ASME.
- Park, K. (1975b). An improved stiffly stable method for direct integration of nonlinear structural dynamic equations. *Journal of Applied Mechanics* 42, 464–470.
- Peerlings, R., R. de Borst, W. Brekelmans, and J. de Vree (1996). Gradient enhanced damage for quasi-brittle materials. *International Journal for Numerical Methods in Engineering* 39, 3391–3403.
- Rankin, C., F. Brogan, W. Loden, and H. Cabiness (1997). STAGS User Manual, version 3.0. Technical report, Lockheed Martin Missiles & Space Co. Inc., Palo Alto, CA, USA.
- Remmers, J. (1998). Mode-jumping with b2000. Master thesis, Delft University of Technology, Faculty of Aerospace Engineering, Delft, The Netherlands.
- Remmers, J. and R. de Borst (2001). Numerical modelling: Delamination buckling. In A. Vlot and J. W. Gunnink (Eds.), *Fibre Metal Laminates*



- an Introduction*, Dordrecht, The Netherlands, pp. 281–297. Kluwer Academic Publishers.
- Reuss, A. (1929). Berechnung der Fliegrenze von Mischkristallen auf Grund der Plastizitätsbedingung für Einkristalle. *Zeitschrift für Angewandte Mathematik und Mechanik* 9, 49–58.
- Riks, E. (1970). *On the numerical solution of snapping problems in the theory of elastic stability*. Ph. D. thesis, Stanford University.
- Roebroeks, G. (1991). *Towards Glare - The development of a fatigue insensitive and damage tolerant aircraft material*. Ph. D. thesis, Delft University of Technology, Delft, The Netherlands.
- Roebroeks, G. (1996). Strength of Glare after exposure. Technical Report TD-R-96-002, Structural Laminates Company.
- Roebroeks, G. (1997). Glare, a structural material for fire resistant aircraft fuselages. In *published in AGARD Conference Proceedings 587*, Volume Dresden, Germany, 14-17 October 1996, pp. 26/1–26/13.
- Roebroeks, G. (2000). The Metal Volume Fraction approach. Technical Report TD-R-00-003, Structural Laminates Industries.
- Roebroeks, G. (2001). Glare features. In A. Vlot and J. W. Gunnink (Eds.), *Fibre Metal Laminates an Introduction*, Dordrecht, The Netherlands, pp. 23–37. Kluwer Academic Publishers.
- Rolfes, R. and U. Hammerschmidt (1995). Transverse thermal conductivity of cfrp laminates: A numerical and experimental validation of approximation formulae. *Composite Science and Technology* 54, 45–54.
- Rolfes, R., J. Noack, and M. Taeschner (1999). High performance 3D-analysis of thermo-mechanically loaded composite structures. *Composite Structures* 46, 367–379.
- Rolfes, R., J. Tessmer, and K. Rohwer (2003). Models and tools for heat transfer, thermal stresses and stability of composite aerospace structures. *Journal of Thermal Stresses* 26-6, 641–670.
- Schipperen, J. (2001a). Glare blunt notch, finite element model description. Technical Report 01002-R01, Advanced Lightweight Engineering.
- Schipperen, J. (2001b). Glare blunt notch, FE model description. Technical Report 01002-R01, Advanced Lightweight Engineering, Delft, The Netherlands.
- Shenoi, R. and J. Wellicome (1993). *Composite Materials in Maritime Structures, Volume 1: Fundamental Aspects*. Cambridge University Press.

- Spies, G. (1978). *Composietmaterialen*. Technical Report lecture notes 7075-1, Delft University of Technology, Faculty of Aerospace Engineering, Delft, The Netherlands.
- Structural Laminates Industries (1993a). Customer data information sheet, Properties of FML constituents - Prepregs.
- Structural Laminates Industries (1993b). Internal data information sheet, Properties of FML constituents - Fibers & Adhesive.
- Sun, C., B. Quinn, J. Tao, and D. Oplinger (1996). Comparative evaluation of failure analysis methods for composite laminates. Technical Report DOT/FAA/AR-95/109, Federal Aviation Administration, Washington D.C.
- Tessmer, S. Waitz, R. Rolfes, J. Ackva, and T. de Vries (2003). Thermal analysis computation and experimental validation of fiber metal laminates. In *Proceedings 5th International Conference on Thermal Stresses*, Blacksburg, Virginia.
- van der Hoeven, W. and P. Nijhuis (2004). Mechanical properties of thin aluminium 2024-T3 sheets used for the production of Glare laminates. Technical Report NLR-TR-2004-044, National Aerospace Laboratory.
- van der Hoeven, W. and L. Schra (1999). Interim report, Qualification testing for the Glare panel in the A310p /F MSN 484 aircraft, Results of tests on non-exposed specimens. Technical Report NLR-CR-99269, National Aerospace Laboratory.
- van der Hoeven, W. and L. Schra (2000). Final report Glare durability program, Results of tests carried out at NLR. Technical Report NLR-CR-2000-237, National Aerospace Laboratory.
- van der Kevie, G. (1997). The modification of Glare to develop a more fire-resistant and non-delaminating fuselage skin for the Airbus A3XX. Master thesis, Delft University of Technology, Faculty of Aerospace Engineering, Delft, The Netherlands.
- van Tooren, M. (1998). *Sandwich fuselage design*. Ph. D. thesis, Delft University of Technology, Faculty of Aerospace Engineering, Delft, The Netherlands.
- Vermeeren, C. (1988). The Arall blunt notch. Master thesis, Delft University of Technology, Faculty of Aerospace Engineering, Delft, The Netherlands.

- Vlot, A. (1991). *Low-velocity impact loading on fibre reinforced aluminium laminates (Arall) and other aircraft sheet materials*. Ph. D. thesis, Delft University of Technology, Delft, The Netherlands.
- Vlot, A. (2001a). *Glare-history of the development of a new aircraft material*. Dordrecht, The Netherlands: Kluwer Academic Publishers.
- Vlot, A. (2001b). Historical overview. In A. Vlot and J. W. Gunnink (Eds.), *Fibre Metal Laminates an Introduction*, Dordrecht, The Netherlands, pp. 3–21. Kluwer Academic Publishers.
- Vogelgesang, L., J. Schijve, and R. Fredell (1995). Fibre-metal laminates: damage tolerant aerospace materials. *Case Studies in Manufacturing with Advanced Materials 2*, 253–271.
- Voigt, W. (1889). über die Beziehung zwischen den beiden Elastizitätskonstanten isotroper Körper. *Wied. Ann.* 38, 573–587.
- Ypma, M. (2000). Overview of tests concerning the influence of temperature and environmental exposure on Glare. Technical Report Report B2v-00-41, Delft University of Technology, Faculty of Aerospace Engineering, Delft, The Netherlands.



# Index

- (non-)associated flow rule, 86
- aluminium
  - 7475-T761, 13
- assumed natural strains, 117
- burn-through resistance, 18
- Cauchy stress tensor, 67
- Classical Laminate Theory, 38
- crack bridging effect, 8
- creep, 24
- damage evolution law, 92
- damage growth, 91
- damage loading function, 91
- differential operator, 82
- displacement-control, 84
- epoxy
  - AF163-2, 26
  - FM906, 12
  - FM94, 12, 26
  - glass-rubber transition, 35
  - temperature sensitivity, 31, 32
- equivalent strain, 90
- equivalent stress, 85
- Euler backward method, 87
- Eulerian strain tensor, 68
- fibre bridging effect, 9
- fibre shearing, 155
- first law of thermodynamics, 71
- Gear's method, 80
- generalised momentum vector, 79
- Gibbs relation, 72
- Glare
  - acronym, 10
  - bond-strength, 12
  - Glare Research Program, 11
  - Glare Technologie Ontwikkeling, 11
  - material handling, 15
  - special-lay-up, 49
  - sub variants, 14
- Green-Lagrange strain tensor, 69, 102
- hardening law, 85
- hardening parameter, 85
- Jensen's transformation algorithm, 79
- Kirchhoff assumption, 76
- Kuhn-Tucker conditions, 85, 92
- linear multi-step method, 79
- linearisation, 83
- load-control, 84
- loading function, 85
- mesh-dependency, 155
  - gradient method, 155
  - localisation, 155
- mesoscopic scale, 25
- metal bonding, 8
- Metal Volume Fraction method, 24
- multiple site damage, 9

- Newton-Raphson procedure, 82
- orthotropy  
  aluminium, 24  
  thermal, 24
- Park's method, 78, 79
- path-following technique, 84
- Piola-Kirchhoff stress tensor, 69
- plastic multiplier, 85
- Poisson-thickness locking, 97
- qualitative analysis  
  (micro) voids content, 29  
  fibre volume fraction, 29  
  SEM imaging, 29  
  ultrasonic C-scan, 29
- Rayleigh damping factors, 79
- residual stresses, 7, 97  
  post-stretching, 10
- return-mapping algorithm, 87
- S<sub>2</sub> glass-fibre, 26
- secondary bending, 50
- self-forming technique, 19
- snowball effect, 16
- splicing concept, 19
- Stefan-Boltzmann constant, 75
- Stefan-Boltzmann law, 75
- tangent modulus, 52
- tangent stiffness matrix, 82  
  consistent, 89, 95  
  material, 84, 112  
  structure, 83, 84, 112
- temperature effect  
  fatigue properties, 21  
  moisture ingress, 21  
  specific heat, 21  
  thermal conductivity, 21  
  thermal expansion, 21
- temperature range, 24
- thermal strain tensor, 104, 107
- Total Lagrange approach, 68
- UD glass-fibre epoxy  
  bond-strength, 12  
  cohesive failure, 12  
  fibre volume fraction, 27  
  Reuss bound, 27  
  rule-of-mixtures, 27
- yield function, 85

# Samenvatting

Vezel metaal laminaten, zoals Arall of Glare, zijn in staat betere eigenschappen te bieden in vergelijking tot monolitische materialen. Glare bijvoorbeeld laat betere vermoeiings-, reststerkte-, brandwerendheid-, impact- en corrosie-eigenschappen zien dan aluminium 2024, met daarnaast een aanzienlijke gewichtsbesparing en concurrerende kostprijs. Een groot onderzoeksprogramma heeft aangetoond dat de Glare technologie volwassen is en het vezel metaal laminaat heeft inmiddels zijn toepassing gevonden in de primaire constructie van de Airbus A380 superjumbo.

Desondanks is het effect van temperatuur op het gedrag van vezel metaal laminaten nog niet volledig gekarakteriseerd. Verschillen in uitzettingscoëfficiënten veroorzaken restspanningen in het laminaat na het uitharden. Tijdens het gebruik kan de temperatuur van de vliegtuighuid variëren tussen -55 en 70 °C door zonnestraling en convectie, wat van invloed is op de thermische en mechanische eigenschappen van Glare. Een goed begrip van het gedrag van deze laminaten is noodzakelijk om de prestaties en duurzaamheid ervan verder te kunnen verbeteren. Door de toename in complexiteit van constructies en materiaal-samenstellingen wordt het belang van krachtige ontwerp-technieken duidelijk.

In dit proefschrift is het thermo-mechanisch gedrag van vezel metaal laminaten gekarakteriseerd door middel van experimenteel testwerk en numerieke modellering. Experimentele testen zijn uitgevoerd om het temperatuur-afhankelijke gedrag van unidirectionele (UD) glasvezel-epoxy te bepalen. Berekeningen, gebaseerd op deze test resultaten, bij kamertemperatuur en 80 °C voor de trek- en schuifstijfheid van drie verschillende composiet lay-ups kwamen goed overeen met experimentele test resultaten. The UD glasvezel-epoxy data dient als invoer voor het eindige elementen model, samen met aluminium 2024-T3 data uit de literatuur.

Glare laminaten met een speciale lay-up zijn experimenteel getest om het effect van temperatuur en mechanische belasting op de laminaat-eigenschappen te bepalen. De test resultaten laten zien dat het off-axis en temperatuur effect een reductie van 24% in ultimate sterkte kunnen geven bij

kamertemperatuur ten gevolge van off-axis belasting, en een verdere reductie van 17% bij een temperatuur van 80 °C. Voor standaard Glare uit de literatuur, waarvoor testen bij verhoogde temperatuur alleen in vezelrichting zijn uitgevoerd, is de afname in sterkte en stijfheid ten hoogste 12% in vergelijking tot kamertemperatuur.

Numerieke simulatie is een zeer krachtig middel om het gedrag van materialen en constructies te onderzoeken. Daarom is er een thermo-mechanisch eindig elementen model ontwikkeld, gebaseerd op een solid-like shell element inclusief thermische expansie en warmtetransport, om het gedrag van Glare in een volledig drie-dimensionale toestand te kunnen beschrijven. De temperatuur- en spanningsverdeling in dikte richting kan daarbij worden bepaald, zodat schade- en plasticiteitsmodellen direct geïmplementeerd kunnen worden. Bovendien is het solid-like shell element ideaal voor dunwandige (luchtvaart-) constructies, omdat het hoge aspect ratio's kan hebben zonder Poisson-locking in dikterichting te vertonen, wat voorkomt in standaard continuum elementen, en omdat het meerdere lagen in een element kan hebben.

Om fysische niet-lineariteiten mee te nemen wordt er een plasticiteitsmodel gebruikt voor aluminium 2024-T3 en een orthotroop schade-model voor de UD glasvezel-epoxy lagen in Glare. Het verstevigingsgedrag van aluminium is gemodelleerd met een vloeicriterium gebaseerd op een isotrope Von Mises plasticiteit formulering. Er is een exponentieel-verzadigende verstevigingswet verondersteld, wat een goede overeenkomst met de experimentele aluminium 2024-T3 spannings-rek kromme geeft. Een return-mapping algoritme wordt gehanteerd om de spanning terug op het vloeioppervlak te projecteren als de spanningstoestand de belastingscondities overtreedt.

Het concept van continuum damage-mechanica is toegepast, met een aparte schade-parameter voor vezel en matrix, om het verschijnsel van micro-scheuren te beschrijven wat leidt tot het uiteindelijk bezwijken. De maat voor de equivalente rek wordt verkregen door het vloeicriterium uit het orthotrope Hoffman plasticiteitsmodel om te schrijven in een rekgebaseerd formaat. De schade-parameters worden direct in de stijfheidsmatrix geïmplementeerd om ongewenste koppeling termen in de schade-matrix te vermijden. The simulaties van de schuif- en trektesten in transversale richting sluiten goed aan bij de experimentele krommen voor de UD glasvezel-epoxy.

Het transiente gedrag kan worden bepaald door de warmte capaciteit, de traagheidskrachten en de demping mee te nemen. De methode van Park wordt gebruikt om het dynamische stelsel van vergelijkingen op te lossen. De goede eigenschappen van het thermo-mechanische solid-like shell el-



ement en van de transient solver zijn gedemonstreerd voor een enkel element met thermo-mechanische belastingen en voor het doorknikken van een cilindrisch paneel onder een geconcentreerde belasting.

via een aantal benchmark testen voor praktische toepassingen is het verkregen numerieke model vergeleken met experimentele test resultaten. Blunt notch simulaties zijn uitgevoerd op Glare3-3/2-0.4 en op een speciaal Glare laminate (getest met 0, 45, 67.5, en 90° off-axis hoek), en laten een goede overeenkomst zien met experimentele resultaten. Simulaties van off-axis trektesten op een 0/90 composiet, trektesten op standaard Glare laminaten, en off-axis trektesten op speciale Glare laminaten met additionele vezellagen in -45 en 45° richting, laten ook een goede overeenkomst met experimentele resultaten zien.

Het thermo-mechanisch solid-like shell element en de experimenteel verkregen materiaal data, gepresenteerd in dit proefschrift, creëren samen een krachtig simulatie-gereedschap voor een effectieve en accurate karakterisering van vezel metaal laminaten onder thermo-mechanische belastingen.



# Publications

- [1] M. Hagenbeek. Impact of ice, Impact properties of Glare. Technical Report B2v-98-15, Delft University of Technology, Faculty of Aerospace Engineering, Delft, The Netherlands, 1999.
- [2] M. Hagenbeek. Fatigue and residual strength after impact, Impact properties of Glare. Technical Report B2v-98-16, Delft University of Technology, Faculty of Aerospace Engineering, Delft, The Netherlands, 1999.
- [3] M. Hagenbeek. Impact tests on lap joints, Impact properties of Glare. Technical Report B2v-98-32, Delft University of Technology, Faculty of Aerospace Engineering, Delft, The Netherlands, 1999.
- [4] M. Hagenbeek. Impact comparison between Glare, carbon and aluminium, Impact properties of Glare. Technical Report B2v-99-03, Delft University of Technology, Faculty of Aerospace Engineering, Delft, The Netherlands, 1999.
- [5] M. Hagenbeek. Impact tests on splices, Impact properties of Glare. Technical Report B2v-99-17, Delft University of Technology, Faculty of Aerospace Engineering, Delft, The Netherlands, 1999.
- [6] M. Hagenbeek. The MVF method for shear yield strength prediction. Technical Report B2v-99-26, Delft University of Technology, Faculty of Aerospace Engineering, Delft, The Netherlands, 1999.
- [7] M. Hagenbeek. Stress-strain calculation program, computer software stress-s9.xls. Technical report, Delft University of Technology, Faculty of Aerospace Engineering, Delft, The Netherlands, 1999.
- [8] M. Hagenbeek. Derivation of shear yield values from uniaxial tests. Technical Report B2v-99-38, Delft University of Technology, Faculty of Aerospace Engineering, Delft, The Netherlands, 2000.
- [9] M. Hagenbeek. Fatigue and residual strength effect of scratches. Technical Report B2v-00-14, Delft University of Technology, Faculty of Aerospace Engineering, Delft, The Netherlands, 2000.

- 
- [10] M. Hagenbeek. Fatigue and residual strength of Glare 2 after impact. Technical Report B2v-00-21, Delft University of Technology, Faculty of Aerospace Engineering, Delft, The Netherlands, 2000.
- [11] M. Hagenbeek. Impact damage assessment of Glare 2. Technical Report B2v-00-27, Delft University of Technology, Faculty of Aerospace Engineering, Delft, The Netherlands, 2000.
- [12] M. Hagenbeek. Estimation tool for basic material properties. Technical Report B2v-00-29, Delft University of Technology, Faculty of Aerospace Engineering, Delft, The Netherlands, 2000.
- [13] M. Hagenbeek. Estimation tool for basic material properties, computer software ETMP\_R2.xls. Technical report, Delft University of Technology, Faculty of Aerospace Engineering, Delft, The Netherlands, 2000.
- [14] M. Hagenbeek. Theory and application of statistical analysis. Technical Report B2-00-51, Delft University of Technology, Faculty of Aerospace Engineering, Delft, The Netherlands, 2000.
- [15] M. Hagenbeek. Investigation into applicability of analytical methods for blunt notch strength prediction of fml's. Technical Report B2v-00-57, Delft University of Technology, Faculty of Aerospace Engineering, Delft, The Netherlands, 2000.
- [16] M. Hagenbeek. Impact properties of PM1000/2000 sandwich. Technical Report B2v-00-62, Delft University of Technology, Faculty of Aerospace Engineering, Delft, The Netherlands, 2000.
- [17] M. Hagenbeek. Feasibility of Tsai-Hill criterion for yield and ultimate strength of unnotched material, Memo. Technical report, Delft University of Technology, Faculty of Aerospace Engineering, Delft, The Netherlands, 2001.
- [18] M. Hagenbeek. Investigation of the finite width and notch size effect for the analytical blunt notch strength prediction method. Technical Report B2v-01-20, Delft University of Technology, Faculty of Aerospace Engineering, Delft, The Netherlands, 2002.
- [19] M. Hagenbeek. The feasibility of static tests on realistic door corner lay-up. Technical Report B2v-02-10, Delft University of Technology, Faculty of Aerospace Engineering, Delft, The Netherlands, 2002.
- [20] B.C.L. Out and M. Hagenbeek. Mechanical properties of cured cross-ply prepreg. Technical Report B2V-01-31, Delft University of Tech-

- nology, Faculty of Aerospace Engineering, Delft, The Netherlands, 2002.
- [21] M. Hagenbeek. Off-axis tests on realistic door corner lay-up. Technical Report Report B2v-02-41, Delft University of Technology, Faculty of Aerospace Engineering, Delft, The Netherlands, 2002.
- [22] M. Hagenbeek. Thermal and mechanical properties of UD glass-fibre epoxy. Technical Report Report B2v-04-01, Delft University of Technology, Faculty of Aerospace Engineering, Delft, The Netherlands, 2004.
- [23] M. Hagenbeek. Off-axis properties of glass-fibre epoxy composites, test report for 0/90, 0/90/0, and 0/90/ $\pm 45$  laminates. Technical Report B2v-04-04, Delft University of Technology, Faculty of Aerospace Engineering, Delft, The Netherlands, 2004.
- [24] M. Hagenbeek. Impact properties. In Ad Vlot and Jan Willem Gunnink, editors, *Fibre Metal Laminates an Introduction*, pages 409–426, Dordrecht, The Netherlands, 2001. Kluwer Academic Publishers.
- [25] M. Hagenbeek. Shear yield strength. In Ad Vlot and Jan Willem Gunnink, editors, *Fibre Metal Laminates an Introduction*, pages 111–116, Dordrecht, The Netherlands, 2001. Kluwer Academic Publishers.
- [26] M. Hagenbeek, J.J.C. Remmers, and R. de Borst. Numerical modelling of Fibre Metal Laminates under thermo-mechanical loading. In *AIAA Conference Proceedings*, Norfolk, Virginia, 2003.
- [27] M. Hagenbeek, C. van Hengel, O.J. Bosker, and C.A.J.R. Vermeeren. Static properties of Fibre Metal Laminates. *Applied Composite Materials*, 10:207–222, 2003.
- [28] M. Hagenbeek, C. van Hengel, and J. Sinke. Analytical modelling of stress-strain curves for fibre metal laminates. In *ICCM-14 Conference Proceedings*, San Diego, California, 2003.
- [29] R.C. Alderliesten, M. Hagenbeek, J.J. Homan, P.A. Hooijmeijer, T.J. de Vries, and C.A.J.R. Vermeeren. Fatigue and damage tolerance of Glare. *Applied Composite Materials*, 10:223–242, 2003.
- [30] M. Hagenbeek, J. Sinke, and R. de Borst. Off-axis effects on the mechanical properties of fibre metal laminates. *Journal of Composite Materials*, To be published, 2006.
- [31] M. Hagenbeek, J. Sinke, and R. de Borst. The effect of temperature on the thermo-mechanical properties of fibre metal laminates. *Composites: Part A*, To be published, 2006.

- [32] M. Hagenbeek, S.R. Turteltaub, and R. de Borst. Numerical modelling of damage and plasticity in fibre metal laminates. *Composites Science and Technology*, To be published, 2006.
- [33] M. Hagenbeek, S.R. Turteltaub, and R. de Borst. Numerical modelling of fibre metal laminates under thermo-mechanical loadings. *Composite Structures*, To be published, 2006.

# Curriculum Vitae

Michiel Hagenbeek was born in Nunspeet on January 31<sup>st</sup> 1974. In 1992, after high school, he started the study aerospace engineering at the Faculty of Aerospace Engineering of the Delft University of Technology. During his studies he focused on composites and gained direct insight in the design and manufacturing process at two composite aircraft builders: EuroEnair in Den Helder and Isravation in Israel. In may 1998 he graduated by Prof.dr.ir. Th. de Jong on the damage tolerance of the Eaglet, a composite trainer-aircraft.



After his graduation he joined the Glare Research Group, which was formed half a year before as a cooperation between Structural Laminates (nowadays Fibre Metal Laminates Centre of Competence), Stork-Fokker, the National Aerospace Laboratory, and Delft University of Technology. The aim of the group was to make Glare ready for large-scale industrialisation, which was successfully realised with the introduction and application of Glare on the Airbus A380. From June 1998 till the end of the project in January 2003, the author performed research on diverse topics, such as impact, fatigue, static properties, and the influence of temperature, and developed several analytical calculation methods for Glare properties.

In March 2000 parallel to the research in the Glare Research Group, he started a Ph.D. research under supervision of the late Prof.dr.ir. A. Vlot from the Aircraft Materials department and Prof.dr.ir. R. de Borst from the Engineering Mechanics department. He is author of about 30 scientific publications, amongst which reports, journal and conference papers, and book contributions in the field of analytical and numerical modelling and testing of fibre metal laminates.

